Phytoplankton Functional Groups from Hyperspectral Satellite Data and its Application for Studying Phytoplankton Dynamics in Selected Oceanic Regions

Dissertation

submitted to the Department of Physics and Electrotechnics

of University of Bremen in partial fulfillments for the degree of

Doktor rer. nat.

presented by:

Alireza Sadeghi

University of Bremen, 2012

Auswertung von funktionellen Gruppen des Phytoplanktons aus hyperspektralen Satellitendaten und ihre Anwendung für die Untersuchung der Dynamik des Phytoplanktons in ausgewählten Meeresregionen

Dissertation

zur Erlangung des akademischen Grades

eines Doktor der Naturwissenschaften

(**Doktor rer. nat.**)

von Fachbereich Physik und Elektrotechnik der Universität Bremen

vorgelegt von:

Alireza Sadeghi

Universität Bremen, 2012

1. Gutachter: Prof. Dr. Astrid Bracher

Alfred-Wegener-Institut für Polar- und Meeresforschung (AWI), Bremerhaven

2. Gutachter: Prof. Dr. John P. Burrows

Institut für Umweltphysik (IUP), Universität Bremen, Bremen

Tag der Disputation: 17.04.2012

Selbstständigkeitserklärung:

Hiermit erkläre ich, Alireza Sadeghi, die vorliegende Arbeit ohne fremde Hilfe verfasst und nur die angegebene Literatur und die angegebenen Hilfsmittel verwendet zu haben.

To my wife Zahra; to my family

and to the memory of my mother

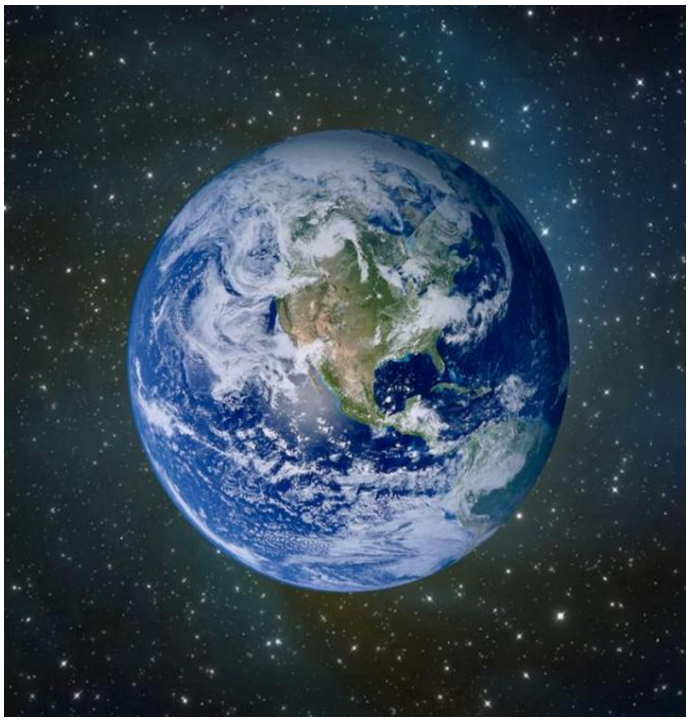

In respect for the people who struggle(d) for a better Planet

Abstract

Phytoplankton play a unique role in the marine ecosystem as the basis of the marine food-web. They are the main drivers of the biogeochemical cycles in the ocean, as well as influencing the ocean-atmosphere exchanges of carbon dioxide and particular gases and particles. Based on these exchanges, phytoplankton influence the chemistry of atmosphere and the balance of global climate. Moreover, through interaction with light (absorption and scattering), phytoplankton have significant a impact on the underwater optics, being also responsible for the variations in ocean color. However, performing all these roles depends significantly on the type of phytoplankton, as indeed they comprise of a wide range of species and groups, with different capabilities and different distribution patterns in the World Ocean. Therefore, distinguishing between different types of phytoplankton is important to improve the knowledge of their actual roles in the ocean and climate system. As the spectral patterns of light absorption (essential for photosynthesis) vary among different groups of phytoplankton, the backscatter light from ocean preserves the spectral fingerprints of the inhabitant groups of phytoplankton. This feature can be used to determine remotely different types of phytoplankton.

The purpose of this PhD-work was to improve a phytoplankton retrieval method, which was established to distinguish quantitatively major phytoplankton groups based on their absorption characteristics. The method, called PhytoDOAS, uses high spectrally resolved satellite data, provided by SCIAMACHY sensor. So far, by applying PhytoDOAS method to SCIAMACHY data, two main phytoplankton groups, diatoms and cyanobacteria, have been successfully distinguished. Through this work the method was improved to detect additionally coccolithophores, another important taxonomic group with significant biogeochemical functions. In this improvement, instead of the usual approach of the PhytoDOAS, which was based on single-target fitting, the simultaneous fitting of a certain set of phytoplankton groups was implemented within a wider wavelength window, thereby the new approach is called *multi-target fit*. Selection of the set of phytoplankton targets was according to the spectral analysis of absorption features of those groups that are most important with respect to the principal biogeochemical impacts, based on which marine microalgae are grouped as phytoplankton functional types, PFTs.

The improved method was successfully tested through detecting independently reported blooms of coccolithophores, as well as by comparison of PhytoDOAS coccolithophores with global distributions of Particulate Inorganic Carbon (PIC), which is used as a proxy of coccolithophores. As the next step of this PhD-work, the results of the improved PhytoDOAS method were used to investigate temporal variations of coccolithophore blooms in selected regions. Eight years of SCIAMACHY data, from 2003 to 2010, were processed by the PhytoDOAS *triple-target* mode to monitor the biomass of coccolithophores in three oceanic regions, characterized by the frequent occurrence of large blooms. Then the PhytoDOAS results, as monthly mean time-series, were compared to appropriate satellite products, including the total phytoplankton biomass (total *chl-a*) from GlobColour data-set and the PIC distribution from MODIS-Aqua.

To study the dynamics of coccolithophore blooms, the variations of coccolithophores, overall *chl-a* and PIC, as monthly mean time series, were investigated in the context of variations in the main oceanic geophysical parameters: sea-surface temperature (SST), mixed-layer depth (MLD) and surface wind speed. As a general result, it was observed that the inter-annual variations of the coccolithophore bloom cycles followed well the respective variations in the mentioned geophysical parameters, as they have been reported being associated with coccolithophore blooms. Observed anomalies were investigated based on the specific regional features of the geophysical conditions.

Using the results of regional time series, the hypothesis that close coccolithophore blooms succeed the diatom blooms was roughly approved, suggesting, however, a weekly-based averaging of coccolithophores and diatoms for a more precise analysis. It has been frequently reported that high reflectance from surface waters in coccolithophore rich areas affects the performance of standard *chl-a* algorithms. The regional time series studies of this thesis indicated an underestimation of total *chl-a* by the standard algorithm during the time of coccolithophore blooms. However, a comprehensive validation of the ocean color algorithms with in-situ phytoplankton data is needed to reach the final assessment of the short-comings.

Contents

Abstract . . . iii
List of publications . . . vii

1 Introduction **7**
1.1 The importance of phytoplankton: a brief overview . . . 7
1.2 Ocean color remote sensing . . . 7
1.2.1 Space-borne ocean color sensors . . . 7
1.2.2 Chlorophyll-based methods . . . 8
1.2.3 Satellite PFT retrieval and current algorithms . . . 11
1.3 Motivation and Objectives . . . 12
1.3.1 The necessity to improve PFTs' retrieval algorithms . . . 12
1.3.2 Towards an alternative PFT algorithm . . . 12
1.3.3 Objectives of this study . . . 13
1.4 Outline of the thesis . . . 13

2 Scientific Backgrounds **15**
2.1 Bio-Optics: a short overview . . . 15
2.1.1 Basic concepts and quantities in radiometry . . . 15
2.1.2 Apparent and inherent optical properties . . . 21
2.1.3 Absorption . . . 22
2.1.4 Scattering . . . 23
2.1.5 Classification of ocean waters . . . 30
2.2 Marine phytoplankton: general characteristics . . . 31
2.2.1 Phytoplankton taxonomic classification . . . 31
2.2.2 Alternative classifications of phytoplankton communities . . . 32
2.2.3 Phytoplankton and nutrients . . . 35
2.2.4 Seasonal cycles and mixed layer depth . . . 36
2.2.5 Phytoplankton blooms: definition and dynamics . . . 38
2.3 Environmental impacts of phytoplankton: a climate view . . . 40
2.3.1 Phytoplankton and the global carbon cycle: biological pump . . . 41
2.3.2 Phytoplankton and the global sulfur cycle: DMS emission . . . 45
2.3.3 Other emissions by phytoplankton: Halocarbons and VOCs . . . 48

3 Methodology **51**
3.1 Differential Optical Absorption Spectroscopy . . . 51
3.2 From DOAS to PhytoDOAS . . . 53
3.3 Material and Data . . . 55
3.3.1 Satellite data: SCIAMACHY . . . 55
3.3.2 Spectral data . . . 56
3.4 Improvements to PhytoDOAS: challenges and approaches . . . 56

3.5 SCIAMACHY sensor, the data provider of PhytoDOAS 64
3.5.1 General overview 64
3.5.2 Spectral characteristics: channels and resolutions 65
3.5.3 Spatial characteristics: viewing geometries 65

4 PFT retrievals using the PhytoDOAS Multi-target fit 67
4.1 PhytoDOAS monthly PFTs in comparison with other products: 2005 67
4.1.1 Global distributions of retrieved PFTs: 2005 monthly mean chl-a 67
4.1.2 PhytoDOAS coccolithophores vs. MODIS PIC: 2005 monthly means . . 70
4.1.3 PhytoDOAS diatoms in comparison with modeled data: 2005 monthly mean chl-a 71
4.1.4 PhytoDOAS cyanobacteria via single-target fit: 2005 monthly mean chl-a 75
4.2 PhytoDOAS annual PFTs in comparison with other products: 2005 79
4.2.1 Global distributions of retrieved PFTs: 2005 annual mean chl-a 79
4.2.2 PhytoDOAS coccolithophores and diatoms in comparison with products of MODIS and NOBM: 2005 annual means 79
4.2.3 PhytoDOAS PFTs in comparison with products of Hirata's PFT algorithm: 2005 annual mean chl-a 80

5 Application of PhytoDOAS to study the dynamics of coccolithophore blooms 85
5.1 Overview 85
5.1.1 Motivation 85
5.1.2 Objectives 86
5.2 Study setup 87
5.2.1 Initial tests 87
5.2.2 Selection of the study regions 89
5.2.3 Satellite data and geophysical variables 91
5.2.4 Further processing of the data 91
5.3 Results of PhytoDOAS coccolithophore blooms 93
5.3.1 Time series of biological and geophysical parameters 93
5.3.2 Interrelations between biological and geophysical parameters 99
5.3.3 Annual patterns of phytoplankton development associated with the developments of geophysical variables in selected regions 100
5.3.4 Climatological analysis 103
5.4 Conclusions of bloom study 105

6 General conclusions and Outlook 107
6.1 Summary 107
6.2 General conclusions 108
6.3 Future directions of the study 109

Appendix 111

Bibliography 123

Acknowledgements 139

List of publications

Peer-reviewed publications

Sadeghi A., Dinter T., Vountas M., Taylor B., Altenburg-Soppa M., and Bracher A. (2012). Remote sensing of coccolithophore blooms in selected oceanic regions using the PhytoDOAS method applied to hyper-spectral satellite data. Biogeosciences 9, 2127-2143, doi:10.5194/bg-9-2127-2012.

Sadeghi A., Dinter T., Vountas M., Taylor B., Altenburg-Soppa M., Peeken I., and Bracher A. (2012). Improvements to PhytoDOAS method for identification of major phytoplankton groups using high spectrally resolved satellite data. Ocean Sci., 8, 1055-1070, doi:10.5194/os-8-1055-2012.

Sadeghi A., Dinter T., Vountas M., Taylor B., and Bracher A. (2012). Improving the PhytoDOAS method to retrieve coccolithophores using hyper-spectral satellite data. In G. Lohmann, D. Wolf-Gladrow, J. Notholt, V. Unnithan, K. Grosfeld, and A. Wegner (eds.): Earth System Sciences: Bridging the gaps between disciplines | A multi-disciplinary Helmholtz Graduate Research School, Springer.

Conference and workshops contributions

Sadeghi A., Dinter T., Taylor B., Vountas M., Blum M., and Bracher A. (2011). Remote sensing of coccolithophore blooms in selected oceanic regions using PhytoDOAS method applied to hyper-spectral SCIAMACHY data. Proceedings of the "EARSeL 7th SIG-Imaging Spectroscopy Workshop, Edinburgh, 13 Apr 2011".

Sadeghi A., Dinter T., Vountas M., Schmitt B., and Bracher A. (2010). Improvements to PhytoDOAS method for identification of major phytoplankton groups using high spectrally resolved data. Talk: COSPAR 38th COSPAR Scientific Assembly, Bremen, Germany, 22 July 2010.

Sadeghi A., Dinter T., Vountas M., and Bracher A. (2011). Remote sensing of coccolithophore blooms in selected oceanic regions using PhytoDOAS method applied to hyper-spectral satellite data. Poster: EGU General Assembly 2011, Vienna, 4 Apr 2011.

Sadeghi A., Dinter T., Taylor B., Vountas M., Blum M., and Bracher A. (2011). Remote sensing of coccolithophore blooms in selected oceanic regions using PhytoDOAS method applied to hyper-spectral SCIAMACHY data. Talk: EARSeL 7th SIG-Imaging Spectroscopy Workshop, Edinburgh, 13 Apr 2011.

Sadeghi A., Dinter T., Taylor B. Vountas M., and Bracher A. (2011). PhytoDOAS: an extension of DOAS to aquatic media for retrieving phytoplankton groups from hyperspectral satellite data. Poster: 5th International DOAS Workshop, Landesmuseum Mainz, 14 July 2011.

Sadeghi A., Dinter T., Taylor B. Vountas M., and Bracher A. (2011). Marine phytoplankton groups retrieval using hyperspectral satellite data. Talk: IUP ocean and Atmosphere Seminar, IUP, Bremen, 21 June 2011.

Dinter T., Sadeghi A., Vountas M., Blum M., Bracher A., and Taylor B. (2011). Marine phytoplankton groups retrieval using hyperspectral satellite data. Talk: AWI Climate Seminar, AWI, Bremerhaven, 17 June 2011.

Bracher A., Sadeghi A., Dinter T., Taylor B., Vountas M., Röttgers R., and Peeken I. (2011). Global quantitative observation of various phytoplankton groups from space by analysis of hyperspectral satellite data. Talk: Earth System Science Seminar, Hokkaido University, Sapporo, Japan, 21 Nov 2011.

Bracher A., Sadeghi A., Dinter T., Taylor B., Röttgers R., Peeken I., Vountas M., and Ye Y. (2010). Phytoplankton groups from space using PhytoDOAS: Improvements by multi-target fitting, yearly data set, preliminary validation and first application. Talk: Ocean Optics XX, 30 Sep. 2010, Captain Cook Conference Center, Anchorage, Alaska, U.S.A.

Bracher A., Sadeghi A., Altenburg Soppa M., Dinter T., and Taylor B. (2011). Proposal for using OLCI/sentinel-3 data for retrieving different phytoplankton groups from space by including information obtained via PhytoDOAS products retrieved from SCIAMACHY and sentinel-5 precursor (TROPOMI). Poster: Sen4Sci, ESA-ESRIN, Frascati, 22 Mar 2011.

Dinter T., Sadeghi A., Vountas M., Blum M., Schmitt B., and Bracher A. (2010). Exploiting Hyper Spectral Satellite Measurements to Deduce Oceanic Components using Phytodoas. In: Poster: ESA Living Planet Symposium, 28 Jun-2 Jul 2010, Bergen, Norway.

Bracher A., Sadeghi A., Dinter T., Taylor B., Vountas M., Röttgers R., and Peeken I. (2011). The PhytoDOAS technique to retrieve phytoplankton groups from hyperspectral satellite data. Talk: Satellite PFT Algorithm Intercomparison Workshop, Hokkaido University, Sapporo, Japan, 22 Nov 2011.

Bracher A., Sadeghi A., Dinter T., Taylor B., Torrecilla E., Krüger K., Wittke F., and Quack B. (2011). Temporal and spatial dynamics of phytoplankton composition in the Western Pacific and its link to halocarbon emissions. Poster: Earth Observation for Ocean-Atmosphere Interactions Science Conference, ESRIN, Frascati, Italy, 29 Nov-2 Dec 2011.

Dinter T., Sadeghi A., Taylor B., Vountas M., Blum M., and Bracher A. (2011). Retrieval of oceanic components with Phytodoas by using hyper spectral satellite measurements. Poster: EARSeL 7th SIG-Imaging Spectroscopy Workshop, Edinburgh, 12 Apr 2011.

Bracher A., Dinter T., Sadeghi A., Schmitt B., Vountas M., Röttgers R., Peeken I., and Ye Y. (2010). Phytoplanakton groups from space using PhytoDOAS: Improvements by multi-target fitting, yearly data set, validation and first application. In: Proceedings of the Ocean Optics XX, Anchorage, Alaska, U.S.A.

Bracher A., Dinter T., Sadeghi A., Schmitt B., Peeken I. Ye Y., Vountas M., Burrows J.-P., and Röttgers R. (2010). SCIAMACHY PhytoDOAS: Global data set of different phytoplankton groups: retrieval, validation and first application. In: Proceedings "Oceans from Space" Venice 2010, Publication Office of the European Union, doi: 10.2788/8394, pp. 49-50.

Bracher A., Dinter T., Sadeghi A., Schmitt B., Peeken I. Ye Y., Vountas M., and Röttgers R. (2010). SCIAMACHY PhytoDOAS: Global data set of different phytoplankton groups: retrieval and first application. Poster: Oceans from Space, 27 April 2010, Venice, Italy.

Bracher A., Dinter T., Taylor B., Sadeghi A., Quack B., and Torrecilla E. (2011). Phytoplankton composition and distribution in the Western Pacific: Insight on temporal and spatial dynamics from in-situ and satellite data. Talk: EGU General Assembly 2011, Vienna, 5 Apr 2011.

Bracher A., Dinter T., Taylor B., Sadeghi A., and Torrecilla E. (2011). In-situ und Satelliten Phytoplankton-Messugen im West-Pazifik. Extended abstract of BMBF Statusseminar "Meeresforschung mit FS Sonne", Bundesanstalt für Geowissenschaften und Rohstoffe (BGR), Hannover, 9-10 Feb 2011.

Bracher A., Dinter T., Taylor B., and Sadeghi A. (2011). Global Assessment of phytoplankton groups from satellite data using PhytoDOAS. Talk: Marine Resources and Beyond - BluePhotonics2, IMARE, Bremerhaven, 6 Sep 2011.

Bracher A., Dinter T., Schmitt B., Peeken I., Röttgers R., Sadeghi A., Vountas M., and Ye Y. (2010). Global yearly observation of phytoplanakton groups using PhytoDOAS on SCIAMACHY data: validation and first application. Talk: ESA Living Planet Symposium, 29 Jun 2010, Bergen, Norway.

Bracher A., Dinter T., Schmitt B., Peeken I., Röttgers R., Sadeghi A., Vountas M., and Ye Y. (2010). Global yearly observation of phytoplankton groups using PhytoDOAS on SCIAMACHY data: validation and first application. In: Proceedings of the ESA Living Planet Symposium, 28 Jun-2 Jul 2010, Bergen, Norway, ESA Publications Division, Nordwijk, The Netherlands, SP-686.

Bracher A., Taylor B., Dinter T., Bange H., Helmke H., Krüger K., Peeken I., Quack B., Sadeghi A., and Wittke F. (2011). Phytoplankton composition and relation to in water VSLS and DMS during Transbrom/SONNE – preliminary results.Talk: EU project SHIVA Annual Meeting, Paris, France, 5 Jul 2011.

Bracher A., Taylor B., Dinter T., Bange H., Helmke H., Krüger K., Peeken I., Quack B., Sadeghi A., and Wittke F. (2011). Phytoplankton as source of VSLS studied during two cruises: Poseidon #399 and Transbrom Sonne. Talk: EU project SHIVA Annual Meeting, Leeds, United Kingdom, 14 Jul 2011.

Chapter 1

Introduction

1.1 The importance of phytoplankton: a brief overview

Marine phytoplankton play various important roles not only in the World Ocean but also in the global climate. As the main oceanic primary producers, phytoplankton form the basis of the ocean food web and therefore are vital for the marine ecosystems. Moreover, phytoplankton have major contribution to the global carbon cycle by acting as a biological pump [Raven and Falkowski, 1999] of organic matter to the deep ocean (see sec. 2.3.1). Thereby, for instance, phytoplankton influence the rate of sea-air CO_2 exchange, phytoplankton affect the amount of carbon in the atmosphere. More precisely, through photosynthesis, dissolved carbon dioxide is taken up and released as organic carbon to ocean environment, where it can directly sink down or indirectly transported through other trophic levels to the ocean floor, or just is recycled in the upper ocean (see Fig. 1.1). Phytoplankton are widely involved in the processes of trace gas- and particle emissions from the marine environments into the atmosphere, among which the most notable substances are dimethylsulfide (DMS), volatile halocarbons and biogenic hydrocarbons (see sec. 2.3.2 and 2.3.3). Particularly, due to the DMS emission, phytoplankton contribute strongly in the global sulfur cycle [Andreae, 1990] (see Fig. 2.11 in Chapter 2). Participating in the global carbon and sulfur cycles connects phytoplankton directly to the global climate and introduces them as a biogenic regulating factor. On the other hand, apart from regulating the global climate, it has been revealed that marine phytoplankton are also very sensitive to global warming [Dufresnes et al., 2002; Sarmiento et al., 2004], suggesting the study of dynamics of phytoplankton growth as a proxy for the actual rate of climate change. In the next chapter, general information is given on the contribution of phytoplankton in the global carbon (sec. 2.3.1) and sulfur cycles (sec. 2.3.2), as well as on the mechanisms through which phytoplankton influence the balance of global climate.

1.2 Ocean color remote sensing

1.2.1 Space-borne ocean color sensors

The most suitable approach to monitor the global distribution of marine phytoplankton and to estimate their total biomass is the use of satellite data (e.g., Platt and Herman [1983]; Aiken et al. [1992]; Sathyendranath et al. [2001]), which corresponds to the field of ocean color remote sensing, developed since the 1980s (e.g., see IOCCG report 7, 2008). The principle behind is that the color of the ocean (more generally, the backscattering light) carries information about the water's optical components, including the pigment and particulate content of the water. The most well-known ocean color satellite sensors have been CZCS (Coastal Zone Color Scanner, 1978-1986), SeaWiFS (Sea-viewing Wide Field-of-view Sensor, 1997-present), MODIS

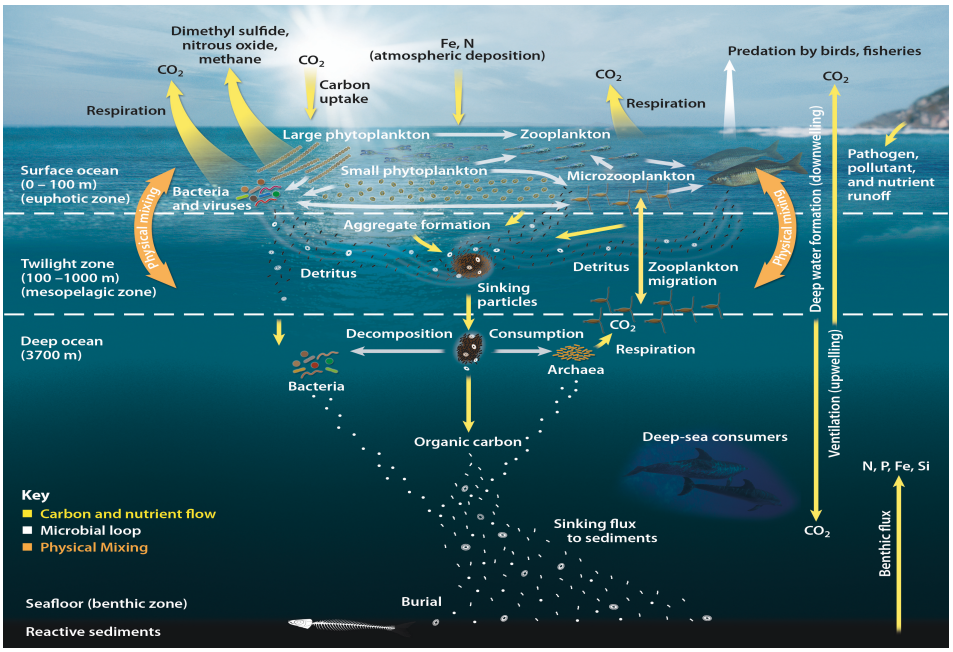

Figure 1.1: A simple scheme of the major biogeochemical cycles in ocean, including the role of phytoplankton in ocean's carbon cycle and marine food web. Courtesy to U.S. Department of Energy Genomic Science program (`http://genomicscience.energy.gov`).

(Moderate Resolution Imaging Spectroradiometers, Terra/2000-present and Aqua/2002-present) and MERIS (Medium Resolution Imaging Spectrometer, 2002-present). Applying ocean color sensors, long-term records of aquatic parameters are provided remotely on a global scale with a vast range data products, covering essential climate variables [Maritorena et al., 2010]. There are a large variety of applications for ocean color data products applications; e.g., to improve the understanding of ocean biogeochemistry and marine ecosystem dynamics; to assess fisheries productivity and the distribution of harmful algal blooms; and to be used as input data for mesoscale open ocean processes and ocean modeling [McClain, 2009].

1.2.2 Chlorophyll-based methods

In retrieving phytoplankton biomass, most bio-optical ocean color algorithms (e.g., O'Reilly et al. [1998]) derive the concentration of chlorophyll *a*, *chl-a* (see Fig. 1.2). The reason is that *chl-a* is a common photosynthetic pigment among all phytoplankton species [Kirk, 1994], and therefore is generally used as the measure of phytoplankton biomass [Falkowski et al., 1998]. According to Morel and Gordon [1980] there are three different methods for estimating the *chl-a* concentration or the concentrations of other optically active constituents of the water in open oceans (or *Case-1* waters, see sec. 2.1.5): purely empirical methods, analytical methods and semi-empirical methods, which are briefly summarized below: [1]

purely empirical methods: The purely empirical models are based on extracting direct relations between optical field measurements (of reflectance or water-leaving radiance) and pigment concentrations (mainly chlorophylls). More precisely, these models establish a statistical relationship

[1] The brief summary given here, for the classification of chlorophyll algorithms, has been adapted from Algorithm Theoretical Basis Document (ATBD 2.9) for the MERIS sensor provided by Morel and Antoine [1998]. The radiometric concepts and quantities represented in this summary are defined in sec. 2.1.1.

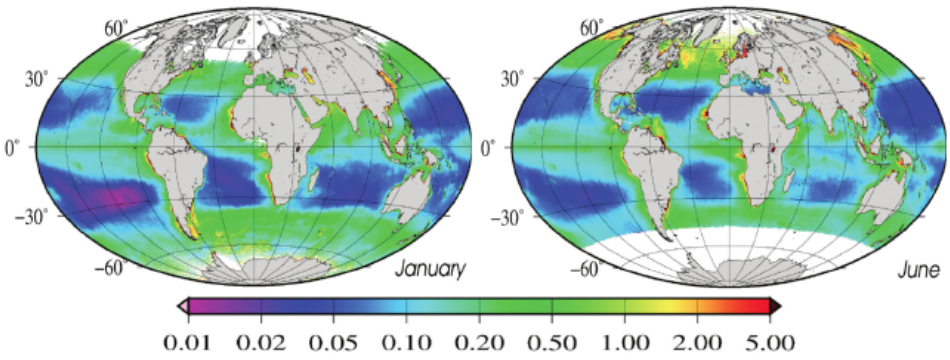

Figure 1.2: SeaWiFS' global climatology of mean *chl-a* $[mg\,m^{-3}]$ for January and June, from 1997 to 2008. Courtesy to Alvain et al. [2010].

between a certain ratio of spectral reflectances and chlorophyll concentrations. The statistical relationship is obtained from analyzing large sets of bio-optical in-situ measurements. This leads to a linear regression (log-log) curve, based on which the chlorophyll content of seawater is presented as a function of reflectances ratio. The final chlorophyll product can be formulated as follows:

$$[Chl] = A\,[\,\frac{R(\lambda_i)}{R(\lambda_j)}\,]^B \tag{1.1}$$

where $[Chl]$ refers to the chlorophyll concentration; $R(\lambda_i)$ and $R(\lambda_j)$ represent the spectral reflectances at certain wavelengths in the blue and green bands, respectively; and the parameters A and B come from a linear regression analysis. The most sensitive *blue-to-green* ratio, compared to any other ratio, is corresponding to the $\frac{R(445)}{R(550)}$ [Gordon and Morel, 1983], although some alternative wavelengths have also been repeatedly utilized (e.g., 440, 555 and, 560 nm). This method was used as the basis for the chlorophyll algorithms in early generation of ocean color sensors, such as CZCS. However, it has been revealed that there are large uncertainties (more than 35%) associated with these methods [Morel and Antoine, 1998; Lee and Hu, 2006].

analytical methods: In analytical approaches, based on the additivity principle, the inherent optical properties (IOPs) of water, such as absorption and backscattering coefficients (a and b_b, respectively), are split into all optical components that contribute partially to the ocean's backscatter radiation:

$$a = a_w + a^\star_\phi[Chl] + a^\star_g[G] + a^\star_{nap}[Nap] + ... \tag{1.2}$$

$$b_b = b_{bw} + b^\star_{b\phi}[Chl] + b^\star_{bg}[G] + b^\star_{bnap}[Nap] + ... \tag{1.3}$$

where the subscripts w, ϕ, g and nap refer to water, phytoplankton, *Gelbstoff* and non-algal particulate matter, respectively; the star subscripts refer to the absorption/scattering coefficients normalized by concentrations of respective components (specific absorption/scattering coefficients); and the quantities within the square-brackets represent the concentrations of different components. Due to the lack of precise knowledge of the specific coefficients (as they are variable) and the absence of tight relationships between the concentrations, this rigorous approach is too complicated for practical purposes. Therefore, the entirely analytical approach, still very uncertain, has to be kept for advanced research and products [Morel and Antoine, 1998].

semi-empirical methods: There are approximate models, which rely realistically on the present state of bio-optical knowledge. A semi-empirical method (or alternatively, semi-analytical approach) uses some bio-optical models to simplify the above equations into following forms:

$$a = a_w + F_a\,[Chl] \tag{1.4}$$
$$b_b = b_{bw} + F_{bb}\,[Chl] \tag{1.5}$$

where average relationships (for Case-1 waters) between other concentrations and chlorophyll concentration (i.e., $[Chl]$) are merged within the F_a function; similarly, contributions of phytoplankton, Gelbstoff and non-algal particles are merged within the F_{bb}, which is itself a certain function of $[Chl]$. Then, based on Morel and Prieur [1977], the reflectance at the null depth (just below the water surface) is approximated:

$$R(0^-, \lambda) = f\,\frac{b_b(\lambda)}{a(\lambda)} \tag{1.6}$$

where f is an empirical value (between 0.3 and 0.5). In practice, since determination of spectrally detailed absorption of seawater is difficult, the absorption term in Eq. 1.6 is parameterized and replaced by the diffuse attenuation coefficient of downwelling irradiance (K_d) [Gordon et al., 1988]. Subsequent algorithms are based on the variation of the ratio: $\frac{R(\lambda_i)}{R(\lambda_j)}$ (denoted hereafter by $\rho_{i,j}$) with chlorophyll concentration. It must be mentioned that for substituting λ_i and λ_j into $\rho_{i,j}$, a range of values are utilized by different algorithms. The output chlorophyll biomass is then given under a polynomial form as follows:

$$Log_{10}[Chl] = \sum_{x=0}^{n} A_x\,(Log_{10}\,\rho_{i,j})^x \tag{1.7}$$

where A_x and x are parameters which are fixed variously by different algorithms.

Based on semi-empirical approaches, various models were developed (e.g., by Morel [1988] and Gordon et al. [1988]). Validation of such models, however, requires to compare their predictions with large sets of in-situ measurements. Fig. 1.3 illustrates an example of these types of validation.

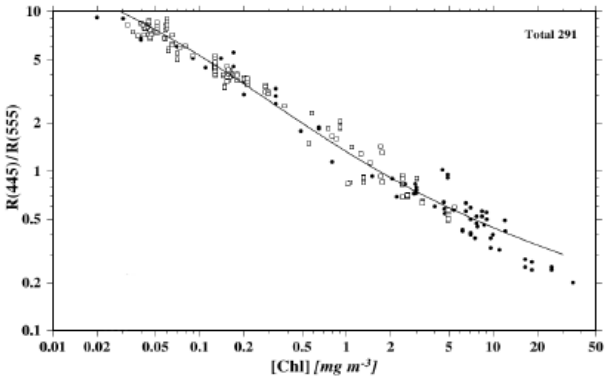

Figure 1.3: The ratio of reflectances as a function of chlorophyll concentrations. The curve corresponds to a semi-analytical approach, for which this typical comparison serves as part of the validation process. Courtesy to Morel and Antoine [1998].

The major global-oriented ocean color methods (e.g., SeaWiFS' OC4.v4 empirical algorithm [O'Reilly et al., 2000] and MODIS's OC3M semi-analytic algorithm [Carder et al., 2004]), rely in various extent on empirical approaches to relate satellite remote-sensing reflectance (R_{rs}) to the in-situ geophysical parameters or to the inherent optical properties of seawater. This feature, which is also common in the regional-oriented algorithms (e.g., Arrigo et al. [1998]), requires to access and process large sets of bio-optical data from field measurements. Moreover, the parameterizations utilized by theses methods involve several steps of approximations. And finally, these algorithms are basically formed - to different extents- through analyzing regionally-collected bio-optical data.

1.2.3 Satellite PFT retrieval and current algorithms

Over the past decade, in the field of ocean color remote sensing, attentions have been also drawn to the extraction of more information about the marine microscopic algae (besides chlorophyll content). For instance, in this context, remote identification of phytoplankton size classes (PSCs) and phytoplankton functional types (PFTs) have also become the topics of interests. The terms PSCs and PFTs refer to the certain approaches for classification of phytoplankton groups [Nair et al., 2008]. In the size-class approach phytoplankton are categorized based on their cell-sizes (see sec. 2.2.2); whereas in the function-based approach phytoplankton are grouped based on their specific impacts on the biogeochemical cycles (see sec. 2.2.2). The main reason for the necessity of going beyond the *chl-a* retrieval is that different phytoplankton groups (based on size, composition and physiology) are known to have different biogeochemical impacts and hence taking various roles in marine ecosystems, primary production (carbon fixation) and biological pump (carbon export). More precisely, total phytoplankton biomass represented as *chl-a* concentration can not directly be converted into carbon biomass, which is currently used in modeling of marine carbon cycle. For instance, the specific role of diatoms in the marine carbon and silicate export, due to their large cells and heavy silicate skeletons (e.g., Lochte et al. [1993]; Bopp et al. [2005]; Nelson et al. [1995]) or the effective role of the coccolithophore *E. huxleyi* in the marine sulfur cycle (see sec. 2.3.2), as well as in the carbonate pump (e.g., Thierstein and Young [2004]; Malin and Steinke [2004]; see also sec. 2.3.1). Therefore, recent ocean carbon studies tried to conjunct the quantification of carbon pools (PIC and POC) with the estimation of PFTs' spatial distribution and temporal variation (e.g., Gregg et al. [2003]; Quere et al. [2005]), since there have been also well-known methods to estimate PIC and POC from ocean color data (e.g., Stramski et al. [1999] for POC and Balch et al. [2005] for POC). Moreover, apart from the good performance of satellite-derived *chl-a*, overall on the global scale (e.g., Gregg and Casey [2004]), regional differences can be large. For instance, Mitchell and Holm-Hansen [1991] showed that the standard CZCS pigment algorithm underestimated concentrations near the Antarctic Peninsula by $50-70\%$. This was assigned to the regional differences in pigment absorption and scattering, which in turn can be a result of variety in the dominant phytoplankton types [Garcia et al., 2005]. Therefore, even for improving the retrieval accuracy of *chl-a*, the knowledge on PFTs' distribution is essential.

On the other hand, the knowledge of *chl-a* content alone is not sufficient to distinguish and/or assess quantitatively specific phytoplankton blooms with large environmental impacts, e.g., harmful algal blooms (HABs). On this background, several attempts have been done to retrieve PFTs and also PSCs from space-borne sensors, oriented in various purposes: detection of harmful algal blooms [Millie et al., 1997], global-scale mapping of dominant phytoplankton groups (Alvain et al. [2005]) and improving the accuracy of satellite-derived marine *chl-a* or marine carbon (e.g., Sathyendranath et al. [2004]; Devred et al. [2006]; Alvain et al. [2005]; Aiken et al. [2007]; Raitsos et al. [2008]; Bracher et al. [2009]; Hirata et al. [2011] for PFTs and Devred et al. [2006]; Ciotti and Bricaud [2006]; Uitz et al. [2006]; Hirata et al. [2008]; Brewin et al. [2010a] for PSCs). Most of these studies relate the alterations observed in optical parameters to the variations measured

in pigment compositions, cell size and phytoplankton populations. Some studies have suggested the application of a regionally parameterized algorithm instead of the universal retrieval algorithm (e.g., Sathyendranath et al. [2004]). In general, two main approaches for retrieving PFTs/PSCs are *chl-a*-based and optic-based, however, according to Brewin et al. [2011], current retrieval methods of PFTs and PSCs can be categorized more precisely based on following approaches:

- **spectral response**: the scattering or absorption footprints of phytoplankton on the incident light are analyzed as the differences in the spectral shapes/magnitudes of backscattering radiation to derive PFTs or PSCs. For instance: Sathyendranath et al. [2004]; Alvain et al. [2005, 2008]; Ciotti and Bricaud [2006]; Bracher et al. [2009]; Brewin et al. [2010a];
- **chlorophyll abundance**: the magnitude of *chl-a* biomass or light absorption are used to derive PSCs or PFTs. For instance: Sathyendranath et al. [2001]; Uitz et al. [2006]; Devred et al. [2006]; Aiken et al. [2007]; Brewin et al. [2010b]; Hirata et al. [2011]; Devred et al. [2011];
- **ecological parameters**: environmental parameters, such as temperature and wind-stress are combined with bio-optical information to derive PFTs. For instance: Raitsos et al. [2008];
- **particle size distribution**: particle backscattering signal retrieved from space-borne sensors are used to derive PSCs and PFTs. For instance: Hirata et al. [2008]; Kostadinov et al. [2009, 2010].

1.3 Motivation and Objectives

1.3.1 The necessity to improve PFTs' retrieval algorithms

Nevertheless, as it was mentioned by Platt et al. [2006], detection of different phytoplankton communities from satellite is still a major challenge in ocean optics. In this respect, complications partly arise due to the shortage of in-situ data required to validate the respective remote sensing algorithms. In particular, Lee and Hu [2006] showed that the satellite-derived *chl-a* carries large errors which vary spatially and temporary. Although the average accuracy of ocean color data products in open ocean, accepted by the international missions, is $\pm 35\%$ for chlorophyll-a [McClain, 2009] (and $\pm 5\%$ for water-leaving radiances), according to Lee and Hu [2006], this amount can reach up to 60% for a wide range of oceanic regions, varying with seasons. It means that the PFTs/PSCs methods relying on *chl-a* abundance obtained from ocean color sensors do carry also this uncertainties.

Moreover, most of the methods linked to the empirical or semi-analytic algorithms are also confronting the limitations associated with those algorithms (e.g., dependency on large sets of a-priori in-situ data); so that they need to collect the additional sets of in-situ data, including regional distributions of PFTs and bio-optical parameters. The methods providing dominant phytoplankton (e.g., Alvain et al. [2005]) represent their results as the percentage of abundance of the dominant species, without any information on the *chl-a* content of the dominant species or the contributions of other species living together with dominant ones (even though they might have high percentages). These facts have motivated more studies recently to improve current PFTs' retrieval algorithms.

1.3.2 Towards an alternative PFT algorithm

In response to this necessity, Bracher et al. [2009] established an alternative method, called Phyto-DOAS (explained in Chapter 3), which is essentially different from the well-known ocean-color

algorithms in several basic features: using hyperspectral radiation measurements (with a high spectral resolution) on a large wavelength range, instead of few wavelength bands reflectance data; being almost independent of the a-priori large data sets, being independent of the *chl-a* products of the major ocean color sensors; assuming multiple-typed of phytoplankton populations, existing simultaneously; and more potential to take the water penetration depth into account (see Chapter 3; described originally by Bracher et al. [2009]). The method is based on detecting variations in specific absorption spectra of target PFTs. Distinguishing fine spectral differences in absorption footprints of different species over a wide wavelength range requires to utilize the data of a hyperspectral sensor, which has been so far provided by SCIAMACHY, a sensor on-board ENVISAT. Applying the PhytoDOAS method on the SCIAMACHY data, global distribution of two major PFTs, diatoms and cyanobacteria, have been quantitatively derived by Bracher et al. [2009] (more details will be given in Chapter 3).

The study presented here has been dedicated to improving the PhytoDOAS method (as an extension of DOAS, Differential Optical Absorption Spectroscopy, to the aquatic media) in order to discriminate more PFTs from SCIAMACHY data. More precisely, in this study solutions have been developed to extend the application of PhytoDOAS onto two other major phytoplankton functional types: coccolithophores and dinoflagellates.

1.3.3 Objectives of this study

Generally speaking, the main objective of this study has been to improve the PhytoDOAS method for detecting more PFTs. However, absorption spectra of phytoplankton species contain strong spectral correlations in any operating wavelength window (contrary to the high-frequency spectral behavior in absorption cross-sections of atmospheric trace gases, which make them fairly straightforward targets to be discriminated by DOAS). This fact is a major challenge in the retrieval of phytoplankton functional types by this method. Regarding this technical background, the objectives of this work can be expressed as follows:

- to develop methods to overcome the spectral correlations between target PFTs, whose final set itself has to be determined through the implemented approaches.
- to process all available SCIAMACHY data with the improved PhytoDOAS in order to obtain global distributions of target PFTs over a long period, as a data-set of monthly mean *chl-a* concentration of specific targets.
- to test the functionality of the improved method by utilizing that for the quantitative identification of major algal blooms with respect to the target PFTs. This task has been done (as a case study) by focusing on coccolithophore blooms in selected oceanic regions (due to their vital environmental impacts and also their frequent occurrences, which make them an available target for detection).
- to investigate and expand the potentials of PhytoDOAS for studying phytoplankton dynamics associated with the variations in environmental factors, which has recently received high attentions in conjunction with climate research.

1.4 Outline of the thesis

The thesis contains six chapters, which have been arranged to cover the work content as follows:

- In Chapter 1 (as seen so far) after a very short glance on the importance of phytoplankton, the motivation and objectives of this study have been presented. Through this very short chapter, a brief overview of the research field and the major methods has been given.

- In Chapter 2 scientific backgrounds of this work (i.e., bio-optics) are briefly presented. The chapter includes three sections, as follows: (a) principal concepts and radiometric quantities concerning to ocean optics and ocean color remote sensing; (b) basic characteristics of phytoplankton, including different classification methods (based on biological taxonomy, cell size and biogeochemical functions), ecological requirements and responses of phytoplankton in marine systems; (c) environmental impacts of phytoplankton, including their roles in biogeochemical cycles (the global carbon and sulfur cycles) and trace gas emission, by focusing on DMS production and its climatic consequences.

- In Chapter 3, to describe the methodology of the study, first the physical core of the retrieval method (i.e., DOAS) is explained in details, from which it is indicated how PhytoDOAS was derived from DOAS. Then the input and output data utilized in PhytoDOAS are introduced, and finally the approaches used for the method improvement are represented. At the end of the chapter, general features and technical specifications of SCIAMACHY sensor, the source of satellite data for PhytoDOAS, are briefly introduced.

- In Chapter 4 the results of applying the improved PhytoDOAS to SCIAMACHY data are presented. The retrieval results include global distribution of target PFTs, coccolithophores, diatoms, dinoflagellates (in addition to cyanobacteria), in 2005. The main results are shown as monthly mean *chl-a* and are compared separately with respective data from other satellite products or models. The same results for the year 2008, associated with respective comparisons, are provided in the appendix.

- In Chapter 5 the application of the improved PhytoDOAS in monitoring coccolithophore blooms is presented as a case study. The chapter contains the study setup and the results, which have been obtained from processing eight years of SCIAMACHY data over three selected (coccolithophore rich) areas. Moreover, the results represent also the investigation of phytoplankton dynamics over selected regions in the context of variations of main oceanic geophysical parameters. All data are shown as monthly mean time series over an 8-year period (2003 to 2010).

- In Chapter 6 an overall conclusion is briefly given along with some further directions of this study as the development perspectives of this study, which can be part of the future works to expand the precision, capabilities and applications of the PhytoDOAS method; e.g., using SCIATRAN (a coupled ocean-atmosphere optical model, based on radiative transfer theory); or applying Longhurst's biogeographical provinces to the method.

Chapter 2

Scientific Backgrounds

This chapter provides an overview to the theoretical basis of the ocean optics in relation with the phytoplankton bio-optical impacts. These principal concepts and quantities are essential in remote sensing of phytoplankton contents and optical properties of seawaters and most of them are directly or indirectly utilized in the following chapters. Moreover, the background information on the role of phytoplankton in the ocean, both in biological and optical aspects, is briefly introduced, as well as the main environmental factors controlling the dynamics of phytoplankton.

2.1 Bio-Optics: a short overview

2.1.1 Basic concepts and quantities in radiometry

Radiometry[1] is the science of measuring light in any position of the electromagnetic spectrum. Electromagnetic radiation transports energy through space, hence is called also *radiant energy*, Q, measured in $joules$, $[j]$. In natural media the radiation field mostly refers to the solar radiation, in which the visible spectral range (from about $400\,nm$ to about $740\,nm$) has a vital role in photosynthetic processes of the biosphere. For introducing the properties of an electromagnetic radiation field, the *spectral radiant energy* is a basic quantity to start with, which is defined as the amount of radiant energy per unit wavelength interval at wavelength λ:

$$Q(\lambda) = \frac{dQ}{d\lambda} \qquad [j\,nm^{-1}] \tag{2.1}$$

However, the amount of incident (solar) light is often introduced by the *radiant flux*, Φ, from which other radiometric quantities can be extracted. Therefore, radiant flux is a good point to start the basic definitions with:

Radiant Flux: *Radiant flux*, Φ, is the time rate of the flow of the radiant energy (radiation) through a hypothetical surface:

$$\Phi = \frac{dQ}{dt} \tag{2.2}$$

Φ is measured in watts ($[W]$, equivalent to joule per second: $[Js^{-1}]$); it might also be presented by *quanta* per second. For monochromatic applications, the *spectral radiant flux* might be more relevant, which can be derived from radiant flux as follows:

[1] The bio-optical materials used in this section have been mostly adapted from Kirk [1994] and Mobley [1994].

$$\Phi(\lambda) = \frac{d\Phi}{d\lambda} \tag{2.3}$$

Radiant Intensity: *Radiant intensity*, I, is a measure of the radiant flux per unit solid angle in a certain direction. Radiant intensity can be defined for a light source or at a point in the light field, the latter of which being referred as *field radiant intensity*. The field radiant intensity is the radiant flux at a given point in a specified direction in an infinitesimal cone containing that direction:

$$I = \frac{d\Phi}{d\omega} \quad ; \quad I(\lambda) = \frac{d\Phi(\lambda)}{d\omega\, d\lambda} \tag{2.4}$$

where ω stands for the solid angle. The radiant intensity has units of $[W\ sr^{-1}]$ (watt per *steradian*).

Radiance: *Radiance*, L, at a point in a filed is the radiant flux in a given direction per unit solid angle per unit area, perpendicular to the direction of the light propagation. Since the direction within the light field is defined by the zenith angle, θ, and the azimuth angle, ϕ, the definition of radiance is also given on this basis:

$$L(\theta, \phi) = \frac{d^2\Phi}{dS\, \cos\theta\, d\omega} \quad ; \quad L(\lambda, \theta, \phi) = \frac{d^3\Phi}{dS\, \cos\theta\, d\omega\, d\lambda} \tag{2.5}$$

where dS is an infinitesimal surface element and the equation on the right hand side corresponds to the definition of the *spectral radiance* and $d\omega = 2\pi\, \sin\theta\, d\theta$ stands for infinitesimal element of solid angle (see Fig. 2.1).

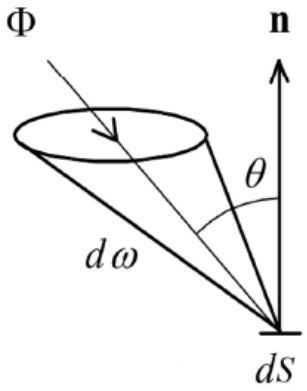

Figure 2.1: Scheme of a radiant flux, Φ, incident on a surface element of dS with the normal vector of $\vec{n}$. The scheme indicates also the solid angle element, $d\omega$, and the zenith angle, θ, which are used in the definition of the radiance.

Radiance is expressed by units of $[W\, m^{-2}\, sr^{-1}]$. The angular structure of the light field is determined by the variation of radiance with θ and ϕ.

Irradiance: *Irradiance*, E, is defined as the radiant flux per unit area of the surface. For a given point with the infinitesimal element of dS around that, irradiance is defined as follows:

$$E = \frac{d\Phi}{dS} \quad ; \quad E(\lambda) = \frac{d^2\Phi}{dS\, d\lambda} \tag{2.6}$$

where the equation on the right corresponds to the *spectral irradiance*. Irradiance, called also *radiant flux density*, is measured in $[W\, m^{-2}]$.

For a given horizontal surface, e.g., the air-water interface, depending on the direction of the light, the total *downward irradiance* and the total *upward irradiance* (E_d and E_u, respectively) can be defined as follows:

$$E_d(\lambda) = \int_{2\pi} L(\lambda, \theta, \phi) \cos\theta \, d\omega \quad ; \quad E_u(\lambda) = -\int_{-2\pi} L(\lambda, \theta, \phi) \cos\theta \, d\omega \tag{2.7}$$

where for E_d (left equation) the integration with respect to solid angle is over the whole upper hemisphere ($0 \leq \theta \leq 90°$); and for E_u the integration is over the lower hemisphere ($90° \leq \theta \leq 180°$).

Thereby, as an important quantity for aquatic media, the *net downward irradiance*, $\vec{E}$, can be presented as the difference of E_d and E_u:

$$\vec{E}(\lambda) = E_d(\lambda) - E_u(\lambda) = \int_{4\pi} L(\lambda, \theta, \phi) \cos\theta \, d\omega \tag{2.8}$$

for which the integration of $L(\lambda, \theta, \phi)cos\theta$ is done over all directions.

Scalar Irradiance: *Scalar irradiance*, E_0, is a measure of the radiant intensity at a point, containing radiation from all directions equally. Thereby, E_0 is computed by integrating the radiance distribution at a point over all directions around it:

$$E_0(\lambda) = \int_{4\pi} L(\lambda, \theta, \phi) \, d\omega \tag{2.9}$$

Irradiance Reflectance: Based on the definition of upward and downward irradiances, the *spectral irradiance reflectance* is defined [Mobley, 1994] as the ratio of the upward and downward irradiances at a certain depth for a specific wavelength:

$$R(z, \lambda) = \frac{E_u(z, \lambda)}{E_d(z, \lambda)} \tag{2.10}$$

which is often measured (or evaluated) in the water just below the surface ($z \cong 0$)

Remote-Sensing Reflectance: *Remote-sensing reflectance* represents the amount of the incident light (onto the water surface) which is eventually returned through the surface in direction (θ, ϕ) into the air, where it can be detected by a downward directed radiometer [Mobley, 1994]. The spectral remote sensing reflectance is defined as:

$$R_{rs}(\theta, \phi, \lambda) = \frac{L(\theta, \phi, \lambda)}{E_d(\lambda)} \tag{2.11}$$

which is evaluated using L and E_d measured in the air just above the water surface. The upward radiance, L, just above the sea surface is often called *water-leaving radiance*, denoted commonly by L_w. After atmospheric correction, spectral water-leaving radiance is derived from the radiance data collected by an ocean color satellite sensor [Gordon, 1997]. Both water-leaving radiance and remote-sensing reflectance serve as key parameters in ocean optics and ocean color remote sensing. R_{rs} has the unit of $[sr^{-1}]$.

Vertical Diffuse Attenuation Coefficients: In the aquatic media optical properties of the light field change significantly with depth due to the absorption and scattering. The accumulative effect of these factors is called the *light attenuation*. The rate of changes of the optical properties of seawater with depth are conventionally introduced by the vertical rates of change of their logarithms and are mainly defined as unitless quantities. The result is called the *vertical diffuse attenuation coefficient* for that property [Mobley, 1994]. As an important example, the For instance, vertical attenuation coefficient for downward irradiance, K_d, is given by:

$$K_d(\lambda) = -\frac{d\,(ln\,E_d(\lambda))}{dz} = -\frac{1}{E_d(\lambda)}\frac{d\,E_d(\lambda)}{dz} \qquad [m^{-1}] \tag{2.12}$$

where z is represents the underwater depth. The same manner can be followed to define the vertical diffuse attenuation coefficients for other properties.

Volume Scattering Function: The penetration of light in a medium, like seawater, is strongly affected by the ways light is absorbed and scattered by the constituents of that medium. The scattering itself, depends not only on the scattering coefficients of the constituents, but also on the angular distribution of the scattered flux from the primary scattering process. This distribution is described by the *volume scattering function*, $\beta(\theta)$, which for a given direction of θ is defined as:

$$\beta(\theta) = \frac{dI(\theta)}{E\,dV} \tag{2.13}$$

where $dV = dS\,dr$ is the volume element of the scattering medium (Fig. 2.2), $E = \frac{\Phi_0}{dS}$ is the irradiance of the incident light and $I(\theta) = \frac{d\Phi(\theta)}{d\omega}$ is the radiant intensity of the scattered beam at that direction.

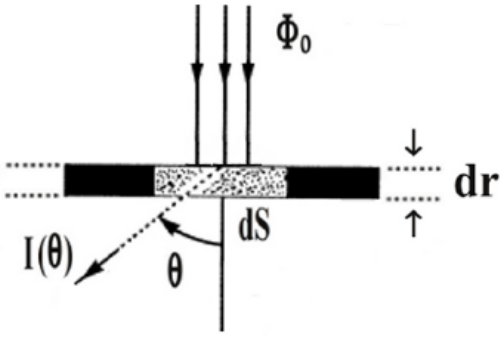

Figure 2.2: Scheme of a radiant flux, Φ_0, incident on an infinitesimal surface of dS with the thickness of dr. The radiant density scattered in the direction of θ is denoted by $I(\theta)$.

Inserting these values into the Eq. 2.13, volume scattering function is written as:

$$\beta(\theta) = \frac{d\Phi(\theta)}{\Phi_0}\frac{1}{d\omega\,dr} \qquad [m^{-1}\,sr^{-1}] \tag{2.14}$$

which can be also used for a standard definition: volume scattering function is the radiant flux per unit solid angle ω, scattered in the direction of θ per unit path-length in the medium, expressed as a proportion of the incident flux [Kirk, 1994].

Scattering Coefficient: The *scattering coefficient*, b, is defined as the fraction of radiant flux scattered by a given substance in all directions per unit path-length of light in the containing medium:

$$b(\lambda) = \frac{1}{\Phi_0}\frac{d\Phi_s}{dr} \qquad [m^{-1}] \tag{2.15}$$

where Φ_0 is the incident radiant flux, dr is the infinitesimal light path-length and $d\Phi_s$ is the pure change occurred in the radiant flux only because of the scattering by the substance. The b is measured in $[m^{-1}]$. Regarding the definition of the volume scattering function, the scattering coefficient can be derived by integrating $\beta(\theta)$ over the whole angular range (i.e., $0 \leq \theta \leq 180°$):

$$b = 2\pi \int_{\theta=0}^{\theta=\pi} \beta(\theta)\sin(\theta)\, d\theta = \int_{4\pi} \beta(\theta)\, d\omega \tag{2.16}$$

where the quantity of $2\pi \sin\theta d\theta$ has been substituted as the infinitesimal element of the solid angle ($d\omega$) in a spherical framework. The scattering coefficient is mostly divided into *forward scattering coefficient* and *backward scattering coefficient*, denoted by b_f and b_b, respectively:

$$b = b_f + b_b \tag{2.17}$$

where b_f represents the light scattered in a forward direction of the incident beam and b_b (called *backscattering coefficient*) corresponds the light scattered in a backward direction. Using Eq. 2.16, b_f and b_b can be written as:

$$b_f = 2\pi \int_{\theta=0}^{\theta=\pi/2} \beta(\theta)\sin(\theta)\, d\theta \quad ; \quad b_b = 2\pi \int_{\theta=\pi/2}^{\theta=\pi} \beta(\theta)\sin(\theta)\, d\theta \tag{2.18}$$

Scattering Phase Function: *Scattering phase function*, $\tilde{\beta}(\theta)$, for a given substance is its volume scattering normalized by respecting scattering coefficient:

$$\tilde{\beta}(\theta) = \frac{\beta(\theta)}{b} \qquad [sr^{-1}] \tag{2.19}$$

whose integral over all solid angles is equal to 1. Moreover, integral of $\tilde{\beta}(\theta)$ up to any given value of θ is the proportion of the total scattering which occurs in the angular interval between 0° and θ.

Extinction Coefficient: *Extinction coefficient*, or the beam attenuation coefficient, c, is the total rate by which the incident light is attenuated in a medium. Hence, for a given medium the extinction coefficient is the overall effect of absorption and scattering, as the summation of their respective coefficients:

$$c(\lambda) = a(\lambda) + b(\lambda) \qquad [m^{-1}] \tag{2.20}$$

where $a(\lambda)$ and $b(\lambda)$ are the (total) absorption and scattering coefficients of the medium, respectively. The definition of $a(\lambda)$ and general explanation about features and components of both $a(\lambda)$ and $b(\lambda)$ in aquatic media are given in sec. 2.1.2.

Single-Scattering Albedo: Given the extinction and scattering coefficients of a substance/medium, the *single-scattering albedo*, most relevant for small-particle scattering, is defined as the ratio of the scattering to the beam attenuation coefficients:

$$\omega_0(\lambda) = \frac{b(\lambda)}{c(\lambda)} = \frac{b(\lambda)}{b(\lambda) + a(\lambda)} \tag{2.21}$$

which is a value between 0 and 1. $\omega_0 = 1$ implies that all particle extinction is due to scattering; conversely, $\omega_0 = 0$ implies that all extinction is due to absorption.

Optical Depth: Due to the effects of scattering and absorption (attenuation of light) the downward irradiance, E_d, decreases with depth when light penetrates into the seawater. This can be stated more apparently by rewriting the Eq. 2.12 as below:

$$E_d(z) = E_d(0)\, e^{-K_d z} \tag{2.22}$$

where $E_d(z)$ and $E_d(0)$ are the values of downward irradiance at the depth z and just below the surface, respectively; and K_d is the mean value of the vertical attenuation coefficient in this interval. Thereby, the *optical depth* for the given interval (from surface down to the depth z) is defined as [Kirk, 1994]:

$$\zeta = K_d\, z \tag{2.23}$$

It means that for a given depth, the value of optical depth is proportional to K_d, which in turn means that turbid waters (as well as waters with high phytoplankton population) have high values of optical depth. As K_d is measured in $[m^{-1}]$, the optical depth is a unitless parameter. The value of ζ is essential for determining the maximum depth down to which an optical sensor can look into the water, e.g., the vertical domain that can be accessible by ocean color remote sensing, which is often referred to as the vertical *light penetration depth*.

Optical depth, ζ, as defined here is distinct from *attenuation length*, τ, which is also sometimes called optical depth or optical distance. The attenuation length is the geometrical path multiplied by the beam attenuation coefficient (c) associated with the path. In plane-parallel water bodies, the dimensionless parameter of τ is defined [Mobley, 1994] for a vertical interval down to the depth z as follows:

$$\tau(\lambda) = \int_0^z c(z', \lambda) dz' \tag{2.24}$$

Photosynthetically Available Radiation: *Photosynthetically Available Radiation*, PAR, refers to the available visible light (i.e., from 390 to 750 nm) at each depth which can be used by marine phytoplankton in their photosynthetic processes. The vertical attenuation coefficient for downward irradiance of PAR is regarded as the best parameter to characterize different water bodies with respect to their potentials of photosynthesis [Kirk, 1994]; thereby, PAR has a key role in the field of ocean productivity and primary production. PAR is dependent on the downward spectral irradiance (in the visible range) and decreases with depth, especially for those parts of wavelength bands which are more absorbed by the phytoplankton species.

Euphotic Zone: In marine bio-optics, the *euphotic zone*, z_{eu}, is the upper layer of the seawater through which (down to a maximum depth) the significant part of the photosynthetic processes occurs. In the context of primary production the euphotic zone is assigned to the depth where the available light (more precisely, E_d) is 1% of the available light just below the sea surface [Kirk, 1994]. By implementing this definition into the Eq. 2.22, it is inferred that the euphotic depth is equivalent to the vertical interval for which the optical depth is equal to 4.6. The depth of the euphotic zone (or *photic zone*), is determined by the transparency of the seawater, which in turn depends on the water constituents, including phytoplankton.

Radiative Transfer Equation: The interaction of light with matter is described by radiative transfer (RT) theory, which quantifies all the processes that affect the direction and the quantity of photons in a radiation field (atmosphere or underwater). Using the radiative transfer theory, measured radiant quantities, can be physically characterized and modeled. This is practically performed by the *radiative transfer equation*, RTE, which is a statement of energy conservation, accounting for all energy losses and energy gains associated with a photon stream moving through the water along a path in a fixed direction. Given a certain incident light, the characteristics of the underwater light field are uniquely determined by the properties of the medium, where various relations between radiometric parameters are interconnected in RTE. Assuming a horizontally stratified water body (i.e., with properties everywhere constant at a given depth), with a constant input of monochromatic unpolarized radiation at the surface, and ignoring the fluorescence emission within the water, the RTE may be written as [Kirk, 1994]:

$$\frac{dL(z,\theta,\phi)}{dr} = -c(z)L(z,\theta,\phi) + L^{\star}(z,\theta,\phi) \tag{2.25}$$

where the term on the left is the rate if change of radiance with distance, r, along a path specified by zenith and azimuth angles θ and ϕ at depth z. The incident radiation undergoes a rate of change as the result of two opposite processes: loss by attenuation ($c(z)$) along the light path (dr), represented by the first term on the right hand side; and gain by scattering along the path from light beams initially traveling in other directions (θ', ϕ') into the direction $\theta\,, \phi$, which is represented by the second term on the right hand side. The total gain of radiance, $L^{\star}(z,\theta,\phi)$, is determined by the volume scattering function of the medium at depth z and the radiance distribution [Kirk, 1994]:

$$L^{\star}(z,\theta,\phi) = \int_{2\pi} \beta(z,\theta,\phi;\theta',\phi')\, L(z,\theta',\phi')\, d\omega(\theta',\phi') \tag{2.26}$$

where $d\omega(\theta',\phi')$ is the solid angle element forming an infinitesimal cone around the direction $\theta'\,, \phi'$.

The variation of radiance in the direction of $\theta\,, \phi$ can be achieved as function of depth, by replacing dr in Eq. 2.25 with $\frac{dz}{\cos\theta}$:

$$\cos\theta \frac{dL(z,\theta,\phi)}{dz} = -c(z)L(z,\theta,\phi) + L^{\star}(z,\theta,\phi) \tag{2.27}$$

The solution of $L(z,\theta,\phi)$ is acquired by integrating each term of Eq. 2.27 over all angles:

$$\int_{4\pi} \cos\theta \frac{dL(z,\theta,\phi)}{dz}\, d\omega = -\int_{4\pi} c(z)L(z,\theta,\phi)\, d\omega + \int_{4\pi} L^{\star}(z,\theta,\phi)\, d\omega \tag{2.28}$$

2.1.2 Apparent and inherent optical properties

Apparent optical properties: AOPs

Apparent optical properties (AOP) are those radiometric quantities of seawater that depend on the compositions of the water body and also on the geometrical structure of the radiation field (e.g, the direction of the incident light, which depends in turn on the position of the Sun in the sky). AOPs include a wide range of the ratios of radiometric quantities: all vertical attenuation coefficients (for different quantities), $R_{rs}(\theta,\phi,\lambda)$ (remote sensing reflectance), $R(z,\lambda)$ (irradiance reflectance), etc.. Overall, the quantities represented by AOPs are not independent of the water constituents, like phytoplankton, which have major influence on the distribution of the light field.

Inherent optical properties: IOPs

Inherent optical properties, IOPs, are those optical parameters of natural waters whose values depend only on the compositions of the water body (not on the geometrical/directional structure of the radiation field). The main parameters of interest in IOPs are: n (refraction index of water), $a(\lambda)$ (absorption coefficient), $b(\lambda)$ (scattering coefficient), $\beta(\theta, \lambda)$ (volume scattering function), $c(\lambda)$ (beam attenuation coefficient), $\omega_0(\lambda)$ (single-scattering albedo), etc.. The IOPs are strictly properties of the medium, unaffected by the ambient light conditions, whereas AOPs are affected by changes in the incident light field [Sathyendranath and Platt, 2007]. As the AOPs are dependent also on IOPs, they can be parametrized to be represented based on the IOPs (mainly absorption and scattering coefficients). This is the basis of the semi-analytic chlorophyll-a algorithms, which use remote sensing measurements of specific parameters of AOPs to evaluate $b(\lambda)$ and $b_b(\lambda)$, being in turn used for estimation of chlorophyll-a concentration.

2.1.3 Absorption

Light absorption occurs when an incident photon onto an atom/molecule is trapped and consumed to be converted into other forms of energy. The absorption characteristic of a substance in aquatic media is represented by its *absorption coefficient*, a, which is defined as the fraction of radiant flux absorbed by a given substance per unit path-length of light in the containing medium:

$$a(\lambda) = \frac{1}{\Phi_0}\frac{d\Phi_a}{dr} \tag{2.29}$$

where Φ_0 is the incident radiant flux, dr is the infinitesimal light path-length and $d\Phi_a$ is the pure change occurred in the radiant flux only because of the absorption by the substance. The a is measured in $[m^{-1}]$.

In natural waters there are four major constituents which affect the radiation field: pure seawater, phytoplankton, yellow substance (*Gelbstoff*) and non-algal particulates. Therefore, the total absorption coefficient in seawater is mostly represented by four separate terms:

$$a(\lambda) = a_w(\lambda) + a_\phi(\lambda) + a_g(\lambda) + a_{nap}(\lambda) \qquad [m^{-1}] \tag{2.30}$$

where the subscripts w, ϕ, g and nap are assigned to water, phytoplankton, *Gelbstoff* and non-algal particulate matter, respectively. Of course, phytoplankton are also parts of suspended particulate matter, but because of their specific bio-optical roles, they are usually separated from non-algal particulates. Spectral measurements of pure seawater (e.g., Morel [1974]; Smith and Baker [1981]) have shown that the absorption coefficient of pure seawater indicates very low values (and almost a flat curve) between $300\,nm$ and $500\,nm$, but increases very fast beyond these spectral limits (in the red and also in the middle UV). Absorption by phytoplankton, $a_\phi(\lambda)$, occurs in various planktonic pigments, among which the chlorophylls are best known.

The absorption of chlorophyll is characterized by strong absorption in the blue and in the red (Fig. 2.3), which for chlorophyll-a are associated with pronounced peaks at about $430\,nm$ and $665\,nm$, respectively. As chlorophyll-a is the main pigment in various phytoplankton cells, its concentration affects strongly the total absorption coefficient (thereby, it is used as the relevant optical measure of the phytoplankton abundance). The absorbing pigments are not uniformly distributed within phytoplankton cells, but are localized in chloroplasts, which are distributed non-randomly throughout the cell. This feature, referred to as the *pigment package effect* (Duysens [1956]; Kirk [1975]; Morel and Bricaud [1981]), implies that the shape of the absorbance spectrum and the specific absorbance per unit pigment are independent of concentration. *Package effect*

causes sort of flatness in the spectral absorption of the cells and is considered as the main source of inter-species (and also intra-species) differences in phytoplankton spectral absorption.

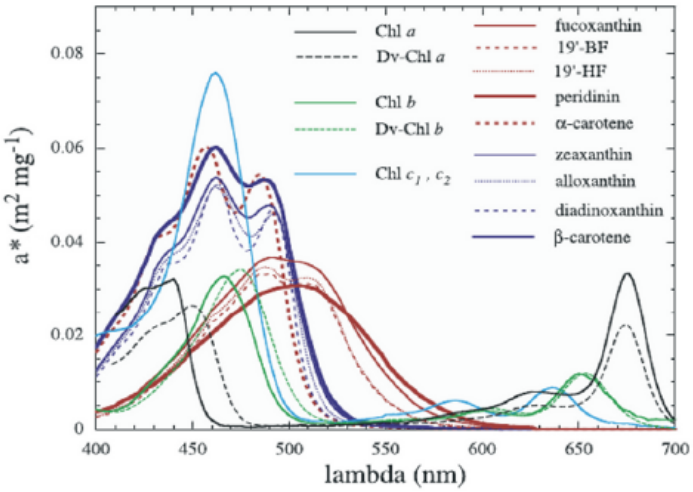

Figure 2.3: Specific absorption spectra for major pigments of marine phytoplankton, measured by Bricaud et al. [2004]. Specific absorption ($a^{\star}$) for a given substance is obtained by dividing the respective absorption coefficient to the measured concentration of that substance. The $a^{\star}$ has the unit of $[m^2\, mg^{-1}]$.

Yellow substance (*Gelbstoff*) refers to the chromophoric dissolved organic matter, CDOM, which are formed in the course of the decomposition process of the organic matter as humic substances. The absorption coefficient of CDOM indicates a semi-exponential decrease with wavelength. Non-algal particulates (inanimate particulate matter) consist of mineral particles, derived from the land or from bottom sediments (e.g., calcite particles) and non-living particulate organic matter (detritus), suspending in seawater. In general, the main optical importance of inanimate particulate matter is their role in the light scattering. However, they influence also the total absorption of seawater: the absorption spectra of inanimate particulate matter ($a_{nap}(\lambda)$) all have much the same shape: low (or no) absorption at the red end of the visible light spectrum and rising steadily as wavelength decreases into the blue and UV [Mobley, 1994]. In this sense, they have very similar absorption patterns as those of the CDOM, but not so sharp and smooth as for CDOM. Fig. 2.4 provides a general comparison of four major components of absorption coefficient in seawater.

2.1.4 Scattering

Light scattering occurs when a photon, during its interaction with a component of a medium, is re-radiated (scattered) and diverged from its original path. For a given substance in aquatic media, the characteristics of light attenuation due to scattering is primarily represented by its *scattering coefficient*, b, which was introduced by Eq. 2.15 and Eq. 2.15 in sec. 2.1.1. However, to assess the scattering features of natural waters in bio-optics and particularly in ocean color remote sensing, it is widely accepted that the backscattering coefficient, b_b, is a more relevant parameter than the scattering coefficient, b. In determination of the (total) backscattering coefficient, the major optical constituents of seawater mentioned for absorption play also main roles, except for CDOM, which has no significant contribution in the total scattering in seawater.

$$b_b(\lambda) = b_{bw}(\lambda) + b_{b\phi}(\lambda) + b_{bnap}(\lambda) \qquad [m^{-1}] \tag{2.31}$$

where the subscripts have the same meanings as for a in Eq. 2.30.

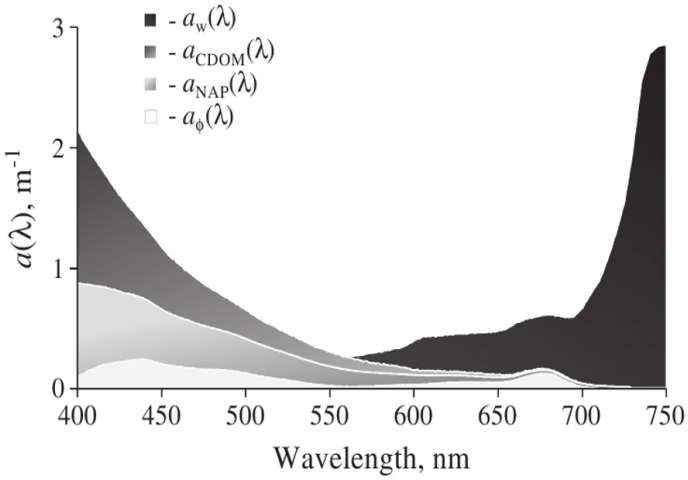

Figure 2.4: Spectral absorption coefficients of major optical constituents of seawater, measured by Gurlin et al. [2011] for a high *chl-a* water body.

In general, the scattering process can be either *elastic* (preserving the incident wavelength) or *inelastic* (changing the incident wavelength). A brief introduction to both types of scattering, with more focus on their features in natural waters, is given in the following subsections.

2.1.4.1 Elastic scattering

The elastic scattering in the atmosphere, depending on the size of scatterer and the wavelength of the incident light, is divided into *Rayleigh* and *Mie* scattering. In general, small particles with sizes much smaller than wavelength of the incident light (like air molecules) favor the *Rayleigh* scattering; whereas, large particles with sizes much larger than wavelength of the incident light (like aerosols) favor the *Mie* scattering. The physical basis of the *Mie* theory [Mie, 1908] is similar to that of *Rayleigh* [Young, 1982], i.e., based on oscillations caused by induced dipoles or polarizable bodies, which give rise to the re-radiation of light (scattering). However, instead of assigning single dipoles to single molecules, as assumed in the *Rayleigh* theory, the *Mie* theory considers the additive contributions of a series of electrical and magnetic multi-poles located within the particles [Mie, 1908; Stone, 1953]. The angular distribution of scattered light in the *Mie* scattering is favored in forward direction within small angles of the beam axis, while in the *Rayleigh* scattering there is no favored angular distribution for the scattered light. Both theories, in principle, apply to spherical scatterers, however, there are practical models that use different approximations based on these theories.

Within the natural waters there exist two types of *elastic* scattering, which are related to density fluctuation of water molecules and also any kind of physical inhomogeneity that is larger than the water molecules. These scattering phenomena are often referred to as the *Rayleigh* and *Mie* scattering in the water bodies, respectively [Kokhanovsky, 2006].

Fluctuation scattering: based on *Einstein-Smoluchowski* theory, the permanent motions of water molecules (and microscopic contents, like ions) leads to localized microscopic fluctuations of density, which in turn causes fluctuations in the refraction index leading to scattering [Mobley, 1994]. The fluctuation scattering is often referred to as *Rayleigh* scattering by oceanographers, because of two main reasons: the dimensions of water microscopic volumes whose densities (and refraction indices) are under fluctuations, are still small relative to the wavelength of light (as in the

Rayleigh scattering). Secondly, the volume scattering function pertaining to the fluctuation scattering of pure seawater is very similar to the *Rayleigh*'s, as presented in the following equations [Mobley, 1994]:

$$\beta_w(\theta,\lambda) = \beta(90^\circ,\lambda_0) + \left(\frac{\lambda_0}{\lambda}\right)^{4.32}(1+0.835\cos^2\theta) \tag{2.32}$$

$$\beta_{Ray}(\theta,\lambda) = \beta(90^\circ,\lambda_0) + \left(\frac{\lambda_0}{\lambda}\right)^{4}(1+\cos^2\theta) \tag{2.33}$$

where the subscripts w and Ray stand for *water* and *Rayleigh*, respectively. Accordingly, the angular distribution of the fluctuation scattering is, like in the *Rayleigh* scattering, identical in both forward and backward directions.

Particle scattering: in natural waters there are a huge number of particles/particulates with a wide range of size distribution and refractive indices that participate in the scattering processes in the underwater light field. As, in general, the dominant size of the in-water particles is more than $1\,\mu m$, which is much larger than the wavelength of the solar visible light, the scattering related to these particles/particulates can be approximated by the *Mie* scattering. This also explains why CDOM has no contribution in the seawater scattering.

The in-water particulates can be divided into two main sets: phytoplankton and non-algal particulates. Phytoplankton cells (and colonies) make a significant contribution to the total scattering behavior of the aquatic medium. The extent of the scattering contribution of Phytoplankton varies among different species (e.g., *E. huxleyi* has a much larger scattering coefficient compared to other species). The convenient parameter to compare the scattering properties of different phytoplankton species is the *specific scattering coefficient,* b_c, which corresponds to the scattering coefficient for a given species with the *chl-a* concentration of $1\,mg.m^{-3}$ [Kirk, 1994]. However, as in natural waters the scattering is dominated by diffraction from poly-disperse particles (independent of particle composition), the estimation of total scattering is too complicated. Therefore, based on very precise measurements of seawater scattering (e.g., by Petzold [1972]), some bio-optical models have been developed. According to Mobley [1994], a commonly used bio-optical model for $b(\lambda)$ is that of Gordon and Morel [1983]:

$$b(\lambda) = \left(\frac{550}{\lambda}\right)0.30\,C^{0.62} \qquad [m^{-1}] \tag{2.34}$$

where C stands for the *chl-a* concentration in $[mg\,m^{-3}]$.

It must be noted that, apart from the (total) scattering coefficient of seawater, the characteristic of the scattered light in a medium depends on the angular distribution of the primary scattering, which is described by the volume scattering function, $\beta(\theta,\lambda)$. For instance, Kopelevich [1983] developed a well-known model for approximation of the spectral volume scattering function in seawaters. This model separates the contributions by small and large particles, which are assigned to the mineral particles and biological particulates, respectively. In this model, small particles are associated with sizes less than $1\,\mu m$ and refractive indices (relative to water) of $n = 1.15\,\mu m$; and large particles are associated with sizes larger than $1\,\mu m$ and refractive indices of $n = 1.03\,\mu m$.

$$\beta(\theta,\lambda) = \beta_w(\theta,\lambda) + \nu_s\beta_s^*(\theta)(\frac{550}{\lambda})^{1.7} + \nu_l\beta_l^*(\theta)(\frac{550}{\lambda})^{0.3} \tag{2.35}$$

with the following parametrization: $\beta_w(\theta,\lambda)$ as the volume scattering function of water as defined by Eq. 2.32, with $\lambda_0 = 550\,nm$; ν_s and ν_l as the volume concentrations of small and large

particles, respectively, with the unit of parts per million (ppm); $\beta_s(\theta)$ as the small-particle volume scattering function per unit volume concentration of the small particles; and $\beta_l(\theta)$ as the analogous quantity for the large particles. For more details, see: e.g., Mobley [1994].

2.1.4.2 Inelastic scattering

What has been so far mentioned about scattering, has only covered (briefly) the dominant part of the scattered light, i.e., the *elastic scattering*, which refers to the directional deviation of the light beam without any change in wavelength. However, a non-negligible fraction of the scattered light is associated with change in wavelength of the incident light, which is called *inelastic scattering*. In fact, the inelastic scattering involves an energy exchange between light and the molecules of the substance/medium and thereby, leads to redistribution of photons over the wavelength. The major source of inelastic scattering in the aquatic medium is *Raman scattering*. However, under certain circumstances (e.g., depending on the contents of *chl-a* and CDOM), the *fluorescence emission*, as a trans-spectral process, plays a similar role in redistribution of the radiation in the underwater light field. Both phenomena are very briefly introduced below.

Raman scattering: during the early 1980's, all oceanographic measurements of radiometric parameters indicated significant deviation from the magnitudes expected by theoretical principles. More precisely, the measurements of diffuse attenuation coefficients, K_d and K_u (see Eq. 2.12), were confusingly far from the values suggested by the *Gershun*'s law [Mobley, 1994]. *Gershun*'s law is a well-known solution of the radiative transfer equation (RTE, see Eq. 2.27) in the aquatic media, being written as:

$$\frac{d}{dz}[E_d(z,\lambda) - E_u(z,\lambda)] \;=\; -a(z,\lambda)E_0(z,\lambda) \qquad [Wm^{-3}\,nm^{-1}] \tag{2.36}$$

where a, and E_0 stand for the absorption coefficient and the *scalar irradiance*, respectively;

While these unexpected results were often attributed to the imperfect instrumentation, Sugihara et al. [1984] recognized that *Raman scattering* by water molecules leads to inelastic scattering of light from shorter to longer wavelengths, which explains the above observations as well. In Raman scattering (occurring in solids, liquids and gases) a molecule is excited into a higher rotational or vibrational quantum state by an incident photon (of certain energy). The exited molecule then emits a photon of higher wavelength than the incident photon, with the energy difference being transfered by the molecule to the internal rotational or vibrational energy. If the molecule is already in an exited state, then it may emit a photon of a shorter wavelength than the incident photon and thereby return to its ground state [Mobley, 1994]. However, at terrestrial temperatures of liquid water, Raman scattering from longer to shorter wavelengths is insignificant. The frequency of the scattered photon is determined by the vibrational and rotational frequencies of the molecule (i.e., its quantum energy structure), not by the frequency of the incident light. Indeed, the uniqueness of the Raman spectral footprint for each molecule, provides a powerful spectroscopic tool to identify the composition of a given substance, as well as to obtain more information on the internal structure of the molecules in a quantum level.

In quantum mechanics, the energy E of vibrating and rotating molecules such as O_2 and N_2 is given by:

$$E(v,J) \;=\; E_{vib}(v) + E_{rot}(J) \tag{2.37}$$

where $E_{vib}(v)$ is the vibrational energy, with the quantum number of v and $E_{rot}(J)$ is the rotational energy, with J as the quantum number of the total angular momentum. According to

quantum theory, each molecular transition process obeys this rule: $\Delta J = \pm 1$. As the scattering process involves two energy transitions (once by absorbing the incident photon and then by re-emitting a secondary photon), the transition rule mentioned above leads to the following condition for scattering: $\Delta J = -2,\ 0,\ +2$. In addition, the probable changes in vibrational energy occur under this quantum rule: $\Delta v = -1,\ 0,\ +1$. As elastic scattering (e.g., *Rayleigh* scattering) involves no net exchange of energy between molecules and photons, it corresponds to this quantum rule: $\Delta J = 0 \ \ and \ \ \Delta v = 0$.

Hence, in occurrence of an inelastic scattering either ΔJ or Δv (or both of them) have non-zero values. While, pure vibrational Raman scattering (VRS) is equivalent to a transition of $\Delta v = \pm 1 \ \ and \ \ \Delta J = 0$, pure rotational Raman scattering (RRS) is equivalent to a transition of $\Delta v = 0 \ \ and \ \ \Delta J = \pm 2$. In principle, for specific molecules, such as O_2 and N_2, both types of Raman scattering are simultaneously plausible, satisfying the quantum energy transition of: $\Delta v = \pm 1 \ \ and \ \ \Delta J = \pm 2$. In practice, however, as the atmospheric contribution of VRS in the UV-visible spectral ranges is very low (compared to RRS), for the usual scientific purposes, the atmospheric VRS is often neglected [Burrows et al., 1996; Joiner et al., 2012].

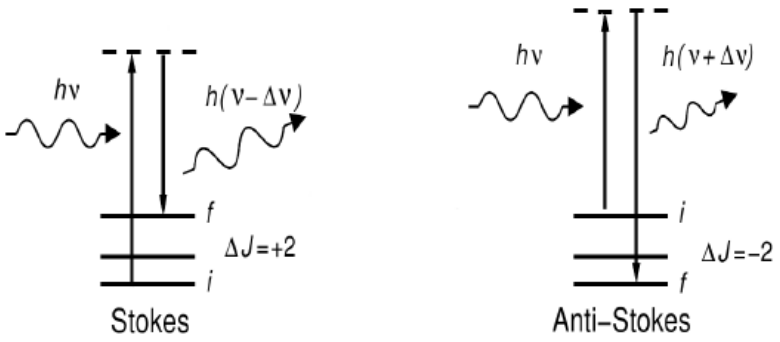

Figure 2.5: A diagram of energy transitions pertaining to the inelastic Raman scattering. In both cases an incident photon with the energy quanta of $h\nu$ induces a (rotational) energy transition from an initial state i to an virtual excited level (dashed line). However, contrary to the elastic scattering, the secondary transition to the lower level does not finalize to the initial state i, rather to the final state f, whose energy can be higher (Stokes lines) or lower (anti-Stokes lines) than that of the initial state. The energy difference between the initial and final states, is equal to the amount of energy change induced by the inelastic scattering. While the secondary photon has a lower energy (longer wavelength) for Stokes lines (left), it has a higher energy (shorter wavelength) for anti-Stokes lines (right).

- **Rotational Raman Scattering (RRS)**[2]: In the atmosphere, Raman scattering in the UV-visible ranges is mostly induced by O_2 and N_2 molecules [Kattawar et al., 1981]. Under certain observation geometries (e.g., at very large solar zenith angles) atmospheric Raman scattering is predominated by the rotational Raman scattering (i.e., the respective energy transitions occur mostly between molecular rotational states). Indeed, in the UV-visible range, the contribution of vibrational inelastic scattering is only around $1/30\,th$ of the total Raman scattering under common observation geometries [Burrows et al., 1996].

  Rotational Raman scattering in the air is often referred to as the *Ring effect* [Grainger and Ring, 1962; Vountas et al., 1998], causing *filling-in* of Fraunhofer lines in a daytime spec-

[2]Although RRS is mainly an atmospheric phenomenon, it is worth explaining that here because in the PhytoDOAS method it is regarded as a spectral component of the atmosphere.

trum (aside from other trans-spectral processes). Raman scattering in the atmosphere (i.e., the Ring effect) is responsible for approximately 4% of all scattering events occurring by the air molecules, causing spectral fine-structure (e.g., Joiner et al. [1995]). Rotational Raman scattering by air molecules that involves a released photon with less energy than the incident one ($\Delta J = +2$) is referred to as RRS *Stokes lines* and those inelastic scattering that involves an energy gain of the released photons ($\Delta J = -2$) is called RRS *anti-Stokes lines* [Young, 1982] (see Fig. 2.5).

In this study, based on the above arguments, in setting up the atmospheric optical components of the retrieval process, only rotational Raman scattering has been taken into account.

- **Vibrational Raman Scattering (VRS)**: In seawater, vibrational Raman scattering is the dominant form of the Raman scattering, because the rotational modes are restricted by the strong hydrogen bonds of water molecules [Kattawar and Xu, 1992; Sathyendranath and Platt, 1998]. In addition to elastic scattering, inelastic scattering of VRS by liquid water contributes significantly in the spectral distribution of the outgoing radiance, which is more pronounced in oligotrophic waters, which have low *chl-a* concentration and low *Gelbstoff* [Vasilkov et al., 2002; Vountas et al., 2003]. Due to the impact of redistribution of photons by Raman scattering, the aquatic VRS (along with the atmospheric RRS) participates in the *filling-in* effect of solar Fraunhofer lines, as well as the absorption lines of trace gases. This feature is observed more pronounced in space-borne measurements of backscattered radiance over (oligotrophic) oceanic regions. As oligotrophic waters cover large parts of the World's ocean, accounting for the spectral signature of VRS is important in atmospheric remote sensing of trace gases over the oceans [Vountas et al., 2003], as well as in the ocean color remote sensing. Although in both cases RRS has a larger impact than VRS, it was shown by [Vountas et al., 2003] that neglecting VRS would lead to an error of the magnitude of 30% in the retrieval of some trace gases (such as BrO) over oligotrophic waters. A particularly strong VRS emission by liquid water arises from the vibrational stretching mode of O-H, whose Stokes lines show a peak at $560\,nm$ [Kirk, 1994].

  Vountas et al. [2003] used the wavelength window of $345 - 385\,nm$ to measure and model the impact of VRS over the oceanic areas (based on a model proposed by Sathyendranath and Platt [1998]) and found that in biologically active regions (i.e., in phytoplankton rich areas) the VRS impact is much lower than in oligotrophic waters. This is justified by the fact that waters with high *chl-a* concentrations have higher values of *optical depth*, which implies the lower amount of scattering events by water molecules. This observation was then parameterized and implemented into the DOAS retrieval by Vountas et al. [2007] to apply the VRS spectral footprint for estimation of the light path-length in the water. The estimated path-length of light is considered as an approximation of the *light penetration depth* into seawater, which is the maximum depth accessible through ocean color remote sensing. However, because of two main reasons the parametrization has been done by (satellite) data collected from the UV range: firstly, the phytoplankton rich waters, along with water molecules themselves, absorb strongly parts of the visible range, weakening the footprint of VRS (see Fig. 2.6); secondly, due to the wavelength-dependency of seawater VRS ($b^{VRS} \propto \lambda^{-5.3}$) [Bartlett et al., 1998], VRS signal in the visible range is weaker than in the UV. It means that in the visible range VRS signal has a very lower chance to compete the spectral impacts of RRS, to be observed clearly. Therefore, VRS signature is obtained in the UV and then is extrapolated (based on Bartlett et al. [1998]) onto the visible range.

  In this study, based on the method developed by Vountas et al. [2007], the VRS measure-

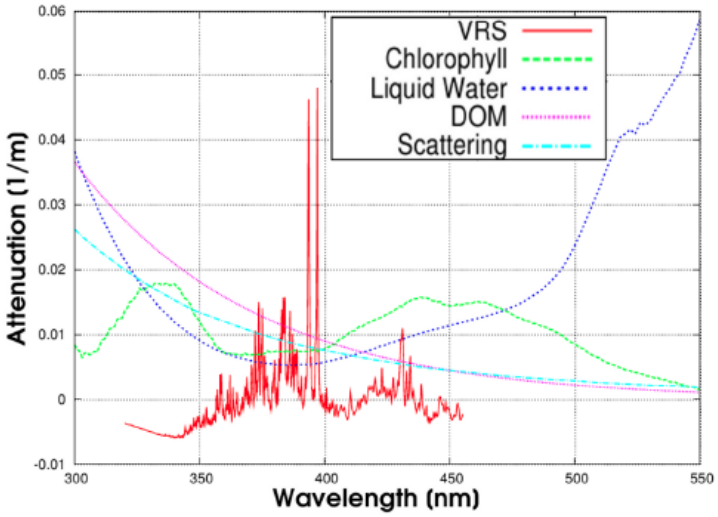

Figure 2.6: Absorption coefficients for phytoplankton (Bracher and Tilzer [2001], assuming a *chl-a* conc. of 0.1 $[mg.m^{-3}]$), DOM (Morel [1988]) and pure water (Buiteveld et al. [1994]), together with the total backscattering coefficient (Smith and Baker [1981], in $[m^{-1}]$), and a unitless spectral signature of VRS as defined by Vountas et al. [2007]. (The figure adapted from Vountas et al. [2007]).

ments (by SCIAMACHY) have been used as a proxy of the light path-length in the seawater. The latter quantity was later used in PhytoDOAS process to convert the main output of the retrieval (the absorption fit-factor) into the *chl-a* concentration.

Fluorescence emission

In interaction of light with substance, incident photons of the UV-visible part of the spectrum, have (in principle) sufficient energy to cause a molecular transition from one electronic state (usually the ground state) to another. However, for a certain molecule, the incident photon to be captured by the molecule needs to have an amount of energy among a specific range of distinct quanta. Excitation occurs to one of the many vibrational/rotational levels belonging to the given electronic energy level. But under certain circumstances (not very usual), the captured photon, can induce a scenario apart from the absorption and scattering scenarios, called fluorescence emission: after absorption of a photon there is a very rapid series of transitions downwards through the rotational/variational levels until the lowest electronic energy state (the lowest excited singlet state) is reached; the excited molecule (at the lowest excited singlet state) can then undergo a transition to one of the vibrational/rotational levels of the ground state by re-emitting a photon of longer wavelength than incident one [Valeur, 2001] (see Fig. 2.7). This phenomenon is referred to as *fluorescence*, through which in living algal cells (mainly by *chl-a*) around 1% of the absorbed light is lost. If photosynthesis is inhibited, then fluorescence increases to about 3% of the absorbed light. Thus, most of the light energy absorbed by the aquatic ecosystem ends up either as heat (vibrational/rotational energy distributed amongst all the molecules of the system) or as the chemical energy in the process of photosynthesis.

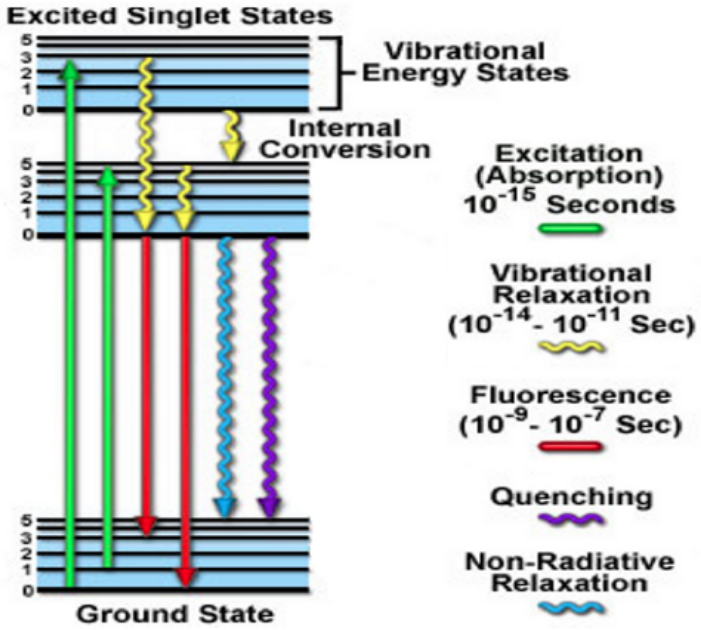

Figure 2.7: A simplified process of the fluorescence emission based on Jablonski energy diagram. The transitions pertaining to excitation (absorption) and fluorescence transition are illustrated by green and red arrows, respectively. Typical life-time of each process is also shown on the right hand side. Figure adapted from: `http://www.olympusmicro.com/primer/java/jablonski/jabintro/index.html`.

2.1.5 Classification of ocean waters

In bio-optical models which have been developed for the prediction of IOPs (i.e., $a(\lambda)$, $b(\lambda)$ $b_b(\lambda)$) oceanic regions are classified as Case-1 and Case-2 waters. This classification originally was proposed by Morel and Prieur [1977]. However, the concept of *bio-optical state* was first introduced by Smith and Baker [1978] to represent the effect of biological processes on ocean optical properties. Smith and Baker [1978] indicated that those optical properties are mainly related to the water content of *chl-a*. This finding in turn led to the applications of *chl-a* concentration as the proxy for phytoplankton and related water constituents in bio-optical models [Mobley et al., 2004].

- **Case-1 waters:** optical properties are determined primarily by phytoplankton and related CDOM and detritus degradation products. In general, Case-1 waters refer to the open oceans, the off-shore aquatic areas beyond significant coastal influence. It is believed that in open oceans the amounts of CDOM and detritus matter covary strongly with phytoplankton activity and thereby *chl-a* conc. is the main biological parameter, determining the optical properties of Case-1 waters.

- **Case-2 waters:** optical properties are significantly influenced by other constituents such as mineral particles, CDOM, or micro-bubbles, whose concentrations do not covary with the phytoplankton concentration. In general, coastal waters are the typical example of Case-2 waters, where high turbidity is induced by non-biological processes, including: river outflows, terrestrial runoff or erosion, dust and aerosol transports, sediment re-suspension by currents, air bubbles injected into surface waters by breaking waves, etc..

This classification has been of particular relevance for bio-optical algorithms used in ocean color remote sensing. In retrieving optical properties and constituents of ocean waters by bio-

optical algorithms, Case-1 waters are much easier targets than Case-2 waters, which are optically complicated. However, beside all advantages, there are some limitations associated with the above classification (although Morel and Prieur [1977] mentioned that there is no sharp dividing line between Case-1 and Case-2 waters). For instance, Bricaud et al. [1981] indicated that even in open-ocean waters dominated by phytoplankton, the CDOM concentration does not covary with the existing amount of *chl-a*, because the CDOM concentration is influenced by past phytoplankton concentrations as well. Additionally, Gordon et al. [1988] mentioned the problem of high coccolith concentrations, causing very high scattering effect without co-varying with pigment concentrations.

2.2 Marine phytoplankton: general characteristics

2.2.1 Phytoplankton taxonomic classification

Marine phytoplankton are biologically classified into taxonomic groups, in which the main categories, representing them at the highest rank, are bacteria (prokaryotic cells) and microalgae (eukaryotic cells). The prokaryotes are the organisms that lack a cell nucleus or any other membrane-bound organelles, while eukaryotes are organisms that have a cell nucleus. The prokaryotes and eukaryotes have long been the two basic (life) domains in the taxonomic ranking of living organisms; however, recently the domain prokaryotes has been replaced by two separate domains: bacteria and archaea (unicellular micro-organisms, genetically distinct from bacteria). The *family tree* of a living creature begins from a domain down to a certain species, containing hierarchical levels, which (in a downward order) are: domain, kingdom, phylum, class, order, family, genus and species [Medlin et al., 2008].

Cyanobacteria

In marine ecosystem, the domain bacteria includes two phyla (divisions): eubacteria and cyanobacteria. Since the first phylum (eubacteria) is heterotroph, only the latter (cyanobacteria), which is phototroph, belongs to the phytoplankton compartment. Cyanobacteria, called also blue-green algae, are recognized by certain characteristics: nonmotile or having gliding motility, heterocyst or capable of nitrogen fixation, photosynthetic (as being phototrophic bacteria), having chlorophyll and carotenoid pigments, and sometimes even phycobiliproteins (to capture light). Cyanobacteria comprise two following classes: "real cyanobacteria" and prochlorophytes. The real cyanobacteria itself includes two orders: filamentous cyanobacteria (occurring in colonies) and coccoid cyanobacteria (occurring unicellular).

Microalgae

Pelagic microalgae (eukaryotic cells), the other category of marine phytoplankton, can be roughly divided into following phyla and respective classes and orders (`http://www.jochemnet.de/fiu/OCB3043_21.html`):

- chromophyta (possess chlorophyll a and c):
  - cryptophyceae
  - dinophyceae (dinoflagellates): possessing a transverse girdle and a longitudinal furrow

  - chrysophyceae
  - prymnesiophyceae (haptophytes)
    e.g., coccolithophores and *Phaeocystis* sp.
  - bacillariophyceae
    e.g., diatomophyceae (diatoms): unicellular algae with siliceous frustules

- chlorophyta (possess chlorophyll a and b):
  - chlorophyceae
  - prasinophyceae
  - euglenophyceae

However, for our purpose, other types of classifications, focusing on general functionalities of different phytoplankton groups are more relevant for ocean color remote sensing. These are briefly discussed below.

2.2.2 Alternative classifications of phytoplankton communities

Understanding interactions between phytoplankton and marine environments is vitally important to improve the knowledge of marine biogeochemical cycles. However, this goal goes beyond the taxonomic classification of phytoplankton species. Hence, during recent scientific challenges in this field, phytoplankton size classes (PSC) and phytoplankton functional type (PFT) emerged as relevant approaches for the mentioned purpose.[3]

Phytoplankton Size Classes, PSCs

An early approach to classify marine phytoplankton was based on cell size [Sieburth et al., 1978], in which phytoplankton are divided into the following size classes: picophytoplankton ($0.2-2\,\mu m$; e.g., cyanobacterial *Prochlorococcus sp.*), nanophytoplankton ($2-20\,\mu m$; e.g., coccolithophores), and microphytoplankton (more than $20\,\mu m$; e.g., diatoms and dinoflagellates). There are several advantages of this approach, among which the most recognized ones are addressed below. Firstly, cell size has a well-known influence on the phytoplankton physiology [Chisholm, 1992; Raven, 1998]. Secondly, variability in some biogeochemical functions can be addressed by the cell size approach. Main examples for the latter are as follows: high ratios of surface-area to volume in picophytoplankton provide them with high efficiency in uptake of nutrients under nutrient-limited conditions, thereby to become dominant in oligotrophic waters (they also sink more slowly than larger cells); moreover, due to the *package effect* (briefly explained in sec. 2.1.3), small cells are more efficient in light harvesting. Thirdly, microphytoplankton, in general, dominate nutrient-rich waters and are the principal agents of the carbon export to deeper waters. And finally, picophytoplankton and nanophytoplankton play important roles in the food web (e.g., Caddy et al. [1995]; Platt et al. [2003] showed the correlation between microphytoplankton blooms and fish productivity).

The applications of the size-class approaches in ocean color remote sensing have been shown by several studies (e.g., Devred et al. [2006]; Uitz et al. [2006]; Ciotti and Bricaud [2006]; Fuentes-Yaco et al. [2007]; Hirata et al. [2008]; Brewin et al. [2010a]). However, from a biogeochemical

[3]The descriptions of PSCs and PFTs used in this subsection have been mostly adapted from the seminal paper of Nair et al. [2008].

perspective a size-based approach to phytoplankton functionality is not fully satisfactory. Because the size-based approach fails to separate the biogeochemical functions of some phytoplankton communities of the same size class, which are characterized by different functions. For instance, while both DMS producers and calcifiers are often grouped under the size class of nanophytoplankton, the two groups have different effects on atmospheric CO_2: DMS producers, with their ability to form cloud-condensation nuclei cause a negative feedback on temperature under increasing atmospheric CO_2, whereas change in alkalinity associated with calcification increases release of CO_2 to the atmosphere, causing a reverse change. Concerning these limitations, the concept of functional types received more attentions.

Phytoplankton Functional Types, PFTs

The concept of PFT originates from a biogeochemical viewpoint, that phytoplankton differ greatly in their biogeochemical functions. According to PFT perspective, groups of marine phytoplankton can be categorized in the same compartment without (necessarily) having a common taxonomy/phylogeny. Based on distinct biogeochemical roles of phytoplankton, they can be classified functionally into nitrogen-fixers, calcifiers, silicifiers and DMS producers. A brief description of each group is given below.

Nitrogen-fixers: The marine diazotrophic organisms have a direct impact on the nitrogen cycle by consuming atmospheric nitrogen as a raw material for their growth. *Trichodesmium*, a genus member of cyanobacteria, is the dominant nitrogen-fixing organism in oligotrophic oceans. It has been revealed (by molecular techniques) that a large cyanobacterial population with cell size in the range of $3 - 10\,\mu m$ have the potential for diazotrophy [Zehr et al., 2001], e.g., *Katagnymene* species. Apart from certain cyanobacterial species, there are some cyanobacterial symbionts who are also nitrogen fixing phytoplankton in open oceans: e.g., certain species of diatoms such as *Chaetoceros*, *Rhizosolenia* and *Hemiaulus* [Scharek et al., 1999; Fuhrman and Capone, 2001].

Silicifiers: Four phytoplankton taxonomic groups are recognized to be the main silicifiers in the marine ecosystem: bacillariophyta (diatoms), silicoflagellates, chrysophyta and xanthophyta [Brownlee and R.Taylor, 2002], among which, in turn, diatoms (bacillariophyta) are the dominant silicifiers in the oceans. Diatoms, usually found in nutrient-rich waters, are known to be the major organisms in the spring bloom occurring in temperate and polar regions [Lochte et al., 1993], being responsible for about 40% of the total marine primary production [Sarthou et al., 2005]. Diatoms use silica to construct their cell walls (frustules) to be protected against grazing by zooplankton [Smetacek, 2001]. As a consequence, the cell density of diatoms increases, which leads in turn to sink faster into the deep ocean. Hence, diatoms contribute strongly in the ocean (vertical) carbon export, as well.

Calcifiers: The main planktonic calcifiers belong to the coccolithophores, characterized by their calcite external plates, called coccoliths. The formation of calcite (calcium carbonate) lowers carbonate concentration in surface ocean, reducing sea water alkalinity, also associated with release of CO_2 (see sec. 2.3.1). The increase in the partial pressure of CO_2 in surface waters during calcification is a potential source of CO_2 to the atmosphere [Robertson et al., 1994; Rost and Riebesell, 2004]. The increasing concentration of atmospheric CO_2 in turn lowers the carbonate concentration of the surface ocean and affects calcification. The planktonic formation of calcite (predominantly by coccolithophores) provides a potential sink for particulate inorganic carbon,

PIC. Moreover, calcium carbonate also serves as a ballast for the efficient transport of particulate organic carbon (POC) to deep ocean [Armstrong et al., 2002]. Regarding to the concept biological pump (see sec. 2.3.1), this means that coccolithophores are involved in both *hard tissue pump* and *soft-tissue pump*, referring to the sinking processes of PIC and POC, respectively. The distribution of coccolithophores ranges from oligotrophic subtropical gyres to temperate and high latitude semi-eutrophic waters [Brown and Yoder, 1994a].

DMS producers: Dimethyl sulphide, DMS, possesses an essential role in the global sulfur cycle [Simo, 2001]. DMS has also a significant influence on the climate balance, through formation of sulphate aerosols, which serve as cloud condensation nuclei (CCN), affecting the total albedo and thereby causing a cooling effect (more details about formation and global impacts of DMS are given in sec. 2.3.2). Marine phytoplankton are the main source of DMS emissions into the atmosphere. The main phytoplankton taxonomic groups involved in DMS emissions are dinoflagellates and haptophytes [Sunda et al., 2002; Malin and Steinke, 2004; Thierstein and Young, 2004]. More precisely, *E. huxleyi* and *Phaeocystis sp.* (both from haptophytes) and certain species of dinoflagellates are known to be the most prominent DMS producers [Keller et al., 1989; Liss et al., 1997].

E. huxleyi is the globally-dominant species of coccolithophores, recognized by forming large blooms with significant environmental impacts. *E. huxleyi* can be found in all oceans (even in the permanently oligotrophic waters of the subtropical gyres), except in high latitudes of polar regions. However, large blooms of *E. huxleyi* have been observed mostly in the subarctic North Atlantic and adjacent seas [Brown and Yoder, 1994a; Winter et al., 1994; Tyrrell and Merico, 2004]. Apart from high rate of DMS emission, *E. huxleyi* blooms increase surface albedo (reflectance), accelerate calcite fluxes (to deep ocean) and affect the oceanic uptake of CO_2 [Westbroek et al., 1993].

The *Phaeocystis* genus contributes annually around 10% to the global marine primary production (due to high carbon biomass of the cells). Particular species of *Phaeocystis* form monospecific blooms of gelatinous colonies exist in both oceanic and coastal areas. The largest *Phaeocystis* blooms occur in the Northern and Southern polar waters, where *P. pouchetii* and *P. antarctica* form the blooms, respectively [Schoemann et al., 2005].

Dinoflagellates are unicellular micro-organisms with an extremely wide bio-diversity, consisting of about 2000 species, almost half of them being phototrophs [Gaines and Elbrächter, 1987]. Dinoflagellates are recognized to comprise a lot of toxic species, forming the so-called harmful algal blooms (HABs). During the warm months of summer some toxic species in temperate coastal waters form often extensive blooms in golden or red color, called *red-tides*, some of which harm extremely fish communities due to releasing neurotoxins [Smayda and Reynolds, 2003].

The applications of the functional-type approaches in ocean color remote sensing have been shown by several studies (e.g., Sathyendranath et al. [2004]; Alvain et al. [2005]; Aiken et al. [2007]; Raitsos et al. [2008]; Bracher et al. [2009]; Hirata et al. [2011]). However, it most be noted that even PFT-based classification of phytoplankton is not straightforward: firstly, the same taxonomic class of phytoplankton may include phytoplankton with diverse biogeochemical functions (and may contain a wide range of size classes); for instance, *E. huxleyi* is not only a DMS producer, but also a calcifier, as being a coccolithophore species. Furthermore, no single in-situ technique for identification of phytoplankton types is completely satisfactory [Nair et al., 2008].

2.2.3 Phytoplankton and nutrients

Different oceanic regions allow different types of microalgae to survive and grow, with different growth rates. This phenomenon is primarily due to the diversity of nutrient regimes supplied by different geographical/ecological areas, which in turn matches to the physiological varieties in phytoplankton species and respective metabolic processes. However, spatial variations of temperature and available sunlight are more direct factors to explain the geographical biodiversity of phytoplankton (as adaptation capabilities of phytoplankton to them are different) [Kirk, 1994]. Through photosynthesis, phytoplankton use sunlight, dissolved CO_2 and water to produce organic compounds, which are then used as food and building-blocks of cells. As photosynthesis is based on light absorption by photosynthetic pigments (e.g., chlorophylls), for marine microalgae photosynthesis occurs most significantly in surface water, which is often the upper $100\,m$ layer of the ocean. Part of the absorbed solar energy is used to break down water molecules into oxygen and hydrogen. The oxygen is partly released and the obtained hydrogen reacts with CO_2 to form simple organic molecules such as glucose ($C_6H_{12}O_6$), which are building-blocks for more complex organic compounds. However, the real process of photosynthesis is more complicated than described above; for instance, as part of its internal materials, photosynthesis requires certain types of nutrients, which are also essential for the growth and reproduction of phytoplankton.

Main nutrients Phytoplankton, in their life cycles, need a wide range of minerals, among which the most vital ones are nitrogen and phosphorous, as commonly used elements. These two elements are used by phytoplankton to build up proteins, nucleic acids and other cell parts; hence, are vitally important for growth and reproduction of phytoplankton [Kirk, 1994]. The uptake of nitrogen and phosphorous is a matter of competition, because while they are needed in large amounts for phytoplankton life/growth processes, their concentrations in seawater are very low in most regions. As most of phytoplankton can not directly take up atmospheric nitrogen (N_2), chemically reactive forms of nitrogen compounds, such as nitrate (NO_3^-) or ammonium (NH_4^+), are commonly used. Certain phytoplankton species (from cyanobacteria) can take up and consume molecular nitrogen and thereby are characterized as nitrogen fixers [Kirk, 1994]. The uptake of phosphorous occurs in the form phosphate (PO_4^{3-}) compounds. Phytoplankton keep growing until all of usable nitrogen and phosphorous are used up. In the most oceanic areas, nitrogen is depleted first and a nitrogen-limited growth will be the case, which ceases the increase in phytoplankton biomass.

Other nutrients It has been observed that in significantly large areas of the World Ocean (e.g., Southern Ocean, the equatorial Pacific and the northeast Pacific) even availability of large amounts of nitrate and phosphate in surface water does not lead to an expecting increase in phytoplankton biomass. To explain this fact, it has been proposed that, apart from nitrogen and phosphorous, there are also other nutrients regulating phytoplankton activities, especially iron [Martin, 1991; Morel et al., 1991]. Iron is used as a catalyzer of the electron transfer reactions in photosynthesis. Therefore, this trace element is necessary for the performance of photosynthesis in all phytoplankton species. As iron is highly insoluble in seawater, it is often a limiting nutrient with significant influence on regulation of phytoplankton biomass. Aside from iron, other trace metals such as copper, zinc and cobalt are also important for photosynthetic process in different species.

Silicon is another nutrient, which is vitally important for life cycles of a wide range of phytoplankton. Diatoms, the globally largest group of phytoplankton [Lochte et al., 1993], use silicon to make their silica skeletons (frustules). Depletion of silicon prevents the reproduction of diatoms (and certain other species) and can bring diatom spring blooms to an end; but silicon is not usually a limiting element for diatom growth in most oceanic areas, except in the very productive coastal

upwelling systems [Dortch et al., 1992].

It must be also noted that phytoplankton need nutrients in well-defined ratios, recognized as *Redfield ratios* [Redfield et al., 1963], stating that (in a revised empirical estimation) for each 117 atoms of carbon, 16 atoms of nitrogen and one atom of phosphorous are needed to be combined in an organic matter [Samiento and Gruber, 2006].

Sources of nutrients Nutrients enter the ocean basically through natural processes, the main sources of which are: weathering of rocks (e.g., silicates), conversion of atmospheric nitrogen into biologically usable forms, re-suspension of sediments (e.g., phosphorus-containing particles), aerosol load and dust deposition (e.g., iron and some trace metals), and remineralization processes. Remineralization refers to the process, by which the organic matter of phytoplankton cells is converted back into constructing nutrients (and CO_2). The organic agents of remineralization are zooplankton and bacteria, which eat living phytoplankton and their death bodies, respectively. As the remineralization process occurs both in surface water and deep ocean, the latter one serves as a nutrient source when the released nutrients (in depth) are brought back to the upper layer through upwellings. Moreover, anthropogenic inputs to the ocean are another source of nutrients. Examples of inputs from human activities are: sewage and detergents are the main human sources of oceanic phosphorous; nitrate-based compounds (e.g., as results of agriculture fertilizers, vehicles, etc.) are the anthropogenic source of oceanic nitrogen, entering oceans through rivers or raining precipitation.

Nutrient-based classification of waters In oceanography the regions of extremely low nutrient concentrations, often with very low phytoplankton productivity, are called oligotrophic waters or "ocean deserts". The regions of extreme scarcity of nutrients are referred to as hyper-oligotrophic waters: in the World Ocean, the subtropical gyres north and south of the equator are nutrient depleted areas all year round, exhibiting low surface chlorophyll. Contrary, the nutrient-rich aquatic areas, possessing high phytoplankton populations are called eutrophic waters: coastal areas or Case-2 waters, due to the large inputs of nitrogen and phosphorous from land, are the most biologically active regions of the oceans. Degrees of eutrophication typically range from hyper-oligotrophic water (maximum transparency, minimum chlorophyll-a) through oligotrophic, mesotrophic, eutrophic, to hyper-eutrophic waters (minimum transparency, maximum chlorophyll-a). It is worth mentioning that excess supply of nutrients, occurring in some coastal areas due to human activity, leads to enhanced phytoplankton growth. This phenomenon, which is called "eutrophication", can cause extensive blooms which harm the living constituents of seawater by lowering the oxygen content or by releasing toxins (in the case of HABs).

2.2.4 Seasonal cycles and mixed layer depth

Phytoplankton growth has a well-defined seasonal pattern in temperate and polar oceanic regions. Generally speaking, there are three types of processes, which control and regulate phytoplankton growth and respective biomass through seasons: physical, biological and chemical processes. At the physical level, temperature (T) and density (ρ) of seawater play the major role in the dynamics of surface water, which affect strongly the phytoplankton activities and life cycles. Heating from sun controls the temperature of seawater and the latter controls in turn water density: the more sunlight, the higher (surface) temperature and the lower water density, and vice versa. On the other hand, density is dependent also on the salt content of seawater (salinity, S). It means that the density of the upper ocean is primarily a function of temperature and salinity. However,

there are also other factors affecting these parameters: e.g, evaporation of water increases water salinity and density; while inputs of fresh water by rain and rivers lower both salinity and density. The temporal changes in temperature and salinity of seawater around the globe, along with specific characteristics of water (e.g., a huge heat capacity), lead to the stratification of water bodies. Consequently, in different oceanic areas there are varieties of vertical profiles of density and temperature, each of them following its own temporal variation.

To understand the seasonal variation of phytoplankton biomass, it should be discussed how the changes in heating (from sun) influence the vertical structure of the upper layers of oceans (usually the top few hundred meters). Since in the ocean the vertical transport of heat is carried out by the bulk movement of water-bodies (convection), the concept of *mixed-layer* is relevant for describing the variations in vertical structure. The surface mixed layer is the upper layer within which salinity, temperature and density are almost vertically uniform, due to the turbulences induced by winds, cooling/heating processes and other factors such as evaporation. The homogeneity is not perfect because velocities exhibit significant shears within the mixed layer [Boyer-Montegut et al., 2004]. The bottom of the mixed layer is characterized by a gradient in the vertical variation of water properties (T, S and ρ). The depth of mixed layer determines the average level of light seen by marine organisms (e.g., in very deep mixed layers phytoplankton are not able to absorb enough light for photosynthesis). Moreover, variations of the mixed layer depth (MLD) with the heating process (or density change) regulates the distribution of nutrients in surface waters. Therefore, the depth of surface mixed layer (i.e., MLD) and its temporal variations are very important factors in marine biology [Obata et al., 1996]. For instance, Sverdrup [1953] proposed a useful criterion for describing the initiation of a spring bloom, called *critical depth*. Shallowing of the mixed-layer depth to a depth less than the critical depth is coincident with the rapid growth of phytoplankton (or spring bloom).

Winter: in winter, very low heat flux from the Sun leads to the cooling of surface waters, in a more rapid rate than in the autumn. The result is a high increase in the density of upper layer. Consequently, the surface waters are mixed up with the less dense waters below, which in turn brings the deep water nutrients (e.g., accumulated through re-mineralization processes) back to the surface. Therefore, the surface waters become nutrient-rich during the winter. However, as sunlight is not sufficient for a substantial rate of photosynthesis, phytoplankton do not grow. The winter season, in this context, is recognized by a deep mixed layer and nutrient-rich surface waters. Due to lasting of the cooling process and the mixing of adjacent layers, the value of MLD increases, as well as the amount of surface nutrients (see Fig. 2.8).

Spring: in spring, due to the availability of sunlight, surface waters become warm and lose density, which makes them floating on top of the colder and therefore more dense layer below. As a result, phytoplankton growth occurs in surface waters, where plenty of nutrients are available after being mixed up from the deep waters during winter. Therefore, rapid growth in phytoplankton biomass occurs, which is called the spring bloom. However, in most regions, phytoplankton spring blooms are followed by zooplankton blooms, which reduce phytoplankton population (as a biological factor) and balance it to some steady levels (see Fig. 2.8). The spring season, in this context, is recognized by moderate mixed layer depth and falling nutrient levels in the surface waters. High density difference between surface waters and the layer below, leads to a relatively fixed value of MLD.

Summer: in summer, although there is high amount of sunlight, phytoplankton growth stops, because nutrients have been already used up by the large phytoplankton population appearing by

the spring bloom. On the other hand, the warm and light surface water does not allow any mixing-up with the cold layers below. Hence, algal activities decrease strongly during summer; when all nutrients are eaten up, the summer phytoplankton biomass will reach its minimum. However, remineralization of nutrients in the surface waters provides, to some extent, phytoplankton with required nutrients. Moreover, using the atmospheric inputs of nutrients (i.e., dust decomposition) certain types of phytoplankton can survive and grow. The same is true for the riverine inputs to the coastal waters). Overall, in large parts of the World Ocean (e.g., in temperate latitudes) summer is not a biologically active period, compared to spring. The summer season, in this context, is recognized by shallow mixed layer and low nutrient levels in the surface waters (see Fig. 2.8). High density difference between surface waters and the layer below, leads to a fixed value of MLD.

Autumn: in autumn, day-time becomes shorter, which (along with the reduced solar elevation) leads to less heating from the sun and thereby to cooling down of surface waters. Consequently, the density of surface waters increases, which in turn causes a small density difference with the layer below. As a result, the upper layer sinks down and the nutrient-rich waters from below come to the top (mixing up process). As there is still enough sunlight for photosynthesis, a phytoplankton growth occurs, observed as an elevated biomass, which is called the fall bloom. The biomass magnitude of the fall blooms is always smaller than spring blooms, because both available sunlight and nutrients during the autumn are lower than the respective quantities in spring. This can also be seen in Fig. 2.8, where the higher peak is assigned to the spring bloom, and a secondary peak to the fall bloom. The autumn season, in this context, is recognized by moderate mixed layer depth and rising nutrient levels in the surface waters. The small density difference (reversely) between surface waters and below layer, leads to a continuous increase in the value of MLD.

It must be noted that the seasonal cycles described above are not so pronounced in the tropical waters, because in these areas the temporal variations in sunlight are not strong; therefore, phytoplankton can (in principle) grow throughout the year (depending on the nutrients' conditions). Moreover, there are oceanic regions of high upwelling characteristic, where nutrient-rich waters are regularly brought to the surface and cause high phytoplankton productivity. In upwelling areas the patterns of phytoplankton growth do not follow simply the seasonal patterns, even though they are affected by the temporal variations in available sunlight. Upwelling regions can be specific points of the deep-ocean circulation, or simply the areas where ocean currents meet an ocean bank or a sea mount. One of the most well-known upwelling region is the Mauritanian upwelling area off the coast of Mauritania in the west of Africa. Unordinary increases in phytoplankton biomass (beyond the typical seasonal patterns) can also occur when iron-rich minerals are carried into the ocean either via the winds transporting dusts from deserts (e.g., Sahara and Patagonia) or by glacial rivers and icebergs. Strong oceanic storms (e.g., hurricanes and typhoons) and eddies have also been repeatedly reported to trigger rapid growth of phytoplankton in some regions, due to affecting the ecology of upper ocean on a regional scale (e.g., Babin et al. [2004]; Lin [2011]; Williams [2011]).

2.2.5 Phytoplankton blooms: definition and dynamics

Phytoplankton blooms are recognized by rapid and temporary increases in the amount of cells of marine algae (mono-species or multi-species) in certain areas [Smayda, 1997b]. Apart from the significant rise in cell concentrations, "bloom", as generally used, is an imprecise term, because of the variations associated with species and environmental conditions. However, at the peak of massive blooms, cell concentrations typically reach the range of $1,000,000$ cells per liter or higher (depending on the species and the nutrient condition, etc.) [Tyrrell and Merico, 2004].

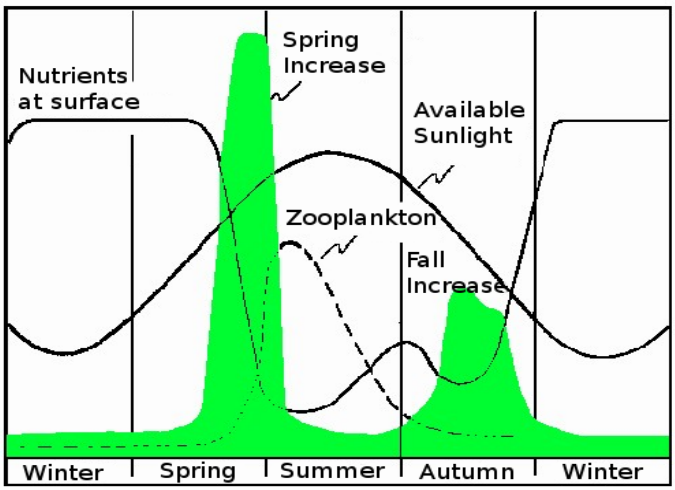

Figure 2.8: Typical pattern of seasonal variations of phytoplankton biomass in the temperate North Atlantic, compared with the variations of sunlight, zooplankton activity and nutrients' availability. The figure adapted from: `http://www.jochemnet.de/fiu/OCB3043_23.html`.

Mass occurrences of phytoplankton populations are common and natural events, appearing under favorable conditions as availability of sufficient nutrients and sunlight, are intrinsically beneficial to marine food-web processes. Periodic spring blooms occur in most sea-waters when increased sunlight causes the thermocline layer to be formed, which in turn leads to the well-mixed water columns in the upper ocean and abundance of nutrients after scarcity of winter season. Fall blooms are also abundant, though weaker than spring blooms, when the nutrient rich waters in autumn are turbulently stirred by winds to the surface [Smayda, 1997a].

The most abundant (and the largest) spring blooms are globally formed by diatoms, which are considered to be the first primary producers in marine environments [Lignell et al., 1993]. Hence, current concepts, models and experimental approaches of studying bloom dynamics/regulations are primarily based on diatom-dominated spring blooms. Accordingly, blooms of other species have been so far dismissed or received very low attentions (for instance, blooms of dinoflagellates or even small blooms of diatoms in other seasons); the reason is that it was traditionally widely accepted that the spring (upwelling) blooms of diatoms are driving the whole marine trophodynamics and can "sufficiently" explain the nutrient regulations, growth dynamics and respective mass balance. Moreover, there are methodological limitations to deal with the successions of blooms and subordinate species occurring during bloom events, their variable ecophysiology and the potentials of bloom magnitude [Smayda, 1997a]. Bloom abundance and fluctuations are commonly expressed in terms of community biomass, where chlorophyll-a content is usually representing the abundance index and the rate processes of total community (such as primary production) is normalized by that. Therefore, phytoplankton growth is conventionally measured as a whole community response, based on chlorophyll-a index.

Community growth measurements presume that: (a) community's taxonomic elements are physiologically equivalent, and (b) chlorophyll-based estimates of community growth-rate are adequate to measure the behavior of the dominant species. However, these assumptions provide limited insight into bloom dynamics. In reality, community growth is only one of three different, concurrent growth modes which characterize phytoplankton population dynamics: cellular growth, population growth, and community growth. [Smayda, 1997a]. For instance, while coccolithophore blooms, dominated by *E. huxleyi*, are also globally abundant, due to very small cell size,

E. huxleyi blooms are usually associated with low rather than high *chl-a* concentrations [Tyrrell and Merico, 2004]. This fact, with respect to the above discussion, becomes more notable by considering that there are big overlaps (spatially and temporary) between the blooms of diatoms and coccolithophores; e.g., in relatively eutrophic waters of temperate latitudes *E. huxleyi* blooms occur just following the diatom spring blooms [Tyrrell and Merico, 2004].

On the other hand, it was observed that during the second half of the 20th century algal bloom events have been increased on global scale in duration, intensity, and frequency [Anderson et al., 1989, 2000; Bianchi et al., 2000]. Main reasons proposed for this increase have been:[4]

- transformations associated with climate change [Taylor, 1990; Smayda, 1997b], most notably:
  - rise in sea surface temperature [Stumpf and Tomlinson, 2005],
  - rise in storm events, increasing re-suspension rates of nutrients and spores [Babin et al., 2004],
  - rise in oceanic acidification (decreased pH-values of seawater) [Bianchi et al., 2000],
  - change in ecosystem and marine diversity [Andrefouet et al., 2008],
- increase in coastal eutrophication due to agriculture, aquaculture and anthropogenic effects [Anderson et al., 2002],
- ship transports of alien phytoplankton species (carried by ballast waters) [Hallegraeff, 2003].

Therefore, developing alternative methods for studying the evolution and dynamics of phytoplankton blooms (beyond in-situ sampling and microscopic measurements) becomes more and more important. In this sense, a global framework (using satellite remote sensing) is a vital factor, as well as considering the species-diversity of the blooms, especially with respect to the biogeochemical impacts of different phytoplankton functional types involved in the prevalent bloom events.

2.3 Environmental impacts of phytoplankton: a climate view

Oceans and climate: a general overview

Around 71% of Earth's surface is covered by oceans that play a critical role in climate, both on global and on regional scales. First of all, due to the very high specific heat capacity of water, oceans moderate significantly the global temperature and prevent it from dramatic changes (the huge specific heat capacity of water is a consequence of hydrogen bonds among water molecules). Secondly, through thermohaline circulation and wind-driven circulation, ruled by a temperature gradient between the polar regions and the equator, oceans redistribute the heterogeneous incoming solar energy over the Earth. Oceans determine and affect the temporal and spatial regimes of major winds, which have high contribution in the Earth's climate. Moreover, by permanent evaporation and supplying the *cloud condensation nuclei* (CCN), oceans have an essential role in cloud formation and through which in the overall atmospheric albedo [Charlson et al., 1987]. Oceans take up atmospheric carbon dioxide and control the exchange-rate of CO_2 with the atmosphere. Accordingly, oceans link the physical processes to the biological processes (phytoplankton primary production) to convert part of the dissolved CO_2 into organic matter. The organic matter

[4] The reasons classified here for the globally observed increase in the phytoplankton bloom events have been adapted from Ebert [2009].

partly sinks down to the deep ocean, where it can be stored for a long time either as dissolved CO_2 or as carbonate sediment at the ocean floor. Therefore, oceans have a vital role in global carbon cycle, as well as being the main sink for atmospheric CO_2 [Sabine et al., 2004]. Roughly speaking, the total amount of carbon in the ocean is about 50 times greater than the amount in the atmosphere. As pointed out above, apart from the physical impacts of the ocean onto the climate, oceans influence the climate also through biological processes, which are mainly mediated by the functions of marine phytoplankton. Indeed, it is thought that climate is partly controlled/regulated by marine algae.

2.3.1 Phytoplankton and the global carbon cycle: biological pump

Global carbon cycle

There are two forms of carbon: organic carbon, which is part of compounds formed by living organisms (biomass) bonded to hydrogen or nitrogen; and inorganic carbon, which is mostly oxidized form of carbon (e.g., CO_2, $CaCO_3$). The global carbon cycle includes terrestrial and marine domains, which can involve organic or inorganic carbon. The main classification of the global carbon cycle corresponds to the durations of the cycles, or the residence times. The residence time is the average amount of time during which a substance stays in a given reservoir at steady state. For a natural cycle the term *Steady State* refers to the state for which the size of reservoir does not change with time, though varying with seasons; namely, the rate of the inputs are equal to the rate of the outputs. In this sense, the global carbon cycle includes the short-term cycles, with residence times of several days to several years, basically happening in biosphere (e.g., carbon exchange between surface-ocean and atmosphere); the intermediate-term cycles, with residence times of 100 to 1000 years, happening mostly in the deep ocean; and the long-term cycles, with residence times of millions of years, happening in the geosphere (sediments and rocks). Oceanic organic carbon contribute both in the short-term and long-term cycles, while oceanic inorganic carbon (e.g., $CaCO_3$) are mostly involved in the intermediate-term cycle [Bolin, 1983; Siegenthaler and Sarmiento, 1993]. The main global reservoirs of carbon, in a decreasing order, are: geosphere, oceans and hydrosphere, soil, atmosphere and biosphere. In the global ocean, upwelling waters (rich in CO_2) are the source regions for carbon and downwelling regions (with high productivity) are the respecting sink regions (`www.globe.gov/projects/carbon`). Since oceans contain 60 times more C than atmosphere, thus the short-term and intermediate-term C cycles are driven by oceans. As 92 GtC/yr (gigaton carbon per year) atmospheric input C into the oceans are compensated by 90 GtC/yr output C to the atmosphere, the exchange with atmosphere through surface out is not balanced and ocean is a regarded as a sink [Sabine et al., 2004]. If the contribution of sediment sink (about 0.2 GtC/yr) is taken into account, then the annual C input of 92 GtC/yr from atmosphere into the global ocean is corresponding to the total output of 90.2 GtC/yr.

Inorganic C enters into the ocean based on gas solubility and biological pump of organic C (explained in the next subsection). According to the *Henry's Law* ($S * P_{CO2} = [CO_{2(aq)}]$; with S as the solubility constant), the gas solubility depends on the partial pressure of CO_2 and water temperature as follows: the lower temperature and higher P_{CO_2} result in higher solubility, i.e., higher $[CO_{2(aq)}]$ [Feely et al., 2001]. Inorganic C exists as different forms of dissolved inorganic carbon (DIC), most of which being transported towards the deep ocean. Deep DIC is the largest storage of carbon in the global ocean, with very long residence time, even though contributing partially in the sediment flux. After a very long period DIC is transported towards the upper ocean along with the oceanic deep circulation.

Oceanic organic carbon is produced in the surface ocean on a daily basis through primary and secondary productions, existing in two forms of dissolved and particulate organic carbon (DOC and POC, respectively). After being produced by biological processes (e.g., photosynthesis) in

the upper ocean, organic carbon is mixed downward and diluted by physical processes. Within the water column (or in shallow sediment), most of the released organic carbon is remineralized by micro-organisms within several hours to days and recycled back into surface ocean DIC or deep ocean DIC [Hansell and Carlson, 2001]. Fig. 2.9 provides an overall view of the main sinks, sources and fluxes of carbon of the Earth System (IPCC 2007: Solomon et al. [2007]). The exchange rates of carbon between ocean, atmosphere and land, with respective estimated fluxes, have been schematically illustrated in this figure. The contribution of anthropogenic carbon emission is highlighted.

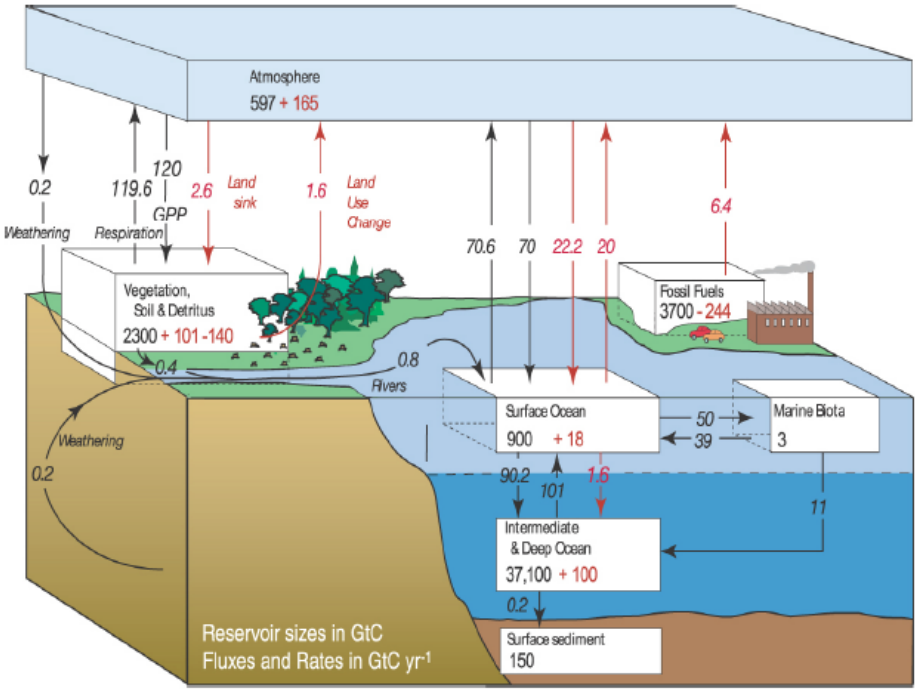

Figure 2.9: The IPCC 2007 report on global carbon cycle for the 1990s. The main annual fluxes in GtC/yr are shown both for pre-industrial natural fluxes (black) and anthropogenic fluxes (red) based on Samiento and Gruber [2006]; Sabine et al. [2004]. IPCC stands for the Intergovernmental Panel on Climate Change.

Ocean's biological pump and carbon flux

Around a quarter of anthropogenic carbon dioxide, produced by burning fossil fuels, are stored in the oceans. Although carbon dioxide is continuously exchanged between oceans and atmosphere (driven by air-sea heat flux), part of dissolved CO_2 is sank down to the deep ocean (directly or indirectly) and stays away from the surface water, where it can be transported back into the atmosphere. This sinking process of carbon can occur directly as a pure physical process during the formation of deep waters (mostly in the Labrador Sea and the Greenland Sea in the northern North Atlantic), where cool surface waters, containing high amount of dissolved CO_2 sink down and convey dissolved CO_2 to the depth (solubility of carbon dioxide increases in cold waters). This process of direct transport of *dissolved inorganic carbon* (DIC) to the deep ocean is known as *solubility pump*, which is regarded as a thermally-driven gas-exchange pump. As a brief result of the *solubility pump*, in cold-fresh waters CO_2 uptake from atmosphere is favored and in warm-haline waters CO_2 release into the atmosphere is favored [Volk and Hoffert, 1985; Siegenthaler and Sarmiento, 1993].

Dissolved inorganic carbon (DIC), exists in the ocean as the following forms: $CO_{2(aq)}$ (aqueous carbon dioxide), H_2CO_3 (carbonic acid), HCO_3^- (bicarbonate ion) and CO_3^{-2} (carbonate ion). The abundant form is determined by the actual rate of pH, which for a normal oceanic condition would favor the bicarbonate ion (HCO_3^-). The abundance ratios of $[CO_{2(aq)}]$, $[HCO_3^-]$ and $[CO_3^{-2}]$ are believed to be 1:100:10 [Dickson, 1991].

Different forms of DIC existing in the ocean transform to each other as follows:

Dissolution of aquatic carbon dioxide, $CO_{2(aq)}$, in seawater:

$$CO_{2(aq)} + H_2O \Longleftrightarrow H_2CO_3 \quad (carbonic\ acid) \tag{2.38}$$

Dissociation of carbonic acid, H_2CO_3 (depending on pH):

$$H_2CO_3 \Longleftrightarrow H^+ + HCO_3^- \quad (bicarbonate) \tag{2.39}$$

Dissolution of bicarbonate, HCO_3^- (depending on pH):

$$HCO_3^- \Longleftrightarrow H^+ + CO_3^{-2} \quad (carbonate\ ion) \tag{2.40}$$

The last equation controls the pH of seawater; i.e., when pH increases (decreasing H^+, because: $pH = -log[H^+]$) the forward reaction is favored, which means a higher production of carbonate ion; and when pH decreases (increasing $[H^+]$) the backward reaction is favored, which means a higher production of carbonic acid. In general, the ratio of $[HCO_3^-]/[CO_3^{-2}]$ varies to keep the level of pH at about 8.

Moreover, there is another process of carbon transport driven by phytoplankton activity, happening almost all over the global ocean, however, in much lower rates in oligotrophic regions, which are characterized by very low levels of nutrient concentration and phytoplankton population. This process is called *biological pump*, which will be briefly described in the next passages.

Via photosynthesis, phytoplankton convert dissolved carbon dioxide ($CO_{2(aq)}$) into glucose ($C_6H_{12}O_6$) (Eq. 2.41), which is then consumed for constructing more complex organic compounds needed for phytoplankton's life-cycle and reproduction. The net equation of photosynthesis process, occurring mainly within the *euphotic zone* or roughly within the upper 150 m of water column, is the following reaction:

$$6CO_2 + 6H_2O + light \Longrightarrow C_6H_{12}O_6 + 6O_2 \tag{2.41}$$

Photosynthesis, as seen in Eq. 2.41, is considered as the main step to convert dissolved inorganic carbon into organic matter. Furthermore, as part of the short-term C cycle, photosynthesis results in seasonal cycling of atmospheric CO_2. Beside sunlight and $CO_{2(aq)}$, marine phytoplankton require adequate supply of essential nutrients (mainly phosphate, nitrate, silicate, iron) to form organic carbon/tissue through photosynthesis. The ratios at which CO_2, nitrate and phosphate are cycled are known as *Redfield ratios* [Redfield et al., 1963]. The *Redfield ratios*, as an empirical estimation (with uncertainty) is written as follows:

$$CO_2 : NO_3^- : PO_4^{3-} \simeq 117 : 16 : 1 \tag{2.42}$$

The stoichiometric results of *Redfield ratios* imply that oceanic organic matters involve almost a "fixed" ratio of carbon and nutrients [Samiento and Gruber, 2006].

Based on nutrient consumption, oceanic photosynthesis can be represented in a more precise way to include also the remineralization/respiration process (as backward reaction):

$$106CO_2 + 16HNO_3 + H_3PO_4 + 78H_2O \Longleftrightarrow C_{106}H_{175}O_{42}N_{16}P + 150O_2 \qquad (2.43)$$

where the first term on the right is the produced organic matter. This term can be ideally stated as a hypothetical molecule containing the mean composition of the oceanic organic matter: $(CH_2O)_x(NH_3)_y(H_3PO_4)_z$.

As phytoplankton have typically very short lives, after few days their dead bodies are remineralized by surface water bacteria, producing back CO_2 into the water, part of which is reused in photosynthesis and the rest is transfered back into the atmosphere (see Fig. 1.1 in Chapter 1). However, for larger species of phytoplankton, deceased organisms sink down directly and together with aggregates and faecal pellets form the so-called *marine snow*. The marine snow is a precipitation flux of mostly organic detritus (including zooplankton's as well), exporting particulate carbon from the upper layers of water column to the deep water, where it can be temporarily suspended or also be buried onto the ocean floor (Fig. 1.1). Again, the deep ocean organic matter will be remineralized (via bacterial respiration) to be decomposed into dissolved CO_2 and different minerals (nutrients). Dissolved CO_2 is trapped there for several thousands of years, until the water body reaches the surface along the upwelling process of the ocean circulation. In general, the vast majority ($>99\%$) of sinking organic matter is degraded within the upper water column, reproducing DIC and nutrients [Wakeham et al., 1997]. From 50 GtC produced annually by the marine biosphere, about 40 GtC is recycled back as DIC into surface ocean, and 10 GtC is stored as deep DIC [Hansell and Carlson, 2001; Feely et al., 2001]. This process, through which particulate carbon is transported from surface water (euphotic zone) to the deep water, is called ocean's *biological pump*. The *Biological pump* links atmospheric processes to the oceanic biogeochemical processes and is much faster than the *solubility pump*. However, both pumps end up with storing carbon as DIC in the deep ocean [Raven and Falkowski, 1999; Ducklow et al., 2001].

The term of *biological pump* can be applied to refer to two different types of carbon export: the transport of particulate organic carbon (POC) is denoted by *soft-tissue pump* and the transport of particulate inorganic carbon (PIC) is denoted by *hard-tissue pump*, where PIC refers to the suspended calcite particles, composed of calcium carbonate ($CaCO_3$). This distinction is needed because it is believed that the long term carbon cycle is controlled by $CaCO_3$ [Milliman, 1993; Raven and Falkowski, 1999]. Briefly speaking, the *soft-tissue pump* refers to the process, in which the consumed carbon via photosynthesis enters the ocean's food chain, and eventually falls out of the surface layers as organic particulate matter, most of which is redissolved (through remineralization process) into the deep $CO_{2(aq)}$ before reaching the sea floor. However, the *hard-tissue pump* refers to the flux of particulate carbon from the surface ocean to the ocean interior, depleting surface carbon and enriching deep carbon. Since calcite particles (calcium carbonate) are the most abundant carriers of inorganic particulate carbon in the ocean, the *hard-tissue pump* is sometimes called carbonate pump, which is described below.

Carbonate pump and phytoplankton's contribution

Through decomposition of dead materials of calcifying organisms, calcite particulates (PIC) are released. Depending upon the local carbonate chemistry, the released PIC will be either dissolved in surface water or exported to the deep ocean, where they will be sedimented on the ocean floor. The export of carbonate shells, produced in the upper ocean, towards deep waters is known as *carbonate pump*, which is also referred to as the *hard-tissue pump*, because the downward calcite flux can be also part of the sinking process of particulate organic matter (POC). While the *soft-tissue pump* is directly related to photosynthesis, the other part of the biological pump, i.e., the *carbonate*

pump is interrelated to the export of the organic-produced calcium carbonate, occurring not only by calcareous phytoplankton (e.g., coccolithophores), but also by some other marine organisms (e.g., certain types of zooplankton, such as foraminifera). The other compounds containing calcium carbonate, originating from marine organisms, are aragonite (crystal forms of calcite) and magnesian calcite ($MgCO_3$).

The factors controlling the strength of the carbonate pump are less well determined, but generally the downward flux of carbon by the *carbonate pump* is considered to be about 25% of that by the *soft tissue pump* [Ducklow et al., 2001; Samiento and Gruber, 2006].

The oceanic formation of $CaCO_3$ (calcification) and respective dissolution can be expressed by the following reaction:

$$Ca^{2+} + 2HCO_3^- \Longleftrightarrow CaCO_3 + CO_{2(aq)} + H_2O \tag{2.44}$$

The above calcification reaction indicates the pathway through which calcareous plankton (e.g., coccolithophores and foraminifera) build up their shells and skeletons.

Although the CO_2 released by calcification may be completely recycled within the cell by photosynthesis, during organic formation of carbonate shells (forward reaction in Eq. 2.44) slight amounts of CO_2 can be released in surface waters (alkalinity consumption) [Nimer et al., 1994]; whereas during calcite dissolution in deep waters (backward reaction in Eq. 2.44), CO_2 is consumed (alkalinity production). In deep water there is more carbonate dissolution, because cold water under high pressure has a higher saturation value for CO_2, causing more H^+ to be released, which leads to more acidity and then more dissolution of carbonate sediments (the solubility of $CaCO_3$ increases with high pressure and (slightly) with low temperature). As a result, the waters of high HCO_3^- (released through calcite dissolution) can be in turn transported to the surface waters by upwelling circulation and increase the rate of CO_2 uptake from the atmosphere [Volk and Hoffert, 1985]. Hence, the precipitation and dissolution of $CaCO_3$ influence the alkalinity and total CO_2 and can thus change ocean pH and pCO_2.

The importance of the calcification process in the global carbon cycle has been increased [Bates et al., 1996; Balch and Kilpatrick, 1996]. Based on data from vertical distributions of $CaCO_3$ and sediment-trap studies, it has been suggested that, under calcite over-saturated conditions, significant dissolution of calcium carbonate is occurring in the upper 1000 m of the water column, which could act as a potential sink for atmospheric CO_2 [Milliman et al., 1999]. Therefore, a better assessment of factors controlling the production and dissolution of calcium carbonate is of great relevance for research on global climate [Chou et al., 2009].

Generally speaking, the distribution of carbon in the ocean is regulated by a combination of three major factors: transport by circulation, chemical processes and biological processes, which are in turn related to the oceanic parameters of salinity (transportation), temperature (influencing the solubility pump) and nutrient regime (controlling phytoplankton activities and hence biological pumps) [Raven and Falkowski, 1999; Ducklow et al., 2001]. Particularly, the strength of the biological carbon pumps is modulated by the rate at which nutrients are supplied to the euphotic zone. Without the carbon pumps, atmospheric levels of CO_2 would be much higher than at present and the climate condition on the large scale would be much different.

2.3.2 Phytoplankton and the global sulfur cycle: DMS emission

Gas and particle exchanges are very important interactions between oceans and atmosphere. There are several gases and particles emitted by marine phytoplankton, which play vital roles in global

climate. In particular, phytoplankton emission of dimethyl-sulfide (DMS) is known to be very important in the global sulfur cycle and hence in the global climate [Andreae et al., 1983; Charlson et al., 1987]. The marine emissions of biogenic sulfur into the atmosphere is comparable to the total sulfur released by all fossil-fuel burnings [Turner and Liss, 1983; Liss et al., 1997]. It is evident that periods of enhanced activities of marine phytoplankton are directly correlated to the enhanced organic mass in marine aerosols [Singh et al., 2003]. Here, we describe briefly the DMS emission by phytoplankton and its prominent role in climate. Afterwards, in the next subsection, other major phytoplankton emissions are summarized.

Formation of DMS

Dimethyl-sulfide, DMS, with the chemical formula of CH_3SCH_3, is the major volatile sulfur compound in seawater and its emission to the air causes the characteristic smell of the sea. DMS is regarded as an important atmospheric trace gas produced biologically in oceans and at the same time being responsible for the main transfer of reduced sulfur from the ocean to the atmosphere [Andreae and Raemdonck, 1983; Andreae, 1990]. DMS is produced by the enzymatic cleavage of *dimethyl sulphoniopropionate* [DMSP, $(CH_3)_2S^+(CH_2)_2COO^-$], which is found within the cells of certain groups of phytoplankton and also specific types of macro-algae. There are several reasons for the production of DMSP, including avoiding harmful waste products, surviving in cold and salty waters and preventing from being preyed by other organisms [Archer et al., 2001; Kumar et al., 2002]. After the carrier phytoplankton have been infected, died or eaten, the DMSP is broken down and DMS is released. However, between the biogenic synthesis of DMSP and the DMS emission into the atmosphere, many complex biophysical and biochemical processes influence the transformation, including: phytoplankton growth, autolysis, grazing by zooplankton, viral lysis, bacterial consumption, photochemistry, etc. [Malin and Kirst, 1997; Simo, 2001].

Only part of the generated DMS reaches the atmosphere; the remaining is consumed by bacteria in the ocean-water or is converted to other compounds. Since DMS is connected to the phytoplankton activity, the DMS emission is found during phytoplankton growth periods.

It has been estimated that DMS provides about 21% of the global sulfur flux and more than 38% of the sulfur entering the atmosphere and therefore is the major natural input source of the global sulfur cycle [Simo, 2001]. Other natural sources for sulfur flux are volcanic eruptions and organic production of COS and CS_2 from land plants and marine algae. DMS emission can be observed mostly in regions where specific types of phytoplankton are growing.

Although particular members of several classes of phytoplankton (including: dinophyceae, haptophyceae, chrysophyceae, pelagophyceae and prasinophyceae) are recognized to be DMSP producers, however, intracellular concentration of DMSP, as the biogenic precursor of DMS, is highest in haptophytes and dinoflagellates [Liss et al., 1997; Sunda et al., 2002]. Overall, coccolithophores (belonging to the haptophytes) are the most recognized DMS producers in the global ocean [Keller et al., 1989]. Since among several coccolithophore species, all being characterized by constructing calcite shells/skeletons, *E. huxleyi* (Fig. 2.10) is the dominant species in most oceanic regions, it is considered to be the prominent phytoplankton species involved in DMS emission [Liss et al., 1997; Malin and Steinke, 2004].

High amounts of DMS emissions have been observed in northern parts of the North Atlantic Ocean and also in the Bering Sea of the North Pacific Ocean, where large coccolithophore blooms, dominated by *E. huxleyi*, are abundant (Tyrrell and Merico [2004]).

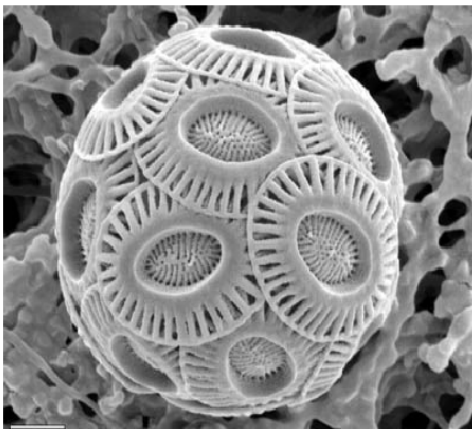

Figure 2.10: A microscopic view of a *E. huxleyi* cell, surrounded by attached coccoliths. By building calcite shells (coccoliths), coccolithophore species contribute strongly in the oceanic carbonate and carbon cycles. (image courtesy of Markus Geisen and Jeremy Young).

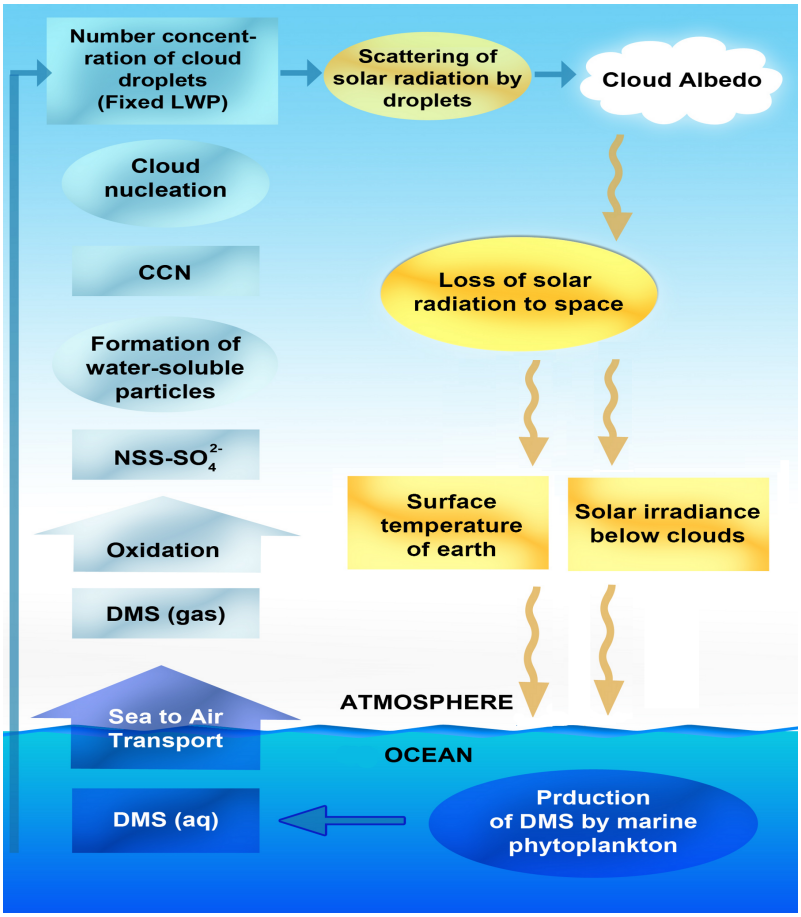

Figure 2.11: A scheme of the cycle of dimethyl-sulfide (DMS) and its exchange between ocean and atmosphere. The figure was taken (and recreated) from: `http://me-www.jrc.it/dms/dms.html`.

DMS emission and Climate

DMS is the predominant form of biogenic sulfur transferred from the ocean into the atmosphere. The total amount of DMS entering annually into the atmosphere has been estimated to be 40 ± 20 Tg S/yr, with Tg denoting *teragram* (10^{12} g or million tonnes). This amount covers $80 - 95\%$ of gaseous sulfur emitted from oceans and about one half of the estimated natural sulfur flux per year [Andreae et al., 1983; Liss et al., 1997]. After being delivered into the atmosphere, DMS is oxidized by OH, NO_3, BrO and Cl to form, via different pathways, sulphate (SO_4^{2-}) and methylsulphonic acid, MSA (while SO_2 is produced also through fossil-fuel combustion and volcanic eruptions, MSA is only originated from DMS). After successive reactions, sulfur dioxide (SO_2) is produced as an intermediate species, which in turn is transformed into sulfuric acid (H_2SO_4). The acidic oxidation products of DMS (like H_2SO_4) react with rain droplets to produce acid rain [Liss et al., 1997]. Acid rainfalls, reduce the amount of atmospheric sulfur by returning parts of the sulfate aerosols back into the land and the ocean. From the reaction between sulfuric acid and ammonia (NH_3), which is another gaseous output of phytoplankton activity, ammonium sulphate aerosols are produced [Malin et al., 1992; Simo, 2001]. Thus, DMS, directly and indirectly, contributes in controlling the rate of atmospheric acidity (along with volcanoes and fossil-fuel combustion).

In the lower atmosphere both sulfuric acid and ammonium sulphate serve as cloud condensation nuclei (CCN), which are essential in cloud formations. Sulphate aerosols, mostly originated from DMS, have two main impacts on climate: located at a stratospheric belt along with other aerosols, they absorb and scatter directly solar radiation and in this way have a direct cooling effect; additionally, acting as CCN, sulphate aerosols are essential for cloud formation and therefore they have indirect cooling effect, due to the cooling effect of clouds' albedo. Both these cooling effects counteract partly the warming effect of carbon dioxide and other greenhouse gases [Charlson et al., 1987; Malin et al., 1992].

Consequently, by producing and emitting DMS into the atmosphere, marine phytoplankton play a vital role in the radiation budget of the Earth, as well as being the main source of acidity of the atmosphere over marine regions [Andreae, 1990]. Fig. 2.11 illustrates schematically the role of DMS in the atmosphere. However, it is worth mentioning that despite some exaggerating views, addressing a compensative role of phytoplankton DMS productivity against the global warming, like *CLAW hypothesis* [Charlson et al., 1987], it is still under debates how large exactly the contribution of phytoplankton in climate control is.

2.3.3 Other emissions by phytoplankton: Halocarbons and VOCs

In addition to DMS, there are other trace gases emitted from seawater, with high climatic impacts. These gases are not directly, like DMS, produced from phytoplankton activity, but are produced from the reaction of sunlight with some organic compounds coming originally from phytoplankton. The main gases produced in this manner are carbonyl sulfide (COS) and halocarbons. Carbonyl sulfide is produced photochemically from dissolved organic matter (DOM) and participates in the stratospheric ozone cycle (COS is not broken in troposphere), as well as in the sulfur cycle and atmospheric albedo, by forming sulfate aerosols [Andreae, 1990]. Marine production of COS is a globally significant source of this gas. Volatile halocarbons (volatile halogenated organic compounds, VHOC) are carbon-based organic compounds, containing halogen elements, i.e, chlorine, iodine and bromine. The contribution of halogens in oceanic chemistry is no surprise, considering that the ocean is globally the main near-surface reservoir of the halogens (chlorine, bromine and iodine), existing as halide ions in seawater, among which the chlorine ion Cl^- and the oxidized iodine (iodate, IO_3^-) are more abundant [Chuck et al., 2005]. Apart from the direct

flux of sea-salt particulates into the air, volatile halogenated compounds are also important to the transfer of halogen elements from the ocean to the atmosphere [Vogt et al., 1999; Yassaa et al., 2008]. The production of halocarbons in seawater is a result of biological processes and the effect of sunlight upon some organic compounds in surface water. For instance, methyl iodide (CH_3I), a major oceanic halocarbons and the main carrier of iodine to the atmosphere [Lovelock, 1975], is produced by some phytoplankton species, some seaweeds species and also by photosynthesis of iodine-containing organic compounds. Volatile halocarbons escaped from ocean become actively involved in atmospheric chemistry, because they can be photodissociated to form reactive radical species that catalytically destroy ozone [Chameides and Davis, 1980].

Many halocarbons break down into reactive halogen radicals in the troposphere after being exposed to sunlight. In the troposphere halogen radicals destroy tropospheric ozone, which has a very strong greenhouse effect and is also harmful for human health. Therefore, marine driven halocarbons are essential for lowering the level of tropospheric ozone; though, they destroy as well some hydroxyl radicals, which are useful for removing harmful chemicals from the tropospheric air. A part of oceanic halocarbons is transferred by atmospheric circulations to the upper troposphere and lower stratosphere. Oceanic bromocarbons such as bromoform ($CHBr_3$) and dibromomethane (CH_2Br_2) are the main biogenic sources of reactive bromine to the upper troposphere, where they contribute significantly to the burden of lower stratospheric bromine and thereby destructing ozone [Chuck et al., 2005]. Reactive iodine appears to be indirectly the major contributor to halogen-related ozone loss in the tropical marine boundary layer, by amplification of bromine cycles [Solomon et al., 1994].

Aside from DMS, COS and halocarbons, there are also some marine biogenic hydrocarbon, influencing the climate. For instance, isoprene (C_5H_8) is a reactive biogenic hydrocarbon, affecting oxidant chemistry in the troposphere and organic aerosol formation. Although the main supply for atmospheric isoprene are terrestrial sources, but they are also produced in oceans by certain types of phytoplankton and seaweeds [Bonsang et al., 1992]. Moreover, marine phytoplankton are indirectly connected to the formation of methane (CH_4) in ocean floor, where huge accumulation of buried organic sediments convert into methane, under the condition of extremely high pressure and lack of oxygen. However, the most of the released methane is used up by bacteria before reaching the surface, preventing the atmosphere from rising the concentration of a major greenhouse gas.

Chapter 3

Methodology

3.1 Differential Optical Absorption Spectroscopy

PhytoDOAS, the retrieval method to derive the quantitative distribution of various phytoplankton groups, is an extension of Differential Optical Absorption Spectroscopy (DOAS; Perner and Platt [1979]) from the atmospheric domain into aquatic media.[1] DOAS expands the *Beer-Lambert* law to all possible interactions between light and all atmospheric optical components. Therefore, it contains all extinction impacts of the atmosphere such as the absorption and scattering by trace gases (scattering is negligible) as well as the scattering by air molecules, such as Rayleigh and Mie scattering. The extension of the original form of the *Beer-Lambert* law, Eq. 3.1, to its applicable form in the atmosphere, is outlined as follows:

$$I(\lambda) = I_0(\lambda) \cdot \exp\left\{-L \sum_{i=1}^{N} (a_i(\lambda) + s_i(\lambda)) n_i\right\} \tag{3.1}$$

where $I(\lambda)$ and $I_0(\lambda)$ are the measured intensities of the incident and the transmitted radiations, respectively; $a_i(\lambda)$ and $s_i(\lambda)$ are the absorption and the scattering cross-sections of the i^{th} species jointly accounting for the *extinction cross-section* in $[cm^2\ molecule^{-1}]$; n_i is the number density of the i^{th} species $[molecules\ m^{-3}]$; L is the total length of the light-path and λ is the wavelength. Here the positive dimensionless argument of the exponential function, $L \sum_{i=1}^{N} (a_i(\lambda) + s_i(\lambda)) n_i$, is called the *optical depth* (or the *optical thickness*) of the medium, denoted by τ. Now, to modify this equation for atmospheric applications, Rayleigh and Mie scattering of the air molecules have to be taken into account. By incorporating these into Eq. 3.1 and integrating over the whole atmospheric light-path, the following equation is obtained:

$$\tau(\lambda) = \ln \frac{I_0(\lambda)}{I(\lambda)} = \int \left[\sum_{i=1}^{N} \sigma_i(\lambda)\rho_i(s) + \sigma^R(\lambda)\rho^R(s) + \sigma^M(\lambda)\rho^M(s)\right] ds \tag{3.2}$$

where ds is the light-path differential element; $\sigma^R(\lambda)$ and $\sigma^M(\lambda)$ are the scattering cross-sections assigned to Rayleigh and Mie scattering, respectively; $\rho^R(s)$ and $\rho^M(s)$ are the number densities associated with Rayleigh and Mie scattering in the atmosphere. Thus the last two terms in Eq. 3.2 correspond to the Rayleigh and Mie *scattering coefficients*. As another modification, the absorption contributions of the different trace gases have been added to Eq. 3.1 via a summation term, $\sum_{i=1}^{N} \sigma_i(\lambda)\rho_i(s)$, which is a valid treatment as long as the atmosphere is *optically thin*, i.e., $\tau \ll 1$. Each trace gas in Eq. 3.2 has an absorption cross-section of $\sigma_i(\lambda)$ and a number-density of $\rho_i(s)$.

[1] This chapter has been partially presented in Sadeghi et al. [2012b].

If the absorption cross-sections do not vary along the light-path, the total amount of the absorber per unit area integrated along the light-path through the atmosphere can be defined as the *slant column density*, SC_i, which has the unit of $[molecules\ cm^{-2}]$:

$$SC_i = \int \rho_i(s)ds \tag{3.3}$$

After incorporation of the *slant column density*, Eq. 3.2 is modified as follows:

$$\tau(\lambda) = \ln \frac{I_0(\lambda)}{I(\lambda)} = \sum_{i=1}^{N} \sigma_i(\lambda)SC_i + \sigma^R(\lambda)SC^R + \sigma^M(\lambda)SC^M \tag{3.4}$$

with SC_i being the *slant column density* of the i^{th} trace gas; and SC^R and SC^M being the slant column densities of Rayleigh and Mie scattering, respectively. The absorption cross-section for any specific species can be split into two components, one slowly-varying with the wavelength, $\sigma_i^s(\lambda)$, and the other rapidly-varying, $\sigma_i'(\lambda)$, called *differential cross-section*:

$$\sigma_i(\lambda) = \sigma_i'(\lambda) + \sigma_i^s(\lambda) \tag{3.5}$$

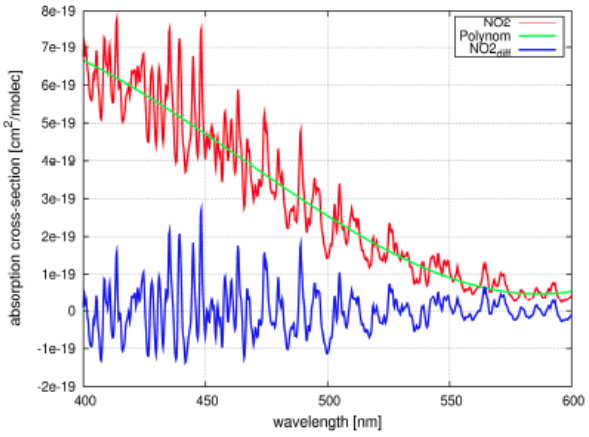

Figure 3.1: This figure shows how a given absorption cross-section (here for NO_2) is split into slowly-varying and rapidly-varying (or differential) components. Differential absorption cross-section (blue) of NO_2 has been computed by subtracting a fitted polynomial (green) from the original absorption cross-section (red).

The slowly- and rapidly-varying spectral components can be calculated by several separation techniques, for example by subtraction of a fitted polynomial, which is equivalent to high-pass filtering. As shown in Fig. 3.1, by subtracting a low-order polynomial, the slowly-varying spectral component can be removed, resulting in the differential cross-section. The separation of cross-sections, is applied to Eq. 3.4, where the right-hand side of the equation is split into rapidly-varying and slowly-varying parts. Furthermore, since Rayleigh and Mie scattering efficiencies exhibit slow-varying wavelength dependence (as follows):

$$\sigma^R(\lambda) \propto \lambda^{-4} \tag{3.6}$$

$$\sigma^M(\lambda) \propto \lambda^{-\kappa}\ ;\ \kappa = 0 \ldots 2 \tag{3.7}$$

the last two terms in Eq. 3.4, corresponding to Rayleigh and Mie scattering, contribute to the slowly-varying component. Accordingly, Eq. 3.4 can be rewritten as:

$$\tau(\lambda) = \ln \frac{I_0(\lambda)}{I(\lambda)} = \underbrace{\sum_{i=1}^{N} \sigma_i'(\lambda) SC_i}_{rapidly\ varying} + \underbrace{\sum_{i=1}^{N} \sigma_i^s(\lambda) SC_i + \sigma^R(\lambda) SC^R + \sigma^M(\lambda) SC^M}_{slowly\ varying} \tag{3.8}$$

Now, assuming that there is a low-order polynomial, denoted by $\sum b_p \lambda^p$, covering the slowly-varying part of Eq. 3.8, this equation can be modified again in the following manner:

$$\tau(\lambda) = \ln \frac{I_o(\lambda)}{I(\lambda)} = \sum_{i=1}^{N} \sigma_i'(\lambda) SC_i + \sum_{p=0}^{M} b_p \lambda^p \tag{3.9}$$

This is the basic equation to establish the DOAS retrieval method. The radiation spectra, I_0 and I, are measured by the satellite sensor (or ground-based instruments) and the absorption cross-sections of trace gases, $\sigma_i(\lambda)$, are measured in the laboratory and then their differential parts are extracted. The *least-square* optimization method is used to fit the parameters assigned to the slant column densities, SC_i and the polynomial coefficients, b_p. The main underlying idea in this optimization approach is to fit the parameters SC_i and b_p, in accordance with the demand of minimizing the residuals. Therefore, the DOAS retrieval method can be introduced by this expression:

$$\left\| \tau(\lambda) - \sum_{i=1}^{N} \sigma_i'(\lambda) SC_i - \rho'(\lambda) S_r - \sum_{p=0}^{M} b_p \lambda^p \right\|^2 \rightarrow min \tag{3.10}$$

The DOAS equation should also account for the (inelastic) rotational Raman scattering by the air molecules, because this phenomenon, called as *Ring effect*, has a filling-in impact on Fraunhofer lines in the UV/visible ranges [Bussemer, 1993; Burrows et al., 1996]. In this way, the weakening effect of the Raman scattering on the measured absorption lines is compensated and the absorption lines of trace gases, those with overlapping bands in the Ring spectral domain, are corrected [Vountas et al., 1998; Wagner et al., 2001]. Therefore, a new term, $S_r \rho'(\lambda)$, has been added to the DOAS equation, accounting for the spectral impact of the Ring effect, which is referred to as a *pseudo-absorber*. To incorporate the Ring effect into the DOAS retrieval, a unitless spectral reference of the Ring, $\rho(\lambda)$, has been computed by a method developed by Vountas et al. [1998], based on modeling of radiative transfer. In the above equation, $\rho'(\lambda)$ corresponds to the differential part of the Ring spectrum. The associated coefficient within the term of the Ring effect, i.e., S_r, is called the Ring *fit-factor*, which like the spectral signature of Ring effect is unitless.

3.2 From DOAS to PhytoDOAS

PhytoDOAS was born following the application of the DOAS method to the retrieval of oceanic phytoplankton, the living light-absorbing particles of the ocean. The underlying idea is that the backscattered light from the ocean into the atmosphere (and hence, to the satellite sensor) carries some information from water and its optical constituents. The method was established by Vountas et al. [2007] for remote identification of total phytoplankton *chl-a* and then improved by Bracher et al. [2009] to identify diatoms and cyanobacteria in *case-1* waters using hyperspectral satellite data. Such an extension demands the incorporation of all optical components of the sea water into the DOAS equation, based on a the prior knowledge of the optical behavior of the main constituents. In addition to phytoplankton, the main optical components of *case-1* waters, the target area of the method, are CDOM, non-algal particulates, absorption of water molecules [Gordon et al., 1975; Kirk, 1994] and VRS of liquid water [Vasilkov et al., 2002; Vountas et al., 2003].

The absorption of CDOM has a spectrally smooth behavior [Bricaud et al., 1981; Carder et al., 1989], and therefore are covered well by the fitted polynomial in the DOAS equation. The same hold for the absorption and scattering of the non-algal particulates [Allali et al., 1995; Mitchell et al., 2003]. The absorption effect of water molecules can be regarded as a fixed spectral background, which can be removed from the main DOAS fit by first applying the method to a phytoplankton-depleted oceanic region, so-called *hyper-oligotrophic*; (this initial run will remove some instrumental artifacts as well). According to Vountas et al. [2003, 2007] backscatter radiation detected by the SCIAMACHY sensor carries the spectral footprint of inelastic scattering, VRS, of water molecules. By embedding the spectral signature of VRS, $v(\lambda)$, as a pseudo-absorber into the DOAS equation, DOAS method shows a quantitative account of the VRS' spectral impact as well. It was shown in Vountas et al. [2007] that there is a strong relation between VRS and *light-penetration depth*, suggesting the former to be used as a proxy for quantitative estimation of the latter. Therefore, to extend the DOAS for retrieving the *chl-a* concentration of a PFT, the VRS reference spectrum must be in parallel fitted (as a pseudo-absorber) to the UV range, which is then used to compute the *light-penetration depth* for each satellite ground pixel. Finally, to extend the DOAS equation (Eq. 3.10) to the aquatic medium, the absorption spectrum of target PFT has to be considered. Now, embedding the two new terms representing the PFT absorption spectrum and the VRS reference spectrum, the relevant equation for PhytoDOAS is achieved as follows:

$$\left\| \tau(\lambda) - \sum_{i=1}^{N} \sigma_i'(\lambda) SC_i - \rho'(\lambda) S_r - a'(\lambda) S_a - v'(\lambda) S_v - \sum_{p=0}^{M} b_p \lambda^p \right\|^2 \rightarrow min \qquad (3.11)$$

with $a'(\lambda)$ being the differential part of *specific absorption spectrum* of target PFT (absorption spectrum of the PFT sample normalized by its measured *chl-a* concentration) in $[m^2\ (mg\ chla)^{-1}]$; S_a being the *fit-factor* of the PFT absorption spectrum in $[mg\ chla\ m^{-2}]$; $v'(\lambda)$ being the differential part of the VRS spectrum, which was obtained from a reflectance model developed by Vountas et al. [2003], originally proposed by Sathyendranath and Platt [1998]; and S_v being the *fit-factor* assigned to the VRS spectrum. It must be noted that since $a'(\lambda)$ is not an absorption cross-section, the absorption fit-factor, S_a, has a different interpretation than in slant-column density. The PFT absorption fit-factor implies the mass per unit area of *chl-a* pigment assigned to the target PFT along the light-path. However, as the spectral signature of VRS is unitless [Vountas et al., 2007], the VRS fit-factor, S_v, is unitless as well, similar to the fit-factor of the other *pseudo-absorber*, i.e., of the Ring spectrum.

The main outputs of PhytoDOAS are S_a and S_v, which are retrieved independently through two separate fitting procedures. The VRS spectral features are weak in the visible, because in this part of the spectrum not only the absorption impacts of phytoplankton and water molecules are dominated, but also the Ring spectral effect is much higher than VRS. Therefore, a second fitting is performed in the UV to evaluate the VRS fit-factor, the result of which is then extrapolated to the visible for estimating the path-length of light in the water body [Bartlett et al., 1998; Vountas et al., 2007].

Regarding the PhytoDOAS equation (Eq. 3.11), three sets of input data are needed to perform this method, being as follows:

1. satellite measurements, i.e., extraterrestrial solar radiation, $I_0(\lambda)$, and Earth's backscattered radiation, $I(\lambda)$ that are both measured by the satellite sensor at the top of the atmosphere and are embedded into the optical depth, through $\tau(\lambda) = \ln \frac{I_0(\lambda)}{I(\lambda)}$;

2. atmospheric spectra, i.e., the absorption cross-sections of the water vapor, trace gases and spectral signature of the Ring effect;

3. aquatic spectra, i.e., the specific absorption spectrum of target PFT and the spectral signature of VRS.

In this study, we have achieved further improvement to PhytoDOAS by simultaneously fitting three selected PFT targets rather than just a single PFT target. We will refer to this new approach as *multi-target fit* (see sec. 3.4).

Vountas et al. [2007] showed that the light-penetration depth, δ, can be determined using the VRS fit-factor. For water molecules, a single event of elastic scattering is always accompanied by an inelastic scattering of VRS. Therefore, the VRS fit-factor, S_v, is directly related to the same quantity of elastic scattering of water molecules, which is described by the *backscattering coefficient*, b_b. The quantitative dependence was previously extracted in Vountas et al. [2003] using a bio-optical model from Morel [1988], stating that the backscattering coefficient scaled by the VRS fit-factor, S_v, can be regarded as the true value of b_b in the observed situation. Therefore, as b_b^{-1} is the modeled *light-penetration depth*, $S_v \cdot b_b^{-1}$ will be the equivalent observed quantity. Here, the *light-penetration depth*, denoted by δ, refers to the depth of the remotely observed water column, up to which the signal can be received by satellite sensor.

As explained in Vountas et al. [2007] and Bracher et al. [2009], the *chl-a* concentration of the target PFT can be estimated from the PFT absorption fit-factor, S_a, determined via PhytoDOAS. This is done for all ground pixels through dividing S_a by the *light-penetration depth* and can be written as follows:

$$C = \frac{S_a}{\delta} \tag{3.12}$$

where C is the *chl-a* concentration of the target PFT in $[mg\ m^{-3}]$.

In PhytoDOAS (as in DOAS), the overall *Chi-square* value, χ^2, is used as a scalar indicator of the total fit-quality. Furthermore, the fit spectrum of the retrieval target is compared with its original spectrum for each oceanic pixel to check the fit-quality. However, as in any other retrieval method, the most reliable approach to investigate the quality of PhytoDOAS retrieval is the validation with high quality in-situ PFT data. It should be noted that, while ocean color observations in general cover only the surface waters, the PhytoDOAS retrieval results are the average value over the light path observed by the satellite. However, the signal measured by the satellite is not weighted equally by the different depths and the surface concentrations are dominating the retrieved values.

3.3 Material and Data

3.3.1 Satellite data: SCIAMACHY

As mentioned before, due to spectral correlation of phytoplankton absorption features, satellite data used in PhytoDOAS must be highly spectrally resolved. To meet this requirement, data measured by the satellite sensor SCIAMACHY. To keep the logical flow of the chapter, more information about the SCIAMACHY sensor, as the main data provider of PhytoDOAS, is given at the end of this chapter (sec. 3.5).

In this study, the SCIAMACHY data in the UV and visible regions, from nadir-viewing geometry (see sec. 3.5.3) with a spectral resolution of $0.24\,nm$ to $0.48\,nm$, have been used. These data correspond to backscatter solar radiation from the Earth's surface, with a spatial resolution of about $30\,km \times 60\,km$, which defines the pixel-size in this wavelength region. Each ground pixel

data is associated with a direct measurement of solar radiation at the top of the atmosphere in the same wavelength region, to be used later in the retrieval as the unattenuated radiation, I_0 (see Eq. 3.9). Within PhytoDOAS, SCIAMACHY data are used in the two following steps: First, SCIAMACHY visible data are used to fit the absorption spectrum of target PFT within the wavelength range of 429 to 495 nm in the study by Bracher et al. [2009] and extended up to 521 nm in this study, leading to PFT absorption fit-factors; secondly, SCIAMACHY data from 340 to 385 nm are exploited to fit the VRS spectral signature of water molecules, leading to VRS fit-factors, which are necessary for the calculation of the light penetration depth for each oceanic pixel (see previous section).

3.3.2 Spectral data

In addition to hyperspectral satellite radiation measurements, the PhytoDOAS retrieval requires reference spectra of atmospheric and oceanic species. For atmospheric spectra, absorption cross-sections of ozone, NO_2, glyoxal (OCHCHO), iodine oxide, O_4, water vapor and the Ring effect (as a *pseudo-absorber* spectrum) are fitted, using the same spectra as were taken in Bracher et al. [2009]. The second set of input parameters includes the spectral signature of VRS, obtained through a modeling approach [Vountas et al., 2003, 2007] and the absorption spectra of PFTs. It must be mentioned that as *E. huxleyi* is the dominant species of the coccolithophores, it has been used in this study as the spectral indicator of this PFT target. The phytoplankton absorption spectra used in this study were acquired from an *E. huxleyi* culture and a natural sample, where the group of dinoflagellates dominated. Both samples were measured with a point-source integrating-cavity absorption meter, so-called PSICAM [Roettgers et al., 2007]. Total *chl-a* concentrations of the *E. huxleyi* culture and of all pigments for the natural dinoflagellate sample were obtained from high-performance liquid chromatography (HPLC) following the method described by Hoffmann et al. [2006]. The dinoflagellate-dominated sample was taken during the OOMPH field experiment (Organics over the Ocean Modifying Particles in both Hemispheres) with RV Marion Dufresne on 2 February 2007, at 59.88°W and 46.01°S, within a dinoflagellate bloom. Performing the CHEMTAX analysis [Mackey et al., 1996] on the HPLC data of the natural sample, the *chl-a* concentrations of all containing phytoplankton groups were calculated, which indicated a contribution over 92% for the dinoflagellates. The rest of the sample consisted of 5% pelagophyceae and less than 3% of prasinophyceae (further details in Yassaa et al. [2008]). To derive the specific absorption spectra of each phytoplankton group, each absorption spectrum was divided by the corresponding *chl-a* concentration (normalization). Additionally, as the third phytoplankton reference spectrum, the absorption spectrum of diatoms was acquired from the in-situ measurements conducted during a cross-Atlantic research cruise. The process to reach the specific absorption spectrum of diatoms was the same as the one explained for dinoflagellates (for details see Bracher et al. [2009]).

Figure 3.2 (left panel) shows the specific absorption spectra of the three PFTs used as the retrieval targets in this study, i.e., for *E. huxleyi*, dinoflagellates and diatoms. From these measured spectra, the corresponding differential absorption spectra have been derived, based on the spectral approach described in section 3.1. The differential absorption spectra for the selected phytoplankton targets are depicted in the right panel.

3.4 Improvements to PhytoDOAS: challenges and approaches

Following the method developed by Bracher et al. [2009], besides cyanobacteria and diatoms, more major PFTs (or dominant species of a PFT) are expected to be retrieved. Nevertheless, there are some challenges to be overcome in order to improve PhytoDOAS as a reliable retrieval tool for other PFTs (or dominant species). The main challenge is the spectral correlation between

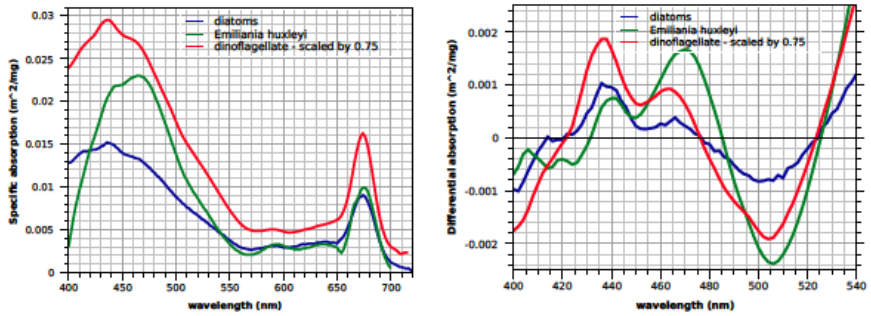

Figure 3.2: Left panel: specific absorption spectra of *E. huxleyi* (green), dinoflagellates (red) and diatoms (blue). The spectra were obtained from a culture and natural samples, respectively, using a point-source integrating-cavity absorption meter. The latter spectrum was taken from Bracher et al. [2009]. Right panel: differential absorption spectra of three phytoplankton targets. Each of them was derived by subtracting a second order polynomial from the corresponding specific absorption spectrum, which is shown in the left panel.

absorption spectra of different phytoplankton targets, which arises from their common photosynthetic pigments and cause in turn difficulties to distinguish different groups remotely. Table 3.1 indicates the correlation coefficients between specific absorption spectra of five major PFTs, calculated for all available pairs based on Spearman's Rank Correlation over different wavelength windows (the output is commented later in this section). With regard to the shortage of in-situ PFT data and difficulties of collocating them with satellite pixels, the second important challenge is finding solutions to test the principal functionality of the modified method and also finding appropriate data sources for comparing the retrievals with (see chapter 4 for the utilized solutions and data sources).

With respect to the main challenge, some approaches have been applied during the study to overcome the correlation effects existing among typical PFTs' absorption spectra. Firstly, investigations proved that fitting several PFT spectral targets simultaneously, within an appropriate fit-window, leads to higher fit-quality as compared to fit only one PFT spectrum at the time. This approach, called *multi-target fit*, results in significantly lower values for the absorption fit-factors of each target, compared to the usual approach of *single-target fit*. This is of importance, because high fit-factors in PhytoDOAS lead to an overestimation of the PFT concentration. This can be explained by the fact that when three (or more) PFT targets are fitted simultaneously, the phytoplankton spectral input of the PhytoDOAS equation becomes bio-optically more realistic; i.e., in this case PhytoDOAS accounts for more optical components of the ocean water, where usually several types of phytoplankton species live simultaneously. Comparably, when we omit some trace gases from our DOAS retrieval, the retrieval results of the others are affected, and this was tested with PhytoDOAS for more confidence, leading to the expected features.

Regarding the PhytoDOAS equation (Eq. 3.11), the *multi-target fit* requires that the term of PFT absorption, $a'(\lambda)S_a$, is replaced by a multiple term including the absorption spectra of selected PFTs, $\sum_{j=1}^{3} a'_j(\lambda)S_{aj}$, which assigns a specific absorption fit-factor to each PFT target. Therefore, the improved PhytoDOAS can be written as:

$$\left\| \tau(\lambda) - \sum_{i=1}^{N} \sigma'_i(\lambda) SC_i - \rho'(\lambda) S_r - \sum_{j=1}^{3} a'_j(\lambda) S_{aj} - v'(\lambda) S_v - \sum_{p=0}^{M} b_p \lambda^p \right\|^2 \rightarrow min \qquad (3.13)$$

Fig. 3.3 shows the differences in the resulting fit-factor maps, which have been obtained

for coccolithophores by implementing *single-target* and *multi-target* fit modes of PhytoDOAS. The *triple-target fit* used here includes *E. huxleyi*, as the dominant species of coccolithophores, together with diatoms and dinoflagellates. The *triple-target fit* results (Fig. 3.3 lower panel) are characterized by lower values of fit-factors, almost over the whole global ocean, as compared to the *single-target fit* results (Fig. 3.3 upper panel).

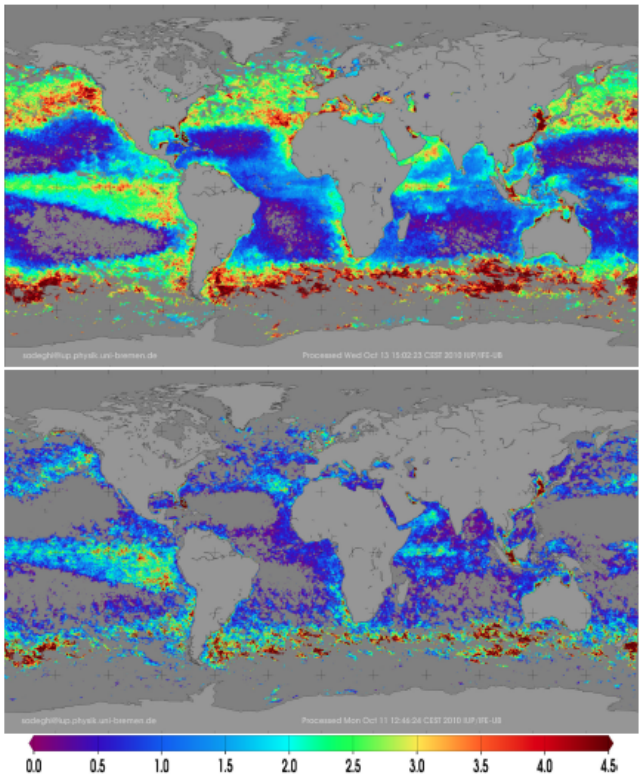

Figure 3.3: Global fit-factor maps [$mg\ m^{-2}$] for coccolithophores in March 2005, obtained by *single-target fit* (upper panel) and *triple-target fit* (lower panel) modes of PhytoDOAS using SCIAMACHY data.

The new results are verified by looking at the fit residuals, as a measure of the fit-quality, represented by the average value of *Chi-square* (χ^2) for all accounting pixels. Since the lower residual corresponds to the more reliable fit, the lower average of χ^2 values in the *triple-target* fits, compared to the *single-target* fits, implies the privilege of the *triple-target* fits. In the sample fit-factor maps shown in Fig. 3.3, the average χ^2 values for the *triple-target* and *single-target* fits are 0.00039 and 0.00052, respectively. This improvement can be seen in the plots of overall residuals corresponding to the different modes of PhytoDOAS operation (see Fig. 3.4) or in the single plots of the fitted specific absorption spectra for selected ground pixels (see Fig. 3.5).

Fig. 3.4 compares fit qualities of different PhytoDOAS retrievals when being performed in the *single-target* fit mode and in *multi-target* mode, using the overall fit residuals. It can be seen that the overall residual for the *single-target* fit of diatoms, almost over the whole fit-window, is higher than its overall residuals for the *triple-target* fit. Furthermore, regarding the DOAS method, this figure also indicates that when spectral contribution of phytoplankton absorption is taken into account by DOAS retrieval (over the ocean), the fit-quality will be clearly better; this can be inferred, in this figure, from the significantly higher residual of the retrieval when no PFT target is accounted for. Figure 3.5 illustrates the fitted spectra of the specific absorptions for the target PFTs, used in the PhytoDOAS *triple-target* mode, associated with respective fit residuals.

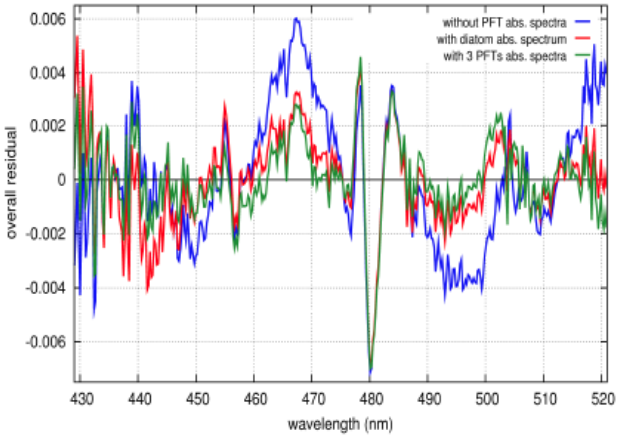

Figure 3.4: The improvement to PhytoDOAS was performed by simultaneous fit of the absorption spectra of selected phytoplankton targets in an appropriate wavelength window. This figure compares the overall residuals of PhytoDOAS retrievals in three different fit-modes: without any PFT target (blue), only with the diatoms abs. spectrum (red) and with the abs. spectra of three selected PFTs (green). All three residual spectra have been obtained via consecutive runs of DOAS for the same SCIAMACHY orbit, passing over North Atlantic (1.07.2005). A sample ground-pixel of this orbit has been taken to plot the residuals, which corresponds to the pixel-center located at $54.51°N$ and $21.47°W$.

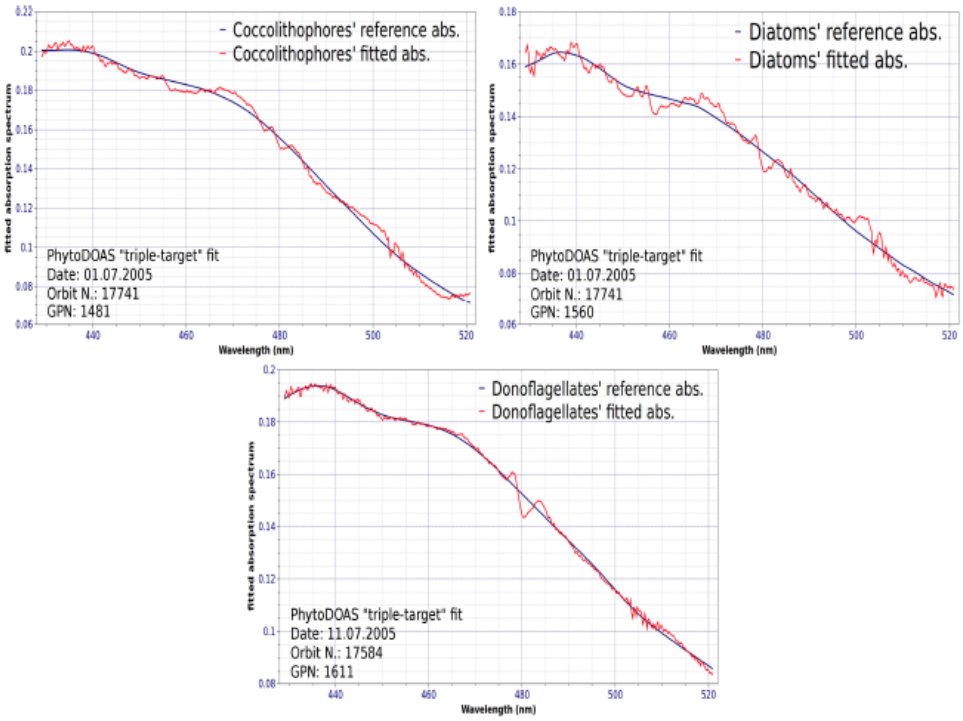

Figure 3.5: Sample result of the specific absorption spectra fitted through the PhytoDOAS *triple-target* mode within the fit-window of 429 to 521 nm *E. huxleyi* (upper left panel), diatoms (upper right panel) and dinoflagellates (lower panel). The PFT target, the date, the orbit number and the ground-pixel number (GPN) of each retrieval are illustrated on the corresponding subplot.

After implementing this modification (*triple-target* fit), the output results are in a better agreement with the other available data sources, such as PFT modeled data acquired from the NASA Ocean Biochemical Model (NOBM, Gregg et al. [2003]; Gregg and Casey [2007]) or certain types of satellite-derived data products, linked to the target PFTs (e.g., PIC product as an indicator of coccolithophores). However, due to the limitations imposed by the spectral correlation (see Table 3.1), it is necessary to determine and optimize some factors when running a *multi-target fit*, in order to receive an acceptable fit-quality: the retrieval should be optimized by identifying how many PFT targets, in which combination and within which wavelength window are fitted simultaneously.

To meet these requirements, the analysis of specific absorption spectra was done in two different ways. The first approach, was based on the definition of *linear independence* in linear algebra and the orthogonality condition for a vector space. More precisely, a number of vectors of the same dimensions (let's take as $\vec{V_i}$, with $i = 1, 2, ..., n$) are linearly independent if for each pair of them the *scalar product* is equal to zero, which means that they are all mutually orthogonal and could be regarded as a basis for the vector space. This condition can be mathematically demonstrated as follows:

$$\vec{V_i} \cdot \vec{V_j} = \sum_{k=1}^{n} V_{ik} V_{jk} = 0 \tag{3.14}$$

However, what happens if two vectors are not linearly independent? Simply, the vectors are not orthogonal, rather they are correlated; the more they are correlated, the more will be the amount of their *scalar product*. Regarding the absorption spectra (over the same wavelength range with the same griding intervals) as different vectors of the same dimension (let's take $\vec{A_i}$, with $i = 1, 2, ..., n$), the concept of *linear dependence* can be used for quantifying the existing correlations. Knowing that the correlations do exist, it can be argued that over a specific wavelength window, a set of vectors (among several vectors) are less correlated if the summation of their mutual linear products is less than the respective summations of the other sets. Therefore, taking each specific absorption spectrum as a vector, the following quantity should be computed and compared for all available sets of PFTs, with certain number of elements:

$$\sum_{i,j=1}^{3} \vec{A_i} \cdot \vec{A_j} = \sum_{i,j=1}^{3} \sum_{k=1}^{n} A_{ik} A_{jk} \tag{3.15}$$

where $\vec{A_i}$ and $\vec{A_j}$ are the normalized absorption vectors ($i \neq j$), being normalized to the length of vectors. Assuming $\vec{a_i}$ as the vector form of a given specific absorption spectrum, being normalization to the vector's length means that: $\vec{A_i} = \frac{\vec{a_i}}{a_i}$.

Additionally, with respect to the efficiency of the *triple-target fit* (achieved by performing χ^2 tests), here the total number of absorption vectors has been set to three; i.e., the above quantity is calculated for 3-element sets among major PFTs (further explanations are given below).

The quantity introduced by Eq. 3.15 has been calculated for five major phytoplankton groups: diatoms, dinoflagellates, coccolithophores (*E. huxleyi*), cyanobacteria and *Phaeocystis*. The resulting values, computed for different wavelength windows, are presented in Table 3.2. Despite Table 3.1, which quantifies the high correlations between phytoplankton absorption spectra, more information can be extracted from Table 3.2, the outline of which can be described as follows: the linear independence, as expected, is different for various sets of PFTs' absorption spectra for a given wavelength range; it also varies with the operational wavelength fit-windows, indicating a decrease with widening the fit-window. However, it does not mean that the wider fit-window (implying lower dependency) would provide us a better fit quality. In practice, by enlarging the fit window, the spectral overlaps of other optical components of seawater (e.g., water molecules)

Table 3.1: Correlation coefficients between specific absorption spectra of major phytoplankton species based on Spearman's rank correlation for different wavelength-windows.

λ (nm)	Diat/ Dino.	Diat/ Emil.	Diat/ Cyan.	Diat/ Phae.	Dino/ Emil.	Dino/ Cyan.	Dino/ Phae.	Emil/ Cyan.	Emil/ Phae.	Cyan/ Phae.
428-560	0.9999	0.998	0.946	0.997	0.999	0.945	0.997	0.941	0.999	0.940
428-550	0.9999	0.998	0.965	0.996	0.998	0.965	0.997	0.960	0.999	0.958
428-540	0.9999	0.997	0.987	0.995	0.998	0.986	0.996	0.980	0.999	0.977
428-530	0.9999	0.997	0.989	0.994	0.997	0.988	0.994	0.980	0.999	0.977
428-522	0.9999	0.996	0.986	0.992	0.996	0.985	0.993	0.975	0.998	0.971
428-510	0.9998	0.993	0.980	0.988	0.995	0.978	0.989	0.963	0.997	0.957
428-500	0.9997	0.990	0.970	0.983	0.992	0.967	0.984	0.945	0.996	0.936
428-496	0.9997	0.989	0.965	0.979	0.991	0.961	0.981	0.935	0.995	0.925
428-490	0.9995	0.985	0.954	0.973	0.988	0.949	0.975	0.915	0.994	0.902
428-486	0.9994	0.982	0.944	0.967	0.985	0.939	0.970	0.897	0.993	0.881

Table 3.2: Summation of scalar products of specific absorption spectra for all 3-element sets of major phytoplankton species for different wavelength-windows.

λ (nm)	Diat/ Dino/ Emil.	Diat/ Dino/ Cyan.	Diat/ Dino/ Phae.	Diat/ Emil/ Cyan.	Diat/ Emil/ Phae.	Diat/ Cyan/ Phae.	Dino/ Emil/ Cyan.	Dino/ Emil/ Phae.	Dino/ Cyan/ Phae.	Emil/ Cyan/ Phae.
428-560	0.0317	0.0331	0.0315	0.0320	0.0305	0.0319	0.0323	0.0308	0.0322	0.0311
428-550	0.0340	0.0354	0.0338	0.0342	0.0327	0.0341	0.0346	0.0331	0.0344	0.0333
428-540	0.0366	0.0378	0.0363	0.0367	0.0353	0.0364	0.0371	0.0356	0.0368	0.0357
428-530	0.0395	0.0406	0.0391	0.0395	0.0381	0.0391	0.0399	0.0384	0.0395	0.0384
428-522	0.0420	0.0431	0.0415	0.0420	0.0405	0.0415	0.0425	0.0409	0.0419	0.0409
428-510	0.0462	0.0471	0.0455	0.0462	0.0446	0.0455	0.0467	0.0451	0.0460	0.0451
428-500	0.0500	0.0507	0.0491	0.0499	0.0484	0.0490	0.0504	0.0489	0.0495	0.0488
428-496	0.0516	0.0521	0.0506	0.0514	0.0499	0.0505	0.0519	0.0505	0.0510	0.0503
428-490	0.0538	0.0542	0.0528	0.0535	0.0522	0.0525	0.0541	0.0528	0.0531	0.0525
428-486	0.0572	0.0574	0.0561	0.0569	0.0556	0.0558	0.0574	0.0561	0.0563	0.0557

will also be increased. Additionally, due to the technical limitations, it is much easier to preserve the fit-window not two wide, to be confined within a single wavelength cluster of the sensor. For instance, the sensor has different integration times (in collecting data) for its different wavelength bands, leading to quite different ground-pixel sizes, which is also the reason that all fit-windows start from $428\,nm$ and end at $523\,nm$, being confined to cluster $\#15$ of channel $\#3$. This leads to finding a compromise between the mentioned effects and the factor of spectral independence, as an optimized fit-window. The final range of fit-window is also dependent on the spectral behavior of the selected set of PFTs, which needs a more precise analysis of the respective spectra to be done (explained as the second approach in following paragraphs). Conversely, reducing the width of the fit-window, causes the loss of information on the spectral variations in the absorption targets, whose existence is vital for functioning the retrieval process.

On the other hand, in comparing the quantities of Eq. 3.15 to decide about the best set of PFTs for simultaneous fit (for a given wavelength window), two restrictions should be considered: firstly, when the values are comparable, the preference would be toward the set of PFTs who are more abundant in the global ocean and also existing together or succeeding each other in the same regions; secondly, as cyanobacteria have a spectral signature distinguishable from the others, they can be excluded from the final set to be retrieved via the PhytoDOAS *single-target* mode (this can be also justified because cyanobacteria are often favored in the oceanic habitats where the other species are not so abundant. See sec. 4.1.4 for more details). Overall, the set of PFTs for performing the simultaneous retrieval process (via the PhytoDOAS *triple-target* fit) has been selected to be consist of diatoms, coccolithophores and dinoflagellates. The appropriate fit-window for retrieving these absorption targets were chosen in conjunction with the results of the derivative spectral analysis (introduced below), leading to the wavelength range of 429 to $521\,nm$. However, to reach the final set of PFTs and the optimized fit-window, above considerations (and derivative analysis) were associated with testing several other possible options, controlled by the χ^2 threshold. As a consequence, regarding Table 3.2, the factor introduced for the spectral independence, shows significantly lower value for the selected fit-window, compared to the fit-window used in Bracher et al. [2009] (i.e., 429 to $495\,nm$).

As a second approach, the spectral behavior of PFTs' absorption spectra have been investigated in more detail, using *fourth-derivative spectroscopy* (according to Aguirre-Gomez et al. [2001], which is a well-known method in spectral studies of phytoplankton species. The core concept here is as follows: in the fourth-derivative curve of a given absorption spectrum, each peak corresponds to the maximum absorption for a specific pigment at the same wavelength position. Therefore, the distribution of peak positions in a fourth-derivative curve is an indicator of pigment composition for that PFT. Fig. 3.6 shows the fourth-derivative curves for the absorption spectra of three phytoplankton targets, which have been fitted simultaneously via PhytoDOAS. The *fourth-derivative method* can be used to identify tiny differences in PFTs' spectral behavior. This is helpful to avoid spectral correlations between different phytoplankton targets and to find the appropriate wavelength window to fit them simultaneously. As shown in Fig. 3.6, there is a spectral difference between target spectra in the interval from 495 to $521\,nm$, especially between diatoms and *E. huxleyi*, for which the spectral behavior are more alike in the wavelengths below $495\,nm$. Practically, in the simultaneous PhytoDOAS fit, the spectral differences seen in the fourth-derivative curves have been used (as one criterion) to select the set of PFT targets, i. e., the proper combination of PFTs, and also to specify the wavelength range of the actual fit-window. This explains why in this study a wider fit-window (429 to $521\,nm$) has been used than in Bracher et al. [2009], which was from 429 to $495\,nm$.

Based on the *fourth-derivative spectroscopy* [Aguirre-Gomez et al., 2001], the spectral peak positions of the phytoplankton constructing pigments are assigned to the peaks of the fourth-

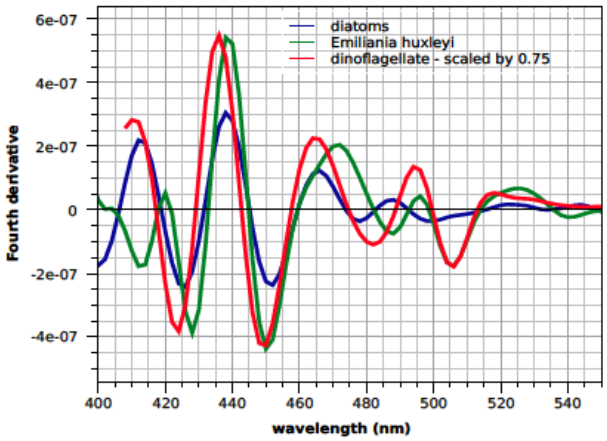

Figure 3.6: Fourth derivative curves of the specific absorption spectra of the three PFTs shown in Fig. 3.2: diatoms (blue), *E. huxleyi* (green) and dinoflagellates (red). The latter curve was scaled to 0.1.

Pigments / PFTs		chla 409		chla 435	chlc 461	chlc 465	carot 490		carot 539		chlc 586	chla 621	chlc 642		chla 675
Diatoms		412		438		466	488	524	546		590	619	640		674
Emiliania hux.	404	418		438		470	494	524		550	592	618	643		676
Dinoflagellate		410		436		465	493	519		-	590	618	643		674
Phaeocystis		410		437		468		510	534	552	594	620	642		676
Cyanobacteria	404		428	444	462		492	518		555	593	611	641	664	677

Figure 3.7: Pigment compositions and the respective wavelength positions of five major phytoplankton species derived from the *fourth-derivative analysis*. The pink values on the top represent the conventional peak positions of the main planktonic pigments; the red values are assigned to the peaks, who were not sufficiently pronounced.

derivative curve obtained from its absorption spectrum. Therefore, comparing to the well-known absorption features of the main photosynthetic pigments, the pigment composition of a given phytoplankton type can be recognized. Fig. 3.7 indicates the results extracted in this way from the absorption spectra of five major groups and species.

All together, by implementing these approaches it was determined so far that among all tested options of PhytoDOAS *multi-target fit* (which was previously found to have better result than the *single-target* fit), the following configuration leads to the best fit-quality: the PhytoDOAS *triple-target* fit containing absorption spectra of diatoms, dinoflagellates and coccolithophores (represented by *E. huxleyi*) over the wavelength window of 429 to 521 nm.

It must be noted that the diatoms' retrieval via the improved PhytoDOAS are very similar to the ones achieved before in Bracher et al. [2009] using the *single-target* mode within the fit-window of 429 to 495 nm (both in distribution patterns and magnitudes of *chl-a*). The minor differences can be assigned to the widening of fit-window up to 521 nm and also to the fact that two more PFT spectral targets have been added into the fit. It seems that the increasing effect of the wider fit-window is compensated by the decreasing effect of the simultaneous fit.

It should also be emphasized that in different steps within the process of method improvement, the fit-quality of the retrievals have been investigated by the following mean:

- comparison of the overall averaged *Chi-square* values of the different fit results,
- comparison of the fit absorption spectra with the input spectra for selected pixels,
- comparison with available satellite-derived products interconnected to target PFTs and also available PFTs' modeled data.

Of course the most reliable criterion is comparison of the results with available high quality in-situ measurements. However, this demand could not always be achieved, which is mainly due to the limited availability of the PFTs' in-situ data, on a global scale. Secondly, there are difficulties associated with the collocating of satellite ground pixels to the existing in-situ data points, as a consequence of the first point and also the large pixel size of SCIAMACHY (details are explained in chapter 4).

3.5 SCIAMACHY sensor, the data provider of PhytoDOAS

3.5.1 General overview

SCIAMACHY (Scanning Imaging Absorption Spectrometer for Atmospheric Chartography) is one of the 10 remote sensing sensors on board ENVISAT (ENVIronmental SATellite) of European Space Agency, ESA, launched in 2002. [2] ENVISAT is a polar, sun-synchronous satellite, flying at the mean altitude of 779.8 km with the orbital period of 100.6 minutes and the repeat cycle of 35 days (501 orbits). SCIAMACHY along with two other sensors, MIPAS and GOMOS, performs the mission of atmospheric chemistry for ENVISAT. The main objective of the SCIAMACHY instrument is the quantitative determination of the atmospheric constituents (e.g., absorbers, clouds, etc.) on a global scale with improved temporal and spatial coverages. This is part of the efforts to expand our knowledge on the physics and chemistry of the whole atmosphere. A detailed explanation of the SCIAMACHY mission objectives is given by Bovensmann et al. [1999]; Nöel et al.

[2] The contents of this subsection have been adapted from a recent book on SCIAMACHY by Gottwald and Bovensmann [2011].

[1999]. SCIAMACHY covers a wide wavelength range from 240 nm to 2380 nm, which makes it an ideal sensor for the detection of aerosols and clouds, as well as being suitable for several retrieval methods of trace gases. Besides the large wavelength range, covering UV/Visible/NIR, this sensor can observe an air volume from three different viewing geometries (nadir, limb and sun/moon occultation; see sec. 3.5.3), leading to precise atmospheric data on vertical column densities and profile information. Furthermore, the instrument benefits from a relatively high spectral resolution, ranging from about 0.2 nm to 1.5 nm for its scanning channels over the range of 240 to 1700 nm, and also selected regions between 2000 nm and 2400 nm [Bovensmann et al., 1999].

Having a broad spectral coverage enables SCIAMACHY to investigate a large variety of atmospheric targets (trace gases, aerosols, etc.) using the absorption, emission and scattering features of them, applied in different spectroscopic methods. SCIAMACHY data products, extracted from the raw data, consist of the following levels in the order of processing:

1. **level-0 data**: instrument source packets as collected from the sensor, with small headers attached to them at the receiving stations.
2. **level-1b data**: geolocated products in physical or engineering units, generated by applying certain algorithms, calibration and auxiliary data on the level-0 data.
3. **level-2 data**: final geophysical parameters extracted from the geolocated level-1b products, by applying further algorithms on them.

3.5.2 Spectral characteristics: channels and resolutions

The SCIAMACHY sensor is an grating spectrometer covering the spectral range from 214 nm in the UV to 2380 nm in the near-IR, with moderate to high spectral resolution. The wavelength range is divided into eight different spectral channels with different retrieval applications. The spectral resolution of SCIAMACHY varies from 0.24 nm in the UV region to 1.48 nm in the near-IR region of the electromagnetic spectrum. Each spectral channel comprises of several wavelength bands, called clusters, for which the integration times for collecting data are mainly different (from 0.25 second to 1.0 second). Table 3.3 provides an overview of the spectral characteristics of each channel. This is also important to note that in the nadir viewing geometry, dependent on the integration time of the cluster under process, the size of ground pixel will be different. For instance, for cluster #18 with the integration time of 1 s, the size of ground pixel is in principle 4 times more than for cluster #15, with the integration time of 0.25 s. As mentioned before, this also limited the selection of wavelength window to $428 - 523\,nm$, because that is the width of cluster #15, which has to be used for the PhytoDOAS phytoplankton fit. For the work presented in this thesis, the level-1b data of channels #2 and #3 (clusters #9 and #15, respectively) from the nadir viewing-mode have been used.

3.5.3 Spatial characteristics: viewing geometries

Nadir mode: In nadir mode, the SCIAMACHY instrument looks directly toward the Earth's surface, scanning across the satellite track by its azimuth mirror. Each nadir-scan contains 13 swaths from left to right and back, with each swath width to be about 960 km across track and about 30 km along track. Hence, the best available spatial resolution along the satellite track is 30 km, while the maximum resolution across track depends on the integration times and the rate of sensor' data-readout, both quantities varying with spectral channel and satellite geolocation. However, the best spatial resolution across track is 60 km. As SCIAMACHY alters between limb and nadir viewing-modes, in order to obtain tropospheric and stratospheric information of the same ground-pixel, the global case of nadir pixels is limited to 6 days at the equator.

Table 3.3: An overview of the spectral channels of SCIAMACHY. The last column includes some of the atmospheric targets that are retrieved by different algorithms within each spectral channel. For a complete list of targets, including the specific method and fit-window for retrieving each target, see: Gottwald and Bovensmann [2011].

Channel #	WL range (nm)	Cluster #	Res. (nm)	Retrieval targets
1 (UV)	214 - 334	1 - 6	0.24	O_3 , NO, ClO, Metals
2 (UV	300 - 412	7 - 11	0.26	NO_2 , O_3, SO_2, BrO, $OClO$, $HCHO$, $CHOCHO$
3 (VIS)	383 - 628	12 - 20	0.44	O_3 , $O4$, NO_2 , IO, Aerosols
4 (VIS)	595 - 812	21 - 28	0.48	O_3 , H_2O, NO_3 , Aerosols
5 (NIR)	773 - 1063	29 - 35	0.54	H_2O, ClO, HNO_3, Aerosols
6 (SWIR)	971 - 1773	36 - 47	1.48	CH_4, CO_2, N_2O, H_2O, Aerosols
7 (SWIR)	1934 - 2044	48 - 53	0.22	CO_2 , H_2O
8 (SWIR)	2259 - 2386	54 - 56	0.26	CO_2 , H_2O, CO

Limb mode: In limb mode, the instrument looks along the flight direction and horizontal scans are performed by the instrument using its azimuth mirror in different tangent altitudes (achieved by an elevation mirror). Starting from the surface, 30 swaths of 960 km width from left to right and back are performed, covering altitudes from 0 to 92 km.

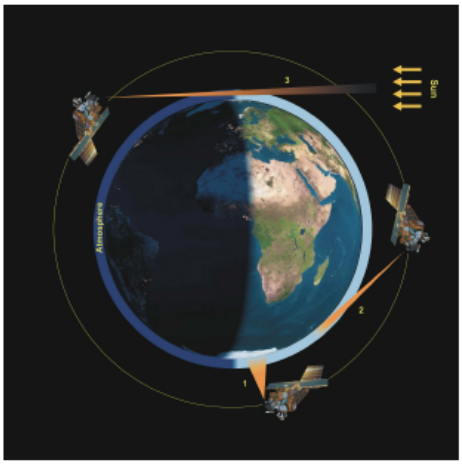

Figure 3.8: Scientific observation modes of SCIAMACHY: 1 = nadir, 2 = limb, 3 = occultation. The picture was adapted from the recent SCIAMACHY book, by Gottwald and Bovensmann [2011].

Occultation mode: Very similar to the limb measurement, in the occultation mode the instrument performs the horizontal swaths while tracking the sun or the moon (at sunrise and "moonrise"), which are called solar occultation and moon occultation, respectively. Fig. 3.8 illustrates schematically the three viewing geometries of SCIAMACHY.

Chapter 4

PFT retrievals using the PhytoDOAS Multi-target fit

4.1 PhytoDOAS monthly PFTs in comparison with other products: 2005

In this study PhytoDOAS was improved to distinguish remotely more major phytoplankton groups using the hyper-spectral data of the SCIAMACHY sensor. The improved method, *multi-target fit* (sec. 3.4), was applied to eight years of SCIAMACHY data (2003 to 2010) in order to retrieve the global distributions of coccolithophores and dinoflagellates along with diatoms. The appropriate fit-window for this simultaneous fit, 429 to 521 nm, was extracted from the derivative spectroscopy method [Aguirre-Gomez et al., 2001], using the fourth-derivative curves of the respecting PFTs' specific absorption spectra (Fig. 3.4). With this configuration, the average values of the overall *Chi-square* were minimal and the fit spectra in selected oceanic pixels were in good agreement with the original PFTs' absorption spectra. In this chapter the corresponding results of the PhytoDOAS *multi-target fit* are presented for the year 2005. This includes intercomparisons of the PFTs' monthly mean *chl-a*, as well as comparison of the retrieval results with appropriate products, in a monthly-mean basis. The same comparisons for the PhytoDOAS results of the year 2008 are shown in App. 1 (sec. 6.3). It must be mentioned that due to the shortage of PFTs' in-situ data and also the difficulties of collocating available PFTs' data points with the large SCIAMACHY pixels, the retrieved concentrations of coccolithophores and diatoms in this study have been only compared with the satellite products and modeled data. However, since there is no satellite product available for the global or regional distributions of dinoflagellates, evaluation of PhytoDOAS products does not comprise any comparison with other dinoflagellates products.

4.1.1 Global distributions of retrieved PFTs: 2005 monthly mean chl-a

The PhytoDOAS PFT products of SCIAMACHY data 2005 are presented in this subsection as monthly mean *chl-a* maps (all on global scales). Fig. 4.1 and Fig. 4.2 provide the concentrations for coccolithophores, dinoflagellates and diatoms for the first and the second half of the year 2005, respectively. There are pronounced differences in the *chl-a* distribution patterns of the three PFTs in each month. The *chl-a* patterns for each PFT are also showing clear temporal variations. For instance, during March: coccolithophores (*E. huxleyi*) show high *chl-a* along a band in the north of the Antarctic Polar Front and also in parts of the tropics and subtropics; while dinoflagellates show elevated *chl-a* only in the North Atlantic and the North Pacific, where coccolithophores have much lower *chl-a*; and diatoms show different patterns than both of them especially in the trop-

ics. Furthermore, while during the winter (or austral summer) there are no coccolithophores in the northern oceans, their values increase from January to March in the Southern Ocean (especially in the north of the Antarctic Polar Front); then, from March there is a gradual increase of coccolithophore biomass in the Arctic Ocean (spring bloom), which reaches to its maximum in July; while in the same period coccolithophores vanish gradually in the Southern Ocean and appear more pronounced over the tropical regions. From August till December the coccolithophores' global patterns follow a reverse way to complete the annual cycle.

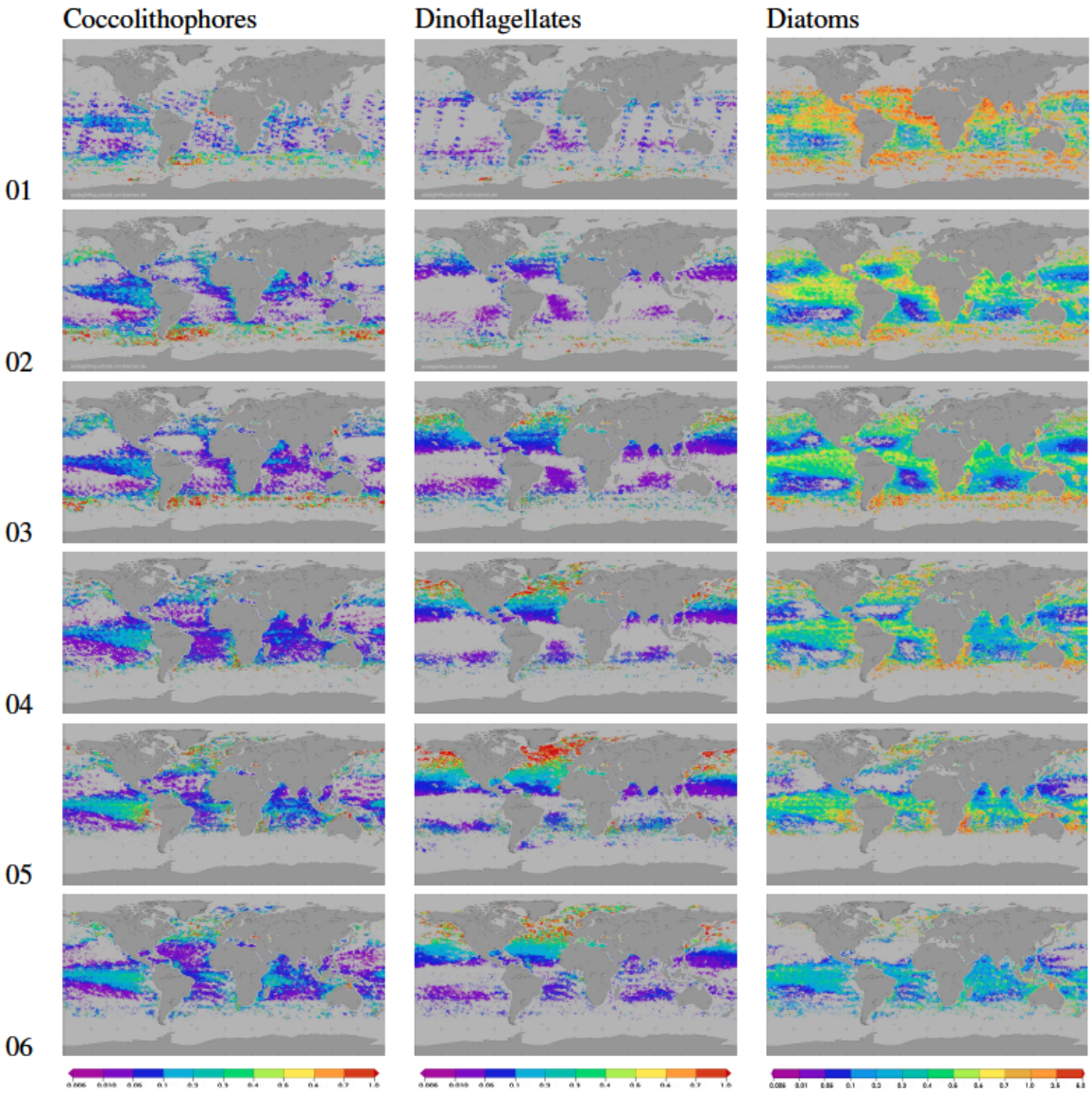

Figure 4.1: Monthly mean *chl-a* maps (in $[mg\,m^{-3}]$) for target PFTs retrieved by PhytoDOAS. The results have been obtained by applying the PhytoDOAS *triple-target* fitting to the SCIAMACHY data for the first half of 2005.

The monthly variations in the *chl-a* patterns of retrieved PFTs' is called *seasonality*, governing all phytoplankton activities. Even by looking at this one-year data of phytoplankton retrieval it can be recognized that the seasonality effect is basically derived from variation in available sunlight. This can be addressed by the fact that there is no month during which the phytoplankton activities could be seen in the high latitudes of both hemispheres; and this behavior is independent of the

type of phytoplankton.

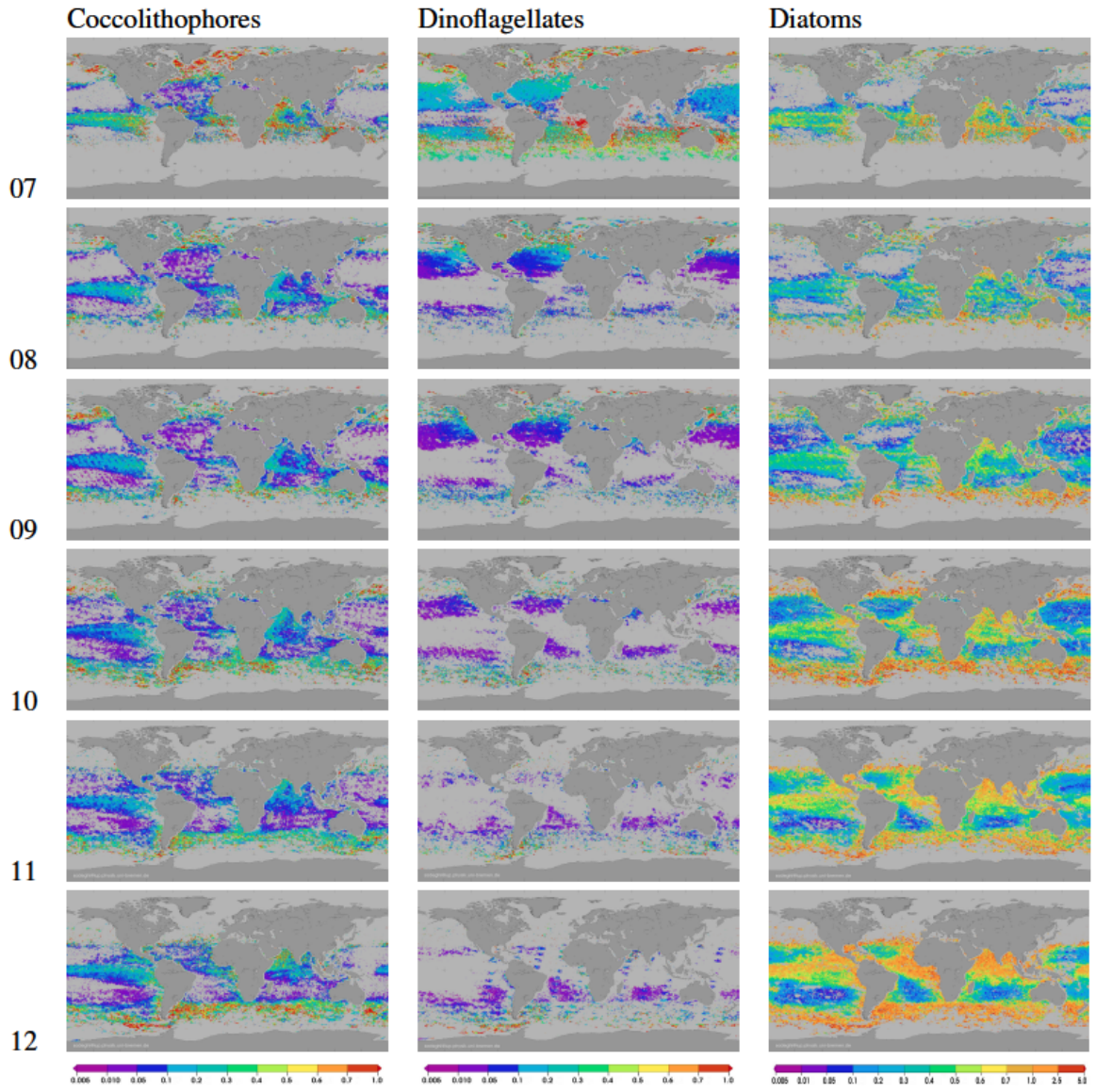

Figure 4.2: Monthly mean *chl-a* maps (in $[mg\,m^{-3}]$) for target PFTs retrieved by PhytoDOAS. The results have been obtained by applying the PhytoDOAS *triple-target* fitting to the SCIAMACHY data for the second half of 2005.

It must be considered that there are other important factors ruling the phytoplankton seasonal patterns (e.g., nutrient regime, mixed layer depth, regional oceanic currents and atmospheric aerosol loads). Hence, it is important to recognize the dominant factor (in general). Of course, satellite sensors can not collect enough water-leaving signals over those regions, where the solar elevations are too low; but this can not justify the whole emptinesses observed in high latitudes during local winters. The main reason can be formulated as follows: "the lower the sunlight, the lower the photosynthesis and therefore, the lower the phytoplankton growth".

Similarities and characteristics in PFT maps

Coccolithophores show elevated *chl-a* in high latitudes during the local blooming periods. In the northern hemisphere this is pronounced from May to August (with the maximum in July especially in the north of the North Atlantic). In the southern hemisphere high elevated *chl-a* is pronounced from October to March especially along a horizontal band in the north of the Antarctic Polar Front, which is referred to as the *Great Calcite Belt* ([Balch et al., 2011]). Dinoflagellates are mostly abundant in the northern oceans, almost in the regions where the coccolithophores are observed, but their development begins earlier, starting from March till July with a maximum in May. Only in July dinoflagellates can be seen pronounced also in the southern tropics. In general, diatoms' *chl-a* contents are higher than the two other PFTs. Except for in the ocean deserts (located in the subtropics), diatoms are growing almost everywhere in the World Ocean. However, they are most abundant in the tropical upwelling regions and also in the sub-Antarctic regions. Seasonality can also be seen with diatoms as behaving inversely at the same time in the high latitudes of the northern and southern regions.

4.1.2 PhytoDOAS coccolithophores vs. MODIS PIC: 2005 monthly means

Since the whole coccolithophores group can not be observed through one in-situ technique, the direct comparison of the retrieved coccolithophores with the in-situ data is not possible, because hardly ever all necessary measurements have been done at the same place. More precisely, with analyzing water samples by microscopy or with the Continuous Plankton Recorder (CPR) only the larger cells ($> 5\,\mu m$ and $> 10\,\mu m$, respectively) can be identified. From HPLC and flow-cytometric analysis only the groups of haptophytes or nano-eukaryotes, respectively (to both coccolithophores belong to), can be identified. In addition, there is a significant difficulty associated with the collocation of the in-situ point measurements to the large SCIAMACHY ground pixels of $30\,km$ by $60\,km$. Therefore, so far, the PhytoDOAS results of coccolithophores, instead of validation, were compared to the global maps of Particulate Inorganic Carbon (PIC) distribution. PIC, or suspended (particulate) calcium carbonate, is regarded as a proxy of coccolithophores in sea waters [Balch et al., 2005], since coccolithophores continuously build and release coccoliths (calcite shells). Therefore, PIC is an appropriate parameter for the evaluation of retrieved coccolithophores.

For the comparisons done in this study, the PIC global distributions were obtained from the MODIS Aqua Level-3 products, as monthly composites with a $9\,km$ gridding (level-3 daily products are obtained by composing level-2 product files for each day into a global grid).

To retrieve PIC concentration in open oceans from satellite radiometric data, two algorithms have been mainly used as follows:

- 3-band PIC algorithm [Gordon et al., 2001] based on remote sensing reflectance in 670, 765, and $865\,nm$ bands, with knowledge on the spectral dependence of coccolith backscattering;
- a backscattering-based algorithm, called 2-band PIC algorithm [Balch et al., 2005], which uses normalized water-leaving radiance in the blue ($440\,nm$) and green ($550\,nm$) plus the scattering cross-sections of calcite coccoliths and chlorophyll-containing cells.

The MODIS PIC product is based on the 2-band PIC algorithm, even though the difference between the two algorithms is not significant [Balch et al., 2005].

The comparison between retrieved coccolithophores (as *chl-a* content) and PIC concentration in this study implies only investigating the similarities in patterns, because the PIC concentration includes not only the living cells of coccolithophores, but also the detached coccoliths from the

cells. The *chl-a* conc. of the coccolithophores is given in $[mg\,m^{-3}]$, whereas the conc. of PIC is given by $[mol\,m^{-3}]$ (of suspended $CaCO_3$). However, the number of suspended coccoliths can be approximated from the PIC concentration through some assumptions. For instance, taking that the observed PIC belongs to a coccolithophores community and itself is dominated by *E. huxleyi*, both are valid assumptions in most cases in the open ocean. Assuming in this way, we would only need to have the average weight of a typical coccolith of *E. huxleyi*. As proposed by Fagerbakke et al. [1994], for *E. huxleyi* species a single coccolith weighs about 1.8×10^{-12} gram. Then, the following can be inferred:

$$1\ mol/m^3\ [CaCO_3] = 80\ g\ \ [CaCO_3]\ \ per\ \ m^3$$

According to Fagerbakke et al. [1994], one single coccolith (of *E. huxleyi*) contains 1.8×10^{-12} grams $[CaCO_3]$. Hence, the average number of coccoliths (per unit volume) equivalent to one mole suspended calcite particles (PIC) per cubic meter can be approximated as:

$$1\ mol/m^3\ [CaCO_3] = \frac{80\,g}{1.8\times10^{-12}} = 4.44\times10^{13}\ \ [coccoliths]\ \ per\ \ m^3$$

As each cell of *E. huxleyi* is surrounded, in average by 30 coccoliths, and due to the fact that there are also detached coccoliths and dead cells suspended in surface water, the number of living cells can be approximated (in a simple cautious scenario) by dividing the above value by 100:

$$\begin{aligned} 1\ mol/m^3\ [CaCO_3] &\simeq \frac{4.44\times10^{13}}{100} \simeq 4.5\times10^{11}\ \ [cells]\ \ per\ \ m^3 \\ &\simeq 0.5\ billion\ \ [cells]\ \ per\ \ liter \end{aligned}$$

Fig. 4.3 and Fig. 4.4 indicate monthly comparisons between the PhytoDOAS coccolithophores and the MODIS-Aqua PIC distribution for the year 2005. According to these figures, the monthly patterns of the retrieved coccolithophores indicate very good agreements with the distribution patterns of PIC: from March both coccolithophores and PIC start growing in the northern waters, especially in the north of the North Atlantic, reaching their maximum in July and then decreasing to be vanished completely in November. At the same course of time, both products indicate a gradual decrease in the northern parts of the Antarctic Polar Front, where they show very high values during austral summer. The raising phase of coccolithophores and PIC in the southern hemisphere starts simultaneously in August, reaching it's maxima in December and staying high till March. However, there are also some minor differences between the patterns of the two products in certain months and regions: in the Indian Ocean, even though the general developments of coccolithophores and PIC coincide with each other, but in May, June and July PIC patterns are not as pronounced for the coccolithophores. The same feature is observed for parts of the Mid-Pacific and the Mid Atlantic all over the year.

4.1.3 PhytoDOAS diatoms in comparison with modeled data: 2005 monthly mean chl-a

Fig. 4.6 and Fig. 4.7 depict the monthly mean conc. of diatoms' *chl-a* for 2005, retrieved from PhytoDOAS and modeled by NOBM (shown on the left and right panels, respectively). The PFT modeled data used for this comparison were acquired from the NASA Ocean Biogeochemical Model (NOBM), which provides time-series of PFT assimilated data. The NOBM model provides partly the biogeochemical output data for the Giovanni project, an acronym for the GES-DISC

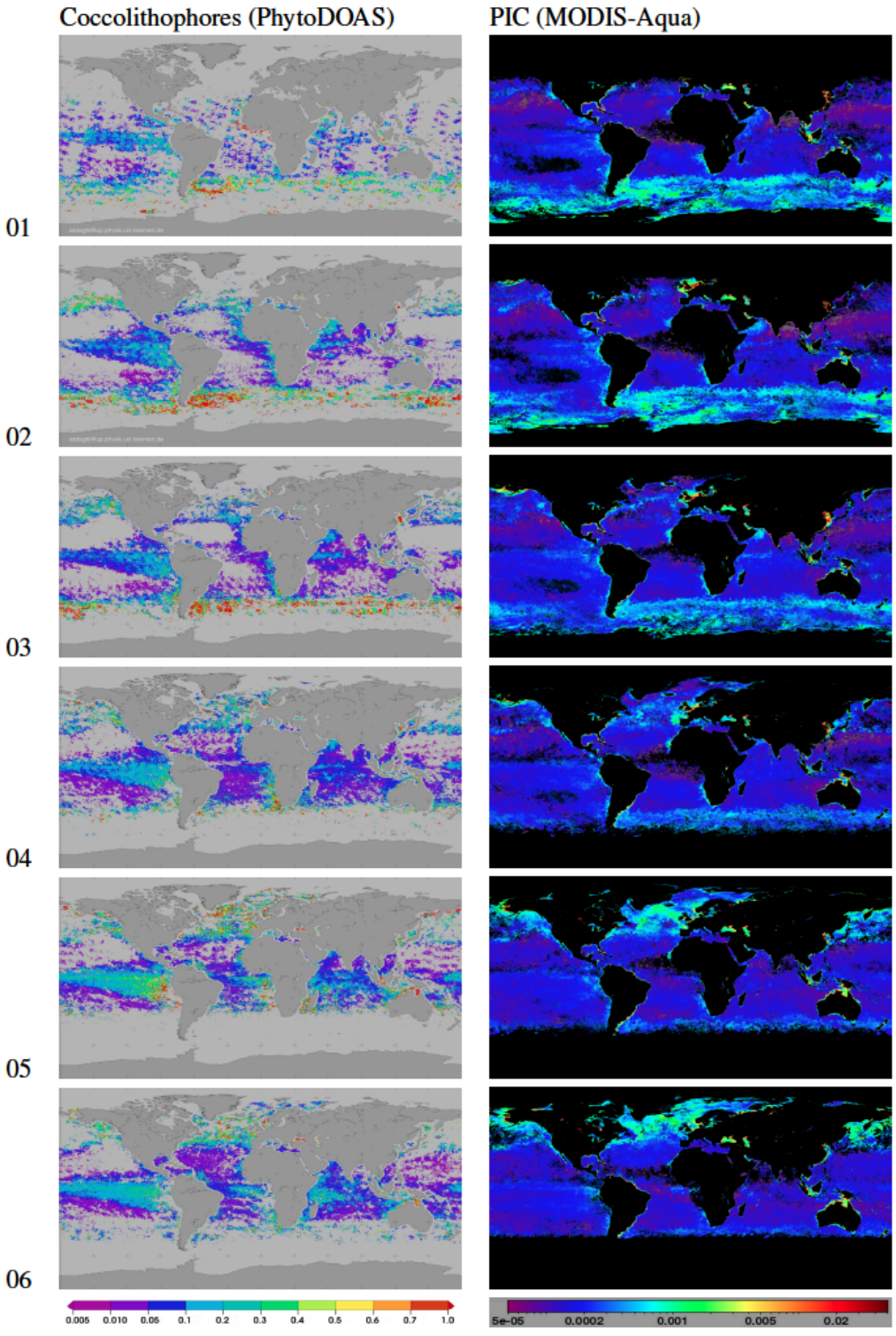

Figure 4.3: Left panels: PhytoDOAS coccolithophores monthly mean *chl-a* $[mg\,m^{-3}]$. Right panels: PIC monthly distribution $[mol\,m^{-3}]$ from MODIS Aqua. All data corresponds to the first half of 2005.

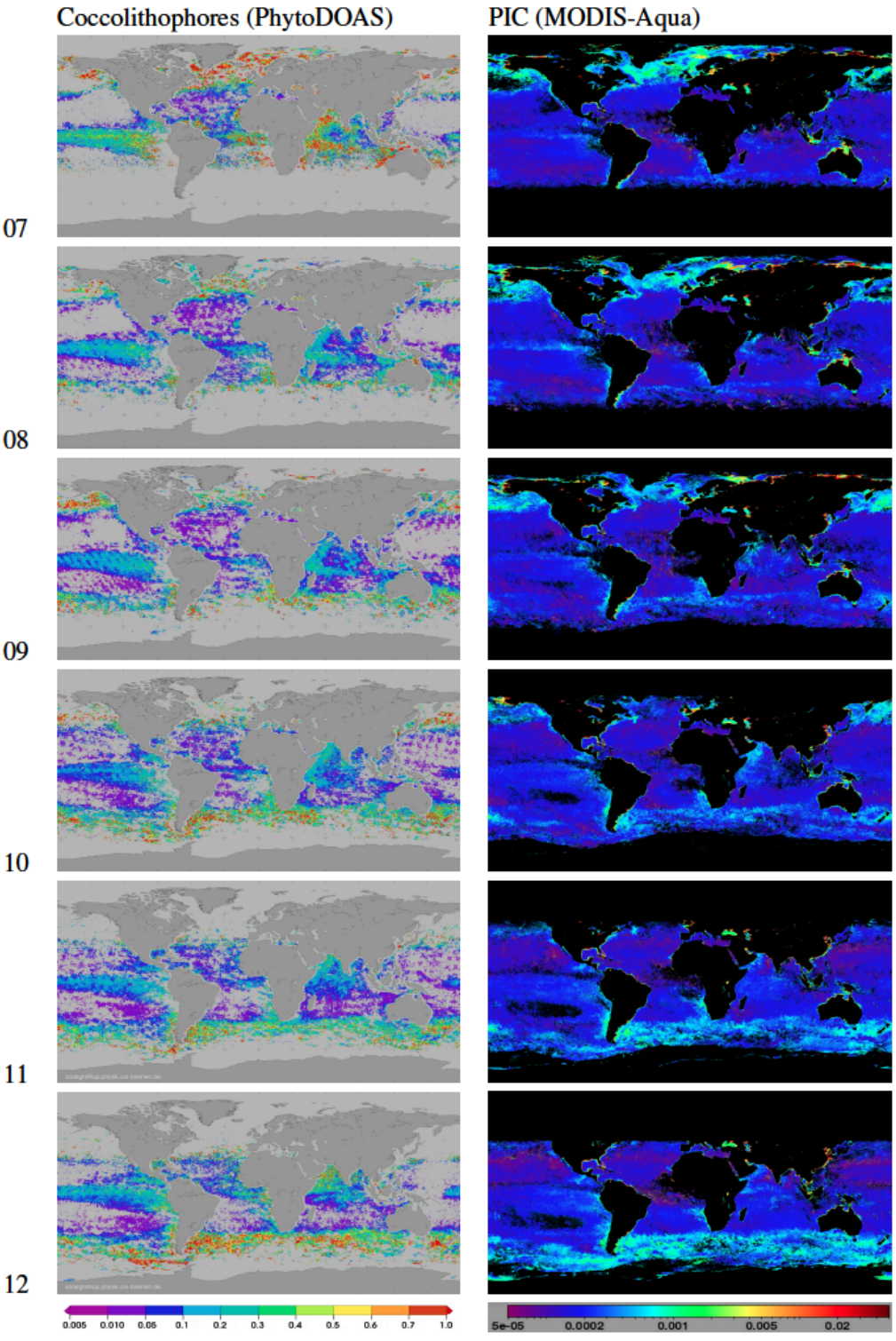

Figure 4.4: Left panels: PhytoDOAS coccolithophores monthly mean *chl-a* [$mg\,m^{-3}$]. Right panels: PIC monthly distribution [$mol\,m^{-3}$] from MODIS Aqua. All data corresponds to the second half of 2005.

(Goddard Earth Sciences Data and Information Services Center) Interactive Online Visualization ANd aNalysis Infrastructure. NOBM is a fully coupled model of three major components simulating general circulation, radiative transfer processes and biogeochemical processes [Nerger and Gregg, 2007]. The ocean general circulation is modeled by the Poseidon model [Schopf and Loughe, 1995]. The radiative model, the Ocean Atmosphere Spectral Irradiance Model (OASIM, Gregg [2002]), provides underwater irradiance fields which drive the growth of the phytoplankton groups. The biogeochemical processes model includes ecosystem and carbon components [Gregg and Casey, 2007]. Fig. 4.5 illustrates the general structure of the NOBM. As the output products of model are not directly based on remote-sensing observations, they are not certainly the best choice or highly reliable for comparison of the satellite retrieved PFTs. However, as mentioned before, collocating the existing field data (of PFTs) with large satellite pixels (of SCIAMACHY) is still a big limitation for validating the retrievals with available (though limited) in-situ data. Nevertheless, in case of dinoflagellates even modeled data are not existing (therefore, no comparison for the dinoflagellates has been provided).

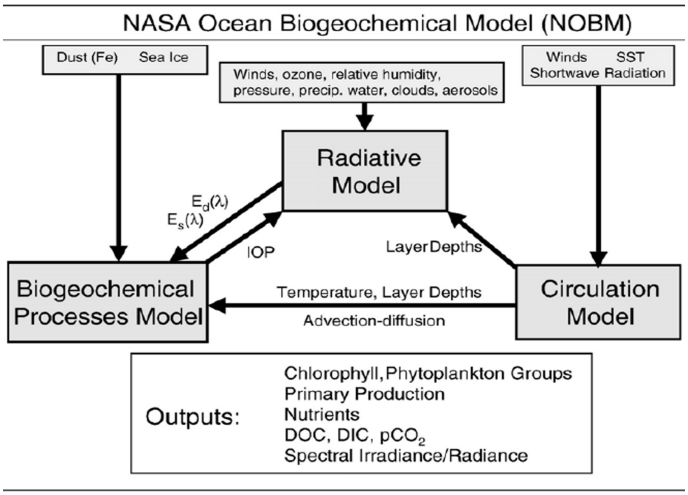

Figure 4.5: General structure of NOBM depicting the interactions among the three main components: general circulation, radiative transfer processes and biogeochemical processes. Courtesy to Nerger and Gregg [2007].

Regarding the usual roughness existing in current PFT models, the comparison indicates a good agreement between *chl-a* distribution patterns of the two methods for diatoms. The best accordance between the two products is observed in the north of the Polar Front in the southern hemisphere. In the northern regions of the North Pacific the agreement is good too, almost the whole year through. In the eastern parts of the Mid-Pacific both products contain stable horizontal patches of elevated *chl-a*, even though this is more pronounced for the retrieved diatoms. In the north-west of the Indian Ocean, off North-east Africa and Arabian Peninsula, the *chl-a* patterns are almost the same in two products, more pronouncedly between July and September (though PhytoDOAS indicates higher range of *chl-a*). There are also clear differences between two sets of diatoms' distributions: the model does not indicate any diatoms in the tropical Atlantic, except a narrow tiny band, whereas the retrieval maps show higher results in this part with wider coverage, especially from October till April; while the NOBM model presents a permanent band of elevated *chl-a* in the sub-Antarctic regions (with seasonal variations in the intensity and the band-width), the retrieved diatoms in this region can be observed only during austral spring and austral summer; in the Indian Ocean, except the north-west regions, the NOBM model does not contain any diatoms, while retrieved diatoms are abundant in this ocean almost whole year. Moreover, contrary to

the model, the retrieval is not covering the very high latitudes, especially during the local winter months, for which the low light availability makes the signal to noise ratio even worse for the large SICMACHY pixels.

4.1.4 PhytoDOAS cyanobacteria via single-target fit: 2005 monthly mean chl-a

Fig. 4.8 shows monthly *chl-a* $[mg\,m^{-3}]$ of cyanobacteria from the PhytoDOAS *single-target* fit for the year 2005. The characteristic feature of these results is that over the whole year hardly any cyanobacteria are observed in the high latitudes of both hemispheres, rather they are concentrated in the tropical and subtropical regions, more pronounced in the southern hemisphere. Cyanobacteria are abundant in the mentioned areas from February to August, showing the highest activity in May with large blooms in the southern hemisphere and lower biomass in the Northern tropical and subtropical areas. While in the high latitudes of the North Atlantic cyanobacteria are observed from March to June, they indicate no activity in the high latitudes of the North Pacific. The second most abundant month for cyanobacteria is in July, when they cover partially the North Atlantic and the North Pacific and show less coverage in the southern hemisphere compared to May. The interesting feature of the retrieved cyanobacteria is that in specific months they cover also the so-called *Ocean Deserts* regions in the Atlantic and the Pacific. For instance, the hyper-oligotrophic region, located in the South Pacific gyre near Easter Island ($20°S$ - $30°S$ and $98°W$ - $122°W$, Claustre and Maritorena [2003]), elevated cyanobacteria can be seen in July and August and also partially in February and October with moderate concentration. The same feature can be seen in the two oceanic deserts of the Atlantic Ocean, situated within the subtropical gyres [Williams and Follows, 1998], in February, May, July and August. However, it is not of surprise to observe cyanobacteria living also in habitats where other phytoplankton do not. For instance, *Trichodesmium* (a major cyanobacterial species) is the dominant planktonic nitrogen-fixer in oligotrophic waters [Capone et al., 1997]. There are plenty of references evidencing that in tropical and subtropical areas cyanobacterial species are dominant, wherever the overall biomass is low (e.g., Zubkov et al. [2000]; DuRand et al. [2001]; Longhurst [2007]).

The results of cyanobacteria shown in Fig. 4.8 have been obtained via the PhytoDOAS *single-target* mode, according to Bracher et al. [2009], while for the retrievals of the other three PFTs (displayed before) the *triple-target* mode was applied. However, for the *single-target* fitting a wider wavelength window ($429 - 521\,nm$) was used, opposed to Bracher et al. [2009] where a fit-window of $429 - 495\,nm$ was performed.

However the results are almost the same. The reason to retrieve cyanobacteria in a different way, i.e., by the PhytoDOAS *single-target* mode, can be explained by the apparent difference existing between the spectral behavior of cyanobacteria and other PFTs. Fig. 4.9 shows these spectral differences in detail: the differential absorption spectra of the target PFTs (used as the phytoplankton input spectra in the retrieval) and the fourth-derivative curves of respective absorption spectra. In both cases cyanobacteria behave quite different, with low spectral correlation with the other targets. Hence, cyanobacteria can be retrieved separately without being affected by the contributions of the other spectra. On the other hand, the oceanic habitats of cyanobacteria are often particular, where the other species can hardly survive, as seen for the hyper-oligotrophic region. For instance, *Prochlorococcus* and *Synechococcus* (two major species of cyanobacteria) are mostly observed in oligotrophic tropical waters. Because, as picophytoplankton, they have large surface-to-volume ratio, making them less sensitive to nutrient limitation than larger phytoplankton groups [Alvain et al., 2008; Longhurst, 2007]. Consequently, cyanobacteria are not detected much to be prevalent simultaneously with the other target PFTs (as it is usual for diatoms, coccolithophores and dinoflagellates). This is more pronounced in the subtropical gyres (oligotrophic areas) and in the

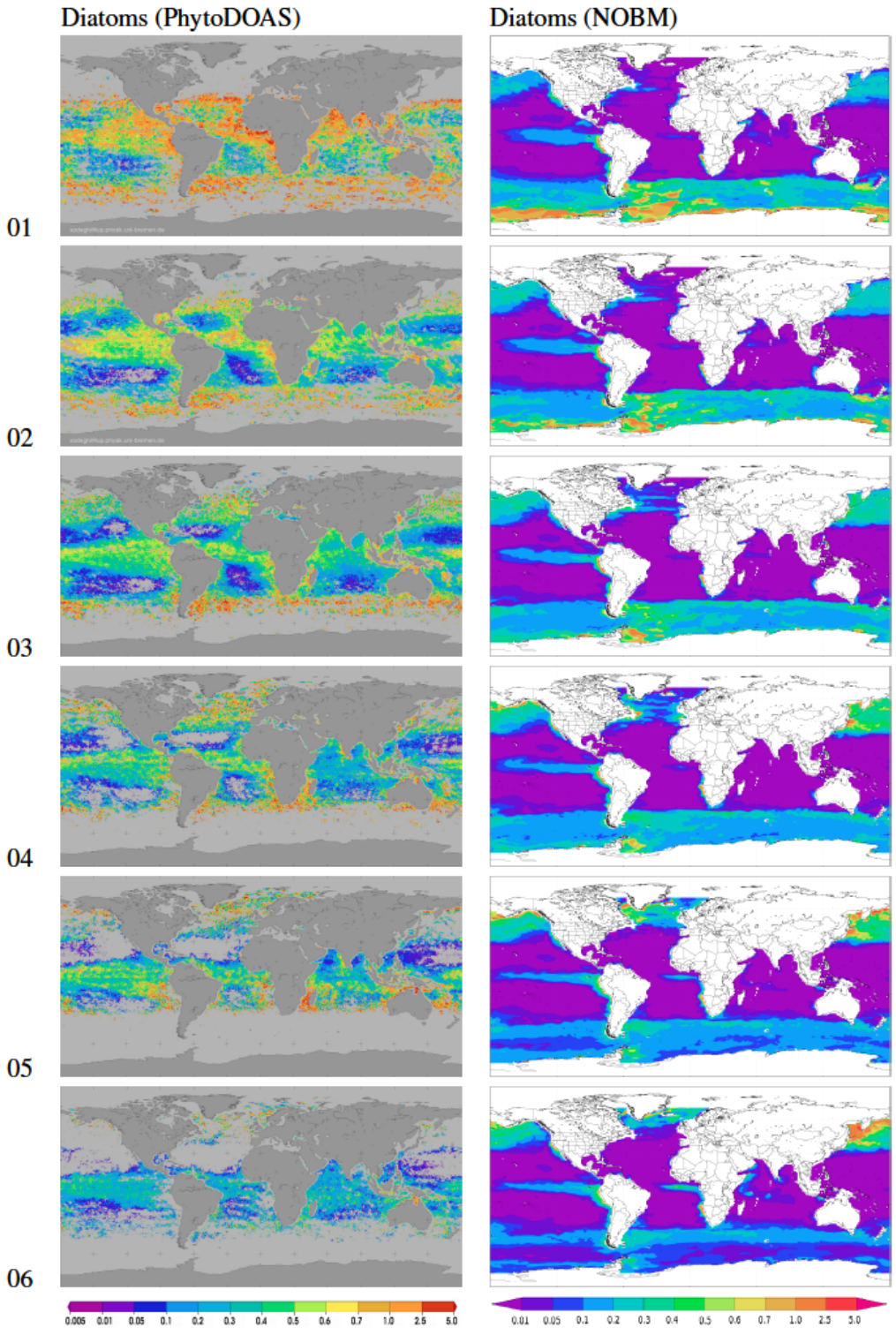

Figure 4.6: Left panels: diatoms monthly mean *chl-a* $[mg\,m^{-3}]$ retrieved by PhytoDOAS from the SCIAMACHY data. Right panels: diatoms monthly mean *chl-a* $[mg\,m^{-3}]$ acquired from the NOBM assimilated data. All data corresponds to the first half of 2005.

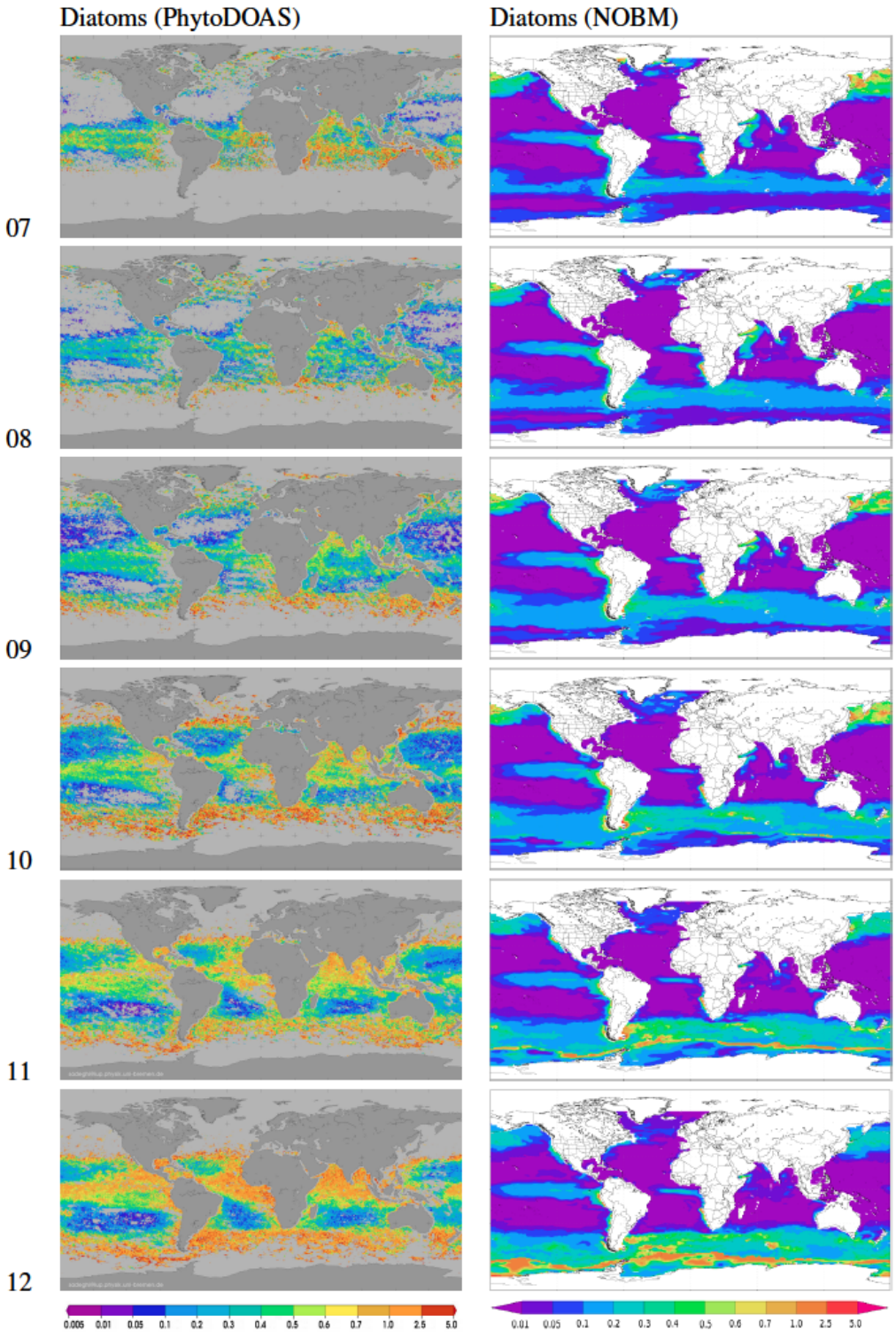

Figure 4.7: Left panels: diatoms monthly mean *chl-a* $[mg\,m^{-3}]$ retrieved by PhytoDOAS from the SCIAMACHY data. Right panels: diatoms monthly mean *chl-a* $[mg\,m^{-3}]$ acquired from NOBM data. All data corresponds to the second six months of the year 2005.

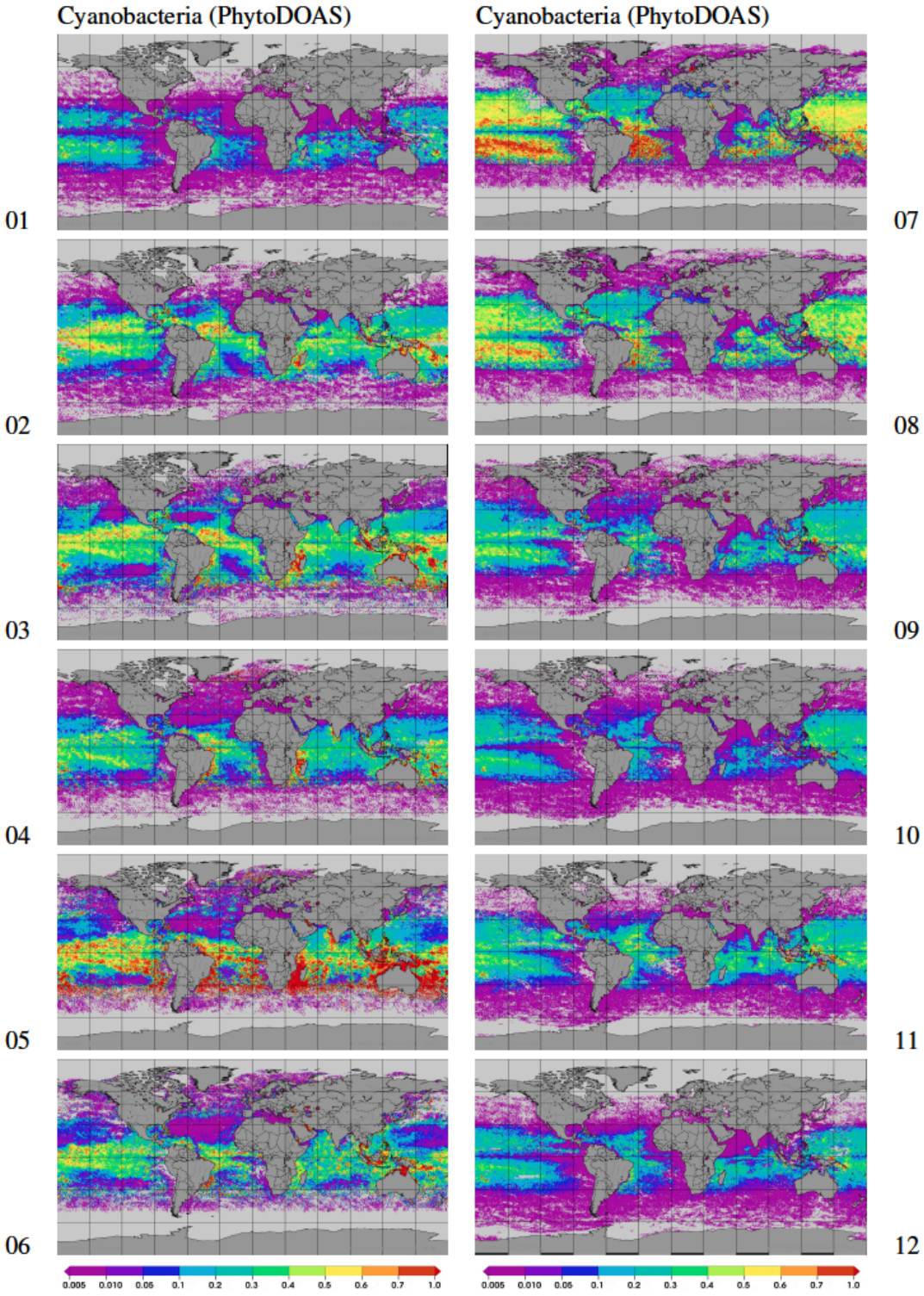

Figure 4.8: Cyanobacteria monthly mean *chl-a* $[mg\,m^{-3}]$ retrieved by PhytoDOAS single-target fit from SCIAMACHY data. All data correspond to the year 2005.

high latitudes (beyond 55°).

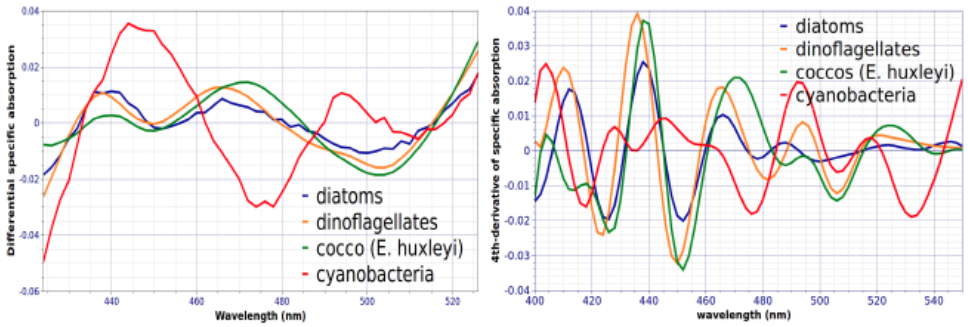

Figure 4.9: The differential absorption (left panel) and the forth-derivative of the absorption spectra (right panel) for the target PFTs retrieved by PhytoDOAS: coccolithophores (green), dinoflagellates (orange), diatoms (blue) and cyanobacteria (red). Each absorption spectrum had been beforehand normalized to the *chl-a* concentration of the respecting species.

4.2 PhytoDOAS annual PFTs in comparison with other products: 2005

4.2.1 Global distributions of retrieved PFTs: 2005 annual mean chl-a

Fig. 4.10 shows annual averages of *chl-a* conc. $[mg\,m^{-3}]$ of the four major PFTs retrieved by PhytoDOAS for the year 2005. These annual composites provide a short overview of the PFTs' global distribution patterns. As a brief comparison: coccolithophores and dinoflagellates show similarities at high latitudes in both hemispheres; at sub-polar latitudes and near the coastal zones, dinoflagellates show slightly higher values; in tropical and sub-tropical regions the two PFTs show completely different patterns. Diatoms are more abundant in the World Ocean than the other PFTs, but more favored at high latitudes (cold oceans) and coastal upwelling areas, showing higher *chl-a* contents than other retrieved PFTs (note the different range of their color-table). The *chl-a* pattern of cyanobacteria is quite different than what is observed for the other PFTs, with elevated *chl-a* at low latitudes, including the subtropical gyres, and very low concentration at high latitudes.

4.2.2 PhytoDOAS coccolithophores and diatoms in comparison with products of MODIS and NOBM: 2005 annual means

In Fig. 4.11 the PhytoDOAS annual composites of coccolithophores and diatoms in 2005 are compared with two other available PFT products: coccolithophores with the MODIS PIC and NOBM data; diatoms with the MODIS total *chl-a* and NOBM data. Coccolithophores and PIC, as expected from monthly comparisons, have very similar annual patterns: the areas of the most coincidences are the high latitudes in both hemispheres, especially in the North Atlantic and in the South Atlantic; both maps match also in their low-content regions, which are confined to the tropical and subtropical oceans. The comparison between coccolithophore results of PhytoDOAS and NOBM are not in good agreement, except for in the North Atlantic, the Tasman Sea and partially in the tropical waters. Regarding the global distribution of PIC and another PFT product relevant for coccolithophores, e.g., haptophytes represented by [Hirata et al., 2011] (panel *b* in

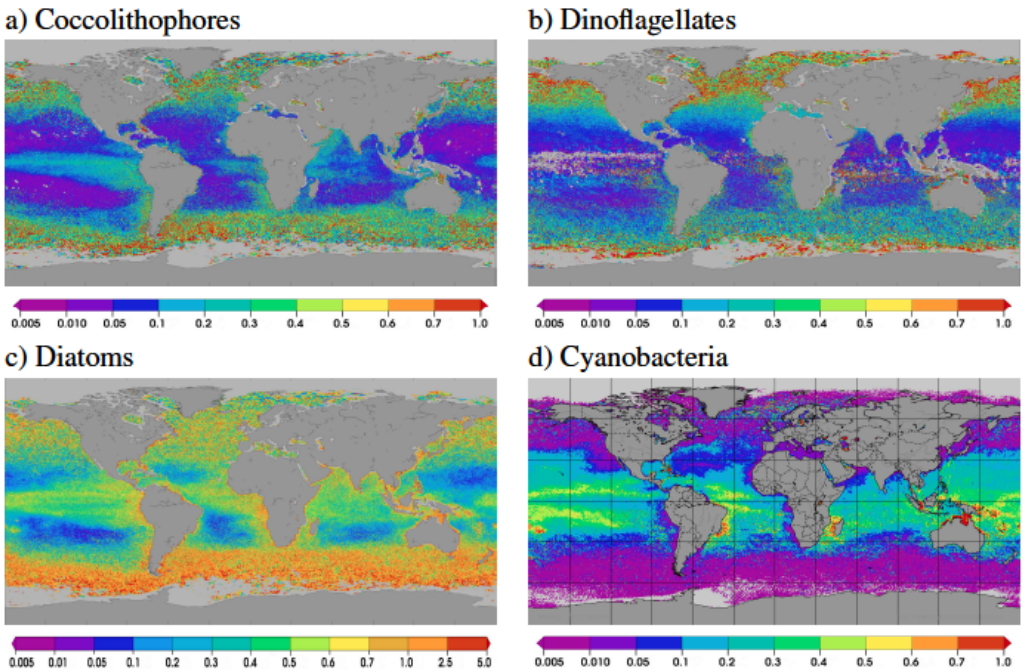

Figure 4.10: PFTs' annual mean *chl-a* $[mg\,m^{-3}]$ in 2005 retrieved by PhytoDOAS from SCIAMACHY data.

Fig. 4.12), it seems that the NOBM data underestimates coccolithophores and do not cover them in most parts of the World Ocean, especially in the southern hemisphere.

Since diatoms have a large contribution to ocean productivity and marine total *chl-a* [Yool and Tyrrell, 2003], and because of the limited data availability of PFTs' global distributions, the PhytoDOAS diatoms (annual mean for 2005) have been compared with the total *chl-a* of MODIS Aqua (panel *b* in Fig. 4.11). Surprisingly, the global pattern of PhytoDOAS diatoms is very similar to MODIS total *chl-a*. Overall, PhytoDOAS diatom values are higher than MODIS total *chl-a*, which indicates an overestimation by PhytoDOAS. However, the distribution patterns of elevated *chl-a* conc. are very similar in both products. The NOBM diatoms also show similar patterns as PhytoDOAS diatoms, even though with less coverage in the North Atlantic and also in the tropical regions of the Indian Ocean and the West Pacific. Moreover, the range of *chl-a* in NOBM diatoms is in overall lower than PhytoDOAS diatoms, because the NOBM products are scaled to the total *chl-a* conc. of MODIS. It must be mentioned that NOBM data products include also global maps of mean *chl-a* for cyanobacteria, for which the comparison with the PhytoDOAS cyanobacteria has not been shown in this thesis.

4.2.3 PhytoDOAS PFTs in comparison with products of Hirata's PFT algorithm: 2005 annual mean chl-a

In Fig. 4.12 the 2005 annual *chl-a* composites of PhytoDOAS coccolithophores, diatoms and cyanobacteria are compared with the results of a PFT retrieval algorithm developed by Hirata et al. [2011], which has been applied on several years data of the SeaWiFS sensor. Hirata et al. [2011] proposed an approach for global estimation of the PSCs (phytoplankton size classes) and PFTs using the synoptic relationships between total *chl-a* and the fractional contribution of three PSCs and seven PFTs, based on analyzing and quantifying biomarker pigments through a large in-situ HPLC data-set. The technique relies on that at large scale the variation in phytoplankton

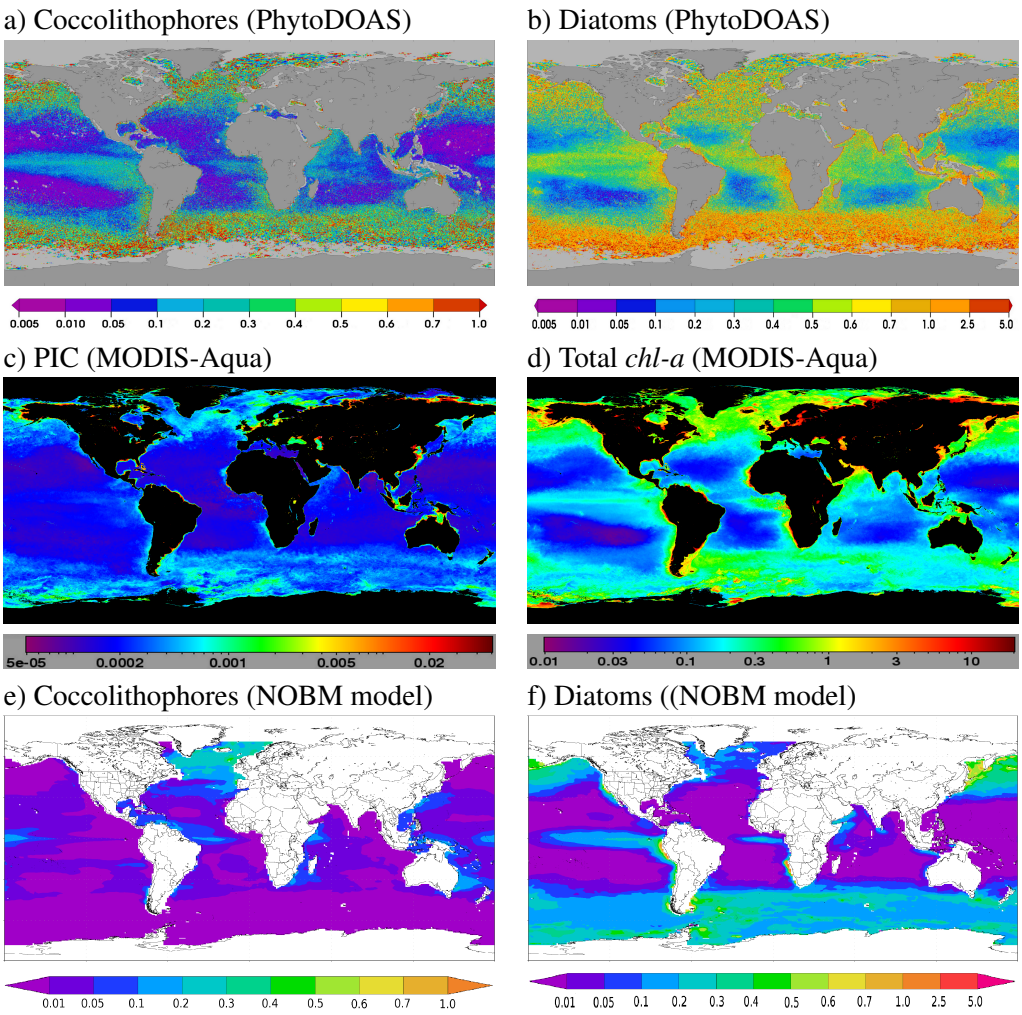

Figure 4.11: Annual averages in 2005 for: PhytoDOAS coccolithophore and diatoms *chl-a* (panels *a* & *b*), MODIS-Aqua PIC and total *chl-a* (panels *c* & *d*) and NOBM coccolithophore and diatoms *chl-a* (panels *e* & *f*).

community structure depends on the variation in total *chl-a*. The method was validated and applied to satellite (SeaWiFS) total *chl-a* data: seven PFTs have been derived globally from SeaWiFS data, presented as separate *chl-a* maps averaged from 1998 to 2009. For our comparison purpose three of them have been used (right panels in Fig. 4.12) which are diatoms, the haptophytes and prokaryotes (cyanobacteria). The haptophytes are used as rough approximation for coccolithophores, although haptophytes not only include coccolithophores, but also *Phaeocystis sp.* and other species.

As shown in Fig. 4.12, the best agreement between PhytoDOAS and the PFT algorithm of Hirata et al. [2011] is observed for coccolithophores and its counterpart: the haptophytes (the first row). The patterns of global coverages are coinciding very well and the respective ranges of *chl-a* are also close to each other; even though the contribution of other haptophytes should be considered. Therefore, due to the very similar spectral behavior of the absorption spectra of *Phaeocystis sp.* and coccolithophores, one possible scenario could be that the PhytoDOAS retrieval of coccolithophores includes *Phaeocystis sp.*, as well, and hence is likely to be representing the haptophytes. The two methods are showing different results for diatoms in the tropical and sub-tropical oceans: while PhytoDOAS assigns high concentrations to diatoms in large parts of these regions, by the Hirata's method diatoms (in respective areas) exist only in coastal waters. However, in high latitudes of both hemispheres the two methods show good agreement. This is more pronounced in the northern hemisphere and also in the southeastern waters of the South America, but in the Southern Ocean PhytoDOAS show higher values than the other algorithm. The PhytoDOAS cyanobacteria hardly match the Hiratas's prokaryotes. Especially, there is no agreement for the high-latitude regions, except for tiny parts in the North Atlantic and the North Pacific. This difference can be partly attributed to the spatial variations in the phytoplankton absorption spectra (here cyanobacteria), which has to be investigated further. Moreover, it can also be the case that because of the very different absorption spectrum of cyanobacteria (compared to the other PFTs), their contribution in the total *chl-a* is generally underestimated by the ocean color *chl-a* algorithms.

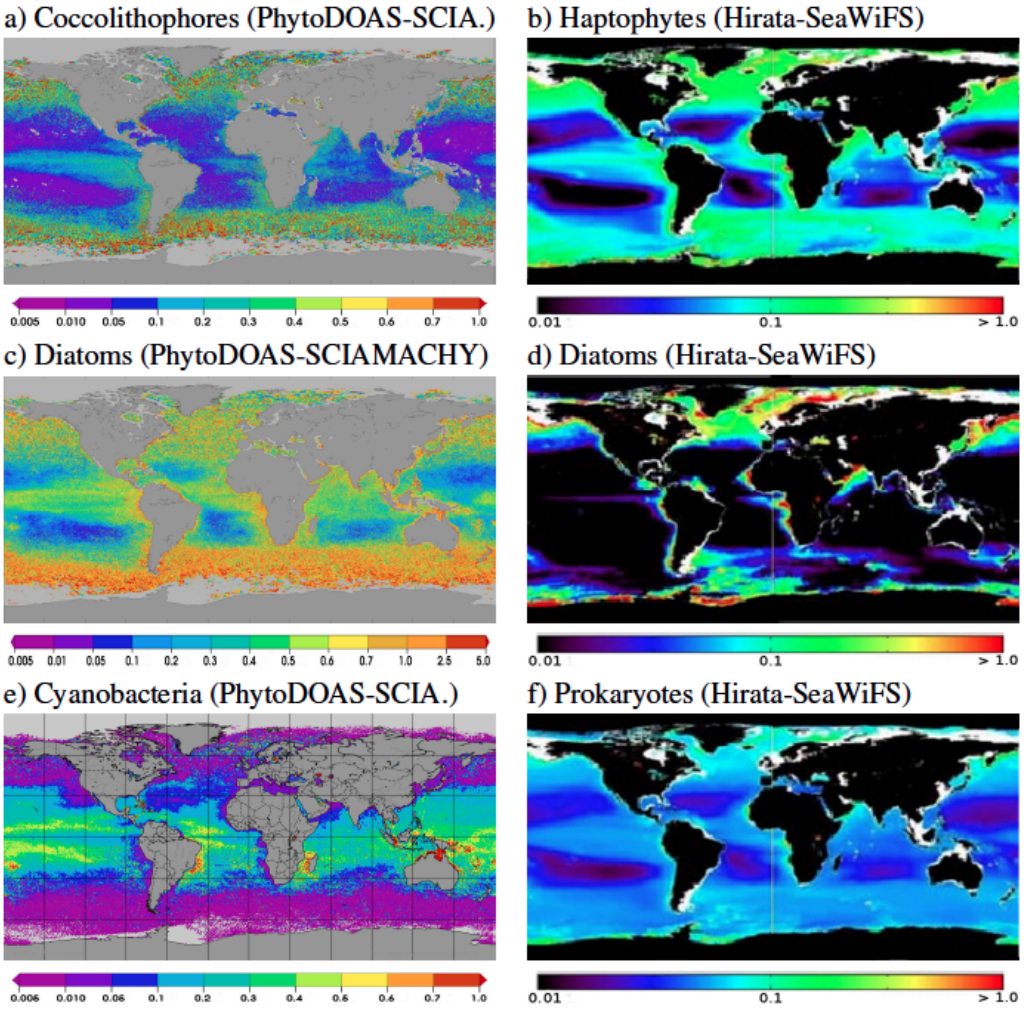

Figure 4.12: Annual averages of 2005 for: PhytoDOAS (left panels) and PFT-retrieval algorithm according to Hirata et al. [2011] (right panels). The PFT results in Hirata et al. [2011] have been extracted by applying the proposed algorithm onto the SeaWiFS data and then averaged over a period from 1998 to 2009. Both set of results are represented as *chl-a* concentration in $[mg\,m^{-3}]$.

Chapter 5

Application of PhytoDOAS to study the dynamics of coccolithophore blooms

5.1 Overview

Sensitive responses of phytoplankton to the environmental and ecological impacts make them reliable indicators of the variations in climate factors. Coccolithophores (*coccos*) are an abundant taxonomic group of phytoplankton with a wide range of effects on the oceanic biogeochemical cycles [Rost and Riebesell, 2004] and a significant influence on the optical features of surface water [Tyrrell et al., 1999]. *Coccos* also affect the atmosphere and climate by emitting dimethylsulfide (DMS) into the atmosphere [Tyrrell and Merico, 2004; Andreae, 1990], where it is converted to the sulfur aerosols and cloud condensation nuclei (CCN) and influence the climate and the Earth's energy budget [Charlson et al., 1987; Andreae, 1990]. Coccolithophores form frequently large blooms, which can be often visually detected by satellite imageries. However, to have a quantitative and continuous estimation of coccolithophore contents on a global scale, ocean color remote sensing algorithms must be used. Improving these algorithms for detecting phytoplankton groups is important because of the different biogeochemical impacts of different groups. In this study, monitoring coccolithophore blooms, through spatial and temporal variations of their abundances and inter-annual cycles, has been the main interest. This is part of the research field of monitoring climate impacts through phytoplankton variations. As retrieval tool, the PhytoDOAS method has been applied to the entire data set of SCIAMACHY to detect coccolithophore blooms in three selected oceanic regions. The retrieval results, shown as time-series, were compared to the appropriate satellite data of total phytoplankton biomass (total *chl-a* from GlobColour) and particular inorganic carbon (PIC, from MODIS-Aqua). The results were also compared with three major oceanic geophysical parameters: sea-surface temperature (SST), mixed-layer depth (MLD) and surface wind speed, for which the two first parameters were obtained from satellite data and the last one from a model.[1]

5.1.1 Motivation

Among different phytoplankton blooms, *coccos* blooms are very important due to their wide coverage and frequent occurrence [Holligan et al., 1983], as well as their unique biooptical and biogeochemical properties [Brown and Podesta, 1997; Balch, 2004]. This importance, which is more explained in below[2], was the main motivation for conducting a *coccos* bloom study via PhytoDOAS

[1] The content of this chapter has been partially presented in Sadeghi et al. [2012a].

[2] To explain the motivation of the work presented in this chapter, some contents of sec. 2.3 were partially used.

method. *Coccos* are the main planktonic calcifiers in the ocean. They make a major contribution to the total content of PIC (suspended $CaCO_3$) in the open oceans via building and releasing *coccolith* plates [Milliman, 1993; Ackleson et al., 1994]. PIC represents about 1/4 of all marine sediments [Broecker and Peng, 1982] and is regarded as a major oceanic sink for atmospheric CO_2. Moreover, by sinking through the water column and getting deposited in the sediments (either directly as *coccoliths* and detritus or after being converted into PIC), *coccos* are considered to be one of the main drivers of the biological carbon pump [Raven and Falkowski, 1999; Rost and Riebesell, 2004; Thierstein and Young, 2004], hence, a key component of the global carbon cycle [Westbroek et al., 1993]. Furthermore, the most dominant species within the *coccos* taxonomic group, i.e., *E. huxleyi*, is known to be a significant producer of DMS [Keller et al., 1989; Malin et al., 1992], which affects the planetary albedo [Charlson et al., 1987]. During their frequently large-scale blooms, *coccos* cause two important optical effects (due to their *coccoliths*): a very high reflectance from the ocean surface, and a wide impact on the light field in upper ocean [Ackleson et al., 1988; Balch et al., 1989]. *Coccos* blooms succeed diatom blooms in response to increasing stabilization and nutrient depletion of surface waters [Margalef, 1978; Holligan et al., 1983; Lochte et al., 1993]. Hence, monitoring *coccos* blooms can also improve our understanding on the global distribution of diatoms.

Some former studies aimed to exploit and develop remote sensing methods for monitoring the distribution of *coccos* on a global scale [Groom and Holligan, 1987; Brown and Yoder, 1994a; Brown, 1995; Gordon et al., 2001], as well as studying corresponding blooms on regional scales [Holligan et al., 1983; Balch et al., 1991; Brown and Yoder, 1994b; Brown and Podesta, 1997; Smyth et al., 2004; Morozov et al., 1993].

5.1.2 Objectives

The main interest of this study was to apply the PhytoDOAS method for quantitative remote sensing of *coccos* using satellite data. Due to the crucial role of *coccos* in the global biogeochemical cycles, this satellite-based method can be used for monitoring temporal and spatial variations of *coccos* on a global scale, which in turn can be used (as a phenomenal study of phytoplankton dynamics) for studying the impacts of a varying climate on marine phytoplankton [Winder and Cloernet, 2010]. To show this capacity, *coccos* blooms in selected regions were monitored over eight years and their inter-annual variations were investigated along with the temporal variations of certain geophysical parameters. On the other hand, PhytoDOAS takes the following factors into account, which are often not considered in current biooptical methods based on band-ratio algorithms: the phytoplankton absorption spectra, the existence of multiple PFTs and the light penetration depth in the water. Therefore, the above specific capacities of the method are investigated by this study. More specifically, concerning *coccos* retrieval, while other phytoplankton pigments cause a decrease in backscatter radiance mostly in the blue part (and slightly in the green), *coccos*, due to their calcite plates, affect the solar irradiance uniformly in both the blue and the green [Gordon et al., 1988]. Furthermore, as *coccos* blooms cause flattening of the reflectance spectrum, the standard ratio pigment algorithms [Gordon and Morel, 1983] will not provide correct pigment retrievals within the blooms [Balch et al., 1989; Balch, 2004]; while, by retrieving the differential absorption features, the PhytoDOAS method has the potential to obtain results on PFT *chl-a* in high *coccos* regions, when hyper-spectral variations are still visible. In this sense, retrieving *coccos* blooms provides a reliable application to test the improved PhytoDOAS method.

5.2 Study setup

5.2.1 Initial tests

As mentioned in detail in sec. 4.1.2, there are limitations in comparing the PhytoDOAS *coccos* (retrieved from SCIAMACHY data) with in-situ *coccos* measurements. Briefly speaking, these limitations arise from collocating satellite data with comparable in-situ data sets, which inquires enough appropriate in-situ data. To avoid this restriction, the PhytoDOAS *coccos* results, instead of validation, were preliminarily compared with the NOBM *coccos* modeled data and then with the global distribution of PIC obtained from the MODIS-Aqua level-3 products. The reasons behind the comparison of retrieved *coccos* with the MODIS-Aqua PIC data, as well as the respective results for 2005, have been presented in sec. 4.1.2. Very good agreements were observed in global patterns of *coccos* and PIC on a monthly and seasonal basis (see sec. 4.1.2).

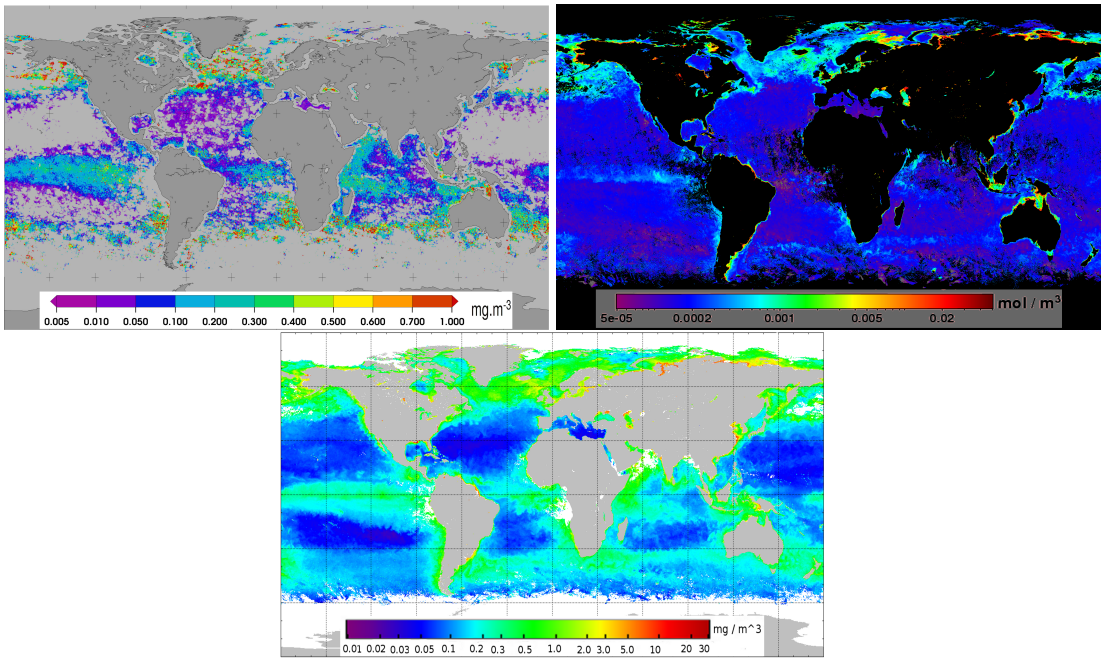

Figure 5.1: An example comparison of three monthly mean products, all obtained in Aug. 2005: the PhytoDOAS *coccos chl-a* (upper left panel) retrieved from SCIAMACHY data, the PIC concentration (upper right panel) from the MODIS-Aqua level-3 products, and the total *chl-a* (lower panel) from the GlobColour level-3 merged data.

Moreover, PhytoDOAS *coccos chl-a* results were compared to the total *chl-a*, provided by GlobColour merged data, as the maximum limit of observed *chl-a* for *coccos*. Fig. 5.1 illustrates a sample comparison of these three products in August 2005, showing consistent patterns between *coccos* (upper panel) and PIC (middle panel), followed by partially similar patterns of the total *chl-a* (lower panel).

Additionally, the improved PhytoDOAS method was used to detect single events of coccolithophore blooms, which is described below: In Fig. 5.2 the upper left panel corresponds to the coccolithophore bloom over Chatham Rise (east side of New Zealand) on 23 December 2009, which was reported as an instantaneous RGB image by NASA. The PhytoDOAS retrieval of this bloom, shown in the middle panel, was obtained from two weeks data of SCIAMACHY (centered at 23 Dec. 2009). The PIC distribution over this region (lower panel) was prepared as an 8-day composite (19-26 Dec. 2009) from MODIS-Aqua level-3 products. Since only few SCIA-

MACHY orbits cross this small region at one day, among which a large fraction of attaining pixels are flagged out due to the sensitivity of the retrieval to cloud contamination, this time frame limitation could not be avoided. The cloud contamination is also the reason for missing a lot of pixels in the eastern parts, where is almost blank in the respecting map. However, regarding the fact that a typical coccolithophore bloom lasts a few days, not just one day, the choice of using a several-day time frame does not spoil the detection. However, within a wider time-frame, the slight motion and spreading of the bloom over the time (caused by wind, for example) will also affect the bloom pattern in the retrieval output.

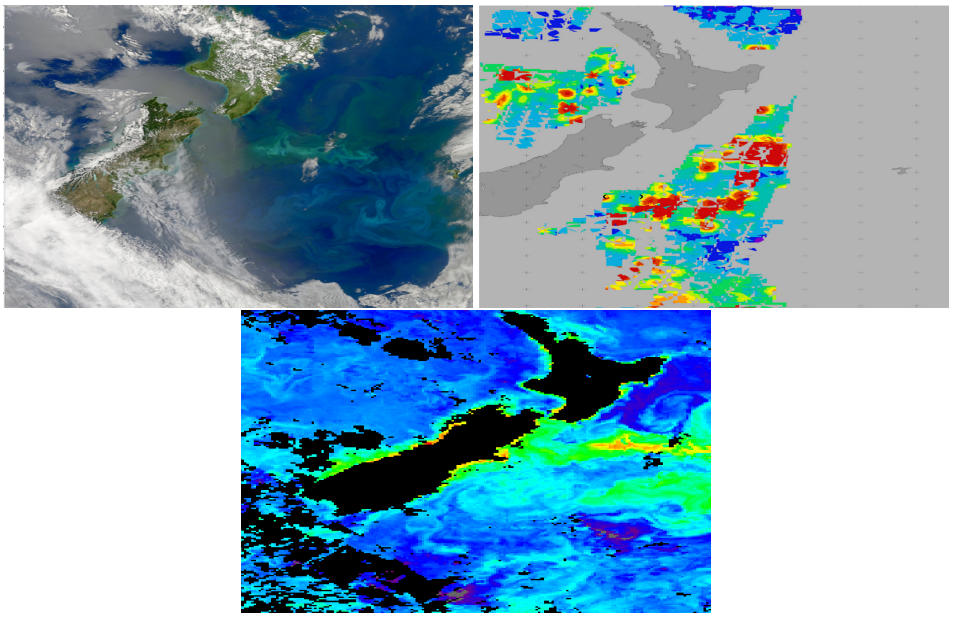

Figure 5.2: A case study of phytoplankton bloom detection by PhytoDOAS: the upper-left panel is a true-color image of MODIS sensor (reported by NASA on 23rd Dec. 2009) showing a coccolithophore bloom near Chatham island, on the eastern side of New Zealand. The upper-right panel depicts the PhytoDOAS retrieval of the coccolithophore *chl-a* for the same region over a period of two weeks (centered at 23rd Dec. 2009). The lower panel illustrates the distribution of MODIS-Aqua PIC for the bloom region as an 8-day composite (19 to 26 Dec. 2009).

Fig. 5.3 indicates another coccolithophore bloom detected by applying the PhytoDOAS *triple-target* method on SCIAMACHY data over the northern parts of the North Atlantic in August 2004. Regarding the fact that coccolithophore blooms are quite abundant in this oceanic region [Brown and Podesta, 1997; Balch et al., 1991; Holligan et al., 1993; Raitsos et al., 2006] and with respect to the pronounced high-valued pattern of PIC distribution on the respective area (lower-panel in Fig. 5.3), this bloom can be addressed as a coccolithophore dominated bloom. The pattern of the MODIS *chl-a* map (upper-left panel) coincide very well to the PIC pattern, confirming the dominance of coccolithophores in the bloom. Overall, the PhytoDOAS retrieval of this bloom (upper-right panel in Fig. 5.3) shows a very good agreement with the MODIS-Aqua products: both PIC and *chl-a*.

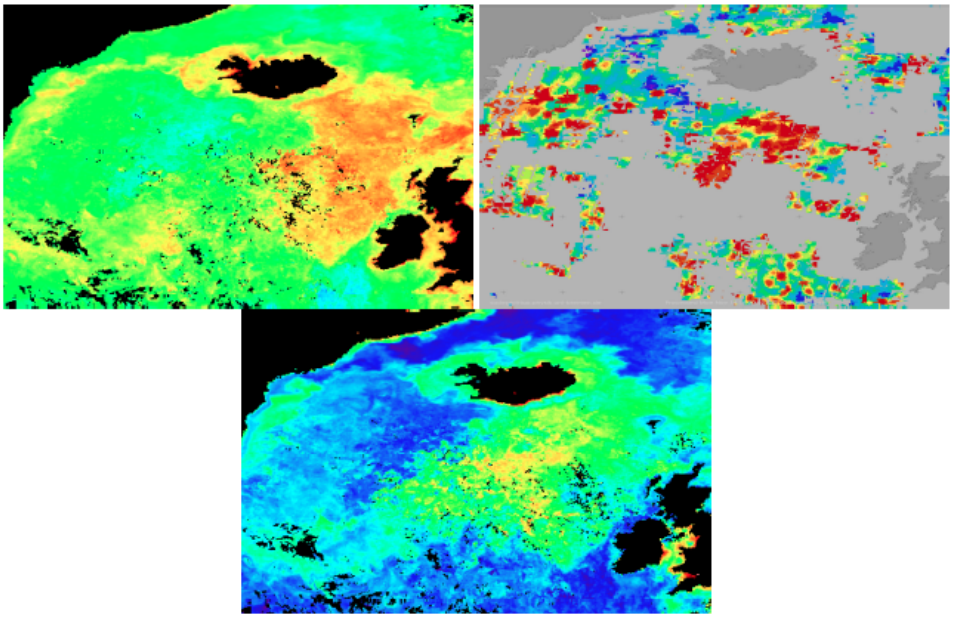

Figure 5.3: Detection of a coccolithophore bloom in the North Atlantic during August 2004 by PhytoDOAS (upper-right panel). The upper-left panel and the lower panel show the distributions of the MODIS-Aqua total *chl-a* and PIC conc. over the bloom period, respectively. All maps are confined to the following geographic borders: $2°W$-$42°W$ and $49°N$-$69°N$.

5.2.2 Selection of the study regions

To monitor the development of *coccos* blooms, regions of high occurrence were selected based on the following procedure: first, a global distribution of *coccos*, mapped by Brown and Yoder [1994a] and Brown [1995] was considered (upper panel in Fig. 5.4); secondly, eight years of global distribution of PIC, from MODIS-Aqua level-3 monthly products was monitored; and finally *coccos* field studies were analyzed [Brown and Podesta, 1997; Balch et al., 1991; Holligan et al., 1993; Raitsos et al., 2006; Painter et al., 2010; Garcia et al., 2011; Burns, 1977; Tilburg et al., 2002]. Based on these pre-investigations, three regions have been selected (lower panel in Fig. 5.4), located in the North Atlantic (south of Iceland), the South-west Atlantic (north of the Falkland Islands), and the South-west Pacific (south-west of New Zealand, surrounded by the Tasman Sea). For simplicity the regions were labeled as: *nAtl*, *sAtl* and *sPac*, respectively. The regions were been selected to be $10° \times 10°$ areas, which regarding their latitudinal distributions means almost the same area for *sAtl* and *sPac* and smaller for *nAtl*. As shown in Fig. 5.4 (the lower panel), on a background of the MODIS PIC product, two regions (*sAtl* and *sPac*) are located in the *Great Calcite Belt* [Balch et al., 2011], which is a great latitudinal belt of elevated PIC concentrations, containing over one-third of all global PIC. The *Great Calcite Belt* is located all the way around the Southern Ocean near the sub-Antarctic front and polar front (between about $30°S$ and $60°S$). In selection of these three regions, also the PhytoDOAS *coccos* monthly-mean *chl-a* (presented in Chapter 4) have been considered. Fig. 5.5 shows three sample coccolithophore blooms over the study regions, which have been detected as true-color images by different satellite sensors, which can be regarded as an evidence for the selection of these specific regions.

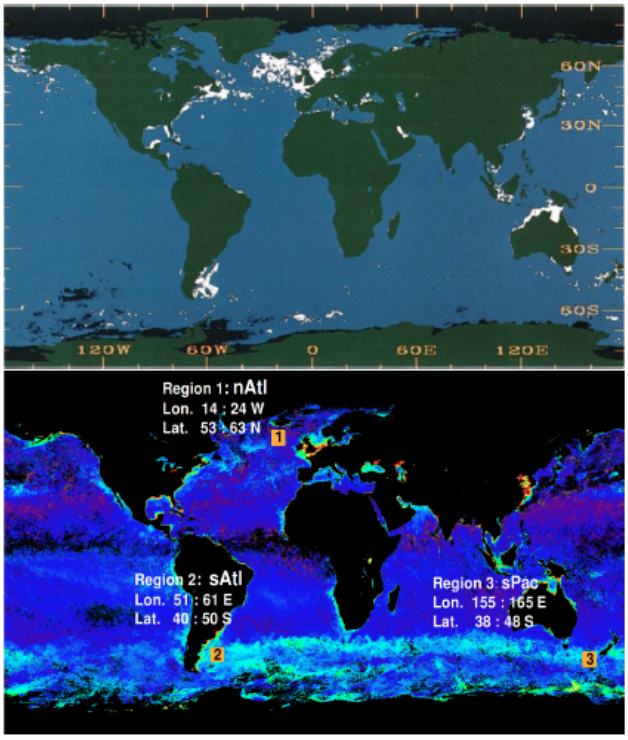

Figure 5.4: The upper panel depicts a coccolithophores climatology by [Brown and Yoder, 1994a] from CZCS imagery dating from Nov. 1978 to Jun. 1986. The regions of coccolithophore blooms are shown in white, containing only measurements with coverages more than $4800\,km^2$. The lower panel indicates the study regions chosen for monitoring the development of coccolithophore blooms. The regions were chosen based on several coccolithophore field studies reported in literatures, along with investigating the variations in global distribution of PIC through eight years data of MODIS-Aqua. For comparison purpose, the regions have almost the same areas.

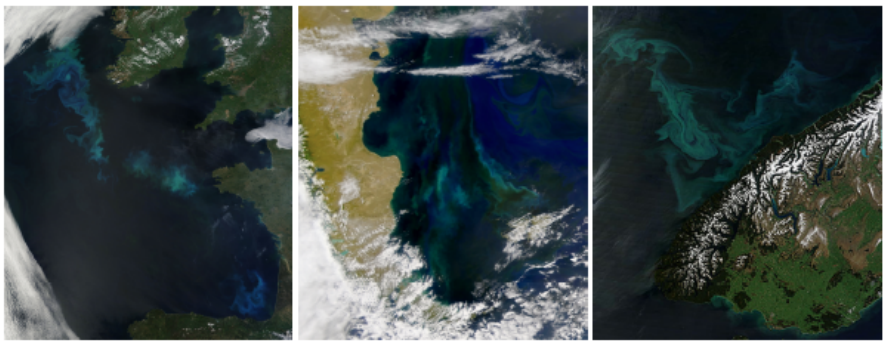

Figure 5.5: True-color images of coccolithophore blooms in selected regions: North Atlantic on 22 May 2010 by MODIS Aqua (left panel); Patagonian Shelf on 18 December 2003 by SeaWiFS (middle panel); and Tasman Sea on 9 November 2011 by MODIS Terra.

5.2.3 Satellite data and geophysical variables

PhytoDOAS *coccos* results for each selected region were retrieved from SCIAMACHY data from Jan. 2003 to Dec. 2010 (with the same setup as described in sec. 3.4). The information about SCIAMACHY sensor, providing PhytoDOAS with hyperspectral satellite data, was given in details in sec. 3.5. Also the two wavelength ranges of SCIAMACHY data used in this study and the specific usage of each of them in PhytoDOAS method were described in sec. 3.3.1.

To compare and evaluate the *coccos* retrieval results and to investigate their probable correlations with climate factors, four other satellite products were collected for the selected regions from Jan. 2003 to Dec. 2010 as follows: (1) total *chl-a* from ESA ocean-color dataset, GlobColour, providing merged data from three major ocean-color sensors: MODIS-Aqua, MERIS and SeaWiFS, with $4\,km$ grid resolution (for details see: `http://www.globcolour.info`); (2) PIC data from MODIS-Aqua level-3 products with $9\,km$ grid resolution (see details on MODIS web-page: `http://modis.gsfc.nasa.gov`); (3) sea surface temperature (SST) from Advanced Very High Resolution Radiometer sensor (AVHRR: `http://nsidc.org/data/avhrr`) with a $4\,km$ spatial resolution (from Pathfinder V5); and finally (4) surface wind-speed data derived from the Advanced Microwave Scanning Radiometer-Earth Observing System (AMSR-E) sensor, globally gridded at $0.25° \times 0.25°$ (more information at `http://remss.com`). The MLD data were obtained from Ocean Productivity (`http://www.science.oregonstate.edu/ocean.productivity/index.php`). For this data product, the MLD monthly data (after June 2005) are provided based on the MLD output of FNMOC (Fleet Numerical Meteorology and Oceanography Center). FNMOC's MLD is determined through the TOPS (Thermal Ocean Prediction) model by identifying the depth where the temperature is 0.5 degree lower than the value at the surface (the so-called isothermal layer depth, ILD). In general, apart from the high latitudes (above +,-70°), the IDL is a good approximation of MLD. For the period before July 2005, the MLD data were obtained from the Ocean Productivity merged data set from the SODA (simple ocean data assimilation) model. The grid resolution of the MLD monthly data is $\frac{1}{6}^{\circ}$ degree.

5.2.4 Further processing of the data

The data of the different parameters were represented as time series of monthly mean values within the same time period. PhytoDOAS results for all pixels within the selected regions were averaged for each month; MODIS-Aqua PIC data, AVHRR SST data and AMSR-E wind-speed data were directly collected as monthly-mean values; daily products of GlobColour total *chl-a* was converted into monthly mean values. Then, for each region, the time-series of all six parameters were built up from Jan. 2003 to Dec. 2010. In the post-processing of the PhytoDOAS retrieved data, two criteria for removing data-points of poor quality were applied: to filter out pixels with poor fit quality, only fit results with *Chi-Square*, χ^2, values below 0.001 were used and a threshold of pixel numbers was applied to the monthly-mean to remove data points that were averaged over an insufficient number of remaining pixels (within a month). The minimum number of pixels (per month) for considering a monthly mean as an acceptable point, was determined by building an occurrence histogram, with the number of pixels per month as the random variable. Taking a coverage less than 10% of total occurrences as the lower limit, the threshold value was ranging, depending on the region, from 40 to 90 minimum observations per month.

The final availability of the SCIAMACHY ground-pixels used for each region based on the above approach is shown in Fig. 5.6. This figure illustrates the number of ground-pixels per month (over the whole eight years), which have been processed in construction of the respecting time-series for each region. The white blocks correspond to those months, for which the data availability was too poor to be accounted in the process. Moreover, from Fig. 5.6 a pattern of

seasonal dependency can be seen in the data availability of the study regions. It means that the months of more acceptable ground pixels (with higher fit-qualities) are mostly residing in the local spring and summer, or blooming seasons. This fact can be assigned to the sensitivity of the PhytoDOAS method to the total available sunlight or to the direction of the solar radiation (solar elevation angle). On the other hand, the seasonal feature observed in the data has urged to calculate the linear trends of the retrievals (and other parameters) only over the seasonal months for each region (see sec. 5.3.3).

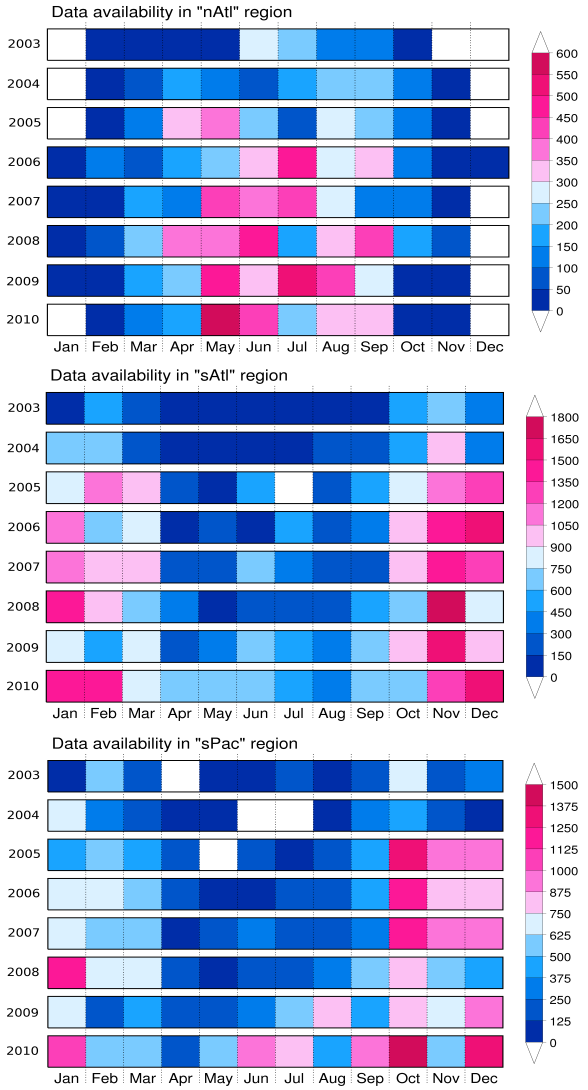

Figure 5.6: The SCIAMACHY data availability for the construction of the monthly time series from PhytoDOAS retrievals. The data availability is depicted separately for three study regions: *nAtl* (upper panel), *sAtl* (middle panel) and *sPac* (lower panel).

5.3 Results of PhytoDOAS coccolithophore blooms

5.3.1 Time series of biological and geophysical parameters

The time series from Jan. 2003 to Dec. 2010 of all parameters over the three selected regions *nAtl*, *sAtl* and *sPac* are shown in Fig. 5.7, 5.8 and 5.9, respectively. These time-series comprise monthly mean values of the following parameters: (a) *coccos chl-a* (denoted by *Ehux*) retrieved by PhytoDOAS, (b) GlobColour total *chl-a*, (c) PIC concentration from MODIS-Aqua, (d) MLD estimates provided by Ocean Productivity, (e) SST from AVHRR dataset, and (f) surface wind-speed from AMSR-E dataset. In the time-series of the PhytoDOAS *coccos* are some missing points, due to the post-processing of the retrieved data; i.e., the fit-quality filter (χ^2) and the average-quality condition (number of pixels per month). On the other hand, one has to keep in mind that our study is focusing only on the surface waters' phytoplankton phenology, even though the in-water light paths measured by PhytoDOAS cover mostly deeper ranges than surface water.

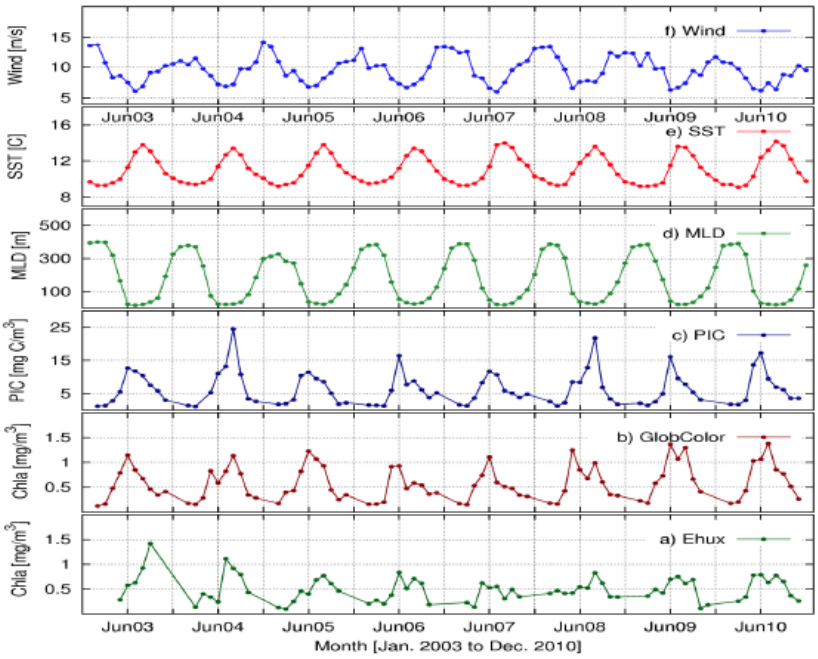

Figure 5.7: Time series of the six parameters monitored in *nAtl* from Jan. 2003 to Dec. 2010: (a) *coccos* [*Ehux*] *chl-a* conc. retrieved by PhytoDOAS; (b) GlobColour total *chl-a*; (c) MODIS-Aqua PIC conc.; (d) MLD from Ocean Productivity; (e) SST from AVHRR; and (f) surface wind-speed from AMSR-E.

Due to these gaps the *coccos* time-series, compared to the time-series of the other parameters, depict more artifact features, which must be distinguished from their natural irregularities. The main reason for this anomaly is that SCIAMACHY (primarily designed for atmospheric missions), compared to usual ocean color sensors, e.g., MODIS-Aqua, SeaWiFS and MERIS, has a very coarse spatial resolution. The characteristic of having large ground pixels makes its surface UV-visible data very sensitive to cloud contaminations, as compared to other sensors with high spatial resolutions. Therefore, the time-series of PIC, provided by MODIS-Aqua, and the time-series of total *chl-a*, obtained from GlobColour merged data, show very few gaps. However, there are still enough data points in the *coccos* time-series, for comparing *coccos* temporal variations with the other parameters.

In the time-series of the *nAtl* region (Fig. 5.7) all parameters show a clear annual cycle; how-

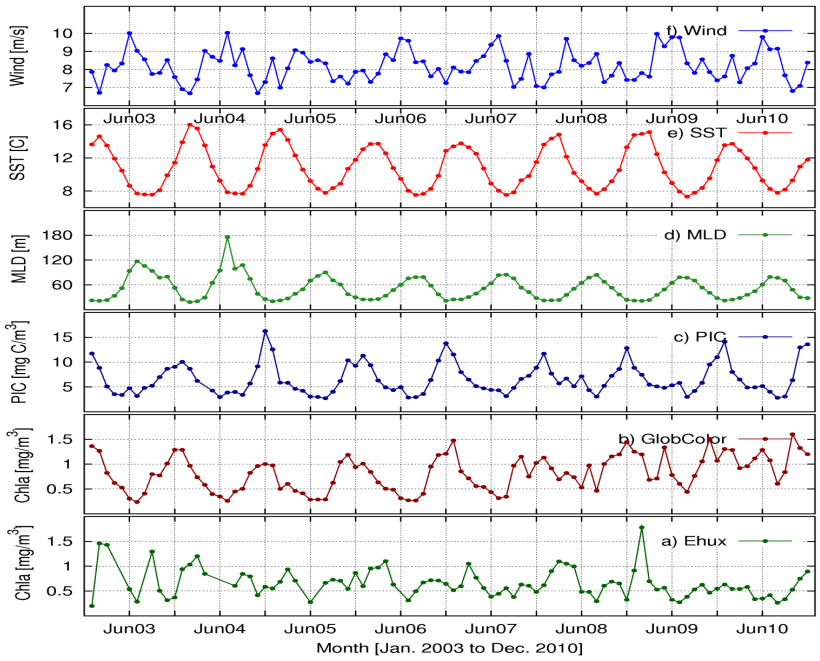

Figure 5.8: Time series as described in Fig. 5.7, but for the *sAtl* region.

ever, for some of the parameters (not for SST and MLD) the inter-annual cyclical periods of high intensities are deviating from one year to another; e.g., from 2008 to 2009 for *coccos* and PIC the period between the maxima is reduced to 10 months, while it is 11-14 for all other years (e.g. 2007 to 2008). However, for GlobColour total *chl-a* the intervals between successive maxima for the periods 2008/2009 and 2007/2008 are about 13 and 10 months, respectively. It can also be seen that the timing of the maximum conc. of *coccos*, PIC and total *chl-a* are positively correlated. These maxima are negatively correlated with the MLD, as they should be, because the rate of *coccos* growth increases rapidly with shoaling of MLD [Raitsos et al., 2006]. More precisely, all three phytoplankton-based time-series in Fig. 5.7 imply that the phytoplankton prosperity is associated with a rapidly decreasing MLD, and reaches its maximum when MLD begins its period of constant minimum. The North Atlantic is generally characterized by an extremely deep winter mixed layer, which causes very low phytoplankton activity in wintertime, which can be seen as well in Fig. 5.7. The phytoplankton and PIC maxima coincide with the high positive gradient of SST, i.e, SST peaks always appear delayed to the phytoplankton peaks, which is in accordance with the results of Raitsos et al. [2006]. Theoretically, it is expected that the maxima of the three phytoplankton-based time-series follow in a sequence as the time elapses: total *chl-a* followed by *coccos* and finally PIC, as *coccos* start growing when the necessary nutrients for the growth or the survival of other species are scarce [Margalef, 1978; Holligan et al., 1983]. On the other hand, the PIC concentration is expected to be proportional to the amount of *coccoliths*, which can be either attached to the living *coccos* or detached from them and suspended in the water, even after the disappearance of the *coccos*. However, this sequence could not be reproduced in our time-series, except for the year 2008. In fact, the peaks of total *chl-a* and PIC appear more or less at the same time, while *coccos* peaks often follow the two former peaks with a slight delay. This systematic behavior might be originated from the large monthly time interval used for averaging the retrieved products and setting up the *coccos* time-series (the lower subplots in Fig. 5.7, Fig. 5.8 and Fig. 5.9); one-month period is probably larger than the real, rather weekly, temporal rhythm of phytoplankton dynamics.

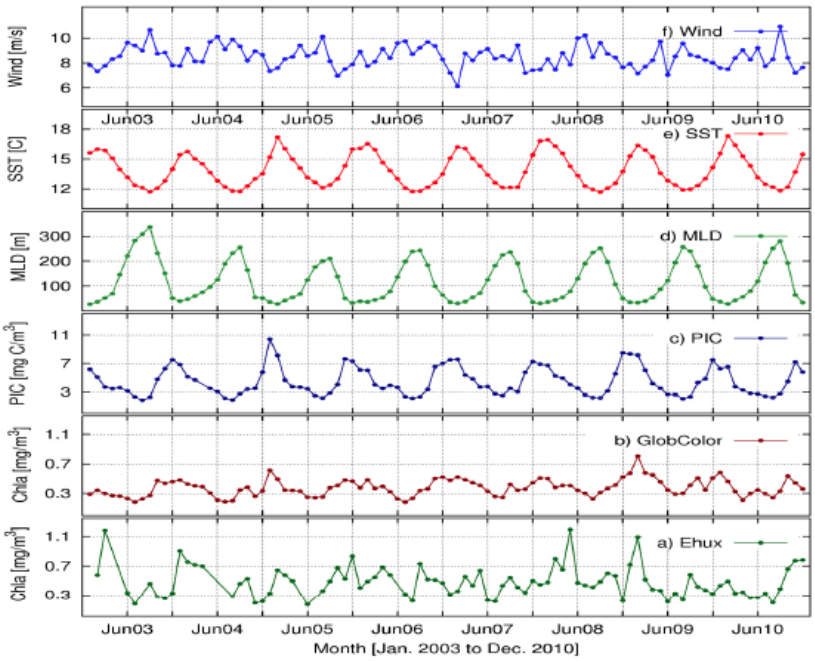

Figure 5.9: Time series as described in Fig. 5.7, but for the *sPac* region.

While the SST, the MLD, and also the PIC conc. show clear annual cycles in the regions of *sAtl* and *sPac* (Fig. 5.8 and Fig. 5.9), the annual patterns for *coccos* and total phytoplankton *chl-a* are much more irregular than in the *nAtl*. This can be explained by the very dynamic wind-speed patterns observed in *sAtl* and *sPac*. As surface wind-stress forces the vertical motion in the water column (in addition to the horizontal motions as surface waves), it is affecting the stratification and the nutrient regime. As the *coccos* are only a group of the phytoplankton it is expected that total *chl-a* would vary more smoothly than this specific PFT. Moreover, there are several other possible reasons for the irregularities observed in phytoplankton conc. in the *sAtl* region:

- The general circulation in the *sAtl* is influenced by the collision of two main currents: the Malvinas (Falklands) current, transporting northwards sub-Antarctic cold and fresh waters and the Brazil current, carrying southwards subtropical saline and warm waters [Gordon, 1989; Spadone and Provost, 2009](left panel in Fig. 5.9). The Brazil/Falklands confluence is an energetic and complex region of interaction and mixing of water masses [Brandini et al., 2000; Oliveira et al., 2009] and hence inducing high productivity, as well as influencing the usual patterns of seasonality. The biological implications of this circulation have been examined by Carreto et al. [1995] and in particular, high *chl-a* conc. have been observed during austral spring and summer in this region (e.g., Podesta and Esaias [1988])(right panel in Fig. 5.10).

- The *sAtl* is located at the eastern part of the Patagonian shelf, which is regarded as one of the richest areas of primary production [Bianchi et al., 2005, 2009; Schloss et al., 2007], and features recurring large *coccos* blooms [Longhurst, 1995; Painter et al., 2010]. The Patagonian shelf, between $38°S$ and $51°S$, is located southwest of the confluence zone and therefore is affected by that. Apart from that, according to hydrography observations and satellite imagery [Saraceno et al., 2004; Bianchi et al., 2005; Romero et al., 2006], there are two other factors affecting the hydrography of the Patagonian shelf: the *shelf break front*, which is a transition between the Malvinas current and shelf waters, existing in both winter and summer seasons (being stronger in the summer months) and the energetic

tidal fronts, with pronounced seasonal variability, causing the vertical stratification of water masses [Sabatini et al., 2004; Bianchi et al., 2005].

- The non-cyclic aerosol-load and dust transport from the Patagonian desert into the South Atlantic Ocean (atmospheric and riverine), affecting the phytoplankton productivity of the Patagonian shelf by changing the nutrient regime [Erickson et al., 2003].

- Due to the South-Atlantic Anomaly (SAA) most of satellite measurements are affected during their passages over parts of South-America and South-Atlantic (see Fig. 5.11). SAA is an area where the specific feature of the Earth's magnetic field (more precisely, of the Van Allen belt) allows charged particles and cosmic rays to reach to the lower altitudes of the atmosphere [Heirtzler, 2002]. The enhanced flux of energetic particles in this region expose the orbiting satellites to higher levels of radiation and thus causing malfunctioning. Although the SAA region lies roughly between latitudes $5°S$ and $40°S$, its precise shape, size and strength are not well known and also vary with the seasons (`http://sacs.aeronomie.be/info/saa.php`). Hence, our *sAtl* region, residing between $40°S$ and $50°S$, could be partly affected by SAA.

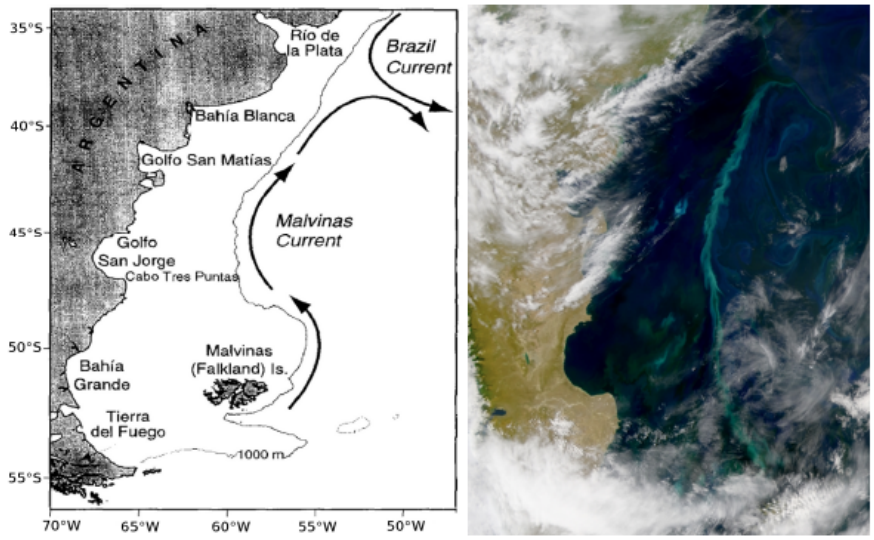

Figure 5.10: Left panel, taken from Brown and Podesta [1997], depicts the two main currents dominating the circulation of the offshore of the Patagonian shelf: warm Brazil current flowing southward along the continental margin and cold sub-Antarctic waters of the Malvinas current flowing northward along the shelf break. After collision at about $36°S$, both currents flow eastward toward the interior of the South Atlantic. Right panel, a SeaWiFS RGB image on Dec. 24 in 2004, illustrates a sample satellite imagery of phytoplankton activity in Patagonian shelf.

The high variations and anomalies seen in the *sPac* time-series, can be attributed to its location, which is surrounded by the Tasman Sea. The Tasman Sea is one of the fastest warming areas in the Southern Hemisphere ocean [Neuheimer et al., 2011; Ridgway, 2007], because of both, globally rising SST and specific local effects, such as the characteristic of the warm poleward waters of the East Australian Current (EAC) [Cai et al., 2005; Ridgway, 2007]. Moreover, large eddies occurring in the Tasman Sea have a great contribution to the vertical mixing within the upper ocean. This increased mixing effectively counteracts the winter stratification and results in a varying *chl-a* seasonal cycle [Tilburg et al., 2002]. In this sense, the seasonal cycle of *chl-a* in *sPac* should be pronounced, similar to the North Atlantic, which has very strong mixing. The

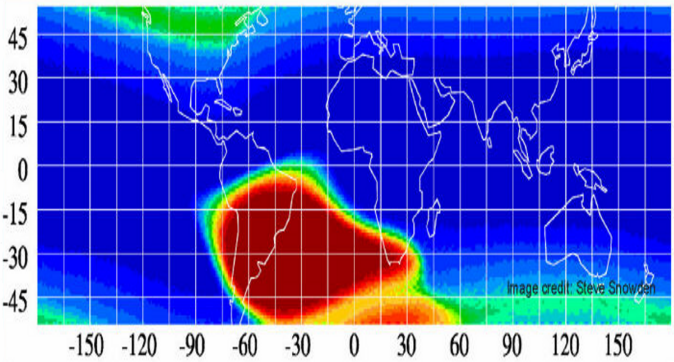

Figure 5.11: The region of the South Atlantic Anomaly (SAA), affecting the measurements of over-passing satellites by exposing them with higher levels of extra-terrestrial radiation. SAA is caused by the non-concentricity of the Earth and its magnetic dipole in the near-Earth region, where the Earth's magnetic field is weakest. Image credit: Steve Snowden.

seasonality in the time-series of GlobColour total *chl-a* for *sPac* is rather weak (less pronounced than in *coccos*). This observation suggests a demand for a regional improvement of the *chl-a* algorithms from ocean-color sensors, at least for the South-west Pacific.

In *sPac*, higher *chl-a* for *coccos* than for the total phytoplankton is observed. Further investigations showed why the PhytoDOAS *coccos* method is overestimating the coccolithophore *chl-a* (Fig. 5.9): studies by Burns [1977] and Rhodes et al. [1995] showed that in the Tasman Sea and also around New Zealand (i.e., in *sPac*) the dominant *coccos* species is varying between *E. huxleyi* and *Gephyrocapsa oceanica* (*G. oceanica*). Whereas, in this study the PhytoDOAS retrieval of *coccos* was based on the specific absorption spectrum of *E. huxleyi*. Fig. 5.12 illustrates the specific absorption spectra of these two *coccos* species, *G. oceanica* and *E. huxleyi*, which were measured on cultures obtained from the isolation of these species from natural samples in different regions. As illustrated in Fig. 5.12, in general, the specific absorption values of *G. oceanica* (red curve) are lower than the respecting values of *E. huxleyi*. In particular, the specific absorption of *G. oceanica* is much lower than the *E. huxleyi* spectrum used in the retrieval process of coccolithophores (blue curve). The reason is that the former species has, compared to *E. huxleyi*, much more *chl-a* pigment contents per cell. Hence, retrieving *G. oceanica* from a *E. huxleyi* specific absorption spectrum results in an overestimation of *chl-a* content. However, the similar absorption patterns of these two species ensures that the retrieval process can identify them as *coccos* target. All together, these samples show the spatial variations in phytoplankton absorption within the same phytoplankton group. This feature and the different photo-acclimation, also changing the specific phytoplankton absorption, can affect the result of the PhytoDOAS retrieval.

The ratios of the GlobColour total *chl-a* to the PhytoDOAS retrieved *chl-a* of *coccos* are depicted in Fig. 5.13 for the three study regions: The retrieved chl-a of *coccos* seem to be overestimated (which is associated with values less than one) in many months. Especially pronounced is this feature in the *sPac* region (lower panel). The reasons of the relatively higher coccos for this region have already been discussed above. However, in *nAtl* and *sAtl* (upper and middle panels in Fig. 5.13, respectively), there are alternating patterns in the months, when the *coccos chl-a* exceed the GlobColour total *chl-a*. In both regions the *coccos chl-a* exceed the total *chl-a* mostly after the summer bloom, i.e., after June in *nAtl* and for the austral summer in *sAtl* (except for the year 2010). Considering that these regions are characterized as high activity areas of *coccos* blooms [Holligan et al., 1993; Raitsos et al., 2006; Painter et al., 2010; Garcia et al., 2011], along with the fact that the large reflectance from coccolithophore-rich surface waters affect the performance

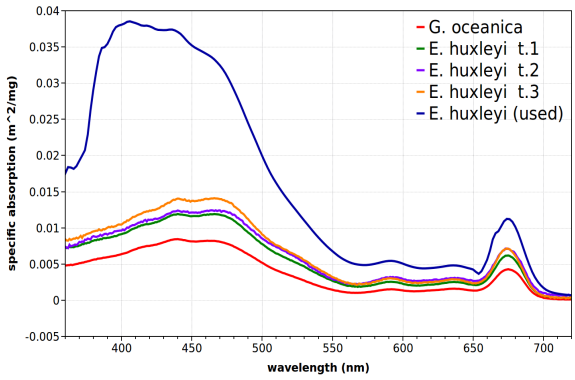

Figure 5.12: Specific absorption spectra of two different coccolithophore species obtained from cultures: the red curve corresponds to *G. oceanica*, which was isolated from the North Atlantic near the Portuguese coast; the other curves correspond to different cultures of *E. huxleyi*, isolated from the Tasman Sea in the South-west Pacific, from which the blue curve has been used in the retrieval process as the reference spectrum of coccolithophores.

of the standard *chl-a* algorithms [Gordon et al., 1988; Ackleson et al., 1988; Balch et al., 1989; Balch, 2004], the overestimation of *coccos* observed in Fig. 5.13 may be assigned to a proposed underestimation of *chl-a* during the *coccos* blooms for the GlobColour data set. This algorithm is based on reflectance ratios. The final validation of the *coccos chl-a* will be part of a future study by comparison of the PhytoDOAS data product to a combination of the above mentioned in-situ measurements of coccolithophores.

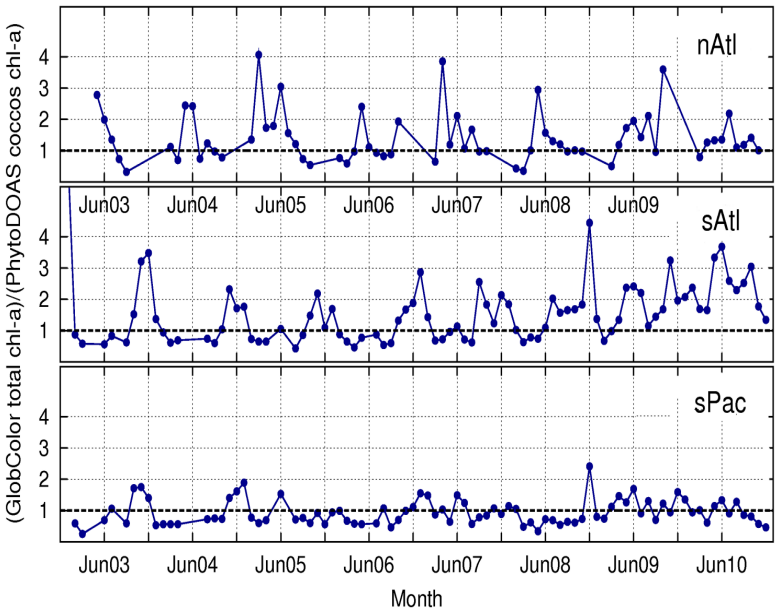

Figure 5.13: Ratios of the GlobColour total *chl-a* to the PhytoDOAS retrieved *chl-a* of *coccos* in three selected regions: *nAtl* (upper panel), *sAtl* (middle panel) and *sPac* (lower panel).

5.3.2 Interrelations between biological and geophysical parameters

To investigate the driving factors behind the development and degradation of *coccos* biomass, the correlation coefficients between PhytoDOAS *coccos chl-a* and all other parameters were computed (Fig. 5.14, left panels). Similarly, the correlation coefficients between PIC conc. and the other parameters were determined (Fig. 5.14, right panels).

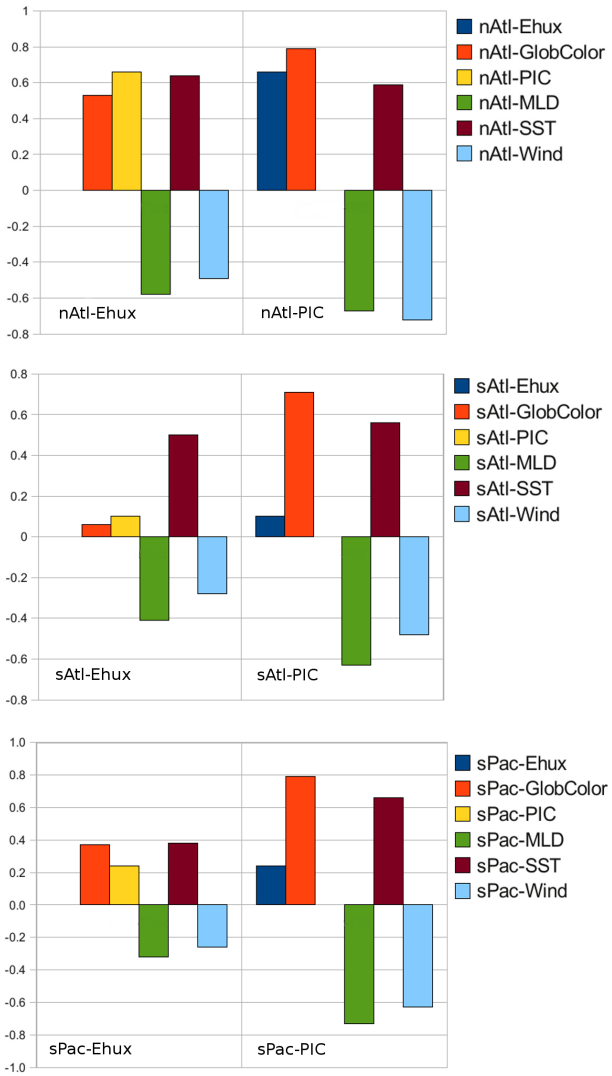

Figure 5.14: Correlation coefficients between the time series of PhytoDOAS *coccos* [*Ehux*] *chl-a* (left hand side of all panels) and the other parameters in the three studied regions: *nAtl* (upper panel), *sAtl* (middle panel) and *sPac* (lower panel). The same quantity is depicted on the right hand side of each panel between the time series of PIC and the other parameters for three regions, respectively.

In *nAtl* the retrieved *coccos* correlated positively with the total *chl-a*, PIC and SST, and negatively with MLD and surface wind-speed (upper left panel in Fig. 5.14). These results are in accordance with the reported dependence of *coccos* on raising SST (or high surface irradiances), shallow MLD (or shallow stratification) and non-turbulent waters [Tyrrell and Taylor, 1996; Nanninga and Tyrrell, 1996; Raitsos et al., 2006], respectively. The correlation pattern of PIC conc. (Fig. 5.14 upper-right panel) was very similar to the PhytoDOAS *coccos*, with close values of

correlation coefficients (except being higher correlated to the GlobColour total *chl-a* and being more inversely correlated to MLD). This similarity indicates the good agreement between the PhytoDOAS *coccos* and the MODIS-Aqua PIC in *nAtl*.

However, in *sAtl* the retrieved *coccos* were hardly correlated with total *chl-a* and PIC (Fig. 5.14, middle-left panel); possible reasons have been discussed before (sec. 5.3.1). The correlations of *coccos* with the geophysical parameters were weaker, compared to *nAtl*, but showing the same pattern. Moreover, despite the anomaly sources mentioned for this region, the correlation of *coccos* with SST, was similar to the situation in *nAtl*, which indicates again the vital importance of the rising SST (or high solar radiation) for occurring *coccos* blooms. The correlations of PIC with other parameters in *sAtl* (middle-right panel) showed the same pattern and levels as in *nAtl*, but weaker with surface-wind, which can be assigned to the complicated regimes of surface currents in this region as explained before.

In *sPac* (Fig. 5.14, lower-left panel) the correlations between *coccos* and total *chl-a* and PIC were slightly better than in *sAtl*, but there was less dependence on SST and MLD. The latter feature can be assigned to the dynamic surface-wind patterns observed in this region, which is associated with the presence of large eddies in the Tasman Sea. These eddies, originated from the separation of the EAC, migrate southwards into the Tasman Sea and cause regions of intense upwelling and downwelling [Tilburg et al., 2002], which results in turn in a strong seasonal cycle of phytoplankton activity with the associated anomalies. Moreover, the specific floor topography of the Tasman Sea, i.e., the presence of an important mid-ocean ridge [der Linden, 1969], and its effects on the surface currents and vertical motions of the water bodies should be kept in mind.

The highest correlation is observed between PIC conc. and GlobColour total *chl-a*. This is not surprising as the algorithms of these two products use the reflectance information from the same wavelength-bands and both products are obtained from the high spatially resolved satellite data (in contrast to the coarse spatially resolved SCIAMACHY data). Moreover, MODIS-Aqua itself is one of the three ocean color sensors used by GlobColour project to provide the merged data (the other two sensors are SeaWiFS and MERIS).

Since it is thought that the blooms of *coccos* usually follow diatom blooms, the time series of diatoms and *coccos* biomass in the selected study regions is shown in Fig. 5.15. As mentioned above, in the PhytoDOAS multi-target fit, *coccos* are simultaneously retrieved with diatoms and dinoflagellates. In all three regions *chl-a* of diatoms was always higher than *coccos*, as is expected in general [Goldman, 1993; Clark et al., 2002]. However, the patterns of the temporal variations of diatoms do not vary significantly from the counterpart patterns of *coccos*. This can be again assigned to the large time period for averaging the PhytoDOAS data, which is much longer than real time-frame of phytoplankton blooms. Due to this averaging, maxima of monthly *coccos* or diatoms' *chl-a* were probably smaller than the absolute maxima they reach during the blooms.

5.3.3 Annual patterns of phytoplankton development associated with the developments of geophysical variables in selected regions

Fig. 5.16 illustrates the linear trends of five parameters for eight years of data (from 2003 to 2010) for the three study regions. To reduce the effects of seasonality on the trend results, and to focus on the inter-annual variations of the parameters in phytoplankton prosperity seasons, only the months that cover the regional spring and summer were taken into account. Additionally, the ocean color winter time data only contain very few ground pixels per month which also increases the uncertainty to the monthly mean values. Hence, for *nAtl* six months from April to September, and for *sAtl* and *sPac* seven months from September to March were considered. Linear regressions were computed for the monthly mean data (Fig. 5.16 upper panel) and for the anomaly time-series data (Fig. 5.16 lower panel); here each data-point was obtained by subtracting the initial monthly

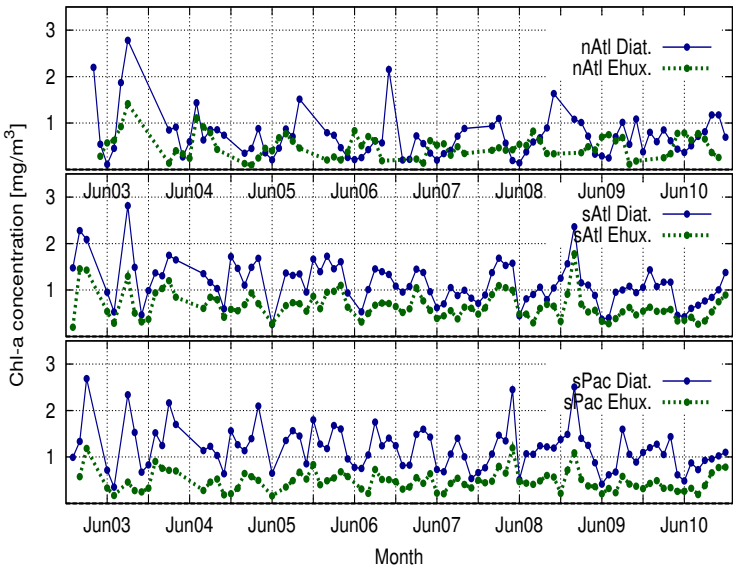

Figure 5.15: Times series of the PhytoDOAS diatoms (blue solid lines) and *coccos* (green dashed lines) *chl-a* in the three selected regions: *nAtl* (lower panel), *sAtl* (middle panel) and *sPac* (upper panel).

mean (e.g., Jun. 2004) from the climatological mean of that particular month (i.e., mean value of all June months over eight years). The respecting time series of the parameters are shown in App. 2 (see 6.3), including the simple and anomaly linear-trends for each region, respectively. We refer hereafter to these approaches as *simple trend* and *anomaly trend*, respectively.

No linear trends for MLD are shown in Fig. 5.16, because the MLD data, as modeled data, involve far more approximations than in the satellite-based retrieved products, making the comparison not suitable. Moreover, the order of magnitudes of the MLD trends are higher than the linear trends of the retrieved products, which could cause an illustration problem. Table 5.1 contains the MLD linear trends in three regions, which were calculated by both *simple trend* and *anomaly trend* approaches.

Table 5.1. MLD trends in selected regions

Region	*Simple trend*	*Anomaly trend*
nAtl	-0.660	0.050
sAtl	-0.219	-0.271
sPac	-0.081	-0.232

Considering the *simple trend* values (Fig. 5.16 upper-left panel), *coccos* grew negligibly in *nAtl* and *chl-a* decreased in the two southern regions by different rates; total *chl-a* increased in all regions, PIC decreased strongly in *nAtl* and *sAtl*, while it strongly increased in *sPac*. This may be caused by the strong SST-rise in the Tasman Sea [Tilburg et al., 2002], even though this SST rise was not observed in our *sPac* simple trend; however, the decreasing rate of SST in *sAtl* and *sPac* was clearly followed by the decrease of *coccos* and consistently, the rate of increase of SST in *nAtl* was associated, at a small rate, with the increase of *coccos*; the surface wind-speeds decreased in *nAtl* and *sPac*, while they slightly increasing in *sAtl*. Only in *nAtl* was the decreasing rate of wind-speed associated with an increasing rate of *coccos*. Considering that there is also no constant relationship between rates of change of wind-speed and PIC in the three regions, it can be inferred that in the studied time-scale of about one decade, the rate of change of *coccos* was not determined

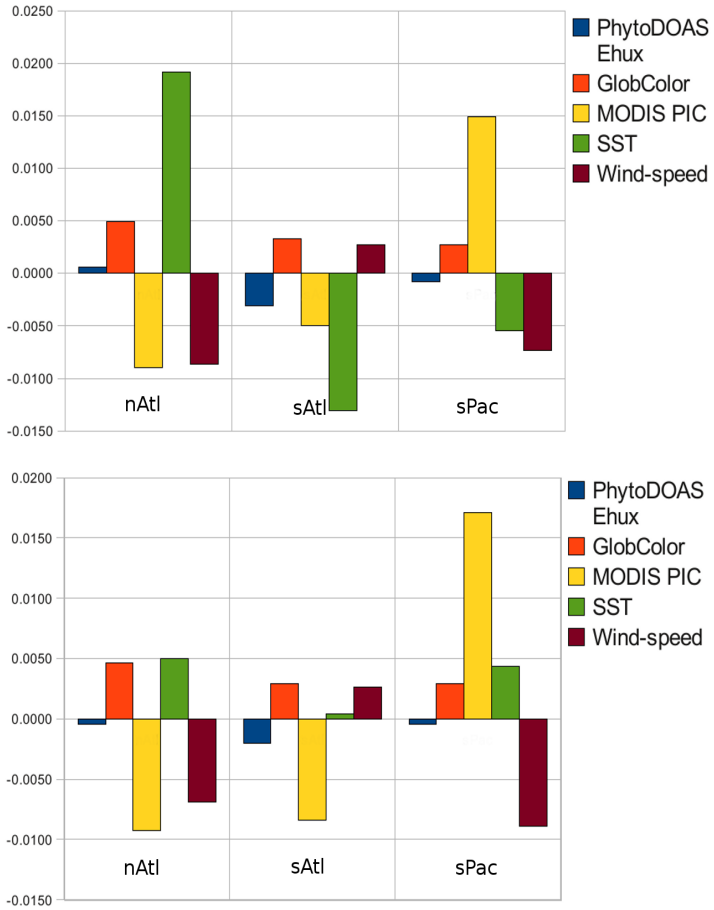

Figure 5.16: Linear trends of five monitored parameters over eight years data (2003 to 2010) in three selected regions: *nAtl* (left sections), *sAtl* (middle sections) and *sPac* (right sections). The upper panel shows the values of the *simple trends*, while the lower panel shows the values of the *anomaly trends*. In both cases only the regional spring and summer months were considered, which means: Apr. to Sep. for *nAtl* and Sep. to Mar. for *sAtl* and *sPac*. The charts do not include the MLD trends, due to their different ranges, which are (as modeled data) much higher in order of magnitude than the other parameters.

by the rate of wind-speed. Comparing the values of the *simple trend* with the *anomaly trend* values (Fig. 5.16 left panel), both showed similar results. Only the SST anomaly trends were different, especially in *sAtl* and *sPac* where the trends were even reversed. To summarize, the results were comparable and the anomaly trend was more appropriate because it removed the seasonal effect.

5.3.4 Climatological analysis

Fig. 5.17 illustrates the climatology curves for the corresponding six parameters in the three selected regions. Each data-point here depicts the mean value of a certain month over eight years' data of the respective time series. In nAtl, the *coccos* reached their maximum in Aug., whereas in *sAtl* and *sPac* two maxima were reached annually, a smaller one in austral spring (between September and October) and a higher one in austral summer (between February and March). The occurrences of two *coccos* blooms annually in the Southern Hemisphere has been reported before [Balch et al., 2011]. In *sPac* these maxima were not as pronounced, showing another weak maximum in May. This may be caused by the effect of large eddies existing in the Tasman Sea. However, the *coccos* maximum in austral spring in *sPac* was also observed by studying SeaWiFS data [Tilburg et al., 2002].

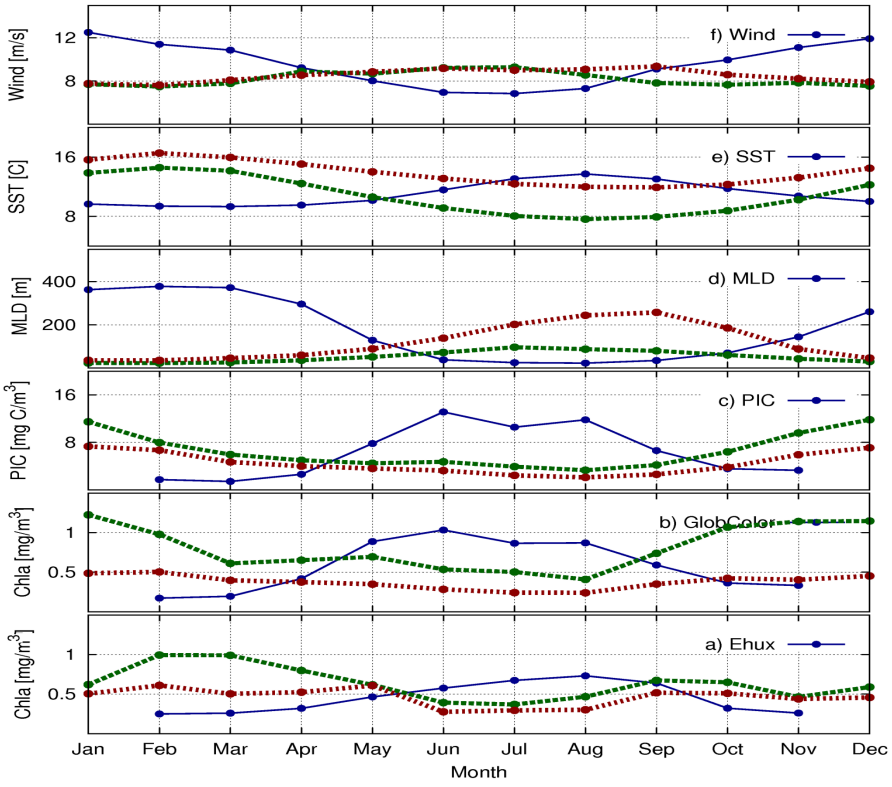

Figure 5.17: Climatology curves of all monitored parameters in three selected regions. Each subplot contains the climatologies of a certain parameter in three regions, which are denoted as follows: *nAtl* (blue line), *sAtl* (green dashed-line) and *sPac* (red dashed-line). The subplots have been arranged in the same order as before: (a) *coccos chl-a* conc.; (b) GlobColour total *chl-a*; (c) PIC conc.; (d) MLD (e) SST, and (f) surface wind-speed.

The GlobColour total *chl-a* showed an annual peak spreading over spring and summer, with two weak shoulders in *nAtl* (higher in June and a smaller in August), one wide peak in *sAtl* from October to January and only a minor peak in *sPac* from October to February. These results in *nAtl* and *sAtl* suggest that the *coccos* are the dominant phytoplankton group succeeding the main

bloom in late summer, which again supports the argument that *coccos* are favored when nutrients are depleted. However, the almost flat curve of GlobColour total *chl-a* in *sPac* is not consistent with SeaWiFS results presented in Tilburg et al. [2002] for the Tasman Sea. MODIS-Aqua PIC showed five months (May to September) of enhanced conc. in *nAtl* with two pronounced shoulders in Jun. and Aug., coinciding temporally with the maxima of GlobColour total *chl-a*, while only the latter peak was coinciding with the *coccos* annual maximum. This may indicate that either during the first total *chl-a* peak (in June) *coccos* were contributing significantly to the biomass and the PhytoDOAS algorithm is underestimating the *coccos chl-a*, or the PIC algorithm is partly incorrect in this region. The PIC climatology curves in *sAtl* and *sPac* varied quite smoothly (similar to each other), with a peak in Dec./Jan., which is more pronounced in *sAtl*. The patterns of PIC climatology in these regions followed the GlobColour total *chl-a* between March and October. The climatology curves of MLD, SST and wind-speed clearly supported the expected geophysical conditions for the formation of *coccos* blooms.

Fig. 5.18 provides a partial comparison of the above climatology, particularly in *sPac*, with other source based on the study done by Tilburg et al. [2002]. The left panel in Fig. 5.18 compares the MLD results for the Tasman Sea ($37°S$-$42°S$, $150°E$-$165°E$) and the North Atlantic, both obtained from Levitus and Boyer [1994]. The right panel depicts the monthly mean *chl-a* of SeaWiFS from 1998 to 2000 for the eastern and western parts of the Tasman Sea [Tilburg et al., 2002].

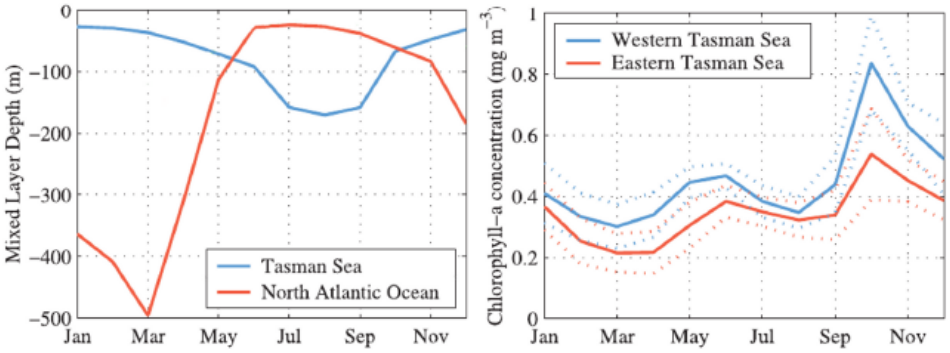

Figure 5.18: Left panel: seasonality in the mixed layer depth for the Tasman Sea and the North Atlantic based on the World Ocean Atlas [Levitus and Boyer, 1994]. Right panel: seasonal variation in sea surface *chl-a* over the eastern and western Tasman Sea, averaged from three years of SeaWiFS data (1998-2000). Here both western and eastern parts of the Tasman Sea have their latitudinal range between $37°S$ and $42°S$, but their longitudinal ranges are ($150°E$- $157°E$) and ($158°E$- $165°E$), respectively. Both figures have been taken from Tilburg et al. [2002].

By comparing the climatology curves for *sPac* in Fig. 5.17 with Fig. 5.18, it can be seen that the MLD maxima have the same magnitude (around 200 m) and almost the same period (from July to September) in both methods. (The accordance between two MLD methods can also be seen in the North Atlantic, where both of them show a deep winter mixed layer of $400\,m$ and $500\,m$ in March). On the other hand, while for *sPac* our climatology indicates a non-sharp peak of *Ehux* in September, October and November (with a maximum of about $0.5\,mg\,m^{-3}$ *chl-a* in October), the SeaWiFS results for the eastern and western parts of the Tasman Sea show sharp maxima of 0.5 and $0.8\,mg\,m^{-3}$ (both in October), respectively. The common value of *chl-a* peak ($0.5\,mg\,m^{-3}$) between SeaWiFS results of the eastern Tasman Sea and coccolithophore retrieval in *sPac* can be attributed to the fact that the *sPac* region ($38°S$- $48°S$ and $155°E$- $165°E$) has almost half of its area in common with the eastern Tasman Sea.

5.4 Conclusions of bloom study

We studied the developments of coccolithophore and total phytoplankton blooms and PIC conc. in three selected regions from Jan. 2003 to Dec. 2010 with satellite data. The time series results of these three phytoplankton-based products reveal the seasonal bloom cycles in a regular order with fairly good accordance to each other. In the *nAtl* region one *coccos* maximum was regularly observed in the summer, while in the *sAtl* and *sPac* regions two maxima in austral spring and summer occurred. The maxima for total *chl-a* and PIC conc. were during the same time period, but in both hemispheric regions only appeared once per year over a longer time period (4-5 months). The results show that the *coccos* blooms generally dominate the total phytoplankton maxima in late summer (August/September in *nAtl* and February/March in two other regions). In the *nAtl* and *sAtl* regions the maximum concentrations are comparable for all three parameters, while they are much lower ($70-50\%$) in the *sPac* regions. Comparisons to time series of geophysical parameters clearly show that the phytoplankton growth is related to shallow MLDs, low wind-speed, and high and sharp-rising SSTs.

Overall, the accordance of the three ocean color data products was better in *nAtl*, as compared to *sAtl* and *sPac*. As a general statement, it can be inferred that even though the seasonality well-known pattern is also evident in *sAtl* and *sPac*, but at the end the regional geophysical conditions are the factors that determine to what extent the phytoplankton growth will follow (or deviate from) the typical seasonal pattern. For instance, in both *sAtl* and *sPac*, the time series of wind-speed show high irregularities, compared to that of *nAtl*. This can partially explain why the time series of PhytoDOAS *coccos* in *sAtl* and *sPac* are not as regular as in as regular as in *nAtl*. The major environmental factors affecting the Patagonian shelf and the Tasman Sea have been briefly mentioned, in order to address the possible causes of turbulent and mixing effects in *sAtl* and *sPac*, respectively. The specific regional characteristics in *sAtl* and *sPac*, probably cause effects in smaller time scales than a month. However, our time series study had to be limited to the monthly resolution because of the coarse spatial resolution and limited global coverage of the available hyper-spectral satellite data used for the PhytoDOAS *coccos* retrieval. For better analysis and interpretation of the results, more investigations on the geophysical parameters ruling the regional climate, as well as on local biological conditions must be done for each region. For instance, due to the importance of light for the formation of *coccos* blooms [Nanninga and Tyrrell, 1996], the variation in solar radiation should be included (e.g., regional time series of water leaving radiance at $555\,nm$, as referred by Raitsos et al. [2006]). The regional variations of nutrient regime, especially phosphate and nitrate, using appropriate modeled data is the other supplementary work to do. Regional adaptations of the PhytoDOAS *coccos* retrieval should account for the spatial variations in specific absorptions with respect to the dominating *coccos* species. In general, to avoid the uncertainties associated with the spatial variations in phytoplankton absorption, an alternative approach would be to establish a multi-regional PhytoDOAS retrieval, using different sets of PFTs' absorption spectra, representing the main regions. For this purpose, the biogeographical provinces presented by Longhurst [1998] could provide a good criterion for dividing the world oceans into the regions.

Chapter 6

General conclusions and Outlook

6.1 Summary

Current algorithms of total phytoplankton biomass do not consider the biodiversity of phytoplankton as different taxonomic and/or functional groups, thereby containing uncertainties, to different extents. On the other hand, the well-known biogeochemical impacts of phytoplankton functional groups make it important to retrieve their global distributions, beyond the total biomass. PhytoDOAS is a method to retrieve the biomass of phytoplankton functional types (PFTs) using hyperspectral satellite data. This study was aimed to improve the PhytoDOAS method for retrieving more PFTs than the two types, which had been successfully performed by Bracher et al. [2009] (i.e., diatoms and cyanobacteria). Overcoming the spectral correlation between absorption spectra of target PFTs, a result of their common absorption pigments, has been the major challenge to achieve the improvement of PhytoDOAS. In this study, two inter-related approaches -still under development- have been used to overcome the correlation effects:

- *fourth-derivative analysis* for the detection of tiny spectral differences between PFTs' spectra, and
- simultaneous fit of certain set of PFTs in each PhytoDOAS process, referred to as *multi-target fit*.

Based on the *multi-target* approach (applied to SCIAMACHY data), coccolithophores, dinoflagellates and diatoms have been simultaneously processed over a wavelength window ($429-521$ nm), determined by the *fourth-derivative analysis* [Aguirre-Gomez et al., 2001]. Likewise, the set of phytoplankton targets used in the *multi-target* fitting has been specified by using a fourth-derivative analysis. Although, in each step of the procedure, we have tried to reduce the overall fit-residuals. The improvement process also included the comparisons of the retrieved PFTs with available satellite products and modeled data, which are (to some extent) appropriate for this purpose (in the case of coccolithophores, detection of some reported blooms has been also used to test the respective retrieval). Using this modification, the global *chl-a* distributions of coccolithophores, dinoflagellates and diatoms have been obtained for eight years of SCIAMACHY data (2003-2010), to serve as a PFT-dataset (e.g., to be used as monthly mean *chl-a*). The monthly and annual results for 2005 and 2008 have been presented in this thesis (in Chapter 4 and App.1, respectively). The improved method was also applied for studying the dynamics of phytoplankton blooms in selected coccolithophore rich areas over an 8-year period. In this case-study application, referred to as coccolithophore "bloom study" in the text, the environmental impacts on the phytoplankton growth has been investigated. More precisely, coccolithophore results, along with two other bio-optical satellite products (total *chl-a* and PIC), have been compared with three geophysical parameters

(SST, MLD and wind-speed) as monthly mean time series (the descriptions and results are given in Chapter 5). Some anomalies seen in the results were addressed to the specific environmental features of respective regions.

6.2 General conclusions

The findings of our study demonstrate that PhytoDOAS method can be successfully applied to hyperspectral satellite data to achieve information of PFTs' biomass; although some uncertainty still remains in the retrieval phase that can be accounted for by factors such as the spatial variation in the absorption spectra. It should be noted that this product is based on a new method, mostly independent from biological a priori data, as opposed to the standard ocean color products. This retrieval method can be reliably used for remote identification of coccolithophores, along with diatoms and cyanobacteria, on global and regional scales. Coccolithophore retrievals can be used, for instance, to track its bloom developments in the global ocean, which is important due to the biogeochemical impacts of this functional type. For dinoflagellates, the evaluation of results has not been so far done, due to the lack of any satellite-based or modeled data for comparison, and also due to the current limitations of validating PhytoDOAS results with in-situ data. The latter problem can be described as follows: as phytoplankton in-situ data are spatially scattered (no uniform coverage) and temporally confined to the limited time-frames (for each set of measurements), it is too difficult to collocate them with the SCIAMACHY-based retrievals, which have large ground pixels ($30 \times 60\, km^2$) and a long repeat cycle (35 days). Moreover, in-situ data do not cover all existing PFTs (at the time of measurement) in the same manner. For instance, in the case of coccolithophores, in-situ data either only consider the large cells (in microscopic techniques) or present also other haptophyte species besides coccolithophores (in HPLC-based and flow-cytometric data). Therefore, the coccolithophore group can not be observed properly through in-situ measurements.

Nevertheless, the PhytoDOAS coccolithophores were overall in a good agreement with PIC conc., which is a well-known bio-optical proxy for coccolithophores. The results also were highly consistent with the repeated observations of the North Atlantic's large coccolithophore blooms, as well as with the hypothesis of the *Great Calcite Belt* [Balch et al., 2011]) in the Southern Ocean. In the latter case, the very good coincidence of PhytoDOAS coccolithophores with the MODIS PIC conc. (in a large horizontal band between $\sim 30°S$ and $\sim 60°S$) implies that the semi-permanent elevated PIC observed in this region by MODIS-Aqua, can be a result of elevated coccolithophore populations. The importance of this coincidence (which was also observed in other regions) is that the retrieval algorithms used by the two methods (PhytoDOAS and MODIS-Aqua's PIC) are completely different.

Based on the results of the regional bloom study, carried out to investigate the phytoplankton dynamics, a seasonality's characteristic pattern was not observed pronouncedly in two regions of our three selected regions, despite the fact that the region located in the North Atlantic showed very good accordance. The observed irregularities were assigned to the known geophysical characteristics of the respective regions. Accordingly, it can be inferred that the regional geophysical conditions are important factors that determine the extent to which phytoplankton growth follows its typical seasonal pattern. For instance, in the two regions, where deviations were observed, the time series of wind-speed indicate high irregularities, compared to the region located in the North Atlantic. Moreover, these results also confirm the studies that address uncertainties in ocean color (total) *chl-a* algorithms for regional levels (e.g., Lee and Hu [2006]). More precisely, the outcomes of the coccolithophore bloom study (in this work) suggest that in coccolithophore rich areas, the total *chl-a* algorithms underestimate phytoplankton *chl-a* contents. However, to gain

more confidence, these results should be completed by further time-series studies in other regions of particular interest (e.g., Bering Sea or appropriate areas located in the *great calcite belt*). This is also a necessary step to assess the overall global picture of coccolithophore distributions and dynamics. For instance, the linear-trend estimations of the parameters, represented by the studied regions, seem to be inconsistent with each other, which can be due to the fact that an 8-year period is too short for a trend analysis. Therefore, taking new regions into account can be of help to find common behaviors.

The bloom study also showed that diatoms and coccolithophores can widely exist in the same oceanic areas at a certain time frame. This is an initial confirmation of a well-known hypothesis of the phytoplankton succession, implying that coccolithophore blooms follow diatom blooms and their fast growth in nutrient depleted waters (e.g., Lochte et al. [1993]). However, to show the precise succession, the current monthly-mean time series must be replaced by a weekly-mean time series, which is not possible with SCIAMACHY data; because on a small regional scale, narrowing the time frame leads to the loss of hitting orbits and hence, lowers the available ground pixels. Applying PhytoDOAS to the data of upcoming hyperspectral satellite sensors (e.g., the Sentinel-5-Precursor, planned to launch in 2014, with $7 \times 7\,km^2$ pixel size and global coverage within two days) will allow the weekly-based monitoring of such phytoplankton blooms dynamics.

Taken together, this study suggests that the PhytoDOAS method is potentially an alternative to retrieve the total phytoplankton biomass from the satellite data with higher accuracy, by summing up *chl-a* contents of all PFTs (to represent total *chl-a*). For this purpose, global distributions of major PFTs should be determined more precisely (spatially and quantitatively), demanding further improvement of the method, as well as more PFTs to be taken into account (especially *Phaeocystis sp.*, which globally has a significant contribution to the phytoplankton biomass). This step provides a more reliable dataset of PFTs global distributions, which is highly needed in several research fields; e.g., in modeling of global biogeochemical cycles.

6.3 Future directions of the study

There are further steps to proceed with the improvement of PhytoDOAS, as well as to expand its applications, all can be regarded as the outlook of this study:

- The quality of the PhytoDOAS retrieval has to be improved by performing further tests with current PFT targets, as well as combining current method with any other approach, which might be helpful to overcome the strong spectral correlations. Introducing more PFT reference spectra into the retrieval (especially in a regional-based application) can also be effective for further improvement. The final modified PhytoDOAS can be applied to the whole set of SCIAMACHY data (since Aug. 2002) to update the PFT-dataset.

- All PFT retrievals must be validated with available collocated HPLC-based in-situ measurements of the target PFTs. For this validation purpose, due to the current problem of collocation, the first task would be to find a solution to match the SCIAMACHY large pixels with the in-situ point measurements, in order to take advantage of all relevant field measurements (e.g., Continuous Plankton Recorder, CPR). Particularly, the results of coccolithophores shall also be compared to *chl-a* conc. of haptophytes, extracted from HPLC pigment analysis. Validation of results by in-situ data is necessary for the further improvement of PhytoDOAS.

- Since absorption spectra of phytoplankton functional types and also of specific species show

some spatial variability over the global ocean (Bricaud et al. [1995]), one of the main future tasks is to obtain and represent PhytoDOAS retrievals on a regional basis. Doing this task requires separate applications of PhytoDOAS to different ocean biogeochemical provinces (e.g., based on Longhurst [1998]; see Fig. 6.1), for each of which the input phytoplankton absorption spectra must be extracted before from the in-situ measurements in that province.

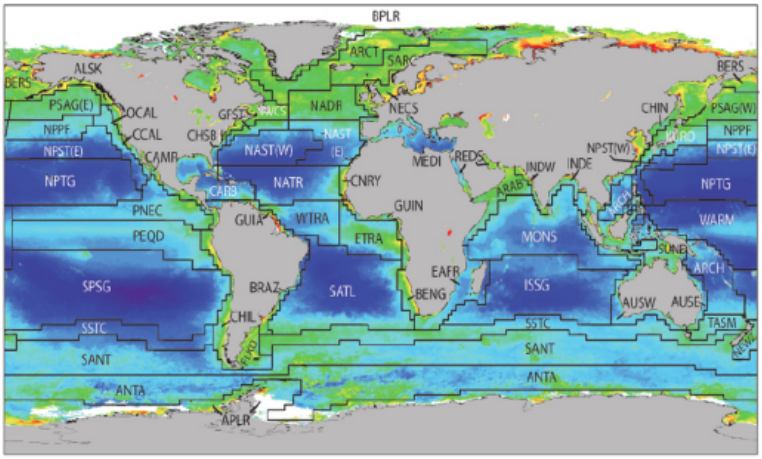

Figure 6.1: Longhurst ocean biogeochemical provinces, based on circulation patterns, nutrient regimes, light conditions, the bathymetry and other regional factors affecting the phytoplankton response to physical forcing. Acronyms of the provinces and respecting definitions are detailed in Longhurst [1998].

- A radiative transfer model, which couples ocean with the atmosphere can be very helpful for further improvement to PhytoDOAS. SCIATRAN, a software package developed by Rozanov et al. [2002], which incorporates a radiative transfer model and a retrieval algorithm, is a powerful tool for performing this task. Using SCIATRAN two types of investigation can be conducted: (a) to examine the relation between phytoplankton concentration and absorption fit-factor (initial output of PhytoDOAS), which has been extracted from an empirical approach and mediated by the light path-length in water; (b) to examine the impact of different PFT constituents of water on the backscatter radiation of the ocean, which is an alternative approach to test the effects of spectral correlations. In both estimations the radiance output of SCIATRAN at the top of the atmosphere is processed by PhytoDOAS as the satellite input of the Earth's backscatter radiation.

- Furthermore, a climatology on the PFT distribution can be developed based on the PhytoDOAS SCIAMACHY results. The resulting data set will be useful for various marine biogeochemical and ecosystem studies and models, as well as being a potential basis for a specific phytoplankton absorption climatology based on the global spatially and temporally resolved PFT distribution. This can be applied to improve the common ocean color *chl-a* retrievals. It could also help to improve the global estimates of trace gas emissions resulting from oceanic phytoplankton.

Appendix

App. 1. PhytoDOAS retrievals of target PFTs in 2008

This section of Appendix contains supplementary results to Chapter 4, including PhytoDOAS' PFT retrievals in 2008, which are shown as monthly mean maps on a global scale.

App. 1.1. Monthly mean chl-a of the retrieved PFTs

The maps shown in Fig. 6.2 and Fig. 6.3 are PFTs' monthly mean *chl-a*, retrieved by the PhytoDOAS *triple-target* mode from the SCIAMACHY date 2008. The respective results for the year 2005 have been presented in section 4.1.1.

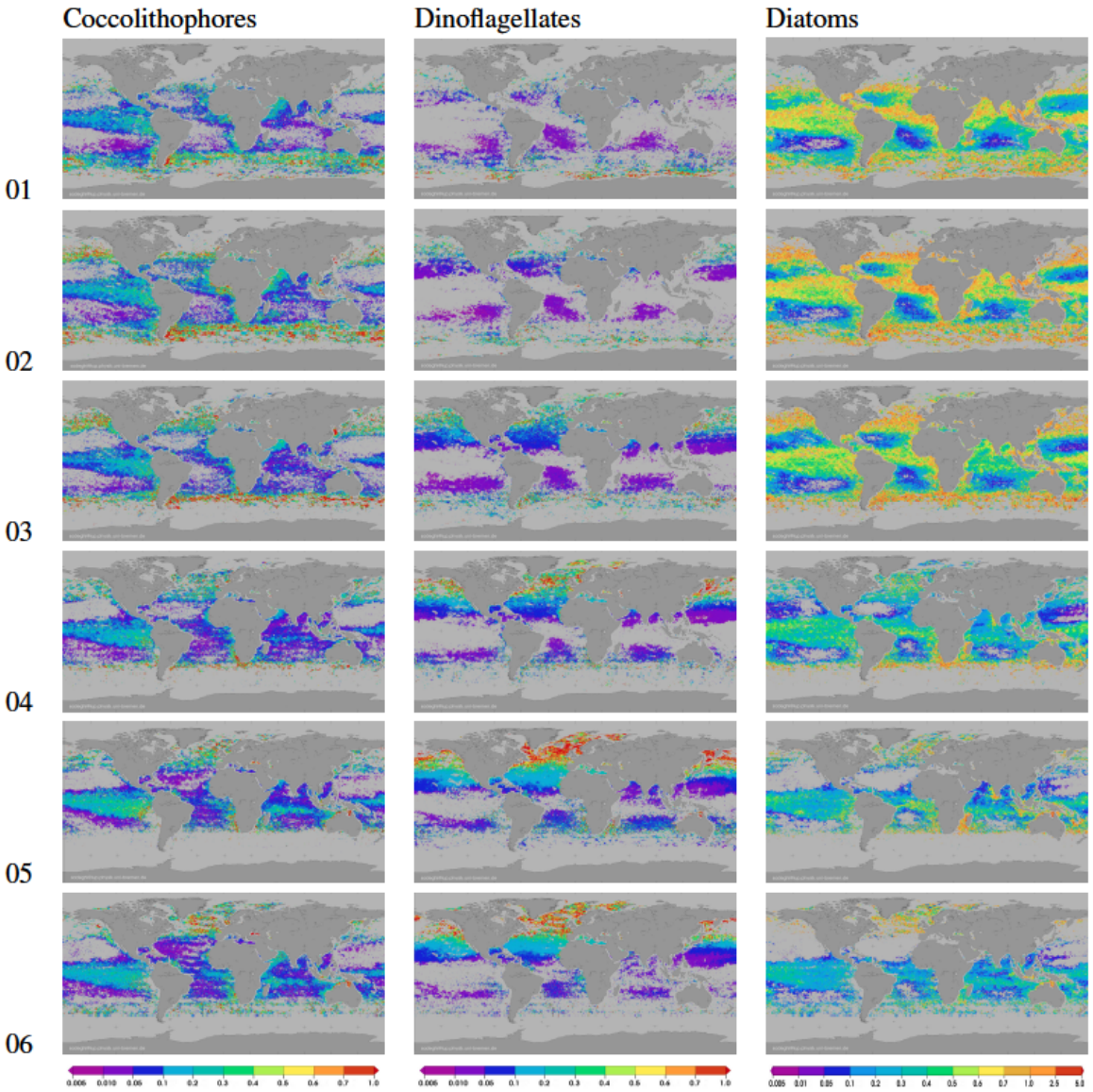

Figure 6.2: Monthly mean *chl-a* maps (in $[mg\,m^{-3}]$) for target PFTs retrieved by PhytoDOAS. The results have been obtained by applying the PhytoDOAS *triple-target* fitting to the SCIAMACHY data for the first half of 2008.

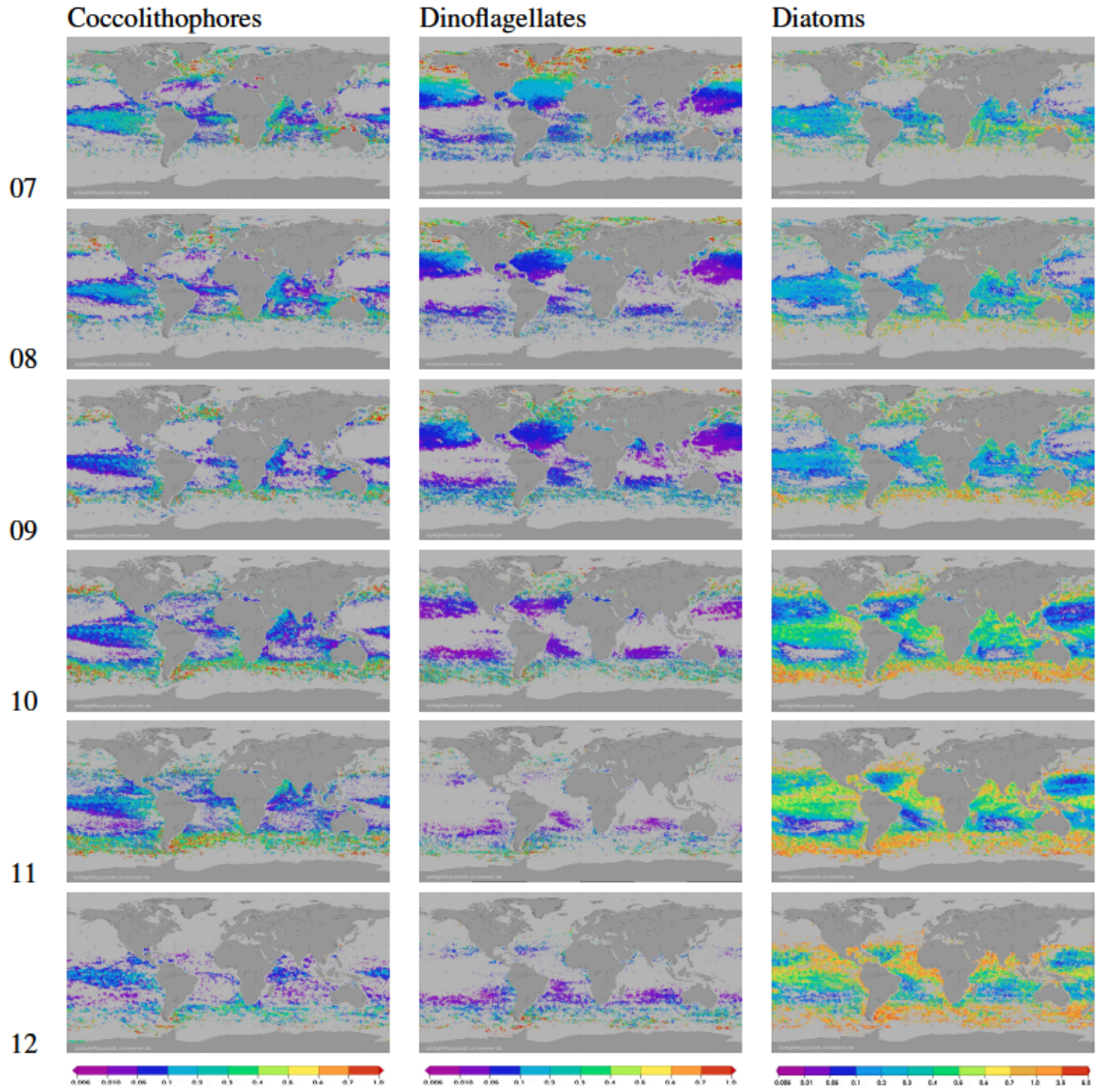

Figure 6.3: Monthly mean *chl-a* maps (in $[mg\,m^{-3}]$) for target PFTs retrieved by PhytoDOAS. The results have been obtained by applying the PhytoDOAS *triple-target* fitting to the SCIAMACHY data for the second half of 2008.

App. 1.2. Coccolithophores vs. PIC: 2008 monthly means

In Fig. 6.4 and Fig. 6.5, monthly mean *chl-a* of the PhytoDOAS coccolithophores (from SCIAMACHY date 2008) are compared with the monthly distributions of PIC conc. (from MODIS-Aqua) on a global scale. The respective results for the year 2005 have been presented in section 4.1.2.

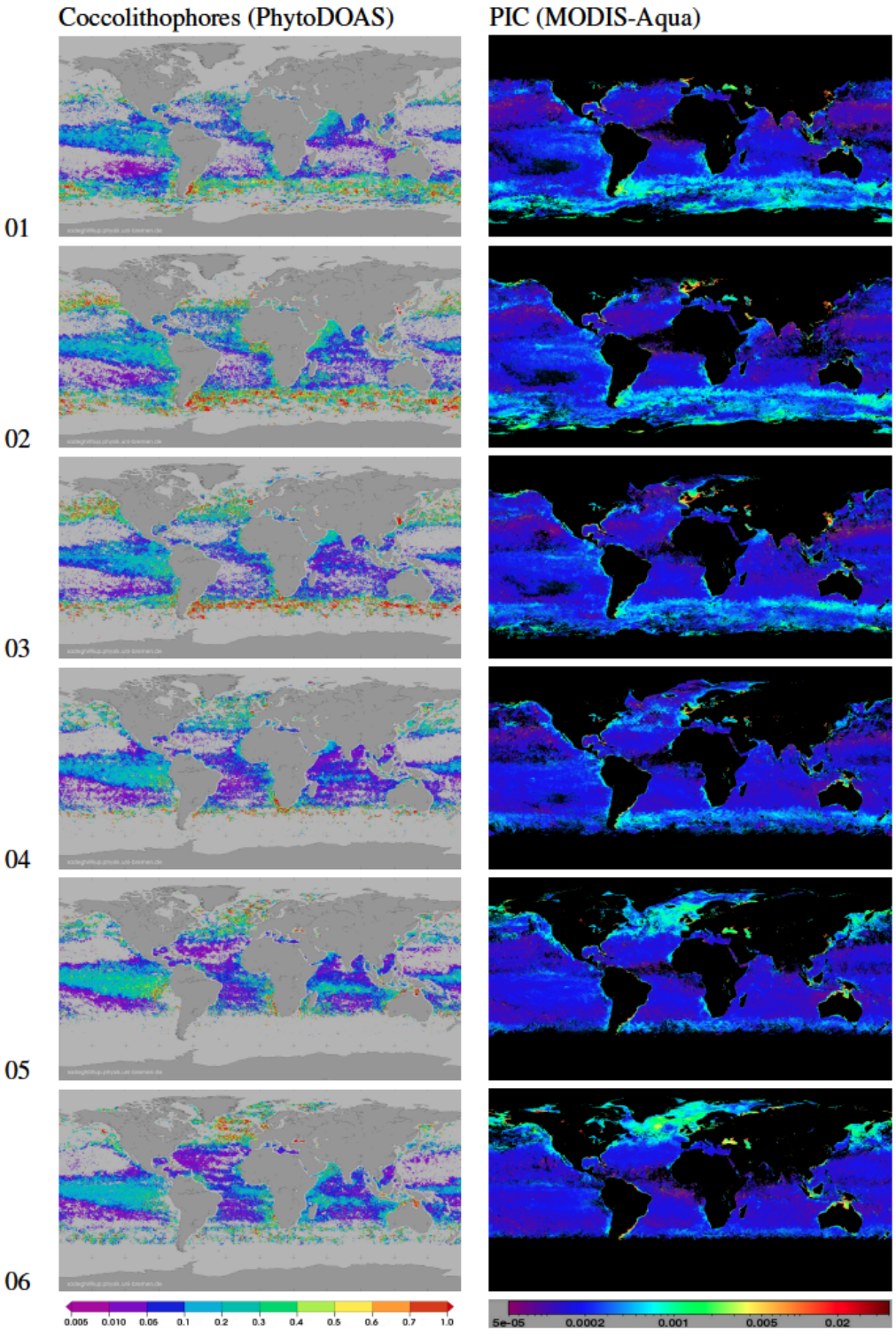

Figure 6.4: Left panels: PhytoDOAS coccolithophores monthly mean *chl-a* [$mg\,m^{-3}$]. Right panels: PIC monthly distribution [$mol\,m^{-3}$] from MODIS Aqua. All data corresponds to the first half of 2008..

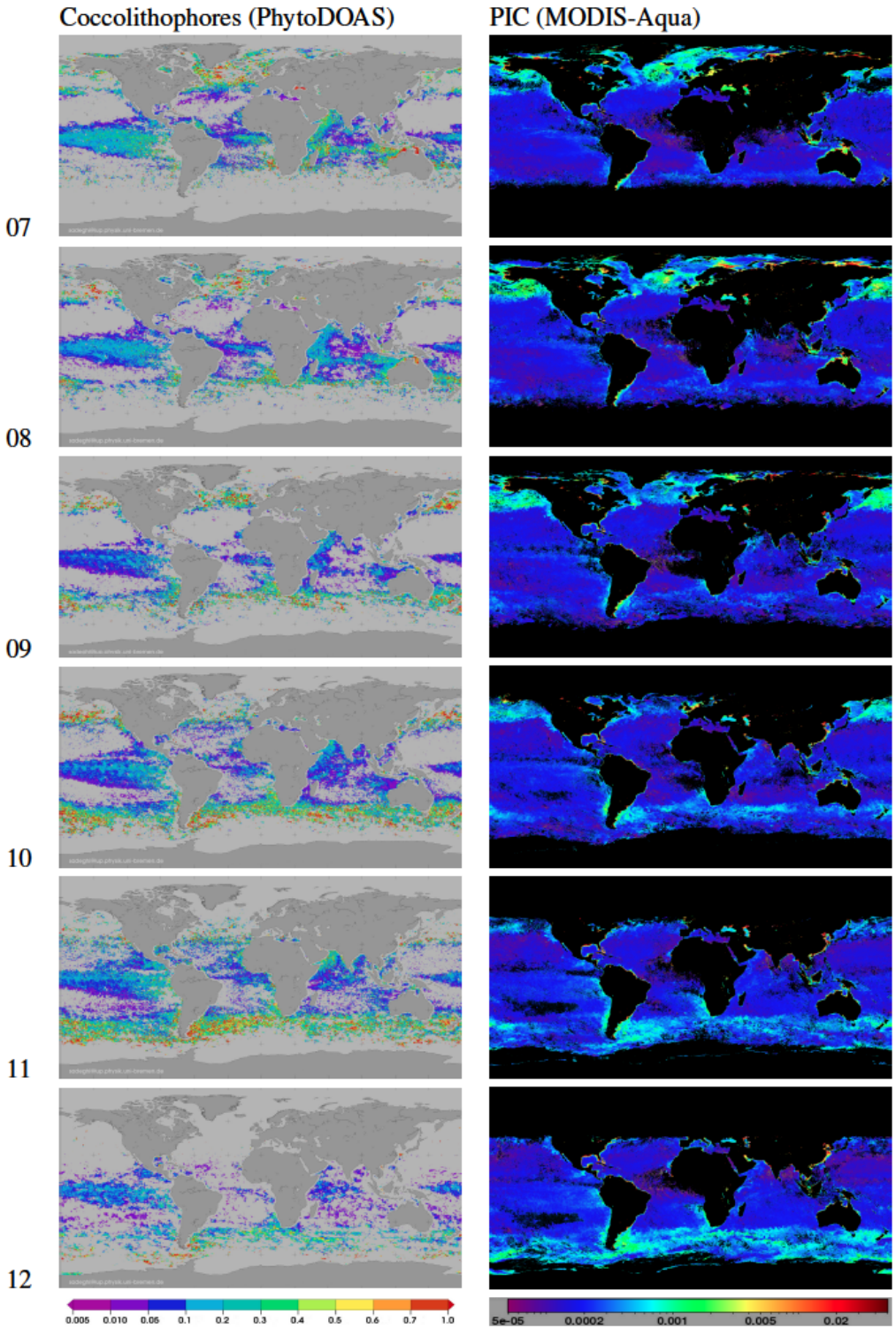

Figure 6.5: Left panels: PhytoDOAS coccolithophores monthly mean *chl-a* [$mg\,m^{-3}$]. Right panels: PIC monthly distribution [$mol\,m^{-3}$] from MODIS Aqua. All data corresponds to the second half of 2008.

App. 1.3. Cyanobacteria via single-target fit: 2008 monthly means

Fig. 6.6 illustrates monthly variations in the retrieved cyanobacteria (as averaged *chl-a*) on a global scale. The results were obtained by applying the PhytoDOAS *single-target* mode to the SCIAMACHY date 2008. The respective results for the year 2005 have been presented in section 4.1.4.

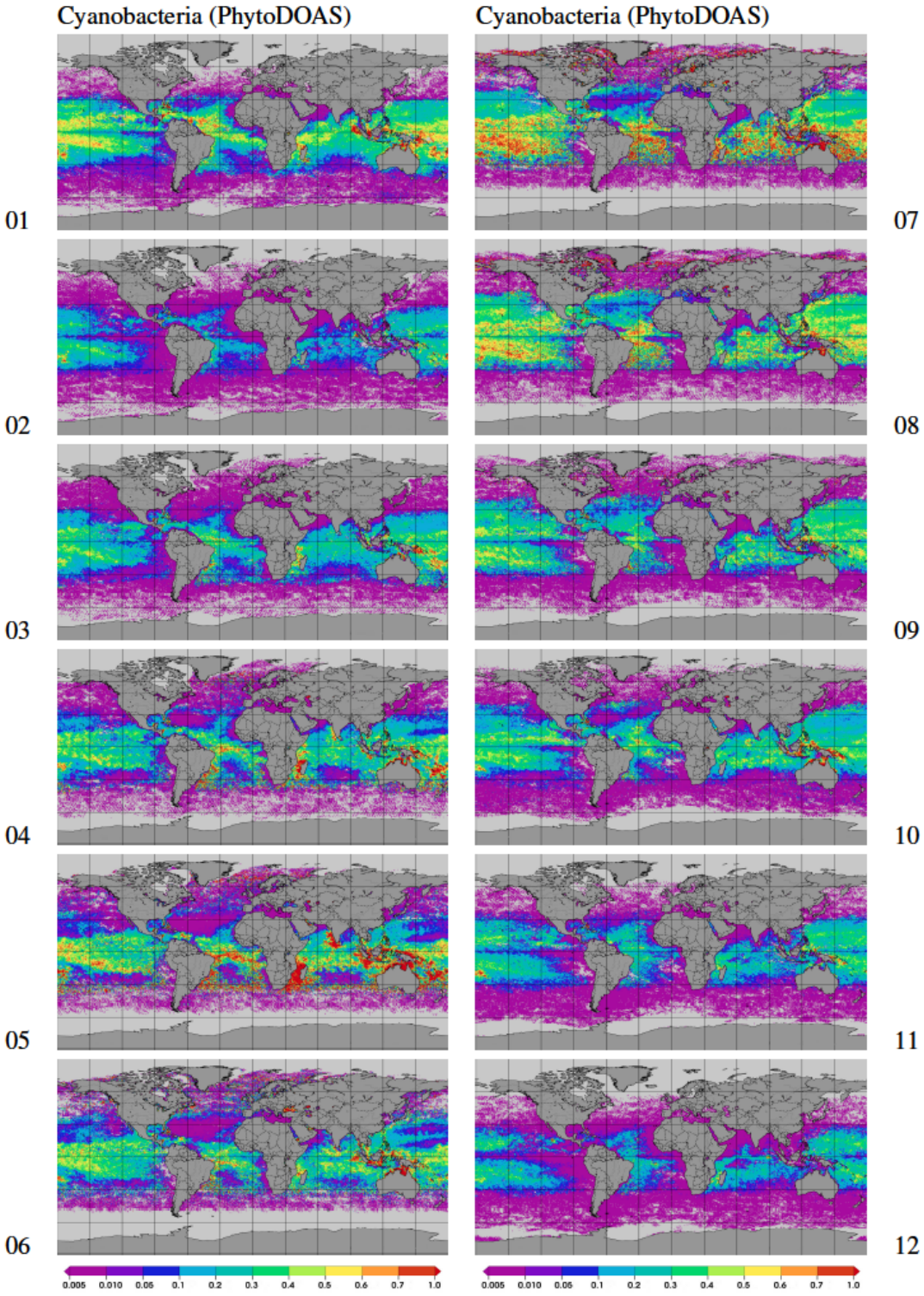

Figure 6.6: Cyanobacteria monthly mean *chl-a* $[mg\,m^{-3}]$ retrieved by PhytoDOAS single-target fit from the SCIAMACHY data. All data correspond to the year 2008.

App. 2. Time-series of the blooming months

App. 2.1. Time-series of the blooming months with simple trends

The time series of the study parameters only for the blooming months over the whole period (2003-2010) are shown in Fig. 6.7, Fig. 6.8 and Fig. 6.9, for each region, respectively. These are the time series based on which the *simple-trends* have been computed. The corresponding results have been discussed in the section: 5.3.3 and the numerical values of the linear trends were shown as *simple-trends* in Fig. 5.13 (upper panel).

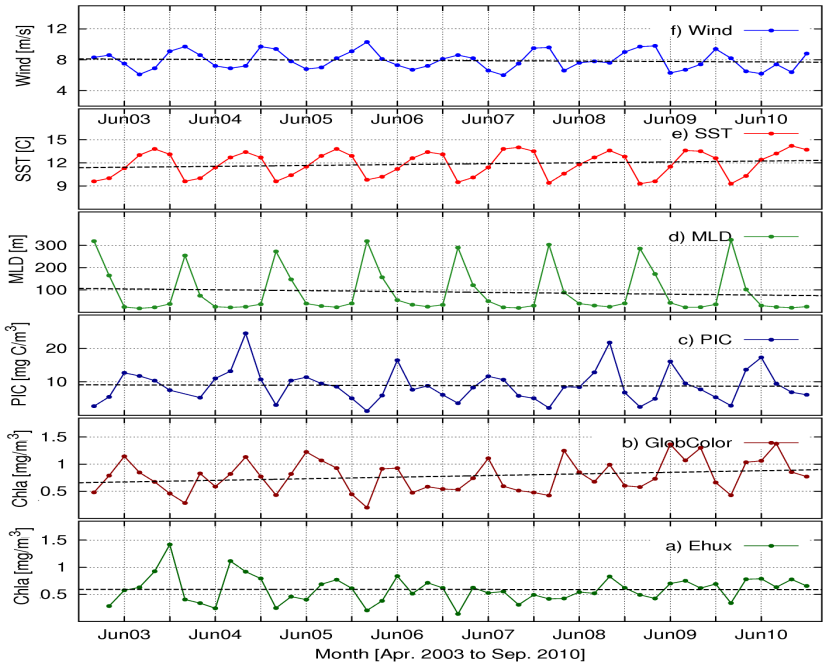

Figure 6.7: Time series of the six parameters monitored in *nAtl* from Jan. 2003 to Dec. 2010: (a) *coccos* [*Ehux*] *chl-a* conc. retrieved by PhytoDOAS; (b) GlobColour total *chl-a*; (c) MODIS-Aqua PIC conc.; (d) MLD from Ocean Productivity; (e) SST from AVHRR; and (f) surface wind-speed from AMSR-E. On each subplot the dashed-line shows the linear-trend for respecting parameter calculated for the selected months.

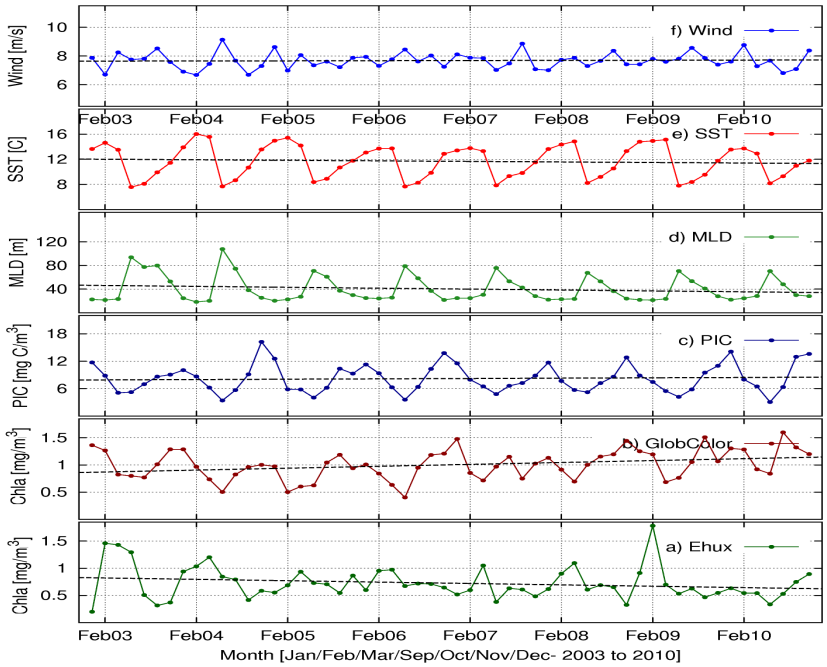

Figure 6.8: Time series as described in Fig. 6.7, but for the *sAtl* region.

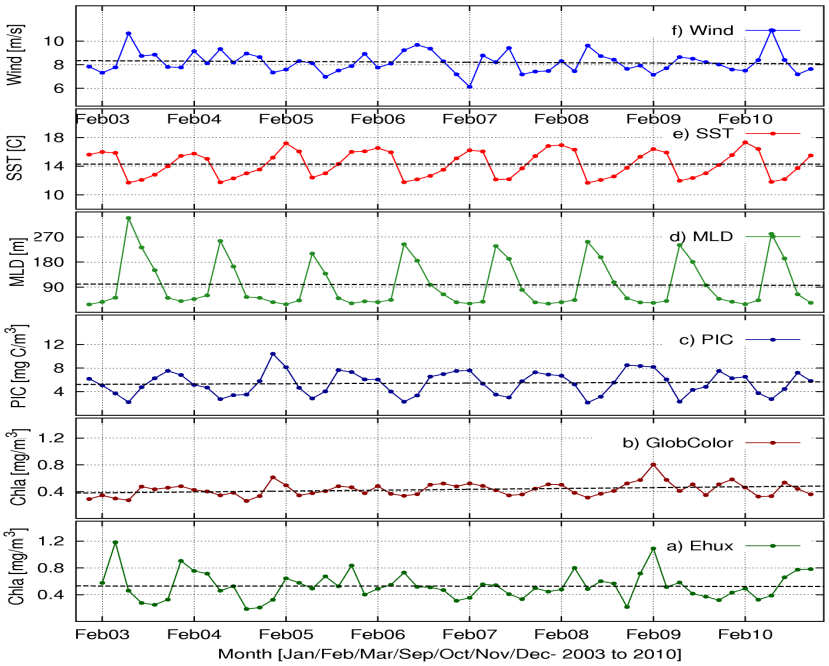

Figure 6.9: Time series as described in Fig. 6.7, but for the *sPac* region.

App. 2.2. Time-series of the blooming months with anomaly trends

The anomaly time series of the study parameters for the blooming months over the whole period (2003-2010) are shown in Fig. 6.10, Fig. 6.11 and Fig. 6.12, for each region,respectively. These are the time series based on which the *anomaly-trends* have been computed. The corresponding results have been discussed in the section: 5.3.3 and the numerical values of the linear trends were shown as *anomaly-trends* in Fig. 5.13 (lower panel).

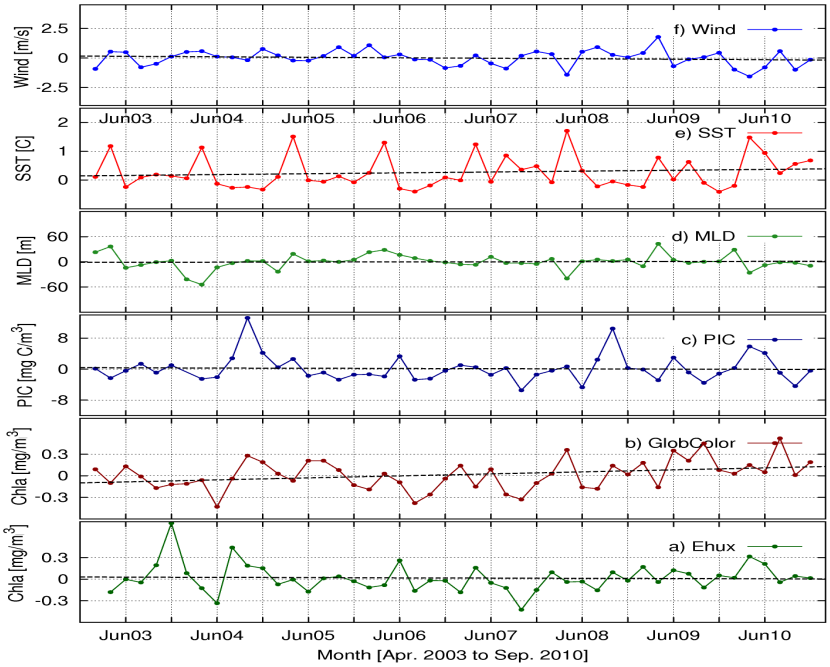

Figure 6.10: Anomaly time series of the six parameters monitored in *nAtl* from Jan. 2003 to Dec. 2010: (a) *coccos* [*Ehux*] *chl-a* conc. retrieved by PhytoDOAS; (b) GlobColour total *chl-a*; (c) MODIS-Aqua PIC conc.; (d) MLD from Ocean Productivity; (e) SST from AVHRR; and (f) surface wind-speed from AMSR-E. On each subplot the dashed-line shows the linear-trend for respecting parameter calculated for the selected months.

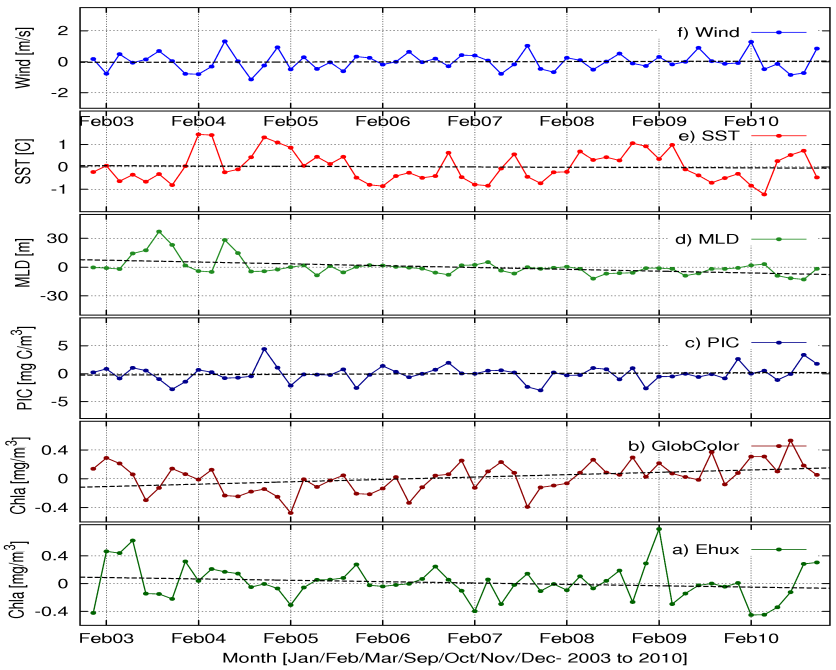

Figure 6.11: Anomaly time series as described in Fig. 6.10, but for the *sAtl* region.

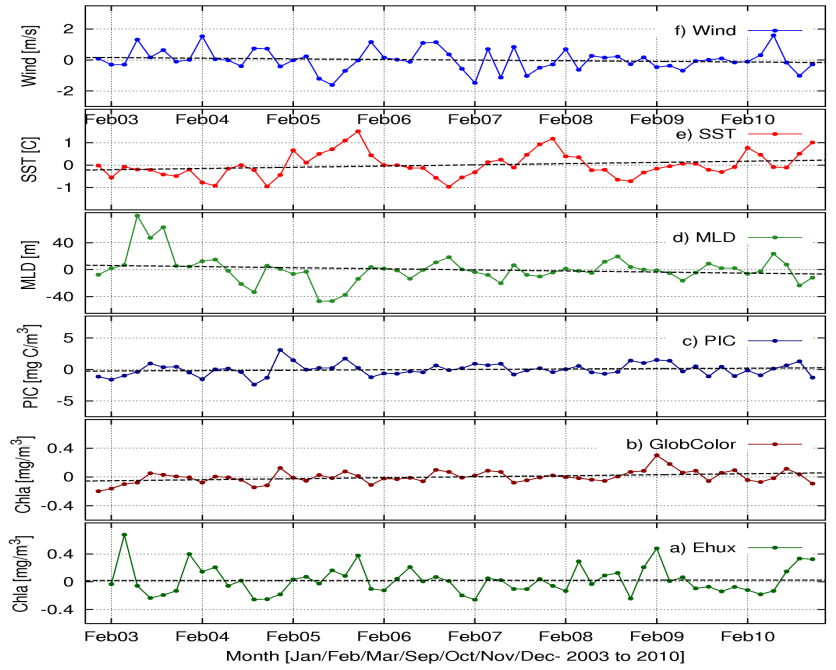

Figure 6.12: Anomaly time series as described in Fig. 6.10, but for the *sPac* region.

Bibliography

Ackleson, S. G., Balch, W. M., and Holligan, P. (1988). White waters of the Gulf of Maine. *Oceanography*, 1:18–22.

Ackleson, S. G., Balch, W. M., and Holligan, P. (1994). Response of water leaving radiance to particulate calcite and chlorophyll-a concentrations: A model for Gulf of Maine coccolithophore blooms. *J. Geophys. Res.*, 99:7483–7499.

Aguirre-Gomez, R., Weeks, A. R., and Boxall, S. R. (2001). The identication of phytoplankton pigments from absorption spectra. *International Journal of Remote Sensing*, 22.

Aiken, J., Fishwick, J. R., Lavender, S. J., Barlow, R., Moore, G., and Sessions, H. (2007). Validation of MERIS reflectance and chlorophyll during the BENCAL cruise October, 2002: Preliminary validation of new products for phytoplankton functional types and photosynthetic parameters. *International Journal of Remote Sensing*, 28.

Aiken, J., Moore, G. F., and Holligan, P. (1992). Remote sensing oceanic biology in relation to global climate change. *J. Phycol.*, 28:579–590.

Allali, K., Bricaud, A., Babin, M., Morel, A., and Chang, P. (1995). A new method for measuring spectral absorption coefficients of marine particles. *Limnol. Oceanogr.*, 40.

Alvain, S., Duforet-Gaurier, L., and Loisel, H. (2010). Observation of ocean colour beyond chlorophyll-a: From particulate organic carbon content and size distribution to phytoplankton functional groups. In Morales, J., Stuart, V., Platt, T., and Sathyendranath, S., editors, *Handbook of Satellite Remote Sensing Image Interpretation: Marine Applications*, chapter 5. IOCCG.

Alvain, S., Moulin, C., Dandonneau, Y., and Brèona, F. M. (2005). Remote sensing of phytoplankton groups in case 1 waters from global SeaWiFS imagery. *Deep-Sea Research*, 52.

Alvain, S., Moulin, C., Dandonneau, Y., and Loisel, H. (2008). Seasonal distribution and succession of dominant phytoplankton groups in the global ocean: A satellite view. *Global Biogeochemical Cycles*, 22.

Anderson, D. M., Cembella, A. D., and Hallegraeff, G., editors (1989). *The Physiological Ecology of Harmful Algal Blooms*. Springer-Verlag, Heidelberg.

Anderson, D. M., Glibert, P. M., and Burkholder, J. M. (2002). Harmful algal blooms and eutrophication: Nutrient sources composition and consequences. *Estuaries*, 25(4):704–726.

Anderson, D. M., Kaoru, Y., and White, A. W. (2000). Estimated annual economic impacts from harmful algal blooms (HABs) in the United States. Technical report, Woods Hole Oceanographic Institute.

Andreae, M. O. (1990). Ocean-atmosphere interactions in the global biogeochemical sulfur cycle. *Marine Chemistry*, 30:1–29.

Andreae, M. O., Barnard, W. R., and Ammons, J. M. (1983). The biological production of dimethylsulfide in the ocean and its role in the global atmospheric sulfur budget. *Environmental Biogeochemistry*, 35:167–177.

Andreae, M. O. and Raemdonck, H. (1983). Dimethyl sulfide in the surface ocean and the marine atmosphere: A global view. *Science*, 221(4612):744–74.

Andrefouet, S., Costello, M. J., Rast, M., and Sathyendranath, S. (2008). Earth observations for marine and coastal biodiversity and ecosystems. *Remote Sensing of Environment*, 112(8):3297–3299.

Archer, S., Widdicombe, C., Tarran, G., Rees, A., and Burkill, P. (2001). Production and turnover of particulate dimethyl-sulphoniopropionate during a coccolithophore bloom in the northern North Sea. *Aquat. Microb. Ecol.*, 24(3):225–241.

Armstrong, R. A., Lee, C., Hedges, J. I., Honjo, S., and Wakeham, S. G. (2002). A new mechanistic model for organic carbon fluxes in the ocean based on the quantitative association of POC with ballast minerals. *Deep-Sea Research*, 49:219–236.

Arrigo, K. R., Robinson, D. H., Worthen, D. L., Schieber, B., and Lizotte, M. P. (1998). Bio-optical properties of the south-western Ross Sea. *Journal of Geophysical Research*, 103.

Babin, S. M., Carton, J. A., Dickey, T. D., and Wiggert, J. D. (2004). Satellite evidence of hurricane-induced phytoplankton blooms in an oceanic desert. *Journal of Geophysical Research*, 109(C03043).

Balch, W. and Kilpatrick, K. (1996). Calcification rates in the equatorial Pacific along $140° W$. *Deep-Sea Research II*, 43.

Balch, W. M. (2004). *Re-evaluation of the physiological ecology of coccolithophores*, chapter in H. R. Thierstein and J. R. Young (eds): Coccolithophores. From Molecular Processes to Global Impact, pages 165–190. Springer-Verlag Berlin Heidelberg.

Balch, W. M., Drapeau, D. T., Bowler, B. C., Lyczskowski, E., Booth, S., and Alley, D. (2011). The contribution of coccolithophores to the optical and inorganic carbon budgets during the Southern Ocean gas exchange experiment: New evidence in support of the Great Calcite Belt hypothesis. *J. of Geophysical Res.*, 116(C00F06).

Balch, W. M., Eppley, R. W., Abbott, M. R., and Reid, F. M. H. (1989). Bias in satellite-derived pigment measurements due to coccolithophores and dinoflagellates. *J. Plankton Res.*, 11(575-581).

Balch, W. M., Gordon, H. R., Bowler, B. C., and Booth, D. T. D. E. S. (2005). Calcium carbonate measurements in the surface global ocean based on Moderate-Resolution Imaging Spectroradiometer data. *Journal of Geophysical Research*, 110(C07001).

Balch, W. M., Holligan, P. M., Ackleson, S. G., and Voss, K. J. (1991). Biological and optical properties of mesoscale coccolithophore blooms in the Gulf of Maine. *Limnol. Oceanogr.*, 36(629-643).

Bartlett, J., Voss, K., Sathyendranath, S., and Vodacek, A. (1998). Raman scattering by pure water and seawater. *Appl. Opt.*, 37(15):3324–3332.

Bates, N. R., Michaels, A. F., and Knap, A. H. (1996). Alkalinity changes in the Sargasso Sea: Geochemical evidence of calcification? *Marine Chemistry*, 51:3347–3358.

Bianchi, A. A., Bianucci, L., Piola, A. R., Pino, D., Schloss, I., Poisson, A., and Balestrini, C. F. (2005). Vertical stratification and air-sea CO_2 fluxes in the Patagonian shelf. *J. of Geophysical Res.*, 110(C07003). doi:10.1029/2004JC002488.

Bianchi, A. A., Pino, D. R., Perlender, H. G. I., Osiroff, A. P., Segur, V., V., V. L., Clara, M. L., Balestrini, C. F., and Piola, A. R. (2009). Annual balance and seasonal variability of sea-air CO_2 fluxes in the Patagonia Sea: their relationship with fronts and chlorophyll distribution. *J. of Geophysical Res.*, 114(C03018).

Bianchi, T. S., Engelhaupt, E., Westman, P., Andren, T., Rolff, C., and Elmgren, R. (2000). Cyanobacterial blooms in the baltic sea: Natural or human-induced? *Limnology and Oceanography*, 45(3):716–726.

Bolin, B. (1983). *The carbon cycle*, chapter in B. Bolin and R.B. Cook (eds): The major biogeochemical cycles and their interactions. John Wiley and Sons, New York. SCOPE 21.

Bonsang, B., Polle, C., and Lambert, G. (1992). Evidence for marine production of Isoprene. *Geophys. Res. Lett.*, 19:1129–1132.

Bopp, L., Aumont, O., Cadule, P., Alvain, S., and Gehlen, M. (2005). Response of diatoms distribution to global warming and potential implications: A global model study. *Geophys. Res. Lett.*, 32(19). L19606.

Bovensmann, H., Burrows, J. P., Buchwitz, M., Frerick, J., Nöel, S., Rozanov, V. V., Chance, K. V., and Goede, A. P. H. (1999). SCIAMACHY - mission objectives and measurement modes. *J. Atmos. Sci.*, 56(2):127–150.

Boyer-Montegut, C., Madec, G., Fischer, A. S., Lazar, A., and Iudicone, D. (2004). Mixed layer depth over the global ocean: An examination of profile data and a profile-based climatology. *Journal of Geophysical Research*, 109(C12003).

Bracher, A. and Tilzer, M. (2001). Underwater light field and phytoplankton absorbance in different surface water masses of the Atlantic sector of the Southern Ocean. *Pol. Biol.*, 24:687–696.

Bracher, A., Vountas, M., Dinter, T., Burrows, J. P., Roettgers, R., and Peeken, I. (2009). Quantitative observation of cyanobacteria and diatoms from space using PhytoDOAS on SCIAMACHY data. *Biogeosciences*, 6.

Brandini, F. P., Boltovskoy, D., Piola, A., Kocmur, S., Roettgers, R., Abreu, P. C., and Lopes, R. M. (2000). Multiannual trends in fronts and distribution of nutrients and chlorophyll in the south-western Atlantic ($30 - 62^{\circ}$ S). *Deep-Sea Research I*, 47:1015–1033.

Brewin, R. J. W., Hardman-Mountford, N. J., Lavender, S. J., Raitsos, D. E., Hirata, T., Uitz, J., Devred, E., Bricaud, A., Ciotti, A., and Gentili, B. (2011). An intercomparison of bio-optical techniques for detecting dominant phytoplankton size class from satellite remote sensing. *Remote Sensing of Environment*, 115:325–339.

Brewin, R. J. W., Lavender, S. J., Hardman-Mountford, N. J., and Hirata, T. (2010a). A spectral response approach for detecting dominant phytoplankton size class from satellite remote sensing. *Acta Oceanol Sin.*, 29:14–32.

Brewin, R. J. W., Sathyendranath, S., Hirata, T., Lavender, S., Barciela, R. M., and Hardman-Mountford, N. J. (2010b). A three-component model of phytoplankton size class for the Atlantic Ocean. *Ecological Modelling*, 221:1472–1483.

Bricaud, A., Babin, M., Morel, A., and Claustre, H. (1995). Variability in the chlorophyll-specific absorption coefficients of natural phytoplankton: Analysis and parameterization. *Journal of Geophysical Research*, 100.

Bricaud, A., Claustre, H., Ras, J., and Oubelkheir, K. (2004). Natural variability of phytoplanktonic absorption in oceanic waters: Influence of the size structure of algal populations. *Journal of Geophysical Research*, 109(C11010).

Bricaud, A., Morel, A., and Prieur, L. (1981). Absorption by dissolved organic matter of the sea (yellow substance) in the UV and visible domains. *Limnology and Oceanography*, 26.

Broecker, W. S. and Peng, T. H. (1982). *Tracers in the Sea*. Eldigio, Palisades, N. Y.

Brown, C. W. (1995). Global distribution of coccolithophore blooms. *Oceanography*, 8(2):59–60.

Brown, C. W. and Podesta, G. (1997). Remote sensing of coccolithophore blooms in the western South Atlantic Ocean. *Remote Sens. Environ.*, 60:83–91.

Brown, C. W. and Yoder, J. A. (1994a). Coccolithophorid blooms in the global ocean. *Journal of Geophysical Research*, 99(C4):7467–7482.

Brown, C. W. and Yoder, J. A. (1994b). Distribution pattern of coccolithophorid blooms in the western North Atlantic. *Cont. Shelf Res.*, 14:175–197.

Brownlee, C. and R.Taylor, A. (2002). *Encyclopedia of life sciences*, chapter in: Algal calcification and silification, pages 1–6. Macmillan Publishers Ltd. Nature Publishing Group.

Buiteveld, H., Hakvoort, J., and Donze, M. (1994). The optical properties of pure water. *SPIE Proc. on Ocean Optics XII*, 2258:174–183.

Burns, D. A. (1977). Phenotypes and dissolution morphotypes of the genus Gephyrocapsa Kamptner and Emiliania huxleyi (lohmann). *N.Z. J. Geol. Geophys.*, 20:143–155.

Burrows, J. P., Vountas, Haug, H., Chance, K., Marquard, L., Miurhead, K., Platt, U., Richter, A., and Rozanov, V. V. (1996). Study of the Ring effect, final report for ESA. Technical report, ESA Technical Report.

Bussemer, M. (1993). Der Ring-Effekt: Ursachen und Einfluss auf die spektroskopische Messung stratosphärischer Spurenstoffe. Master's thesis, University of Heidelberg, Germany.

Caddy, J. F., Fefk, R., and Do-Chi, T. (1995). Productivity estimates for the Mediterranean: Evidence of accelerating ecological change. effects of riverine inputs on coastal. Technical report, FAO Tech. Rep., Rome: FAO.

Cai, W., Shi, G., Cowan, T., Bi, D., and Ribbe, J. (2005). The response of the Southern Annular mode, the East Australian Current, and the southern mid-latitude ocean circulation to global warming. *Geophys. Res. Lett.*, 32(L23706).

Capone, D. G., Zehr, J., Paerl, H., Bergman, B., and Carpenter, E. J. (1997). Trichodesmium: A globally significant marine cyanobacterium. *Science*, 276:1221–1229.

Carder, K. L., Chen, F. R., Cannizzaro, J. W., Campbell, J. W., and Mitchell, B. G. (2004). Performance of the MODIS semi-analytical ocean color algorithm for chlorophyll-a. *Advances in Space Research*, 33:1152–1159.

Carder, K. L., Steward, R. G., Harvey, G. R., and Ortner, P. B. (1989). Marine humic and fulvic acids: their effects on remote sensing of ocean chlorophyll. *Limnology and Oceanography*, 34.

Carreto, J. I., Lutz, V. A., Carignan, M. O., Cuechi-Colleoni, A. D., and De-Marco, S. G. (1995). Hydrography and chlorophyll a in a transect from the coast to the shelf-break in the Argentinian Sea. *Cont. Shelf Res.*, 15:315–336.

Chameides, W. L. and Davis, D. D. (1980). Iodine: Its possible role in tropospheric photochemistry. *J. Geophys. Res*, 85:7383–7398.

Charlson, R. J., Lovelock, J., Andreae, M. O., and Warren, S. G. (1987). Oceanic phytoplankton, atmospheric sulfur, cloud albedo and climate. *Nature*, 326(6114):655–661.

Chisholm, S. (1992). *Phytoplankton size*, chapter in P. G. Falkowski and A. D. Woodhead (eds.): Primary productivity and biogeochemical cycles in the sea, pages 213–237. Plenum press.

Chou, L., Daro, M. H., and Van-Grieken, R. (2009). *Role of oceanic production and dissolution of calcium carbonate in climate change (CCCC)*. Scientific Support Plan for a Sustainable Development Policy (SPSD II). Belgian Science Policy.

Chuck, A. L., Turner, S. M., and Liss, P. S. (2005). Oceanic distributions and air-sea fluxes of biogenic halocarbons in the open ocean. *Geophysical Research*, 110(C10022).

Ciotti, A. M. and Bricaud, A. (2006). Retrievals of a size parameter for phytoplankton and spectral light absorption by coloured detrital matter from water-leaving radiances at seawifs channels in a continental shelf off Brazil. *Limnology and Oceanography: Methods*, 4:237–253.

Clark, D. R., Flynn, K. J., and Owens, N. J. P. (2002). The large capacity for dark nitrate-assimilation in diatoms may overcome nitrate limitation of growth. *New Phytologist*, 155:101–108.

Claustre, H. and Maritorena, S. (2003). The many shades of ocean blue. *Science*, 302:1514–1515.

der Linden, W. V. (1969). Extinct mid-ocean ridges in the tasman sea and in the western pacific. *Earth and Planetary Science Letters*, 6:483–490.

Devred, E., Sathyendranath, S., Stuart, S., and Platt, T. (2011). Absorption-derived phytoplankton cell size: application to satellite ocean-colour data in the North-west Atlantic. *Remote Sensing of Environment*, 115:2255–2266.

Devred, E., Sathyendranath, S., Stuart, V., Maas, H., Ulloa, O., and Platt, T. (2006). A two-component model of phytoplankton absorption in the open ocean: Theory and applications. *J. Geophys Res.*, 111(C03011).

Dickson, A. G. (1991). Measuring oceanic CO_2: progress on quality control. *U.S. JGOFS News*, 3(4).

Dortch, Q., Milsted, D., Rabalas, N. N., Lohrenz, S. E., Redalje, D. G., Dagg, M. J., Turner, R. E., and Whitledge, T. E., editors (1992). *Role of silicate availability in phytoplankton species composition and the fate of carbon*. Texas Sea Grant Technical Publication. p. 76-83.

Ducklow, H. W., Steinberg, D. K., and Buesseler, K. O. (2001). Upper ocean carbon export and the biological pump. *Oceanography*, 14(4).

Dufresnes, J. L., Friedlingstein, P., Berthelot, M., Bopp, L., Ciais, P., Fairhead, L., Treut, H. L., and Monfray, P. (2002). On the magnitude of positive feedback between future climate change and the carbon cycle. *Geophys. Res. Lett.*, 29(10).

DuRand, M. D., Olson, R. J., and Chisholm, S. W. (2001). Phytoplankton population dynamics at the Bermuda Atlantic time-series station in the Sargasso Sea. *Deep Sea Res.*, 48.

Duysens, L. N. M. (1956). The flattening of the absorption spectrum of suspensions as compared to the solutions. *Biochim. Biophys.*, 19:1–12.

Ebert, K. (2009). *Exceptional Phytoplankton Bloom Recognition from Visible Spectral Satellite Radiometry Data*. PhD thesis, Freie Universität Berlin.

Erickson, D. J., Hernandez, J. L., P., Ginoux, Gregg, W. W., McClain, C., and Christian, J. (2003). Atmospheric iron delivery and surface ocean biological activity in the Southern Ocean and Patagonian region. *Geophys. Res. Lett.*, 30(1609).

Fagerbakke, K., Heldal, M., Norland, S., Heimdal, B., and Batvik, H. (1994). Emiliania huxleyi. chemical composition and size of coccoliths from enclosure experiments and a Norwegian Fjord. *Sarsia*, 79(4):349–355.

Falkowski, P. G., Barber, R. T., and Smetacek, V. (1998). Biogeochemical controls and feedbacks on ocean primary production. *Science*, 281.

Feely, R., Sabine, C. L., Takahashi, T., and Wanninkhof, R. (2001). The global CO_2 survey. *Oceanography*, 14(4).

Fuentes-Yaco, C., Sathyendranath, P. A. K. S., and Platt, T. (2007). Shrimp (Pandalus borealis) growth and timing of the spring phytoplankton bloom on the Newfoundland-Labrador Shelf. *Fishery and Oceanography*, 16:116–129.

Fuhrman, J. A. and Capone, D. G. (2001). Nifty nanoplankton. *Nature*, 412:593–594.

Gaines, G. and Elbrächter, M. (1987). *Heterotrophic nutrition*, volume 21, chapter in F. J. R. Taylor (ed.): The biology of dinoflagellates. Blackwell Scientific Publications, Oxford.

Garcia, C. A. E., Garcia, V. M. T., Dogliotti, A. I., Ferreira, A., Romero, S. I., Mannino, A., Souza, M. S., and Mata, M. M. (2011). Environmental conditions and bio-optical signature of a coccolithophorid bloom in the Patagonian Shelf. *Journal of Geophysical Research*, 116(C03025).

Garcia, C. A. E., Garcia, V. M. T., and McClain, C. R. (2005). valuation of SeaWiFS chlorophyll algorithms in the south-western Atlantic and southern oceans. *Remote Sens. Environ.*, 95:125–137.

Goldman, J. C. (1993). Potential role of large oceanic diatoms in new primary production. *Deep-Sea Research I*, 40:159–168.

Gordon, A. L. (1989). Brazil Malvinas Confluence-1984. *Deep-Sea Research*, 36 (3):359–384.

Gordon, H. R. (1997). Atmospheric correction of ocean color imagery in the Earth observing system era. *Journal of Geophysical Research*, 102(D):17081–17106.

Gordon, H. R., Boynton, G. C., Balch, W. M., Groom, S. B., Harbour, D. S., and Smyth, T. J. (2001). Retrieval of coccolithophore from SeaWiFS imagery calcite concentration. *Geophysical Research Letters*, 28(8):1587–1590.

Gordon, H. R., Brown, O. B., Evans, R. H., Brown, J. W., Smith, R., Baker, K. S., and Clark, D. (1988). A semi-analytic radiance model of ocean color. *Geophys. Res.*, 93:10909–10924.

Gordon, H. R., Brown, O. B., and Jacobs, M. M. (1975). Computed relationships between the Inherent and Apparent optical properties of a flat homogeneous ocean. *Applied Optics*, 14.

Gordon, H. R. and Morel, A. (1983). *Remote assessment of ocean color for interpretation of satellite visible imagery: A review*. Springer-Verlag, New York.

Gottwald, M. and Bovensmann, H., editors (2011). *SCIAMACHY, exploring the changing Earth's atmosphere*. Springer, Heidelberg.

Grainger, J. and Ring, J. (1962). Anomalous Fraunhofer line profiles. *Nature*, 193:762.

Gregg, W. W. (2002). A coupled ocean-atmosphere radiative model for global ocean biogeochemical models. Technical Report 104606, NASA.

Gregg, W. W. and Casey, N. W. (2004). Global and regional evaluation of the SeaWiFS chlorophyll data set. *Remote Sens. Environ.*, 93:463–79.

Gregg, W. W. and Casey, N. W. (2007). Modeling coccolithophores in the global oceans. *Deep Sea Research II*, 54:447–477.

Gregg, W. W., Ginoux, P., and aand N. W Casey, P. S. S. (2003). Phytoplankton and iron: validation of a global three-dimensional ocean biogeochemical model. *Deep Sea Res*, 50.

Groom, S. and Holligan, P. M. (1987). Different reactions of southern ocean phytoplankton size-classes to iron fertilization. *Adv. Space Res.*, 7(2):73–78. doi:10.1016/0273-1177(87)90166-9.

Gurlin, D., Gitelson, A. A., and Moses, W. J. (2011). Remote estimation of chl-a concentration in turbid productive waters– return to a simple two-band NIR-red model? *Remote Sensing of Environment*, 115(12):3479–3490.

Hallegraeff, G. M. (2003). *Harmful algal blooms: a global overview*, chapter in G.M. Hallegraeff and D.M. Anderson and A.D. Cembella (eds.): Manual on Harmful Marine Microalgae, pages 25–49. UNESCO Publishing.

Hansell, D. A. and Carlson, C. A. (2001). Marine Dissolved Organic Matter and the carbon cycle. *Oceanography*, 14(4).

Heirtzler, J. R. (2002). The future of the South Atlantic anomaly and implications for radiation damage in space. *Journal of Atmospheric and Solar-Terrestrial Physics*, 64(16):1701–1708.

Hirata, T., Aiken, J., Hardman-Mountford, N. J., Smyth, T. J., and Barlow, R. G. (2008). An absorption model to derive phytoplankton size classes from satellite ocean colour. *Remote Sensing of Environment*, 112:3153–3159.

Hirata, T., Hardman-Mountford, N. J., Brewin, R. J. W., Aiken, J., Barlow, R. G., Suzuki, K., Isada, T., Howell, E., Hashioka, T., Noguchi-Aita, M., and Yamanaka, Y. (2011). Synoptic relationships between surface chlorophyll-a and diagnostic pigments specific to phytoplankton functional types. *Biogeosciences*, 8:311–327.

Hoffmann, L. J., Peeken, I., Lochte, K., Assmy, P., and Veldhuis, M. (2006). Different reactions of Southern Ocean phytoplankton size-classes to iron fertilization. *Limnol. Oceanogr.*, 51.

Holligan, P. M., Fernandez, E., Aiken, J., Balch, W., Boyd, P., Burkill, P., Finch, M., Groom, S., Malin, G., Muller, K., Purdie, D., Robinson, C., Trees, C., Turner, S., and der Wal, P. V. (1993). A biogeochemical study of the coccolithophore Emiliania huxleyi in the North Atlantic. *Global Biogeochemical Cycles*, 7(4):879–900.

Holligan, P. M., Viollier, M., Harbour, D. S., and Champagne-Philipe, M. (1983). Satellite and ship studies of coccolithophore production along a continental shelf-edge. *Nature*, 304:339–342.

Joiner, J., Bhartia, P. K., Cebula, R. P., Hilsenrath, E., McPeters, R. D., and Park, H. (1995). Rotational Raman scattering (Ring effect) in satellite backscatter ultraviolet measurements. *Applied Optics*, 34(21):4513–4525.

Joiner, J., Yoshida, Y., Vasilkov, A. P., Middleton, E. M., Campbell, P. K. E., Yoshida, Y., Kuze, A., and Corp, L. A. (2012). Filling-in of far-red and near-Infrared solar lines by terrestrial and atmospheric effects: simulations and space-based observations from SCIAMACHY and GOSAT. *Atmos. Meas. Tech. Discuss.*, 5:163–210. in press.

Kattawar, G. and Xu, X. (1992). Filling in of Fraunhofer lines in the ocean by Raman scattering. *Appl. Opt.*, 30.

Kattawar, G., Young, A., and Humphreys, T. (1981). Inelastic scattering in planetary atmospheres. i. the Ring effect, without aerosols. *Astrophys. J.*, 243:1049–1057.

Keller, M., Bellows, W., and Guillard, R. (1989). *Dimethylsulfide production and marine phytoplankton: an additional impact of unusual blooms*, chapter in E.M. Cosper and V.M. Bricelj and E.J. Carpenter (eds): Novel phytoplankton blooms, pages 101–115. Springer-Verlag, New York.

Kirk, J. T. O. (1975). A theoretical analysis of the contribution of algal cells to the attenuation of light within natural waters. I. general treatment of suspensions of pigmented cells. *New Phytol.*, 75:11–20.

Kirk, J. T. O. (1994). *Light and Photosynthesis in Aquatic Ecosystems*. Cambridge University Press, 2nd edition.

Kokhanovsky, A. A., editor (2006). *Light Scattering Review: single and multiple light scattering*. Springer-Verlag Berlin. ISBN 3-540-25315-7.

Kopelevich, O. (1983). *Small-parameter model of optical properties of seawater*, chapter 8 in A. S. Monin (Ed.): Ocean Optics, Vol. 1: Physical Ocean Optics, pages 208–235. Nauka, Moscow.

Kostadinov, T. S., Siegel, D. A., and Maritorena, S. (2009). Retrieval of the particle size distribution from satellite ocean color observations. *J. Geophysical Res.*, 114(C09015).

Kostadinov, T. S., Siegel, D. A., and Maritorena, S. (2010). Global variability of phytoplankton functional types from space: assessment via the particle size distribution. *Biogeosciences*, 7:3239–3257.

Kumar, M. D., Shenoy, D. M., Sarma, V. V. S., George, M. D., and Dandekar, M. (2002). Export fluxes of dimethyl-sulfoniopropionate and its break down gases at the air-sea interface. *Geophys. Res. Lett.*, 29(2).

Lee, Z. P. and Hu, C. (2006). Global distribution of Case-1 waters: An analysis from SeaWiFS measurements. *Remote Sensing of Environment*, 101:270–276.

Levitus, S. and Boyer, T. P. (1994). *World Ocean Atlas*, volume 4 of *NOAA Atlas NESDIS 4*. U. S. Govt. Printing Office, Washington, D. C.

Lignell, R., Heiskanen, A. S., Kuosa, H., Gundersen, K., Kuuppo-Leinikki, P., Pajuniemi, R., and Uitto, A. (1993). Fate of a phytoplank ton spring bloom: sedimentation and carbon flow in the planktonic food web in the northern Baltic. *Mar. Ecol. Prog.*, 94:239–252.

Lin, I. I. (2011). Typhoon-induced phytoplankton blooms and primary productivity increase in the western North Pacific subtropical ocean. *Journal of Geophysical Research*. in press.

Liss, P. S., Hatton, A. D., Malin, G., Nightingale, P. D., and Turner, S. M. (1997). Marine sulphur emissions. *Philos. Trans. R. Soc. London*, 352(Ser. B):159–169.

Lochte, K., Ducklow, H., Fasham, M., and Stienen, C. (1993). Plankton succession and carbon cycling at $47°N, 20°W$ during the JGOFS North Atlantic bloom experiment. *Deep-Sea Research Part II*, 40 (1-2):91–114.

Longhurst, A. (2007). *Ecological Geography of the Sea*. Academic Press, San Diego, Calif., 2nd ed. edition.

Longhurst, A. R. (1995). Seasonal cycles of pelagic production and consumption. *Progress in Oceanography*, 36:77–167.

Longhurst, A. R. (1998). *Ecological Geography of the Sea*. Academic Press, 2nd edition.

Lovelock, J. E. (1975). Natural halocarbons in air and in the sea. *Nature*, 256(256):193–194.

Mackey, M. D., Mackey, D. J., Higgins, H. W., and Wright, S. W. (1996). CHEMTAX - a program for estimating class abundances from chemical markers: Application to HPLC measurements of phytoplankton. *Mar. Ecol. Prog. Ser.*, 14.

Malin, G. and Kirst, G. O. (1997). Algal production of volatile sulphur compounds and their role in the atmosphere. *J. Phycol.*, 33:889–896.

Malin, G. and Steinke, M. (2004). *Dimethyl sulphide production: what is the contribution of cocolithophores*, chapter in H. R. Thierstein and J. R. Young (eds): Coccolithophores. From Molecular Processes to Global Impact, pages 127–164. Springer-Verlag Berlin.

Malin, G., Turner, S., and Liss, P. (1992). Sulfur. the plankton-climate connection. *Journal of Phycology*, 28(5):590–597.

Margalef, R. (1978). Life-forms of phytoplankton as survival alternatives in an unstable environment. *Oceanologica Acta*, 1:493–509.

Maritorena, S., d'Andon, O. H. F., Mangin, A., and A.Siegel, D. (2010). Merged satellite ocean color data products using a bio-optical model: Characteristics, benefits and issues. *Remote Sensing of Environment*, 114(8):1791–1804.

Martin, J. H. (1991). Iron, liebig's law, and the greenhouse. *Oceanography*, 4:52–55.

McClain, C. R. (2009). A decade of satellite ocean color observations. *Annu. Rev. Marine Sci.*, 1:19–42. doi:10.1146/annurev.marine.010908.163650.

Medlin, L. K., Doucette, G. J., and Villac, M. C., editors (2008). *Phytoplankton Evolution, Taxonomy and Ecology*. Gebr Borntraeger (Berlin, Stuttgart).

Mie, G. (1908). Beitrage zur optik truber medien, speziell kolloidalen metallosungen. *Ann. Physik*, 25:377.

Millie, D., Schofield, O. M., Kirkpatrick, G. J., Johnsen, G., Tester, P. A., and Vinyard, B. T. (1997). Detection of harmful algal blooms using photopigments and absorption signatures: A case study of the Florida red-tide dinoflagellates, Gymnodinium breve. *Limnol. Oceanogr.*, 42.

Milliman, J. D. (1993). Production and accumulation of calcium in the ocean. *Global Biogeochemical Cycles*, 7:927–957.

Milliman, J. D., Troy, P. J., Balch, W. M., Adams, A. K., Li, Y. H., and Mackenzie, F. T. (1999). Biologically mediated dissolution of calcium carbonate above the chemical lysocline? *Deep-Sea Research I*, 46:91653–1669.

Mitchell, B. G. and Holm-Hansen, O. (1991). Bio-optical properties of Antarctic Peninsula waters: differentiation from temperate ocean models. *Deep-Sea Res*, 38:1009–1028.

Mitchell, B. G., Kahru, M., Wieland, J., and Stramska, M. (2003). Determination of spectral absorption coefficients of particles, dissolved material and phytoplankton for discrete water samples. *Ocean optics protocols for satellite ocean color sensor validation*, 4.

Mobley, C. (1994). *Light and Water- Radiative Transfer in Natural Waters*. Academic Press, Inc.

Mobley, C. D., Stramski, D., Bisset, W. P., and Boss, E. (2004). Optical modeling of ocean waters: Is the Case-1 Case-2 still useful? *Oceanography*, 17(2):60–67.

Morel, A. (1974). *Optical aspects of oceanography*, chapter in N. G. Jerlov and E. Steeman Nielsen (eds.): Optical properties of pure water and pure seawater, pages 1–24. Academic Press.

Morel, A. (1988). Optical modeling of the upper ocean in relation to its biogeneous matter content (Case-1 waters). *J. Geophys. Res.*, 93.

Morel, A. and Antoine, D. (1998). Pigment index retrieval in Case-1 waters. MERIS ATBD 2.9. Technical report, ESA.

Morel, A. and Bricaud, A. (1981). Theoretical results concerning light absorption in a discrete medium, and application to specific absorption of phytoplankton. *Deep-Sea. Res.*, 28:1375–1393.

Morel, A. and Gordon, H. R. (1980). Report of the working group on water color. *Boundary-Layer Meteorol.*, 18:343–355.

Morel, A. and Prieur, L. (1977). Analysis of variations in ocean color. *Limnol. Oceanogr.*, 22.

Morel, F. M. M., Rueter, J. G., and Price, N. M. (1991). Iron nutrition of phytoplankton and its possible importance in the ecology of ocean regions with high nutrient and low biomass. *Oceanography*, 4(2).

Morozov, E., Korosov, A., Pozdnyakov, D., Pettersson, L., and Sychev, V. (1993). A new area-specific bio-optical algorithm for the Bay of Biscay and assessment of its potential for SeaWiFS and MODIS/Aqua data merging. *International Journal of Remote Sensing*, 31(24):6541–6565.

Nair, A., Sathyendranath, S., Platt, T., Morales, J., Stuart, V., Forget, M., Devred, E., and Bouman, H. (2008). Remote sensing of phytoplankton functional types. *Remote Sensing of Environment*, 112.

Nanninga, H. J. and Tyrrell, T. (1996). Importance of light for the formation of algal blooms by Emiliania huxleyi. *Mar. Ecol.-Prog. Ser.*, 136:195–203.

Nelson, D. M., Treguer, P., Brzezinski, M. A., Leynaert, A., and Queguiner, B. (1995). Production and dissolution of biogenic silica in the ocean: Revised global estimates, comparison with regional data and relationships to biogenic sedimentation. *Global Biogeochemical Cycles*, 9:359–372.

Nerger, L. and Gregg, W. W. (2007). Assimilation of SeaWiFS data into a global ocean-biogeochemical model using a local SEIK filter. *Marine Systems*, 68:237–254.

Neuheimer, A. B., Thresher, R. E., Lyle, J. M., and Semmens, J. M. (2011). Tolerance limit for fish growth exceeded by warming waters. *Nature Climate Change*, 1:110–113. doi:10.1038/nclimate1084.

Nimer, N. A., Brownlee, C., and Merrett, M. J. (1994). Carbon dioxide availability, intracellular pH and growth rate of the coccolithophoire Emiliania huxleyi. *Mar. Ecol. Prog. Ser.*, 109:257–262.

Nöel, S., Bovensmann, H., Burrows, J. P., Frerick, J., Chance, K. V., and Goede, A. H. P. (1999). Global atmospheric monitoring with SCIAMACHY. *Physics and Chemistry of the Earth*, 24(5):427–434.

Obata, A., Ishizaka, J., and Endoh, M. (1996). Global verification of critical depth theory for phytoplankton bloom with climatologicalin situ temperature and satellite ocean color data. *Journal OF Geophysical Research*, 101(C9):20657–20667.

Oliveira, L., Piola, A., Mata, M., and Soares, I. (2009). Brazil Current surface circulation and energetics observed from drifting buoys. *Journal of Geophysical Research*, 114(C10006).

O'Reilly, J. E., Maritorena, S., Mitchell, B. G., Carder, K. L., Siegel, D. A., and Garver, S. A. (2000). Seawifs postlaunch calibration and validation analyses. *NASA Tech. Memo.*, 11.

O'Reilly, J. E., Maritorena, S., Mitchell, B. G., Siegel, D. A., Carder, K. L., Garver, S. A., Kahru, M., and McClain, C. (1998). Ocean color chlorophyll algorithms for SeaWiFS. *Journal of Geophysical Research*, 103.

Painter, S., Poulton, A., Allen, J., Pidcock, R., and Balch, W. (2010). The COPAS'08 expedition to the Patagonian shelf: Physical and environmental conditions during the 2008 coccolithophore bloom. *Continental Shelf Research*, 30:1907–1923.

Perner, D. and Platt, U. (1979). Detection of nitrous acid in the atmosphere by differential optical absorption. *Geophys. Res. Lett.*, 93.

Petzold, T. J. (1972). Volume scattering functions for selected ocean waters. *Scripps Inst. Oceanogr.*, page 79. La Jolla.

Platt, T., Fuentes-Yaco, C., and Frank, K. T. (2003). Spring algal bloom and larval fish. *Nature*, 423:398–399.

Platt, T. and Herman, A. W. (1983). Remote sensing of phytoplankton in the sea: surface-layer chlorophyll as an estimate of water-column chlorophyll and primary production. *Int. J. Remote Sensing*, 4(2):343–351.

Platt, T., Sathyendranath, S., and Stuart, V. (2006). Why study biological oceanography? *Aquabiology*, 28:542–557.

Podesta, G. P. and Esaias, W. E. (1988). Satellite-derived phytoplankton pigment concentrations along the shelf break off Argentina, 1979-1980. *EOS*.

Quere, C. L., Harrison, S., Prentice, I. C., Buitenhuis, E. T., Aumont, O., and Bopp, L. (2005). Ecosystem dynamics based on plankton functional types for global ocean biogeochemistry models. *Global Change Biol.*, 11(11).

Raitsos, D., Lavender, S., Pradhan, Y., Tyrrell, T., Reid, P., and Edwards, M. (2006). Coccolithophore bloom size variation in response to the regional environment of the subarctic North Atlantic. *Limnol. Oceanogr*, 51:2122–2130.

Raitsos, D. E., Lavender, S. J., Maravelias, C. D., Haralambous, J., Richardson, A. J., and Reid, P. C. (2008). Identifying four phytoplankton functional types from space: An ecological approach. *Limnology and Oceanography*, 53(2):605–613.

Raven, J. A. (1998). Small is beautiful: The picophytoplankton. *Functional Ecology*, 12:503–513.

Raven, J. A. and Falkowski, P. G. (1999). Oceanic sinks for atmospheric CO_2. *Plant, Cell and Environ.*, 22:741–755.

Redfield, A. C., Ketchum, B. H., and Richards, F. A. (1963). *The influence of organisms on the composition of seawater*, chapter in M. N. Hill (Ed.): The Sea, pages 26–77. John Wiley & Sons, New York.

Rhodes, L., Peake, B., MacKenzie, A., and Marwick, S. (1995). Coccolithophores gephyrocapsa oceanica and Emiliania huxleyi (Prymnesiophyceae= Haptophyceae) in New Zealand's coastal waters: Characteristics of blooms and growth in laboratory culture. *New Zealand J. of Marine and Freshwater Res.*, 29(3):345–357.

Ridgway, K. R. (2007). Long-term trend and decadal variability of the southwardpenetration of the East Australian Current. *Geophys. Res. Lett.*, 34(L13613).

Robertson, J. E., Robinson, C., Turner, D. R., Holligan, P., Watson, A. J., and Boyd, P. (1994). The impact of a coccolithophore bloom on oceanic carbon uptake in the North-east Atlantic during the summer 1991. *Deep-Sea Research I*, 41:297–314.

Roettgers, R., Haese, C., and Doerffer, R. (2007). Determination of the particulate absorption of microalgae using a point-source integrating-cavity absorption meter: verification with a photometric technique, improvements for pigment bleaching, and correction for chlorophyll fluorescence. *Limnol. Oceanogr.: Methods*, 5.

Romero, S., Piola, A., Charo, M., and Garcia, C. (2006). Chlorophyll-a variability off Patagonia based on SeaWiFS data. *Journal of Geophysical Research*, 111(C05021).

Rost, B. and Riebesell, U. (2004). *Emiliana huxleyi: bloom observations and the conditions that induce them*, chapter in H. R. Thierstein and J. R. Young (eds.): Coccolithophores. From Molecular Processes to Global Impact, pages 99–126. Springer, New York.

Rozanov, V. V., Buchwitz, M., Eichmann, K.-U., de Beek, R., and Burrows, J. P. (2002). Sciatran - a new radiative transfer model for geophysical applications in the 240-2400 nm spectral region: the pseudo-spherical version. *Advances in Space Research*, 29(11):1831–1835.

Sabatini, M. E., Reta, R., and Matano, R. (2004). Circulation and zooplankton biomass distribution over the southern Patagonian shelf during late summer. *Cont. Shelf Res.*, 24:1359–1373. doi:10.1016/j.csr.2004.03.014.

Sabine, C. L., Feely, R. A., Gruber, N., Key, R. M., Lee, K., Bullister, J. L., Wanninkhof, R., Wong, C. S., D. W. R. Wallace, a. B. T., Millero, F. J., Peng, T. H., Kozyr, A., Ono, T., and Rios, A. F. (2004). The oceanic sink for anthropogenic CO_2. *Science*, 305(5682):367–371.

Sadeghi, A., Dinter, T., Vountas, M., Taylor, B., Altenburg-Soppa, M., and Bracher, A. (2012a). Remote sensing of coccolithophore blooms in selected oceanic regions using the PhytoDOAS method applied to hyper-spectral satellite data. *Biogeosciences*, 9:2127–2143. doi:10.5194/bg-9-2127-2012.

Sadeghi, A., Dinter, T., Vountas, M., Taylor, B., Altenburg-Soppa, M., Peeken, I., and Bracher, A. (2012b). Improvements to PhytoDOAS method for identication of major phytoplankton groups using hyper-spectral data. *Ocean Sci.*, 8:1055–1070. doi:10.5194/os-8-1055-2012.

Samiento, J. L. and Gruber, N. (2006). *Ocean Biogeochemical Dynamics*. Princeton University Press.

Saraceno, M., Provost, C., Piola, A., Bava, J., and Gagliardini, A. (2004). Brazil Malvinas Frontal system as seen from 9 years of advanced very high resolution radiometer data. *J. Geophys. Res.*, 109(C05027).

Sarmiento, J. L., Slater, R., Barber, R., Bopp, L., Doney, S. C., Hirts, A. C., Kleypas, J., and Stouffer, R. (2004). Response of ocean ecosystems to climate warming. *Global Biogeochem. Cycles*, 18(GB3003).

Sarthou, G., Timmermans, K. R., Blain, S., and Treguer, P. (2005). Growth physiology and fate of diatoms in the ocean: A review. *Journal of Sea Research*, 53:25–42.

Sathyendranath, S., Cota, G., Stuart, V., Maass, H., and Platt, T. (2001). Remote sensing of phytoplankton pigments: a comparison of empirical and theoretical approaches. *Int. J. Remote Sensing*, 22(2 & 3):249–273.

Sathyendranath, S. and Platt, T. (1998). Ocean-color model incorporating transspectral processes. *Appl. Opt.*, 37(12):2216–2227.

Sathyendranath, S. and Platt, T. (2007). Spectral effects in bio-optical control on the ocean system. *Oceanologia*, 49(1):5–39.

Sathyendranath, S., Watts, L., Devred, E., Platt, T., Caverhill, C., and Maass, H. (2004). Discrimination of diatoms from other phytoplankton using ocean-colour data. *Marine Ecology Progress Series*, 272.

Scharek, R., Tupas, L. M., and Karl, D. M. (1999). Diatom fluxes to the deep sea in oligotrophic North Pacific gyre at station aloha. *Marine Ecology. Progress Series*, 182:55–67.

Schloss, I., Ferreyra, G., Ferrario, M., Almandoz, G., Codna, R., Bianchi, A., Balestrini, C., Ochoa, H., Pino, D., and Poisson, A. (2007). Role of plankton communities in sea-air variations in pCO_2 in the SW Atlantic ocean. *Marine Ecology Progress Series*, 332:93–106.

Schoemann, V., Becquevort, S., Stefels, J., W, W. R., and Lancelot, C. (2005). Phaeocystis blooms in the global ocean and their controlling mechanisms: a review. *Journal of Sea Research*, 53:43–66.

Schopf, P. S. and Loughe, A. (1995). A reduced gravity isopycnal ocean model: hindcasts of El-Nino. *Mon. Weather Rev.*, 123:2839–2863.

Sieburth, J. M., Smetacek, V., and Lenz, J. (1978). Pelagic ecosystem structure: Heterotrophic compartments of the plankton and their relationship to plankton size fractions. *Limnology and Oceanography*, 23:1256–1263.

Siegenthaler, U. and Sarmiento, J. L. (1993). Atmospheric carbon dioxide and the ocean. *Nature*, 365:119–125.

Simo, R. (2001). Production of atmospheric sulfur by oceanic plankton: biogeochemical, ecological and evolutionary links. *Trends in Ecology & Evolution*, 16:287–294.

Singh, H. B., Tabazadeh, A., Evans, M. J., Field, B. D., Jacob, D. J., Sachse, G., Crawford, J. H., Shetter, R., and Brune, W. H. (2003). Oxygenated volatile organic chemicals in the oceans: interferences and implications based on atmospheric observations and air-sea flux exchange models. *Geophys. Res. Lett.*, 30.

Smayda, T. J. (1997a). Harmful algal blooms: Their ecophysiology and general relevance to phytoplankton blooms in the sea. *Limnology and Oceaanography*, 42(5(2)):1137–1153.

Smayda, T. J. (1997b). What is a bloom? a commentary. *Limnology and Oceanography*, 42(5(2)):1132–1136.

Smayda, T. J. and Reynolds, C. S. (2003). Strategies of marine dinoflagellate survival and some rules of assembly. *Journal of Sea Research*, 49:95–106.

Smetacek, V. (2001). A watery arms race. *Nature*, 411:745.

Smith, R. C. and Baker, K. S. (1978). The bio-optical state of ocean waters and remote sensing. *Limnol. Oceanogr.*, 23(2):247–259.

Smith, R. C. and Baker, K. S. (1981). Optical properties of the clearest natural waters (200–800nm). *Appl. Opt.*, 20.

Smyth, T., Tyrrell, T., and Tarrant, B. (2004). Time series of coccolithophore activity in the Barents Sea, from twenty years of satellite imagery. *Geophysical Research Letters*, 31(L11302).

Solomon, S., Garcia, R., and Ravishankara, A. R. (1994). On the role of iodine in ozone depletion. *J. Geophys. Res.*, 99(20):491–499.

Solomon, S., Qin, D., Manning, M., Chen, Z., Marquis, M., Averyt, K., Tignor, M., and Miller, H., editors (2007). *Climate Change 2007: The Physical Science Basis. Contribution of Working Group I to the Fourth Assessment Report of the Intergovernmental Panel on Climate Change*. Cambridge University Press, Cambridge, UK and New York, USA.

Spadone, A. and Provost, C. (2009). Variations in the Malvinas Current volume transport since october 1992. *Journal of Geophysical Research*, 114(C02002).

Stone, J. M. (1953). *Radiation and Optics*. McGraw-Hill, New York.

Stramski, D., Reynolds, R., Kahru, M., and Mitchell, B. G. (1999). Estimation of particulate organic carbon in the ocean from satellite remote sensing. *Science*, 285(5425):239–242.

Stumpf, R. P. and Tomlinson, M. C. (2005). Use of remote sensing in monitoring and forecasting of harmful algal blooms. In Frouin, R. J., Babin, M., and Sathyendranath, S., editors, *Remote Sensing of the Coastal Oceanic Environment*, volume 5885, pages 148–151. SPIE.

Sugihara, S., Kishino, M., and Okami, M. (1984). Contribution of Raman scattering to upward irradiance in the sea. *J. Oceanogr. Soc. Japan*, 40:397–404.

Sunda, W., Kleber, D. J., Klene, R. P., and Huntsman, S. (2002). An antioxidant function for DMSP and DMS in marine algae. *Nature*, 418:317–320.

Sverdrup, U. (1953). On conditions for the vernal blooming of phytoplankton. *J. Cons. Cons. Int. Explor. Mer.*, 18:287–295.

Taylor, F. J. R. (1990). Red tides, brown tides and other harmful algal blooms: The view into the 1990's. In *Proceedings of 4th International Conference on Toxic marine phytoplankton*, pages 527–533.

Thierstein, H. R. and Young, J. R., editors (2004). *Coccolithophores: From Molecular Processes to Global Impact*. Springer New York.

Tilburg, C., Subrahmanyam, B., and O'Brien, J. (2002). Ocean color variability in the Tasman Sea. *Geophysical Research Letters*, 29(10):1487–1481. 10.1029/2001GL014071.

Turner, S. and Liss, P. (1983). The oceans and the global sulphur budget. *Nature*, 305(5932):277.

Tyrrell, T., Holligan, P., and Mobley, C. D. (1999). Optical impacts of oceanic coccolithophore blooms. *Journal of Geophysical Research*, 104(C2):3223–3241.

Tyrrell, T. and Merico, A. (2004). *Emiliana huxleyi: bloom observations and the conditions that induce them*, chapter in H. R. Thierstein and J. R. Young (eds): Coccolithophores. From Molecular Processes to Global Impact, pages 75–97. Springer-Verlag Berlin Heidelberg.

Tyrrell, T. and Taylor, A. (1996). A modelling study of Emiliania huxleyi in the NE Atlantic. *J. Mar. Syst*, 9:83–112.

Uitz, J., Claustre, H., Morel, A., and Hooker, S. B. (2006). Vertical distribution of phytoplankton communities in open ocean: An assessment based on surface chlorophyll. *J. Geophysical Res.*, 111(CO8005).

Valeur, B. (2001). *Molecular Fluorescence: Principles and Applications*. Wiley. ISBN: 978-3-527-29919-5.

Vasilkov, A. P., Joiner, J., Gleason, J., and Bhartia, P. (2002). Ocean Raman scattering in satellite backscatter UV measurements. *Geophys. Res. Let.*, 29. doi:10.1029/2002GL014955.

Vogt, R., Sander, R., von Glasow, R., and Crutzen, P. J. (1999). Iodine chemistry and its role in halogen activation and ozone loss in the marine boundary layer: A model study. *J. Atmos. Chem.*, 32:375–395.

Volk, T. and Hoffert, M. I. (1985). *Ocean carbon pumps: Analysis of relative strengths and efficiencies in ocean-driven atmospheric CO_2 changes*, chapter in E.T. Sundquist and W.S. Broecker (eds.): The Carbon Cycle and Atmospheric CO_2: Natural Variations Archean to Present, pages 99–110. 32. Geophys. Monogr., AGU, Washington, D.C.

Vountas, M., Dinter, T., Bracher, A., Burrows, J. P., and Sierk, B. (2007). Spectral studies of ocean water with space-borne sensor SCIAMACHY using differential optical absorption spectroscopy (DOAS). *Ocean Sci.*, 3.

Vountas, M., Richter, A., Wittrock, F., and Burrows, J. P. (2003). Inelastic scattering in ocean water and its impact on trace gas retrievals from satellite data. *Atmos. Chem. Phys.*, 3.

Vountas, M., Rozanov, V. V., and Burrows, J. P. (1998). Ring effect: Impact of rotational Raman scattering on radiative transfer in Earth's atmosphere. *J. Quant. Spectrosc. Radiat. Transfer*, 60.

Wagner, T., Chance, K., Friess, U., Gil, M., Goutail, F., Hoenninger, G., Johnston, P. V., Karlsen-Tornkvist, K., I., I. K., Leser, H., Petritoli, A., Richter, A., Roozendael, M. V., and Platt, U. (2001). Correction of the Ring effect and I_0-effect for DOAS observations of scattered sunlight. In *Proc. book of the 1st DOAS Workshop*, Heidelberg, Germany.

Wakeham, S., Lee, C., Hedges, J. I., Hernes, P. J., and Peterson, M. L. (1997). Molecular indicators of the diagenetic status of marine organic matter. *Geochim. Cosmochim. Acta.*, 61:5363–5369.

Westbroek, P., Brown, C. W., Van-Bleijswijket, J., Brownlee, C., Brummer, G., Conte, M., Egge, J., Fernandez, E., Jordan, R., Knappertsbusch, M., Stefels, J., Veldhuis, M., der Wal, P. V., and Young, J. (1993). A model approach to biological climate forcing. the example of Emiliania huxleyi. *Global and Planetary Change*, 8:27–46.

Williams, R. G. (2011). Ocean eddies and plankton blooms. *Nature Geoscience*, 4:739–740.

Williams, R. G. and Follows, M. J. (1998). Oceanography: Eddies make ocean deserts bloom. *Nature*, 394:228–229.

Winder, M. and Cloernet, J. (2010). The annual cycles of phytoplankton biomass. *Phil. Trans. R. Soc.*, 365:3215–3226.

Winter, A., Jordan, R. W., and Roth, P. H. (1994). *Biogeography of living coccolithophores in ocean waters*, chapter in A. Winter and W.G. Siesser (eds.): Coccolithophores, pages 39–49. Cambridge Univ.

Yassaa, N., Peeken, I., Zöllner, E., Bluhm, K., Arnold, S., Spracklen, D., and Williams, J. (2008). Evidence for marine production of monoterpenes. *Environmental Chemistry*, 5.

Yool, A. and Tyrrell, T. (2003). Role of diatoms in regulating the ocean's silicon cycle. *global biogeochemical cycles*, 17(4):1103.

Young, A. T. (1982). Rayleigh scattering. *Phys. Today*, 35.

Zehr, J. P., Waterbury, J. B., Turner, P. J., Montoya, J. P., Omoregie, E., and Steward, G. F. (2001). Unicellular cyanobacteria fix N_2 in the subtropical north pacific ocean. *Nature*, 412:635–638.

Zubkov, M. V., Sleigh, M. A., Burkill, P. H., and Leakey, R. J. G. (2000). Picoplankton community structure on the Atlantic meridional transect: A comparison between seasons. *Prog. Oceanogr.*, 45.

Acknowledgements

I would like to thank cordially all the people involved in the realization of this work and whoever directly or indirectly helped me to proceed with my PhD work:

I am very grateful to Prof. Dr. Astrid Bracher, who supervised my study carefully and patiently and supported this work thoroughly by spending a lot of time on guiding me, as well as on reviewing chapters of this thesis.

My special thanks to Dr. Marco Vountas who was always available for scientific discussions, sharing ideas and helping. He provided me with valuable hints and technical supports, as well as with his kind encouragements and millions of coffee pads!

I wish to express my deep gratitude to Dr. Tilman Dinter, my pleasant office-mate and friend, who helped me a lot with scientific and technical issues, as well as reviewing carefully two chapters of the thesis.

I wish to acknowledge Prof. Dr. John P. Burrows and Dr. Heinrich Bovensmann for their kind supports and encouragements during my study, in particular their valuable comments as members of my PhD committee.

I thank the rest of my colleagues (and ex-colleagues) in Phytooptics group for their nice collaborations and precise feed-backs during our regular meetings: Dr. Bettina Taylor, Mariana Altenburg Soppa, Mirjam Blum, Anja Bernhardt, Alexandra Cherkasheva, Sonja Wiegmann, Elena Torrecilla, Marc Taylor, Erika Allhusen.

Many thanks to Dr. Christoph Völker for attending my PhD committees and providing me with his clever hints and comments.

I am thankful to ESA, DLR, and the SCIAMACHY Quality Working Group (SQWG) for providing us with SCIAMACHY level-1 data. I thank also NASA-GSFC for NOBM model data (Giovanni GES-DISC project) and the MODIS-Aqua data and RGB pictures. I am also grateful to AVHRR, AMSR-E and FNMOC for providing SST, surface wind-speed and MLD data, respectively.

Funding was provided by the HGF Innovative Network Funds (Phytooptics), to which I express my appreciations.

This work is a contribution to the Earth System Science Research School (ESSReS), an initiative of the Helmholtz Association of German research centers (HGF) at the Alfred Wegener Institute for Polar and Marine Research. Hereby, I acknowledge both. In particular, I thank cordially Dr. Klaus Grosfeld, the coordinator of ESSReS, for his kind supports and valuable efforts.

My cordial appreciations to the kindness of those friends/colleagues who took part in proof-readings of different parts of the thesis: Andreas Hilboll, Aleksandra Wolanin, Christian Gutche, Arezoo P., Mahvash N., Arash K. and AbhinandA.. I owe them my best thanks for their nice efforts.

I thank a lot to Dr. Vladimir Rozanov for his patient and instructive supports during our several training sessions on SCIATRAN.

Many thanks to Farhad Shakeri and Jongmin Yoon for supporting me kindly with some graphics in a short time.

I am thankful to all IUP members for providing the nice atmosphere surrounding us and for their kind helps and encouragements. I also thank Petra Horn, Birgit Teuchert and Lars Jeschke for their administrative supports.

I appreciate greatly the support and flexibility of my new colleagues, Prof. Dr. Notholt and Dr. Mathias Palm, who gave me the opportunity to finalize the thesis in tranquility.

I thank all my friends in ESSReS because of all ideas I learned from them, as well as the nice times we spent together during courses and seminars.

Many thanks to my co-smoker friends (active or passive Raucher!) for sharing and reducing the stress-loads, as well as for their encouragements and friendly supports: Janina, Gregor (passive), Luca, Wissam, Faiza and Shahin.

Many thanks to Carl Kothe and Wolfhardt Lotz for providing happy minutes in our "coffee time" (along with Marco and Tilman). Thanks also to Martin and Jan for their nice tips during our Thursdays lunch times. Thanks to Vladyslav Nenakhov for his coragious company during work in IUP on Christmas vacation time!

And finally, I should thank Christoph Hoffmann for his technical advices for printing the thesis!

Additionally, I would like to express my deepest gratitude to my family members and close friends, who patiently accepted my absebce in the tough times and besides that always encouraged me. I owe also my cordial thanks to my earlier professors and teachers, especially Dr. Hamid R. Sepangi and Hasan Adibi, who inspired me to pursue in science.

I greatly thank you all for your supports and kindness. Danke schön!